Eur. Phys. J. A (2013) **49**: 25
DOI 10.1140/epja/i2013-13025-8

THE EUROPEAN PHYSICAL JOURNAL A

Special Article – Tools for Experiment and Theory

Technical design report for the $\overline{\mathrm{P}}$ANDA (AntiProton Annihilations at Darmstadt) Straw Tube Tracker

Strong interaction studies with antiprotons

W. Erni[1], I. Keshelashvili[1], B. Krusche[1], M. Steinacher[1], Y. Heng[2], Z. Liu[2], H. Liu[2], X. Shen[2], Q. Wang[2], H. Xu[2], A. Aab[3], M. Albrecht[3], J. Becker[3], A. Csapó[3], F. Feldbauer[3], M. Fink[3], P. Friedel[3], F.H. Heinsius[3], T. Held[3], L. Klask[3], H. Koch[3], B. Kopf[3], S. Leiber[3], M. Leyhe[3], C. Motzko[3], M. Pelizäus[3], J. Pychy[3], B. Roth[3], T. Schröder[3], J. Schulze[3], C. Sowa[3], M. Steinke[3], T. Trifterer[3], U. Wiedner[3], J. Zhong[3], R. Beck[4], S. Bianco[4], K.T. Brinkmann[4], C. Hammann[4], F. Hinterberger[4], D. Kaiser[4], R. Kliemt[4], M. Kube[4], A. Pitka[4], T. Quagli[4], C. Schmidt[4], R. Schmitz[4], R. Schnell[4], U. Thoma[4], P. Vlasov[4], D. Walther[4], C. Wendel[4], T. Würschig[4], H.G. Zaunick[4], A. Bianconi[5], M. Bragadireanu[6], M. Caprini[6], D. Pantea[6], D. Pantelica[6], D. Pietreanu[6], L. Serbina[6], P.D. Tarta[6], D. Kaplan[7], T. Fiutowski[8], M. Idzik[8], B. Mindur[8], D. Przyborowski[8], K. Swientek[8], B. Czech[9], M. Kistryn[9], S. Kliczewski[9], A. Kozela[9], P. Kulessa[9], P. Lebiedowicz[9], K. Pysz[9], W. Schäfer[9], R. Siudak[9], A. Szczurek[9], S. Jowzaee[10], M. Kajetanowicz[10], B. Kamys[10], S. Kistryn[10], G. Korcyl[10], K. Korcyl[10], W. Krzemien[10], A. Magiera[10], P. Moskal[10], M. Palka[10], Z. Rudy[10], P. Salabura[10], J. Smyrski[10], A. Wrońska[10], I. Augustin[11], I. Lehmann[11], D. Nimorus[11], G. Schepers[11], M. Al-Turany[12], R. Arora[12], H. Deppe[12], H. Flemming[12], A. Gerhardt[12], K. Götzen[12], A.F. Jordi[12], G. Kalicy[12], R. Karabowicz[12], D. Lehmann[12], B. Lewandowski[12], J. Lühning[12], F. Maas[12], H. Orth[12], M. Patsyuk[12], K. Peters[12], T. Saito[12], G. Schepers[12], C.J. Schmidt[12], L. Schmitt[12], C. Schwarz[12], J. Schwiening[12], M. Traxler[12], B. Voss[12], P. Wieczorek[12], A. Wilms[12], M. Zühlsdorf[12], V.M. Abazov[13], G. Alexeev[13], A. Arefiev[13], V.I. Astakhov[13], M.Yu. Barabanov[13], B.V. Batyunya[13], Yu.I. Davydov[13], V.Kh. Dodokhov[13], A.A. Efremov[13], A.G. Fedunov[13], A.A. Festchenko[13], A.S. Galoyan[13], S. Grigoryan[13], A. Karmokov[13], E.K. Koshurnikov[13], V.I. Lobanov[13], Yu.Yu. Lobanov[13], A.F. Makarov[13], L.V. Malinina[13], V.L. Malyshev[13], G.A. Mustafaev[13], A. Olshevskiy[13], M.A. Pasyuk[13], E.A. Perevalova[13], A.A. Piskun[13], T.A. Pocheptsov[13], G. Pontecorvo[13], V.K. Rodionov[13], Yu.N. Rogov[13], R.A. Salmin[13], A.G. Samartsev[13], M.G. Sapozhnikov[13], G.S. Shabratova[13], A.N. Skachkova[13], N.B. Skachkov[13], E.A. Strokovsky[13], M.K. Suleimanov[13], R.Sh. Teshev[13], V.V. Tokmenin[13], V.V. Uzhinsky[13], A.S. Vodopyanov[13], S.A. Zaporozhets[13], N.I. Zhuravlev[13], A.G. Zorin[13], D. Branford[14], D. Glazier[14], D. Watts[14], P. Woods[14], A. Britting[15], W. Eyrich[15], A. Lehmann[15], F. Uhlig[15], S. Dobbs[16], Z. Metreveli[16], K. Seth[16], A. Tomaradze[16], T. Xiao[16], D. Bettoni[17], V. Carassiti[17], A. Cotta Ramusino[17], P. Dalpiaz[17], A. Drago[17], E. Fioravanti[17], I. Garzia[17], M. Savriè[17], G. Stancari[17], N. Bianchi[18], P. Gianotti[18,a], C. Guaraldo[18], V. Lucherini[18], D. Orecchini[18], E. Pace[18], A. Bersani[19], G. Bracco[19], M. Macri[19], R.F. Parodi[19], D. Bremer[20], V. Dormenev[20], P. Drexler[20], M. Düren[20], T. Eissner[20], K. Föhl[20], M. Galuska[20], T. Gessler[20], A. Hayrapetyan[20], J. Hu[20], P. Koch[20], B. Kröck[20], W. Kühn[20], S. Lange[20], Y. Liang[20], O. Merle[20], V. Metag[20], M. Moritz[20], D. Münchow[20], M. Nanova[20], R. Novotny[20], B. Spruck[20], H. Stenzel[20], T. Ullrich[20], M. Werner[20], H. Xu[20], C. Euan[21], M. Hoek[21], D. Ireland[21], T. Keri[21], R. Montgomery[21], D. Protopopescu[21], G. Rosner[21], B. Seitz[21], M. Babai[22], A. Glazenborg-Kluttig[22], M. Kavatsyuk[22], P. Lemmens[22], M. Lindemulder[22], H. Löhner[22], J. Messchendorp[22], H. Moeini[22], P. Schakel[22], F. Schreuder[22], H. Smit[22], G. Tambave[22], J.C. van der Weele[22], R. Veenstra[22], H. Sohlbach[23], M. Büscher[24], D. Deermann[24], R. Dosdall[24], S. Esch[24], A. Gillitzer[24], F. Goldenbaum[24], D. Grunwald[24], S. Henssler[24], A. Herten[24], Q. Hu[24], G. Kemmerling[24], H. Kleines[24], V. Kozlov[24], A. Lehrach[24], R. Maier[24], M. Mertens[24], H. Ohm[24], S. Orfanitski[24], D. Prasuhn[24], T. Randriamalala[24], J. Ritman[24], M. Röder[24], S. Schadmand[24], V. Serdyuk[24], G. Sterzenbach[24], T. Stockmanns[24], P. Wintz[24], P. Wüstner[24], H. Xu[24], J. Kisiel[25], S. Li[26], Z. Li[26], Z. Sun[26], H. Xu[26], V. Rigato[27], S. Fissum[28], K. Hansen[28], L. Isaksson[28], M. Lundin[28], B. Schröder[28], P. Achenbach[29], S. Bleser[29], U. Cahit[29], M. Cardinali[29], A. Denig[29], M. Distler[29], M. Fritsch[29], P. Jasinski[29], D. Kangh[29], A. Karavdina[29], W. Lauth[29], H. Merkel[29], M. Michel[29], M.C. Mora Espi[29], U. Müller[29], J. Pochodzalla[29], S. Sanchez[29], A. Sanchez-Lorente[29], S. Schlimme[29], C. Sfienti[29], M. Thiel[29], T. Weber[29], V.I. Dormenev[30], A.A. Fedorov[30], M.V. Korzhik[30], O.V. Missevitch[30], V. Balanutsa[31], V. Chernetsky[31], A. Demekhin[31], A. Dolgolenko[31], P. Fedorets[31], A. Gerasimov[31], V. Goryachev[31], V. Varentsov[31], A. Boukharov[32], O. Malyshev[32], I. Marishev[32], A. Semenov[32], F. Böhmer[33],

---

[a] e-mail: paola.gianotti@lnf.infn.it

S. Dørheim[33], B. Ketzer[33], S. Paul[33], A.K. Hergemöller[34], A. Khoukaz[34], E. Köhler[34], A. Täschner[34], J. Wessels[34], R. Varma[35], A. Chaterjee[36], V. Jha[36], S. Kailas[36], B.J. Roy[36], Y. Yan[37], K. Chinorat[37], K. Khanchai[37], L. Ayut[37], S. Pomrad[37], E. Baldin[38], K. Kotov[38], S. Peleganchuk[38], Yu. Tikhonov[38], J. Boucher[39], V. Chambert[39], A. Dbeyssi[39], M. Gumberidze[39], T. Hennino[39], M. Imre[39], R. Kunne[39], C. Le Galliard[39], B. Ma[39], D. Marchand[39], A. Maroni[39], S. Ong[39], B. Ramstein[39], P. Rosier[39], E. Tomasi-Gustafsson[39], J. Van de Wiele[39], G. Boca[40], A. Braghieri[40], S. Costanza[40], P. Genova[40], L. Lavezzi[40], P. Montagna[40], A. Rotondi[40], V. Abramov[41], N. Belikov[41], A. Davidenko[41], A. Derevschikov[41], Y. Goncharenko[41], V. Grishin[41], V. Kachanov[41], D. Konstantinov[41], V. Kormilitsin[41], Y. Melnik[41], A. Levin[41], N. Minaev[41], V. Mochalov[41], D. Morozov[41], L. Nogach[41], S. Poslavskiy[41], A. Ryazantsev[41], S. Ryzhikov[41], P. Semenov[41], I. Shein[41], A. Uzunian[41], A. Vasiliev[41], A. Yakutin[41], T. Bäck[42], B. Cederwall[42], K. Makónyi[43], P.E. Tegnér[43], K.M. von Würtemberg[43], S. Belostotski[44], G. Gavrilov[44], A. Itzotov[44], A. Kashchuk[44], A. Kisselev[44], P. Kravchenko[44], O. Levitskaya[44], S. Manaenkov[44], O. Miklukho[44], Y. Naryshkin[44], D. Veretennikov[44], V. Vikhrov[44], A. Zhadanov[44], D. Alberto[45], A. Amoroso[45], M.P. Bussa[45], L. Busso[45], F. De Mori[45], M. Destefanis[45], L. Fava[45], L. Ferrero[45], M. Greco[45], M. Maggiora[45], S. Marcello[45], S. Sosio[45], S. Spataro[45], L. Zotti[45], D. Calvo[46], S. Coli[46], P. De Remigis[46], A. Filippi[46], G. Giraudo[46], S. Lusso[46], G. Mazza[46], O. Morra[46], A. Rivetti[46], R. Wheadon[46], F. Iazzi[47], A. Lavagno[47], H. Younis[47], R. Birsa[48], F. Bradamante[48], A. Bressan[48], A. Martin[48], H. Clement[49], B. Galander[50], L. Caldeira Balkeståhl[51], H. Calén[51], K. Fransson[51], T. Johansson[51], A. Kupsc[51], P. Marciniewski[51], E. Thomé[51], M. Wolke[51], J. Zlomanczuk[51], J. Díaz[52], A. Ortiz[52], K. Dmowski[53], P. Duda[53], R. Korzeniewski[53], B. Slowinski[53], A. Chlopik[54], Z. Guzik[54], K. Kosinski[54], D. Melnychuk[54], A. Wasilewski[54], M. Wojciechowski[54], S. Wronka[54], A. Wysocka[54], B. Zwieglinski[54], P. Bühler[55], O.N. Hartman[55], P. Kienle[55], J. Marton[55], K. Suzuki[55], E. Widmann[55], and J. Zmeskal[55]

[1] Universität Basel, Switzerland
[2] Institute of High Energy Physics, Chinese Academy of Sciences, Beijing, China
[3] Universität Bochum I. Institut für Experimentalphysik, Germany
[4] Rheinische Friedrich-Wilhelms-Universität Bonn, Germany
[5] Università di Brescia, Italy
[6] Institutul National de C&D pentru Fizica si Inginerie Nucleara “Horia Hulubei”, Bukarest-Magurele, Romania
[7] IIT, Illinois Institute of Technology, Chicago, USA
[8] AGH, University of Science and Technology, Cracow, Poland
[9] IFJ, Institute of Nuclear Physics PAN, Cracow, Poland
[10] Instytut Fizyki, Uniwersytet Jagiellonski, Cracow, Poland
[11] FAIR, Facility for Antiproton and Ion Research in Europe, Darmstadt, Germany
[12] GSI Helmholtzzentrum für Schwerionenforschung GmbH, Darmstadt, Germany
[13] Veksler-Baldin Laboratory of High Energies (VBLHE), Joint Institute for Nuclear Research Dubna, Russia
[14] University of Edinburgh, UK
[15] Friedrich Alexander Universität Erlangen-Nürnberg, Germany
[16] Northwestern University, Evanston, USA
[17] Università di Ferrara and INFN Sezione di Ferrara, Ferrara, Italy
[18] INFN, Laboratori Nazionali di Frascati, Italy
[19] INFN, Sezione di Genova, Italy
[20] Justus Liebig-Universität Gießen II. Physikalisches Institut, Germany
[21] University of Glasgow, UK
[22] Kernfysisch Versneller Instituut, University of Groningen, The Netherlands
[23] Fachhochschule Südwestfalen Iserlohn, Germany
[24] Forschungszentrum Jülich, Institut für Kernphysik, Jülich, Germany
[25] University of Silesia, Katowice, Poland
[26] Chinese Academy of Science, Institute of Modern Physics, Lanzhou, China
[27] INFN, Laboratori Nazionali di Legnaro, Italy
[28] Lunds Universitet, Department of Physics, Lund, Sweden
[29] Johannes Gutenberg-Universität, Institut für Kernphysik, Mainz, Germany
[30] Research Institute for Nuclear Problems, Belarus State University, Minsk, Belarus
[31] Institute for Theoretical and Experimental Physics, Moscow, Russia
[32] Moscow Power Engineering Institute, Moscow, Russia
[33] Technische Universität München, Germany
[34] Westfälische Wilhelms-Universität Münster, Germany
[35] IIT Bombay, Department of Physics, Mumbai, India
[36] Nuclear Physics Division, Bhabha Atomic Research Centre, Mumbai, India
[37] Suranaree University of Technology, Nakhon Ratchasima, Thailand
[38] Budker Institute of Nuclear Physics of Russian Academy of Science, Novosibirsk, Russia
[39] Institut de Physique Nucléaire, CNRS/IN2P3 and Universit Paris-sud, Orsay, France

[40] Dipartimento di Fisica, Università di Pavia, INFN Sezione di Pavia, Pavia, Italy
[41] Institute for High Energy Physics, Protvino, Russia
[42] Kungliga Tekniska Högskolan, Stockholm, Sweden
[43] Stockholms Universitet, Stockholm, Sweden
[44] Petersburg Nuclear Physics Institute of Russian Academy of Science, Gatchina, St. Petersburg, Russia
[45] Università di Torino and INFN, Sezione di Torino, Torino, Italy
[46] INFN, Sezione di Torino, Torino, Italy
[47] Politecnico di Torino and INFN Sezione di Torino, Torino, Italy
[48] Università di Trieste and INFN Sezione di Trieste, Trieste, Italy
[49] Universität Tübingen, Tübingen, Germany
[50] The Svedberg Laboratory, Uppsala, Sweden
[51] Uppsala Universitet, Institutionen för Strålningsvetenskap, Uppsala, Sweden
[52] Universitat de Valencia Dpto. de Física Atómica, Molecular y Nuclear, Spain
[53] University of Technology, Institute of Atomic Energy Otwock-Swierk, Warsaw, Poland
[54] National Centre for Nuclear Research, Warsaw, Poland
[55] Österreichische Akademie der Wissenschaften, Stefan Meyer Institut für Subatomare Physik, Wien, Austria

Received: 18 May 2012 / Revised: 15 January 2013

Communicated by E. De Sanctis

Abstract. This document describes the technical layout and the expected performance of the Straw Tube Tracker (STT), the main tracking detector of the $\overline{\mathsf{P}}$ANDA target spectrometer. The STT encloses a Micro-Vertex-Detector (MVD) for the inner tracking and is followed in beam direction by a set of GEM stations. The tasks of the STT are the measurement of the particle momentum from the reconstructed trajectory and the measurement of the specific energy loss for a particle identification. Dedicated simulations with full analysis studies of certain proton-antiproton reactions, identified as being benchmark tests for the whole $\overline{\mathsf{P}}$ANDA scientific program, have been performed to test the STT layout and performance. The results are presented, and the time lines to construct the STT are described.

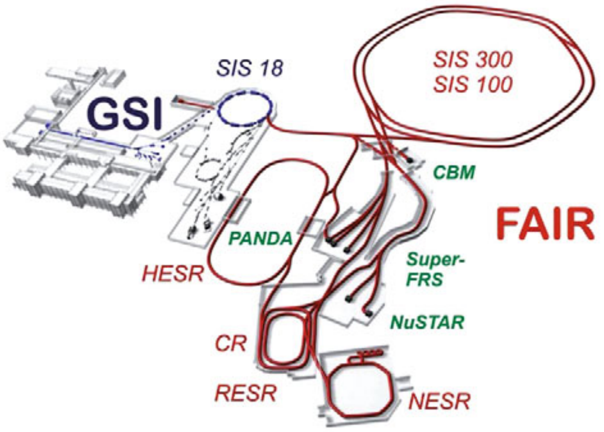

Fig. 1. Overview of the future FAIR facility. The upgraded accelerators of the existing GSI facility will act as injectors. New accelerator and storage rings are highlighted in red, experimental sites are indicated with green letters.

1 The $\overline{\text{P}}$ANDA experiment and its tracking concept

The following sections contain a general introduction to the $\overline{\text{P}}$ANDA experiment and, in particular, a short description of the implemented overall tracking concept. They belong to a common introductory part for the volumes of all individual tracking systems.

1.1 The $\overline{\text{P}}$ANDA experiment

The $\overline{\text{P}}$ANDA (Anti**P**roton **AN**nihilation at **DA**rmstadt) experiment [1] is one of the key projects at the future **F**acility for **A**ntiproton and **I**on **R**esearch (FAIR) [2,3], which is currently under construction at GSI, Darmstadt. For this new facility the present GSI accelerators will be upgraded and further used as injectors. The completed accelerator facility will feature a complex structure of new accelerators and storage rings. An overview of the FAIR facility is given in fig. 1. Further details of the accelerator complex are described in [4]. The FAIR accelerators will deliver primary proton and ion beams as well as secondary beams of antiprotons or radioactive ions, all with high energy, high intensity and high quality. Experiments to be installed at the facility will address a wide range of physics topics in the fields of nuclear and hadron physics as well as in atomic and plasma physics. An executive summary of the main FAIR projects can be found in [2] and [5].

The $\overline{\text{P}}$ANDA experiment will perform precise studies of antiproton-proton annihilations and reactions of antiprotons with nucleons of heavier nuclear targets. It will benefit from antiproton beams with unprecedented intensity and quality. The covered centre-of-mass energy between 2.3 GeV and 5.5 GeV allows for very accurate measurements, especially in the charm quark sector. Based on a broad physics program, studying the non-pertubative regime, it will be possible to explore the nature of the strong interaction and to obtain a significant progress in our understanding of the QCD spectrum and hadron structure.

Nowadays these studies are carried out mainly at electron-positron machines that offer the advantage of kinematically clean reactions but at the price of a reduced set of final states and reduced cross-sections. Also the future experiments currently planned as upgrade at existing high-energy physics facilities will not deliver high-precision data over the full charm spectrum. In this context, the $\overline{\text{P}}$ANDA experiment will be a unique tool to improve both statistics and precision of existing data and to further explore the physics in the charm quark sector. Moreover, the $\overline{\text{P}}$ANDA Collaboration is in the ideal situation to be able to benefit from the expertise gained during the construction of the LHC detectors and of the B-factory experiments, which have determined a significant progress in the detector technology due to the performed optimisation or the introduction of completely new concepts and instruments.

In the first part of this section the scientific program of $\overline{\text{P}}$ANDA will be summarised. It ranges from charmonium spectroscopy to the search for exotic hadrons and the study of nucleon structure, from the study of in-medium modifications of hadron masses to the physics of hypernuclei. Therefore, antiproton beams in the momentum range from 1.5 GeV/c to 15 GeV/c will be provided by the high-energy storage ring (HESR) to the experiment. An overview of this accelerator and storage ring will be given in the second section. To explore the broad physics program, the $\overline{\text{P}}$ANDA Collaboration wants to build a state-of-the-art general purpose detector studying annihilation reactions of antiprotons with protons ($\bar{\text{p}}$p) and in nuclear matter ($\bar{\text{p}}$A). The different target systems will be discussed in sect. 1.1.3. The $\overline{\text{P}}$ANDA apparatus consists of a set of systems surrounding an internal target placed in one of the two straight sections of the HESR. Figure 2 shows the layout of the $\overline{\text{P}}$ANDA detector. It consists of a 4 m long and 2 T strong superconducting solenoid instrumented to detect both charged and neutral particles emitted at large and backward angles (Target Spectrometer, TS) and of a 2 Tm resistive dipole magnetic spectrometer to detect charged and neutral particles emitted at angles between zero and twenty degrees (Forward Spectrometer, FS) with respect to the beam axis. A complex detector arrangement is necessary in order to reconstruct the complete set of final states, relevant to achieve the proposed physics goals. With the installed setup, a good particle identification with an almost complete solid angle will be combined with excellent mass, momentum and spatial resolution. More details of the $\overline{\text{P}}$ANDA detector will be described in sect. 1.2.

1.1.1 The scientific program

One of the most challenging and fascinating goals of modern physics is the achievement of a fully quantitative understanding of the strong interaction, which is the subject of hadron physics. Significant progress has been achieved over the past few years thanks to considerable advances

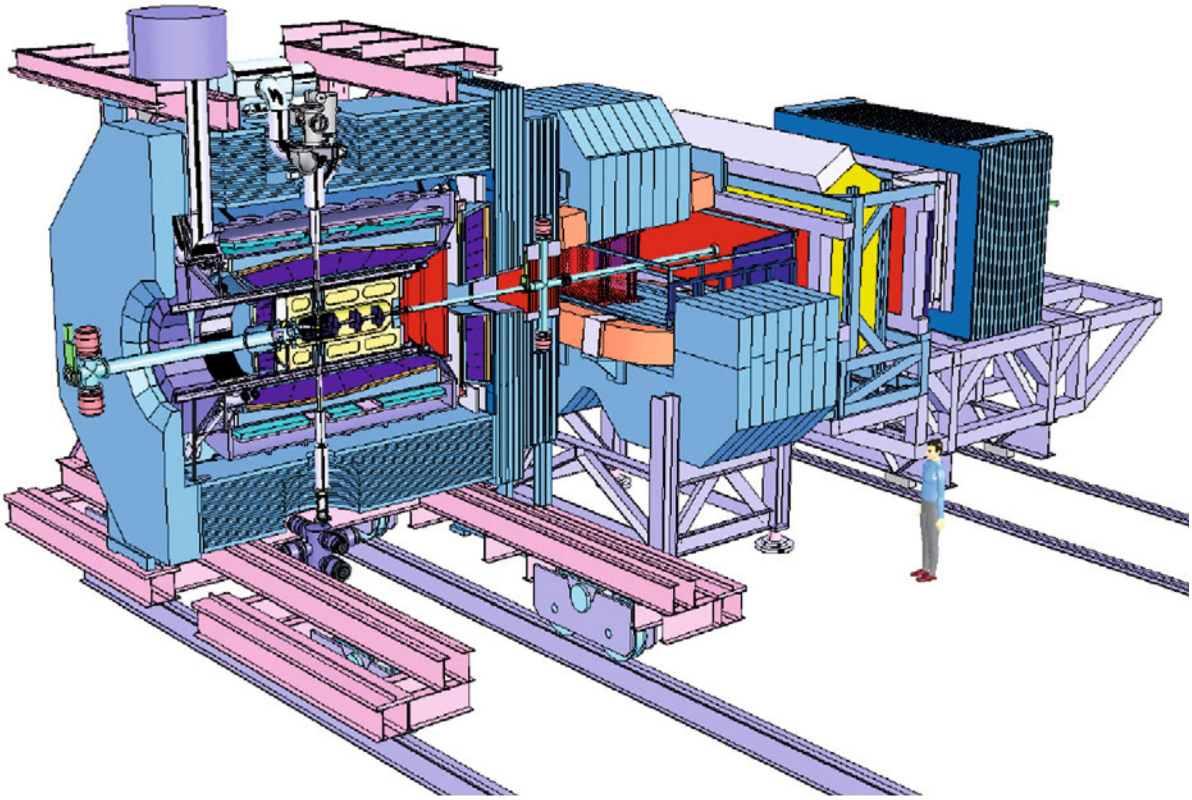

Fig. 2. Layout of the $\overline{\mathrm{P}}$ANDA detector consisting of a Target Spectrometer, surrounding the interaction region, and a Forward Spectrometer to detect particles emitted in the forward region. The HESR antiproton beam enters the apparatus from the left side.

in experiment and theory. New experimental results have stimulated a very intense theoretical activity and a refinement of the theoretical tools.

Still there are many fundamental questions which remain basically unanswered. Phenomena such as the confinement of quarks, the existence of glueballs and hybrids, the origin of the masses of hadrons in the context of the breaking of chiral symmetry are long-standing puzzles and represent the intellectual challenge in our attempt to understand the nature of the strong interaction and of hadronic matter.

Experimentally, studies of hadron structure can be performed with different probes such as electrons, pions, kaons, protons or antiprotons. In antiproton-proton annihilation, particles with gluonic degrees of freedom as well as particle-antiparticle pairs are copiously produced, allowing spectroscopic studies with very high statistics and precision. Therefore, antiprotons are an excellent tool to address the open problems.

The $\overline{\mathrm{P}}$ANDA experiment is being designed to fully exploit the extraordinary physics potential arising from the availability of high-intensity, cooled antiproton beams. The main experiments of the rich and diversified hadron physics program are briefly itemised in the following. More details can be found in the $\overline{\mathrm{P}}$ANDA physics booklet [6].

- *Charmonium spectroscopy*
  A precise measurement of all states below and above the open charm threshold is of fundamental importance for a better understanding of QCD. All charmonium states can be formed directly in $\bar{\mathrm{p}}\mathrm{p}$ annihilation. At full luminosity $\overline{\mathrm{P}}$ANDA will be able to collect several thousand $c\bar{c}$ states per day. By means of fine scans it will be possible to measure masses with accuracies of the order of 100 keV and widths to 10% or better. The entire energy region below and above the open charm threshold will be explored.
- *Search for gluonic excitations*
  One of the main challenges of hadron physics is the search for gluonic excitations, *i.e.* hadrons in which the gluons can act as principal components. These gluonic hadrons fall into two main categories: glueballs, *i.e.* states of pure glue, and hybrids, which consist of a $q\bar{q}$ pair and excited glue. The additional degrees of freedom carried by gluons allow these hybrids and glueballs to have J^{PC} exotic quantum numbers: in this case mixing effects with nearby $q\bar{q}$ states are excluded and this makes their experimental identification easier. The properties of glueballs and hybrids are determined by the long-distance features of QCD and their study will yield fundamental insight into the structure of the QCD vacuum. Antiproton-proton annihilations provide a very favourable environment in which to look for gluonic hadrons.
- *Study of hadrons in nuclear matter*
  The study of medium modifications of hadrons embedded in hadronic matter is aiming at understanding

Table 1. Experimental requirements and operation modes of HESR for the full FAIR version.

Experimental requirements	
Ion species	Antiprotons
$\bar{p}$ production rate	$2 \cdot 10^7$/s ($1.2 \cdot 10^{10}$ per 10 min)
Momentum / Kinetic energy range	1.5 to 15 GeV/c / 0.83 to 14.1 GeV
Number of particles	10^{10} to 10^{11}
Betatron amplitude at IP	1 m to 15 m
Betatron amplitude E-Cooler	25 m to 200 m
Operation modes	
High resolution (HR)	Peak luminosity of $2 \cdot 10^{31}\,\mathrm{cm}^{-2}\,\mathrm{s}^{-1}$ for 10^{10} $\bar{p}$ assuming $\rho_{target} = 4 \cdot 10^{15}$ atoms/cm^2 RMS momentum spread $\sigma_p/p \leq 4 \cdot 10^{-5}$, 1.5 to 8.9 GeV/$c$
High luminosity (HL)	Peak luminosity up to $2 \cdot 10^{32}\,\mathrm{cm}^{-2}\,\mathrm{s}^{-1}$ for 10^{11} $\bar{p}$ assuming $\rho_{target} = 4 \cdot 10^{15}$ atoms/cm^2 RMS momentum spread $\sigma_p/p \sim 10^{-4}$, 1.5 to 15 GeV/c

the origin of hadron masses in the context of spontaneous chiral symmetry breaking in QCD and its partial restoration in a hadronic environment. So far experiments have been focussed on the light quark sector. The high-intensity $\overline{\mathrm{p}}$ beam of up to 15 GeV/c will allow an extension of this program to the charm sector both for hadrons with hidden and open charm. The in-medium masses of these states are expected to be affected primarily by the gluon condensate.
Another study which can be carried out in $\overline{\mathrm{P}}$ANDA is the measurement of J/ψ and D meson production cross sections in $\overline{\mathrm{p}}$ annihilation on a series of nuclear targets. The comparison of the resonant J/ψ yield obtained from $\overline{\mathrm{p}}$ annihilation on protons and different nuclear targets allows to deduce the J/ψ-nucleus dissociation cross section, a fundamental parameter to understand J/ψ suppression in relativistic heavy ion collisions interpreted as a signal for quark-gluon plasma formation.

- *Open charm spectroscopy*
  The HESR, running at full luminosity and at $\overline{\mathrm{p}}$ momenta larger than 6.4 GeV/c, would produce a large number of D meson pairs. The high yield and the well-defined production kinematics of D meson pairs would allow to carry out a significant charmed meson spectroscopy program which would include, for example, the rich D and D_s meson spectra.
- *Hypernuclear physics*
  Hypernuclei are systems in which neutrons or protons are replaced by hyperons. In this way a new quantum number, strangeness, is introduced into the nucleus. Although single and double Λ-hypernuclei were discovered many decades ago, only 6 double Λ-hypernuclei are presently known. The availability of $\overline{\mathrm{p}}$ beams at FAIR will allow efficient production of hypernuclei with more than one strange hadron, making $\overline{\mathrm{P}}$ANDA competitive with planned dedicated facilities. This will open new perspectives for nuclear structure spectroscopy and for studying the forces between hyperons and nucleons.
- *Electromagnetic processes*
  In addition to the spectroscopic studies described above, $\overline{\mathrm{P}}$ANDA will be able to investigate the structure of the nucleon using electromagnetic processes, such as Deeply Virtual Compton Scattering (DVCS) and the process $\overline{\mathrm{p}}\mathrm{p} \to \mathrm{e}^+\mathrm{e}^-$, which will allow the determination of the electromagnetic form factors of the proton in the timelike region over an extended q^2 region. Furthermore, measuring the Drell Yan production of muons would give access to the transverse nucelon structure.

1.1.2 High-Energy Storage Ring – HESR

The HESR is dedicated to supply $\overline{\mathrm{P}}$ANDA with high-intensity and high-quality antiproton beams over a broad momentum range from 1.5 GeV/c to 15 GeV/c [7]. Table 1 summarises the experimental requirements and main parameters of the two operation modes for the full FAIR version. The High-Luminosity (HL) and the High-Resolution (HR) mode are established to fulfil all challenging specifications for the experimental program of $\overline{\mathrm{P}}$ANDA [8]. The HR mode is defined in the momentum range from 1.5 GeV/c to 9 GeV/c. To reach a relative momentum spread down to the order of 10^{-5}, only 10^{10} circulating particles in the ring are anticipated. The HL mode requires an order of magnitude higher beam intensity with reduced momentum resolution to reach a peak luminosity of $2 \cdot 10^{32}\,\mathrm{cm}^{-2}\,\mathrm{s}^{-1}$ in the full momentum range up to 15 GeV/c. To reach these beam parameters a very powerful phase-space cooling is needed. Therefore, high-energy electron cooling [9] and high-bandwidth stochastic cooling [10] will be utilised.

The HESR lattice is designed as a racetrack shaped ring with a maximum beam rigidity of 50 Tm (see fig. 3).

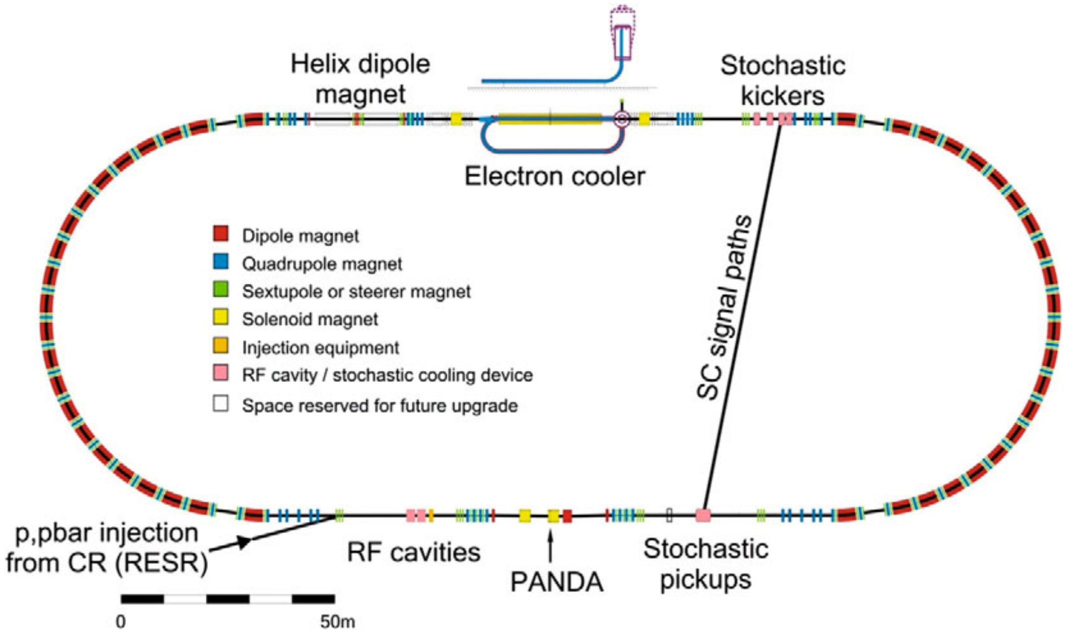

Fig. 3. Layout of the High-Energy Storage Ring (HESR). The beam is injected from the left into the lower straight section. The location of the $\overline{\mathsf{P}}$ANDA target is indicated with an arrow.

It consists of two 180° arcs and two 155 m long straight sections with a total circumference of 575 m [11]. The arc quadrupole magnets will allow for a flexible adjustment of transition energy, horizontal and vertical betatron tune as well as horizontal dispersion. In the straight section opposite to the injection point, an electron cooler will be installed. The $\overline{\mathsf{P}}$ANDA detector with the internal target is placed at the other side. Further components in the straight $\overline{\mathsf{P}}$ANDA section are beam injection kickers, septa and multi-harmonic RF cavities. The latter allow for a compensation of energy losses due to the beam-target interaction, a bunch rotation and the decelerating or accelerating of the beam. Stochastic cooling is implemented via several kickers and opposing high-sensitivity pick-ups on either side of the straight sections.

Special requirements for the lattice are low dispersion in the straight sections and small betatron amplitudes in the range between 1 m and 15 m at the internal interaction point (IP) of the $\overline{\mathsf{P}}$ANDA detector. In addition, the betatron amplitude at the electron cooler must be adjustable within a large range between 25 m and 200 m. Examples of the optical functions for one of the defined optical settings are shown in fig. 4. The deflection of the spectrometer dipole magnet of the $\overline{\mathsf{P}}$ANDA detector will be compensated by two dipole magnets that create a beam chicane. These will be placed 4.6 m upstream and 13 m downstream the $\overline{\mathsf{P}}$ANDA IP thus defining a boundary condition for the quadrupole elements closest to the experiment. For symmetry reasons, they have to be placed at ±14 m with respect to the IP. The asymmetric placement of the chicane dipoles will result in the experiment axis occurring at a small angle with respect to the axis of the straight section. The $\overline{\mathsf{P}}$ANDA solenoid will be compensated by one solenoid magnet. Additional correction dipoles have to be included around the electron cooler due to the toroids that will be used to overlap the electron beam with the antiproton beam. Phase-space coupling induced by the electron cooler solenoid will be compensated by two additional solenoid magnets.

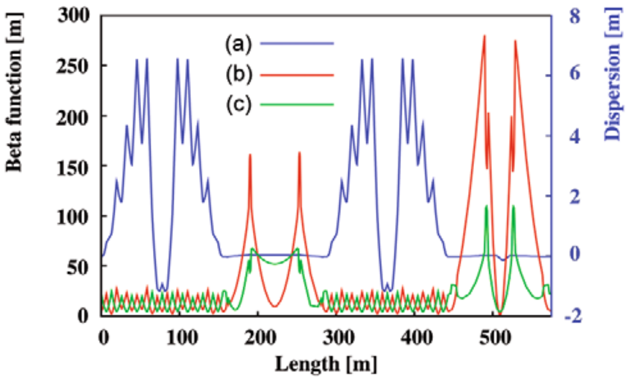

Fig. 4. Optical functions of the $\gamma_{tr} = 6.2$ lattice: Horizontal dispersion (a), horizontal (b) and vertical (c) betatron function. Electron cooler and target are located at a length of 222 m and 509 m, respectively.

Closed orbit correction and local orbit bumps at dedicated locations in the ring are crucial to meet requirements for the beam-target interaction in terms of maximised ring acceptance and optimum beam-target overlap [12]. The envisaged scheme aims on a reduction of maximum closed orbit deviations to below 5 mm while not exceeding 1 mrad of corrector strength. Therefore, 64 beam position monitors and 48 orbit correction dipoles are intended to be used. Because a few orbit bumps will have to be used in the straight parts of the HESR, all correction dipoles

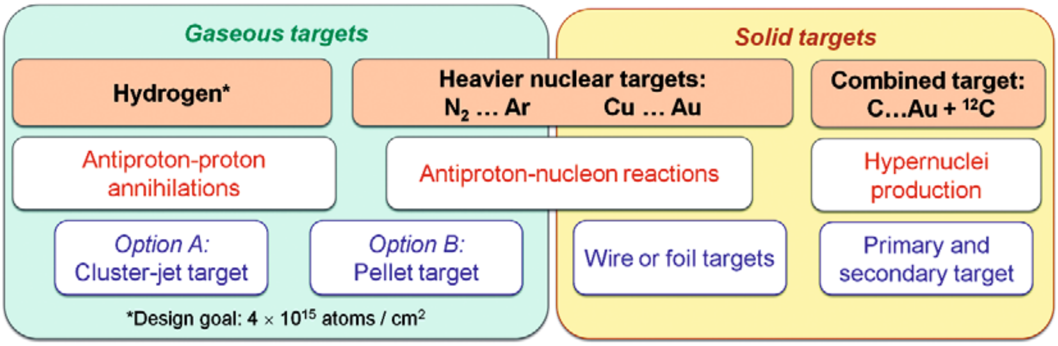

Fig. 5. Summary of the different target options foreseen at $\overline{\mathrm{P}}$ANDA.

therein are designed to provide an additional deflection strength of 1 mrad.

Transverse and longitudinal cooling will be used to compensate a transverse beam blow up and to achieve a low momentum spread, respectively. While stochastic cooling will be applicable in the whole momentum range, electron cooling is foreseen in a range from 1.5 GeV/c to 8.9 GeV/c with a possible upgrade to 15 GeV/c. The relative momentum spread can be further improved by combining both cooling systems. Beam losses are dominated by hadronic interactions between antiprotons and target protons, single large-angle Coulomb scattering in the target and energy straggling induced by Coulomb interactions of the antiprotons with target electrons. Mean beam lifetimes for the HESR range between 1540 s and 7100 s. The given numbers correspond to the time, after which the initial beam intensity is reduced by a factor of $1/e$. A detailed discussion of the beam dynamics and beam equliibria for the HESR can be found in [8, 13–15]. Advanced simulations have been performed for both cooling scenarios. In case of electron cooled beams the RMS relative momentum spread obtained for the HR mode ranges from $7.9 \cdot 10^{-6}$ (1.5 GeV/c) to $2.7 \cdot 10^{-5}$ (8.9 GeV/c), and $1.2 \cdot 10^{-4}$ (15 GeV/c) [16]. With stochastic cooling in a bandwidth of 2 GHz to 6 GHz, the RMS relative momentum spread for the HR mode results in $5.1 \cdot 10^{-5}$ (3.8 GeV/c), $5.4 \cdot 10^{-5}$ (8.9 GeV/c) and $3.9 \cdot 10^{-5}$ (15 GeV/c) [17]. In the HL mode a RMS relative momentum spread of roughly 10^{-4} can be expected. Transverse stochastic cooling can be adjusted independently to ensure sufficient beam-target overlap.

1.1.3 Targets

The design of the solenoid magnet allows for an implementation of different target systems. $\overline{\mathrm{P}}$ANDA will use both gaseous and non-gaseous targets. A very precise positioning of the target is crucial for the exact definition of the primary interaction vertex. In this context, big challenges for either system result from the long distance of roughly 2 m between the target injection point and the dumping system. Hydrogen target systems will be used for the study of antiproton-proton reactions. A high effective target density of about $4 \cdot 10^{15}$ hydrogen atoms per square centimetre must be achieved to fulfill the design goals of the high luminosity mode. Besides the application of hydrogen as target material, an extension to heavier gases such as deuterium, nitrogen or argon is planned for complementary studies with nuclear targets.

At present, two different solutions are under development: a cluster jet and a pellet target. Both will potentially provide sufficient target thickness but exhibit different properties concerning their effect on the beam quality and the definition of the IP. Solid targets are foreseen for hyper-nuclear studies and the study of antiproton-nucleus interaction using heavier nuclear targets. The different target options are shortly described in the following. Figure 5 gives an overview to all target option foreseen at $\overline{\mathrm{P}}$ANDA.

Cluster jet target

Cluster jet targets provide a homogeneous and adjustable target density without any time structure. Optimum beam conditions can be applied in order to achieve highest luminosity. The uncertainty of the IP in a plane perpendicular to the beam axis is defined by the optimised focus of the beam only. An inherent disadvantage of cluster jet targets is the lateral spread of the cluster jet leading to an uncertainty in the definition of the IP along the beam axis of several millimetres.

For the target production a pressurised cooled gas is injected into vacuum through a nozzle. The ejected gas immediately condensates and forms a narrow supersonic jet of molecule clusters. The cluster beam typically exposes a broad mass distribution which strongly depends on the gas input pressure and temperature. In case of hydrogen, the average number of molecules per cluster varies from 10^3 to 10^6. The cluster jets represent a highly diluted target and offer a very homogenous density profile. Therefore, they may be seen as a localised and homogeneous monolayer of hydrogen atoms being passed by the antiprotons once per revolution, *i.e.* the antiproton beam can be focused at highest phase-space density. The interaction point is thus defined transversely but has to be reconstructed longitudinally in beam direction. At a dedicated prototype cluster target station an effective target density of $1.5 \cdot 10^{15}$ hydrogen atoms per square centimetre has been achieved using the exact $\overline{\mathrm{P}}$ANDA geometry [18]. This value is close to the maximum number required by $\overline{\text{P}}$ANDA. Even higher target densities seem to be feasible and are topic of ongoing R&D work.

Hydrogen pellet target

Pellet targets provide a stream of frozen molecule droplets, called pellets, which drip with a fixed frequency off from a fine nozzle into vacuum. The use of pellet targets gives access to high effective target densities. The spatial resolution of the interaction zone can be reduced by skimmers to a few millimetres. A further improvement of this resolution can be achieved by tracking the individual pellets. However, pellet targets suffer from a non-uniform time distribution, which results in larger variations of the instantaneous luminosity as compared to a cluster jet target. The maximum achievable average luminosity is very sensitive to deviations of individual pellets from the target axis. The beam must be widened in order to warrant a beam crossing of all pellets. Therefore, an optimisation between the maximum pellet-beam crossing time on the one hand and the beam focusing on the other is necessary.

The design of the planned pellet target is based on the one currently used at the WASA-at-COSY experiment [19]. The specified design goals for the pellet size and the mean lateral spread of the pellet train are given by a radius of 25 μm to 40 μm and a lateral RMS deviation in the pellet train of approximately 1 mm, respectively. At present, typical variations of the interspacing of individual pellets range between 0.5 mm and 5 mm. A new test setup with an improved performance has been constructed [20]. First results have demonstrated the mono-disperse and satellite-free droplet production for cryogenic liquids of H_2, N_2 and Ar [21]. However, the prototype does not fully include the $\overline{\text{P}}$ANDA geometry. The handling of the pellet train over a long distance still has to be investigated in detail. The final resolution on the interaction point is envisaged to be in the order of 50 μm. Therefore, an additional pellet tracking system is planned.

Other target options

In case of solid target materials the use of wire targets is planned. The hyper-nuclear program requires a separate target station in upstream position. It will comprise a primary and secondary target. The latter must be instrumented with appropriate detectors. Therefore, a redesign of the innermost part of the $\overline{\text{P}}$ANDA spectrometer becomes necessary. This also includes the replacement of the MVD.

1.1.4 Luminosity considerations

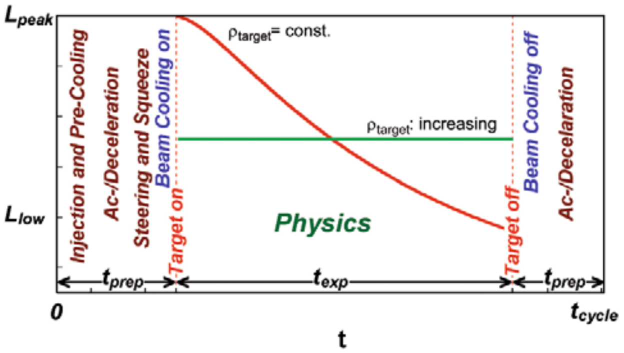

Fig. 6. Time-dependent macroscopic luminosity profile $L(t)$ in one operation cycle for constant (solid red) and increasing (green dotted) target density ρ_{target}. Different measures for beam preparation are indicated. Pre-cooling is performed at 3.8 GeV/c. A maximum ramp of 25 mT/s is specified for beam ac-/deceleration.

The luminosity L describes the flux of beam particles convolved with the target opacity. Hence, an intense beam, a highly effective target thickness and an optimised beam-target overlap are essential to yield a high luminosity in the experiment. The product of L and the total hadronic cross section σ_H delivers the interaction rate R, *i.e.* the number of antiproton-proton interactions in a specified time interval, which determines the achievable number of events for all physics channels and allows the extraction of occupancies in different detector regions. These are needed as input for the associated hardware development.

Obviously, the achievable luminosity is directly linked with the number of antiprotons in the HESR. The particles are injected at discrete time intervals. The maximum luminosity thus depends on the antiproton production rate $R_{\bar{p}} = \mathrm{d}N_{\bar{p}}/\mathrm{d}t$. Moreover, a beam preparation must be performed before the target can be switched on. It includes pre-cooling to equilibrium, the ramping to the desired beam momentum and a fine-tuned focusing in the target region as well as in the section for the electron cooler. Therefore, the operation cycle of the HESR can be separated into two sequences related to the beam preparation time t_{prep} (target off) and the time for data taking t_{exp} (target on), respectively. The beam preparation time t_{prep} also contains the period between the target switch-off and the injection, at which the residual antiprotons are either dumped or transferred back to the injection momentum.

Macroscopic luminosity profile

A schematic illustration of the luminosity profile during one operation cycle is given in fig. 6. The maximum luminosity is obtained directly after the target is switched on. During data taking the luminosity decreases due to hadronic interactions, single Coulomb scattering and energy straggling of the circulating beam in the target. Compared to beam-target interaction, minor contributions are related to single intra-beam scattering (Touschek effect). Beam losses caused by residual gas scattering can be neglected, if the vacuum is better than 10^{-9} mbar. A detailed analysis of all beam loss processes can be found in [13, 14]. The relative beam loss rate R_{loss} for the total cross section

σ_{tot} is given by the expression

$$R_{\text{loss}} = \tau^{-1} = f_0 \cdot n_t \cdot \sigma_{\text{tot}}, \tag{1}$$

where τ corresponds to the mean $(1/e)$ beam lifetime, f_0 is the revolution frequency of the antiprotons in the ring and n_t is the effective target thickness defined as an area density given in atoms per square centimetre. For beam-target interactions, the beam lifetime is independent of the beam intensity. The Touschek effect depends on the beam equilibria and beam intensity. At low momenta the beam cooling scenario and the ring acceptance have large impact on the achievable beam lifetime.

Cycle average luminosity

In physics terms, the time-averaged cycle luminosity is most relevant. The maximum average luminosity depends on the ratio of the antiproton production rate to the loss rate and is thus inversely proportional to the total cross section. It can be increased if the residual antiprotons after each cycle are transferred back to the injection momentum and then merged with the newly injected particles. Therefore, a bucket scheme utilising broad-band cavities is foreseen for beam injection and the refill procedure. Basically, the cycle average luminosity $\bar{L}$ reads as

$$\bar{L} = N_{\bar{p},0} \cdot f_0 \cdot n_t \cdot \frac{\tau \left[1 - e^{-\frac{t_{\text{exp}}}{\tau}}\right]}{t_{\text{exp}} + t_{\text{prep}}}, \tag{2}$$

where $N_{\bar{p},0}$ corresponds to the number of available particles at the start of the target insertion.

For the calculations, machine cycles and beam preparation times have to be specified. The maximum cycle average luminosity is achieved by an optimisation of the cycle time $t_{\text{cycle}} = t_{\text{exp}} + t_{\text{prep}}$. Constraints are given by the restricted number antiprotons in the HESR, the achievable effective target thickness and the specified antiproton production rate of $R_{\bar{p}} = 2 \cdot 10^7\,\text{s}^{-1}$ at FAIR.

Main results of calculations performed for different hydrogen targets are summarised in table 2. The total hadronic cross section, $\sigma_H^{\bar{p}p}$, decreases with higher beam momentum from approximately 100 mbarn at 1.5 GeV/c to 50 mbarn at 15 GeV/c. With the limited number of 10^{11} antiprotons, as specified for the high-luminosity mode, cycle averaged luminosities of up to $1.6 \cdot 10^{32}\,\text{cm}^{-2}\,\text{s}^{-1}$ can be achieved at 15 GeV/c for cycle times of less than one beam lifetime. Due to the very short beam lifetimes at lowest beam momenta more than 10^{11} particles can not be provided in average. As a consequence, the average luminosity drops below the envisaged design value at around 2.4 GeV/c to finally roughly $5 \cdot 10^{31}\,\text{s}^{-1}\,\text{cm}^{-2}$ at 1.5 GeV/c. Due to the lower assumed target density the achievable luminosity of the cluster jet target is smaller compared to the pellet operation.

In case of nuclear targets the total hadronic cross section for the interaction of antiprotons with target nucleons can be estimated from geometric considerations taking into account the proton radius of $r_p = 0.9$ fm and the radius of a spherical nucleus R_A, which can be roughly approximated as $R_A = r_0 A^{1/3}$, where $r_0 = 1.2$ fm and A is the mass number. With the assumption that $\sigma_H^{\bar{p}p} = \pi r_p^2$, the required total hadronic cross section, $\sigma_H^{\bar{p}A}$, for a nucleus of mass number A can be extracted from the given values of $\sigma_H^{\bar{p}p}$ for antiproton-proton collisions as follows:

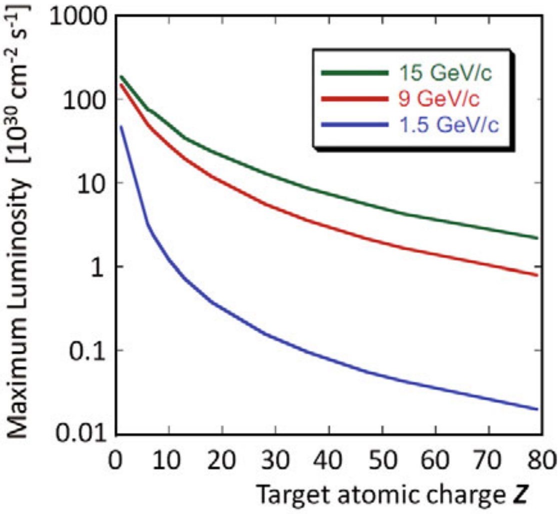

Fig. 7. Maximum average luminosity *vs.* atomic charge, Z, of the target for three different beam momenta.

$$\sigma_H^{\bar{p}A} = \pi (R_A + r_p)^2 = \sigma_H^{\bar{p}p} \cdot \left(\frac{R_A}{r_p} + 1\right)^2. \tag{3}$$

Simulation results on maximum average luminosities based on eq. (3) are shown in fig. 7. They include adapted beam losses in the target due to single Coulomb scattering and energy straggling. Compared to antiproton-proton experiments, the maximum average luminosity for nuclear targets decreases rapidly with both, higher atomic charge Z and lower beam momenta, by up to three orders of magnitude. Specific values for selected nuclear targets are given in table 3 with the effective target thickness required to reach these numbers.

Event rates

Besides the cycle-averaged luminosity an evaluation of the instantaneous luminosity during the data taking is indispensable for performance studies of the $\overline{\text{P}}$ANDA detector. Associated event rates define the maximum data load to be handled at different timescales by the individual subsystems. The discussions in this section are based on the following assumptions.

- Nominal antiproton production rate at FAIR: $R_{\bar{p}} = 2 \cdot 10^7\,\text{s}^{-1}$.
- Effective target density: $n_t = 4 \cdot 10^{15}$ atoms/cm^2.
- Maximum number of antiprotons in the HESR: $N_{\bar{p},\text{max}} = 10^{11}$.
- Recycling of residual antiprotons at the end of each cycle.

Table 2. Calculation of the maximum achievable cycle averaged luminosity for three different beam momenta: Input parameters and final results for different H_2 target setups.

	$1.5\,\mathrm{GeV}/c$	$9\,\mathrm{GeV}/c$	$15\,\mathrm{GeV}/c$
Total hadronic cross section/ mbarn	100	57	51
Cluster jet target			
Target density: $/\mathrm{cm}^{-2}$	$8 \cdot 10^{14}$	$8 \cdot 10^{14}$	$8 \cdot 10^{14}$
Antiproton production rate: $/\mathrm{s}^{-1}$	$2 \cdot 10^{7}$	$2 \cdot 10^{7}$	$2 \cdot 10^{7}$
Beam preparation time: /s	120	140	290
Optimum cycle duration: /s	1280	2980	4750
Mean beam lifetime: /s	~ 5920	~ 29560	~ 35550
Max Cycle Averaged Luminosity: $/\mathrm{cm}^{-2}\,\mathrm{s}^{-1}$	$0.29 \cdot 10^{32}$	$0.38 \cdot 10^{32}$	$0.37 \cdot 10^{32}$
Pellet target			
Target density: $/\ \mathrm{cm}^{-2}$	$4 \cdot 10^{15}$	$4 \cdot 10^{15}$	$4 \cdot 10^{15}$
Antiproton production rate: $/\mathrm{s}^{-1}$	$2 \cdot 10^{7}$	$2 \cdot 10^{7}$	$2 \cdot 10^{7}$
Beam preparation time: /s	120	140	290
Optimum cycle duration: /s	4820	1400	2230
Mean beam lifetime: /s	~ 1540	~ 6000	~ 7100
Max cycle-averaged luminosity: $/\mathrm{cm}^{-2}\,\mathrm{s}^{-1}$	$0.53 \cdot 10^{32}$	$1.69 \cdot 10^{32}$	$1.59 \cdot 10^{32}$

Table 3. Expected maximum average luminosities, $\bar{L}$, and required effective target thickness, n_t, for heavier nuclear targets at $\overline{\mathsf{P}}$ANDA at minimum and maximum beam momentum p_{beam}. Given numbers refer to an assumed number of 10^{11} antiprotons in the HESR.

Target material	$\bar{L}$ ($p_{\mathsf{beam}} = 1.5\,\mathrm{GeV}/c$) $[\mathrm{cm}^{-2}\,\mathrm{s}^{-1}]$	$\bar{L}$ ($p_{\mathsf{beam}} = 15\,\mathrm{GeV}/c$) $[\mathrm{cm}^{-2}\,\mathrm{s}^{-1}]$	n_t $[\mathrm{atoms/cm}^2]$
deuterium	$5 \cdot 10^{31}$	$1.9 \cdot 10^{32}$	$3.6 \cdot 10^{15}$
argon	$4 \cdot 10^{29}$	$2.4 \cdot 10^{31}$	$4.6 \cdot 10^{14}$
gold	$4 \cdot 10^{28}$	$2.2 \cdot 10^{30}$	$4.1 \cdot 10^{13}$

As indicated in fig. 6 the instantaneous luminosity during the cycle changes on a macroscopic timescale. One elegant way to provide constant event rates in case of a cluster jet target is given by the possibility to compensate the antiproton consumption during an accelerator cycle by the increase of the effective target density. Alternatively, using a constant target beam density the beam-target overlap might be increased adequately to the beam consumption. With these modifications the instantaneous luminosity during the cycle is expected to be kept constant to a level of 10%.

The values for the luminosity as given in table 2 are averaged over the full cycle time. However, to extract the luminosity during data taking, $\bar{L}_{\mathsf{exp}}$, these numbers must be rescaled to consider the time average over the experimental time,

$$\bar{L}_{\mathsf{exp}} = (t_{\mathsf{cycle}}/t_{\mathsf{exp}}) \cdot \bar{L}. \tag{4}$$

In addition to the fluctuation of the instantaneous luminosity during the operation cycle as dicussed above ($\Delta L_{\mathsf{inst}}/L_{\mathsf{inst}} \leq 10\%$), it must be considered that the HESR will be only filled by 90% in case of using a barrier-bucket system. As a consequence, values for L_{inst} during data taking are 10% higher than the ones for $\bar{L}_{\mathsf{exp}}$.

An estimate of peak luminosities, $L_{\mathsf{peak}} > L_{\mathsf{inst}}$, must further include possible effects on a short timescale. Contrary to homogeneous cluster beams, a distinct time structure is expected for the granular volume density distribution of a pellet beam. Such time structure depends on the transverse and longitudinal overlap between single pellets and the circulating antiproton beam in the interaction region. Deviations of the instantaneous luminosity on a microsecond timescale are caused by variations of the pellet size, the pellet trajectory and the interspacing between consecutive pellets. The latter must be well controlled to avoid the possible presence of more than one pellet in the beam at the same instant. The resulting ratio $L_{\mathsf{peak}}/L_{\mathsf{exp}}$ depends on the pellet size. First studies on the expected peak values for the $\overline{\mathsf{P}}$ANDA pellet target have been performed [22]. Results indicate that the peak luminosity stays below $10^{33}\,\mathrm{cm}^{-2}\,\mathrm{s}^{-1}$ if the pellet size is not bigger than $20\,\mu\mathrm{m}$.

Finally, for the extraction of event rates the obtained luminosities are multiplied with the hadronic cross section. Table 4 summarises the main results for a hydrogen

Table 4. Summary of expected event rates at $\overline{\mathsf{P}}$ANDA. Numbers for the hydrogen target correspond to the pellet system (see table 2). The given ratio $\bar{L}_{\mathsf{peak}}/\bar{L}_{\mathsf{exp}}$ corresponds to the maximum value to achieve the nominal interaction rate of $R_{\mathsf{nom}} = 2{\cdot}10^7\,\mathrm{s}^{-1}$. Rough estimates for nuclear targets are based on the numbers given in table 3, with $\bar{L} = \bar{L}_{\mathsf{exp}}$, and σ_H calculated according to eq. (3).

Target material	p_{beam} [GeV/c]	$\bar{L}_{\mathsf{exp}}$ [cm^{-2} s^{-1}]	L_{inst} [cm^{-2} s^{-1}]	σ_H [mbarn]	$\bar{R}_{\mathsf{exp}}$ [s^{-1}]	$\bar{L}_{\mathsf{peak}}/\bar{L}_{\mathsf{exp}}$ (R_{nom})
hydrogen	1.5	$5.4 \cdot 10^{31}$	$(5.9 \pm 0.6) \cdot 10^{31}$	100	$5.4 \cdot 10^{6}$	3.7
	15	$1.8 \cdot 10^{32}$	$(2.0 \pm 0.2) \cdot 10^{32}$	51	$9.7 \cdot 10^{6}$	2.1
argon	1.5	$4.0 \cdot 10^{29}$	$(4.4 \pm 0.4) \cdot 10^{29}$	2020	$8.1 \cdot 10^{5}$	–
	15	$2.4 \cdot 10^{31}$	$(2.6 \pm 0.3) \cdot 10^{31}$	1030	$2.5 \cdot 10^{7}$	
gold	1.5	$4.0 \cdot 10^{28}$	$(4.4 \pm 0.4) \cdot 10^{28}$	7670	$3.1 \cdot 10^{6}$	–
	15	$2.2 \cdot 10^{30}$	$(2.6 \pm 0.3) \cdot 10^{30}$	3911	$8.6 \cdot 10^{6}$	

target based on a pellet system, which is expected to deliver upper limits for the occuring event rates. In addition, a rough estimate for nuclear targets based on the input of table 3 and eq. (3) is given. Even though these values still must be verified by detailed studies, it can be seen that the reduced average luminosity for heavier nuclear targets is counterbalanced by an increased cross section that results in comparable event rates.

Based on the given assumptions and caveats, as discussed in this section, a nominal interaction rate of $R_{\mathsf{nom}} = 2 \cdot 10^7\,\mathrm{s}^{-1}$ can be defined that all detector systems have to be able to handle. This specification includes the requirement that density fluctuations of the beam-target overlap have to be smaller than a factor of two ($\bar{L}_{\mathsf{peak}}/\bar{L}_{\mathsf{exp}}$). However, in order to avoid data loss it might be important to introduce a generic safety factor that depends on special features of the individual detector subsystems and their position with respect to the interaction region.

1.2 The $\overline{\mathsf{P}}$ANDA detector

The main objectives of the design of the $\overline{\mathsf{P}}$ANDA experiment are to achieve 4π acceptance, high resolution for tracking, particle identification and calorimetry, high rate capabilities and a versatile readout and event selection. To obtain a good momentum resolution the detector will be composed of two magnetic spectrometers: the *Target Spectrometer* (TS), based on a superconducting solenoid magnet surrounding the interaction point, which will be used to measure at large polar angles and the *Forward Spectrometer* (FS), based on a dipole magnet, for small angle tracks. An overview of the detection concept is shown in fig. 8.

It is based on a complex setup of modular subsystems including tracking detectors (MVD, STT, GEM), electromagnetic calorimeters (EMC), a muon system, Cherenkov detectors (DIRC and RICH) and a time-of-flight (TOF) system. A sophisticated concept for the data acquisition with a flexible trigger is planned in order to exploit at best the set of final states relevant for the $\overline{\mathsf{P}}$ANDA physics objectives.

The Target Spectrometer will surround the interaction point and measure charged tracks in a highly homogeneous solenoidal field. In the manner of a collider detector it will contain detectors in an onion-shell-like configuration. Pipes for the injection of target material will have to cross the spectrometer perpendicular to the beam pipe.

The Target Spectrometer will be arranged in three parts: the barrel covering angles between 22° and 140°, the forward end cap extending the angles down to 5° and 10° in the vertical and horizontal planes, respectively, and the backward end cap covering the region between about 145° and 170°. Please refer to fig. 9 for a complete overview.

1.2.1 Target Spectrometer

Beam-target system

The beam-target system consists of the apparatus for the target production and the corresponding vacuum system for the interaction region. The beam and target pipe cross sections inside the target spectrometer are decreased to an inner diameter of 20 mm close to the interaction region. The innermost parts are planned to be made of beryllium, titanium or a suited alloy which can be thinned to wall thicknesses of 200 μm. Due to the limited space and the constraints on the material budget close to the IP, vacuum pumps along the beam pipe can only be placed outside the target spectrometer. Insections are foreseen in the iron yoke of the magnet which allow the integration of either a pellet or a cluster jet target. The target material will be injected from the top. Dumping of the target residuals after beam crossing is mandatory to prevent backscattering

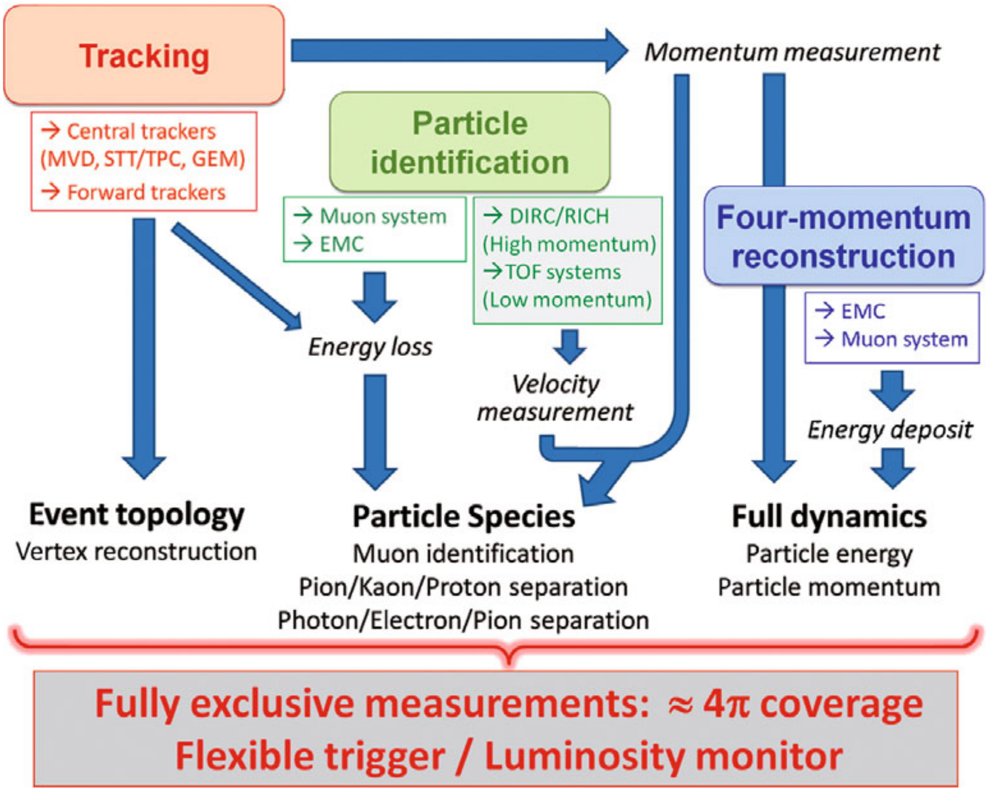

Fig. 8. Basic detection concept. The main components are described in sects. 1.2.1 and 1.2.2.

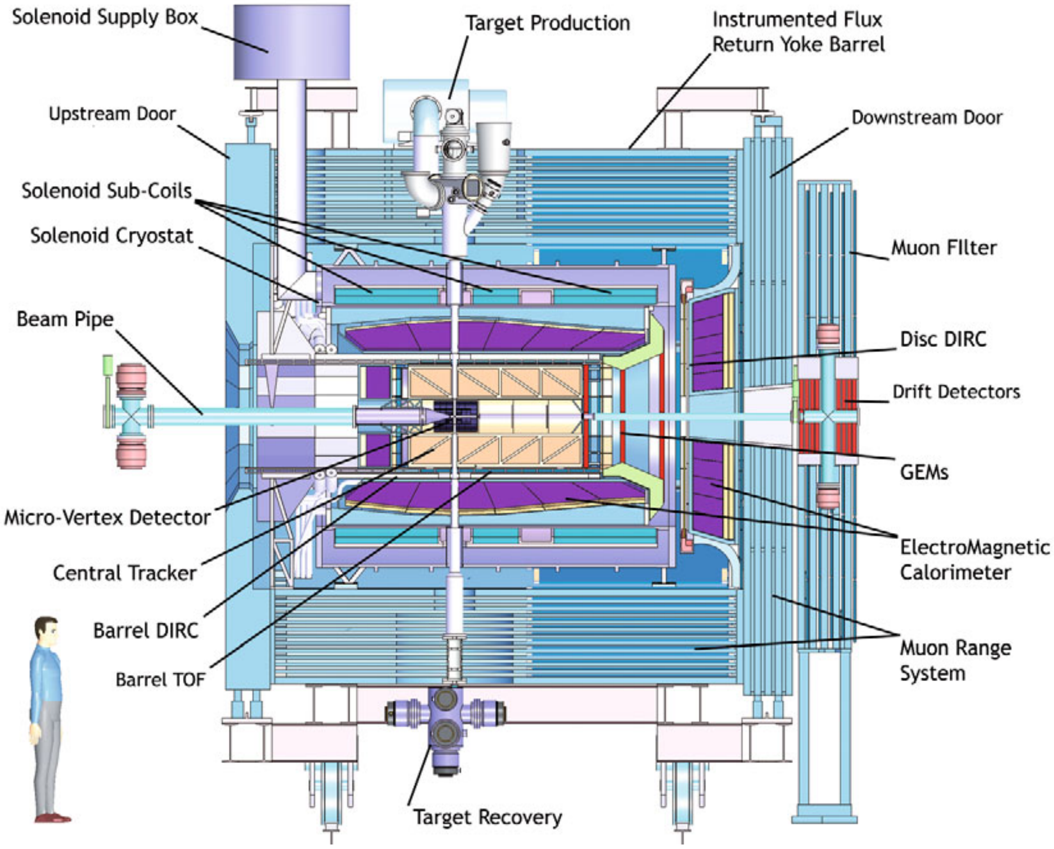

Fig. 9. Artistic side view of the Target Spectrometer (TS) of $\overline{\mathrm{P}}$ANDA. To the right of this the Forward Spectrometer (FS) follows, which is illustrated in fig. 13.

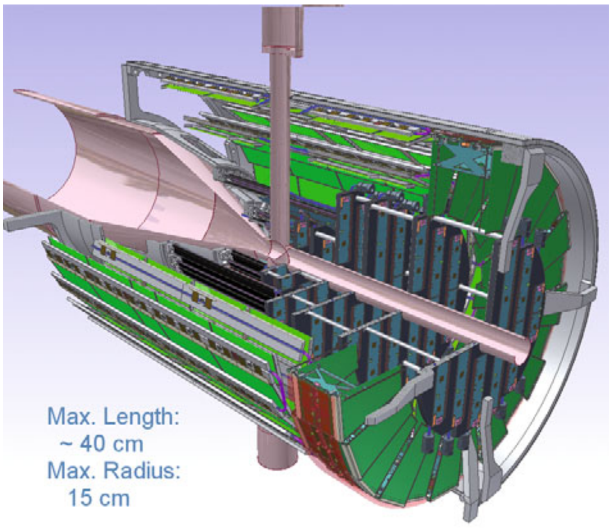

Fig. 10. The Micro Vertex Detector (MVD) of the Target Spectrometer surrounding the beam and target pipes seen from downstream. To allow a look inside the detector a three-quarters portraits is chosen.

into the interaction region. The entire vacuum system is kept variable and allows an operation of both target types. Moreover, an adaptation to non-gaseous nuclear wire targets is possible. For the targets of the planned hypernuclear experiment the whole upstream end cap and parts of the inner detector geometry will be modified. A detailed discussion of the different target options can be found in sect. 1.1.3.

Solenoid magnet

The solenoid magnet of the TS will deliver a very homogeneous solenoid field of 2 T with fluctuations of less than ±2%. In addition, a limit of $\int B_r/B_z \mathrm{d}z < 2\,\mathrm{mm}$ is specified for the normalised integral of the radial field component. The superconducting coil of the magnet has a length of 2.8 m and an inner radius of 90 cm, using a laminated iron yoke for the flux return. The cryostat for the solenoid coils is required to have two warm bores of 100 mm diameter, one above and one below the target position, to allow for insertion of internal targets. The load of the integrated inner subsystems can be picked up at defined fixation points. A precise description of the magnet system and detailed field strength calculations can be found in [23].

Micro vertex detector

The design of the Micro Vertex Detector (MVD) for the target spectrometer is optimised for the detection of secondary decay vertices from charmed and strange hadrons and for a maximum acceptance close to the interaction point. It will also strongly improve the transverse momentum resolution. The setup is depicted in fig. 10.

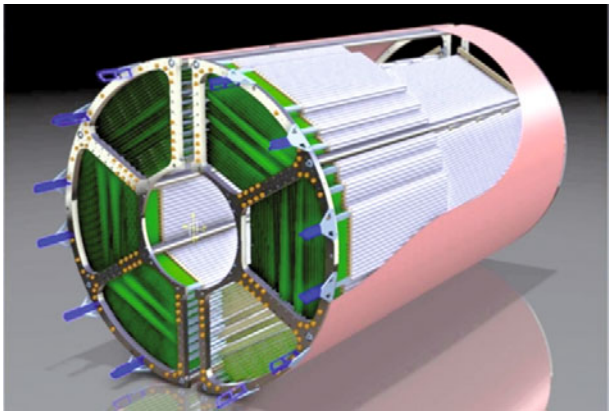

Fig. 11. The Straw Tube Tracker (STT) of the Target Spectrometer seen from upstreams.

The concept of the MVD is based on radiation hard silicon pixel detectors with fast individual pixel readout circuits and silicon strip detectors. The layout foresees a four layer barrel detector with an inner radius of 2.5 cm and an outer radius of 13 cm. The two innermost layers will consist of pixel detectors and the outer two layers will be equipped with double-sided silicon strip detectors.

Six detector wheels arranged perpendicular to the beam will achieve the best acceptance for the forward part of the particle spectrum. While the inner four layers will be made entirely of pixel detectors, the following two will be a combination of strip detectors on the outer radius and pixel detectors closer to the beam pipe.

Additional forward disks

Two additional silicon disk layers are considered further downstream at around 40 cm and 60 cm to achieve a better acceptance of hyperon cascades. They are intended to be made entirely of silicon strip detectors. Even though they are not part of the central MVD it is planned, as a first approach, to follow the basic design as defined for the strip disks of the MVD. However, an explicit design optimisation still has to be performed. Two of the critical points to be checked are related to the increased material budget caused by these layers and the needed routing of cables and supplies for these additional disks inside the very restricted space left by the adjacent detector systems.

Straw Tube Tracker (STT)

This detector will consist of aluminised Mylar tubes called *straws*. These will be stiffened by operating them at an overpressure of 1 bar which makes them self-supporting. The straws are to be arranged in planar layers which are mounted in a hexagonal shape around the MVD as shown in fig. 11. In total there are 27 layers of which the 8 central ones are skewed, to achieve an acceptable resolution of 3 mm also in z (parallel to the beam). The gap to the surrounding detectors will be filled with further individual

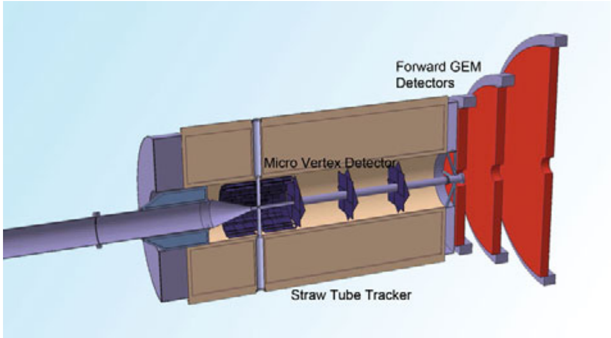

Fig. 12. Schematic drawing of the tracking detectors of the Target Spectrometer.

straws. In total there will be 4636 straws around the beam pipe at radial distances between 15 cm and 41.8 cm with an overall length of 150 cm. All straws have a diameter of 10 mm and are made of a 27 μm thick Mylar foil. Each straw tube is constructed with a single anode wire in the centre that is made of 20 μm thick gold plated tungsten The gas mixture used will be argon based with CO_2 as quencher. It is foreseen to have a gas gain not greater than 10^5 in order to warrant long-term operation. With these parameters, a resolution in x and y coordinates of less than 150 μm is expected. A thin and light space frame will hold the straws in place, the force of the wire however is kept solely by the straw itself. This overall design results in a material budget of 1.2% of one radiation length.

Forward GEM detectors

Figure 12 shows the components of the tracking system of the Target Spectrometer.

Particles emitted at angles below 22° which are not covered fully by the STT will be tracked by three planar stations placed approximately 1.1 m, 1.4 m and 1.9 m downstream of the target. Each of the station consists of double planes with two projections per plane. The stations will be equipped with Gaseous micro-pattern detectors based on Gas Electron Multiplier (GEM) foils as amplification stages. The chambers have to sustain a high counting rate of particles peaked at the most forward angles due to the relativistic boost of the reaction products as well as due to the small angle $\bar{\mathrm{p}}\mathrm{p}$ elastic scattering. The maximum expected particle flux in the first chamber in the vicinity of the 5 cm diameter beam pipe will be about $3 \cdot 10^4\,\mathrm{cm}^{-2}\,\mathrm{s}^{-1}$.

Barrel DIRC

At polar angles between 22° and 140°, particle identification will be performed by the Detection of Internally Reflected Cherenkov (DIRC) light as realised in the BaBar detector [24]. It will consist of 1.7 cm thick fused silica (artificial quartz) slabs surrounding the beam line at a radial distance of 45 cm to 54 cm. At BaBar the light was imaged across a large stand-off volume filled with water onto 11000 photomultiplier tubes. At $\overline{\mathrm{P}}$ANDA, it is intended to focus the images by lenses onto Micro-Channel Plate PhotoMultiplier Tubes (MCP PMTs) which are insensitive to magnet fields. This fast light detector type allows a more compact design and the readout of two spatial coordinates.

Forward End-Cap DIRC

A similar concept is considered to be employed in the forward direction for particles at polar angles between 5° and 22°. The same radiator, fused silica, is to be employed, however in shape of a disk. The radiator disk will be 2 cm thick and will have a radius of 110 cm. It will be placed directly upstream of the forward end cap calorimeter. At the rim around the disk the Cherenkov light will be measured by focusing elements. In addition measuring the time of propagation the expected light pattern can be distinguished in a 3-dimensional parameter space. Dispersion correction is achieved by the use of alternating dichroic mirrors transmitting and reflecting different parts of the light spectrum. As photon detectors either silicon photomultipliers or microchannel plate PMTs are considered.

Scintillator tile barrel (time-of-flight)

For slow particles at large polar angles, particle identification will be provided by a time-of-flight (TOF) detector positioned just outside the barrel DIRC, where it can be also used to detect photon conversions in the DIRC radiator. The detector is based on scintillator tiles of $28.5 \times 28.5\,\mathrm{mm}^2$ size, individually read out by two Silicon PhotoMultipliers per tile. The full system consists of 5760 tiles in the barrel part and can be augmented also by approximately 1000 tiles in forward direction just in front of the endcap disc DIRC. Material budget and the dimension of this system are optimised such that a value of less than 2% of one radiation length, including readout and mechanics and less than 2 cm radial thickness will be reached, respectively. The expected time resolution of 100 ps will allow precision timing of tracks for event building and fast software triggers. The detector also provides well timed input with a good spatial resolution for online pattern recognition.

Electromagnetic calorimeters

Expected high count rates and a geometrically compact design of the Target Spectrometer require a fast scintillator material with a short radiation length and Molière radius for the construction of the electromagnetic calorimeter (EMC). Lead tungsten ($PbWO_4$) is a high-density inorganic scintillator with sufficient energy and time resolution for photon, electron, and hadron detection even at intermediate energies [25–27].

The crystals will be 20 cm long, *i.e.* approximately 22 X_0, in order to achieve an energy resolution below 2%

at 1 GeV [25–27] at a tolerable energy loss due to longitudinal leakage of the shower. Tapered crystals with a front size of $2.1 \times 2.1\,\text{cm}^2$ will be mounted in the barrel EMC with an inner radius of 57 cm. This implies 11360 crystals for the barrel part of the calorimeter. The forward end cap EMC will be a planar arrangement of 3600 tapered crystals with roughly the same dimensions as in the barrel part, and the backward end cap EMC comprises of 592 crystals. The readout of the crystals will be accomplished by large area avalanche photo diodes in the barrel and in the backward end cap, vacuum photo-triodes will be used in the forward end cap. The light yield can be increased by a factor of about 4 compared to room temperature by cooling the crystals down to $-25\,^\circ$C.

The EMC will allow to achieve an e/π ratio of 10^3 for momenta above $0.5\,\text{GeV}/c$. Therefore, e/π-separation will not require an additional gas Cherenkov detector in favour of a very compact geometry of the EMC. A detailed description of the detector system can be found in [28].

Muon detectors

The laminated yoke of the solenoid magnet acts as a range system for the detection of muons. There are 13 sensitive layers, each 3 cm thick (layer "zero" is a double layer). They alternate with 3 cm thick iron absorber layers (first and last iron layers are 6 cm thick), introducing enough material for the absorption of pions in the $\overline{\text{P}}$ANDA momentum range and angles. In the forward end cap more material is needed due to the higher momenta of the occurring particles. Therefore, six detection layers will be placed around five iron layers of 6 cm each within the downstream door of the return yoke, and a removable muon filter with additional five layers of 6 cm iron and corresponding detection layers will be moved in the space between the solenoid and the dipole.

As sensors between the absorber layers, rectangular aluminum Mini Drift Tubes (MDT) are foreseen. Basically, these are drift tubes with additional capacitive coupled strips, read out on both ends to obtain the longitudinal coordinate. All together, the laminated yoke of the solenoid magnet and the additional muon filters will be instrumented with 2600 MDTs and 700 MDTs, respectively.

Hypernuclear detector

The hypernuclei study will make use of the modular structure of $\overline{\text{P}}$ANDA. Removing the backward end cap calorimeter and the MVD will allow to add a dedicated nuclear target station and the required additional detectors for γ spectroscopy close to the entrance of $\overline{\text{P}}$ANDA. While the detection of hyperons and low momentum $K^\pm$ can be ensured by the universal detector and its PID system, a specific target system and a γ-detector are additional components required for the hypernuclear studies.

The production of hypernuclei proceeds as a two-stage process. First hyperons, in particular $\Xi\bar{\Xi}$, are produced on a nuclear target. In addition, a secondary target is needed for the formation of a double hypernucleus. The geometry of this secondary target is determined by the short mean life of the Ξ^- of only 0.164 ns. This limits the required thickness of the active secondary target to about 25 mm to 30 mm. It will consist of a compact sandwich structure of silicon micro-strip detectors and absorbing material. In this way the weak decay cascade of the hypernucleus can be detected in the sandwich structure.

An existing germanium array with refurbished readout will be used for the γ-spectroscopy of the nuclear decay cascades of hypernuclei. The main limitation will be the load due to neutral or charged particles traversing the germanium detectors. Therefore, readout schemes and tracking algorithms are presently being developed which will enable high resolution γ-spectroscopy in an environment of high particle flux.

1.2.2 Forward Spectrometer

The Forward Spectrometer (FS) will cover all particles emitted in vertical and horizontal angles below ±5° and ±10°, respectively. Charged particles will be deflected by an integral dipole field. Cherenkov detectors, calorimeters and muon counters ensure the detection of all particle types. Figure 13 gives an overview to the instrumentation of the FS.

Dipole magnet

A 2 Tm dipole magnet with a window frame, a 1 m gap, and more than 2 m aperture will be used for the momentum analysis of charged particles in the FS. In the current planning, the magnet yoke will occupy about 1.6 m in beam direction starting from 3.9 m downstream of the target. Thus, it covers the entire angular acceptance of the TS of ±10° and ±5° in the horizontal and in the vertical direction, respectively. The bending power of the dipole on the beam line causes a deflection of the antiproton beam at the maximum momentum of $15\,\text{GeV}/c$ of 2.2°. For particles with lower momenta, detectors will be placed inside the yoke opening. The beam deflection will be compensated by two correcting dipole magnets, placed around the $\overline{\text{P}}$ANDA detection system. The dipole field will be ramped during acceleration in the HESR and the final ramp maximum scales with the selected beam momentum.

Forward trackers

The deflection of particle trajectories in the field of the dipole magnet will be measured with three pairs of tracking drift detectors. The first pair will be placed in front, the second within and the third behind the dipole magnet. Each pair will contain two autonomous detectors, thus, in total, 6 independent detectors will be mounted. Each tracking detector will consist of four double layers of straw tubes (see fig. 14), two with vertical wires and two with

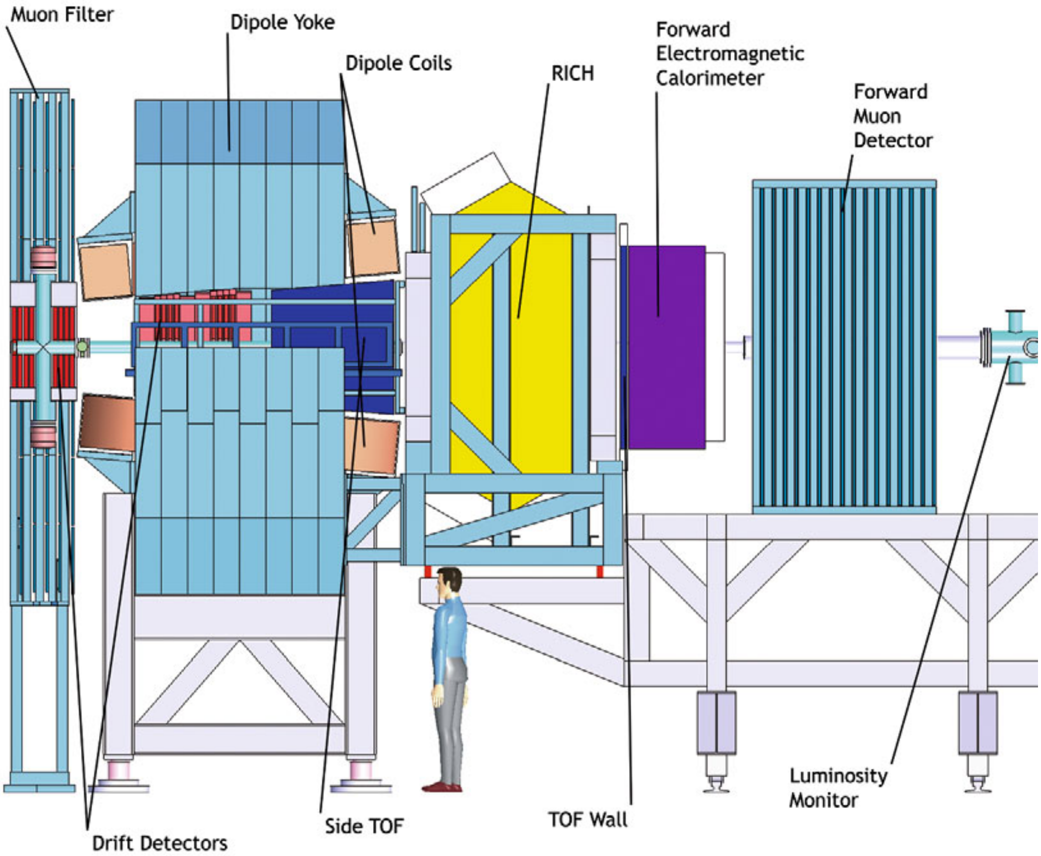

Fig. 13. Artistic side view of the Forward Spectrometer (FS) of $\overline{\text{P}}$ANDA. It is preceded on the left by the Target Spectrometer (TS), which is illustrated in fig. 9.

wires inclined by a few degrees. The optimal angle of inclination with respect to vertical direction will be chosen on the basis of ongoing simulations. The planned configuration of double layers of straws will allow to reconstruct tracks in each pair of tracking detectors separately, also in case of multi-track events.

Forward particle identification

To enable the π/K and K/p separation also at the highest momenta a RICH detector is proposed. The favoured design is a dual radiator RICH detector similar to the one used at HERMES [29]. Using two radiators, silica aerogel and C_4F_{10} gas, provides π/K/p separation in a broad momentum range from 2 to 15 GeV/c. The two different indices of refraction are 1.0304 and 1.00137, respectively. The total thickness of the detector is reduced to the freon gas radiator (5%X_0), the aerogel radiator (2.8%X_0), and the aluminum window (3%X_0) by using a lightweight mirror focusing the Cherenkov light on an array of phototubes placed outside the active volume.

A wall of slabs made of plastic scintillator and read out on both ends by fast photo-tubes will serve as time-of-flight stop counter placed at about 7 m from the target. Similar detectors will be placed inside the dipole magnet opening to detect low momentum particles which do not exit the dipole magnet. The time resolution is expected to be in the order of 50 ps thus allowing a good π/K and K/p separation up to momenta of 2.8 GeV/c and 4.7 GeV/c, respectively.

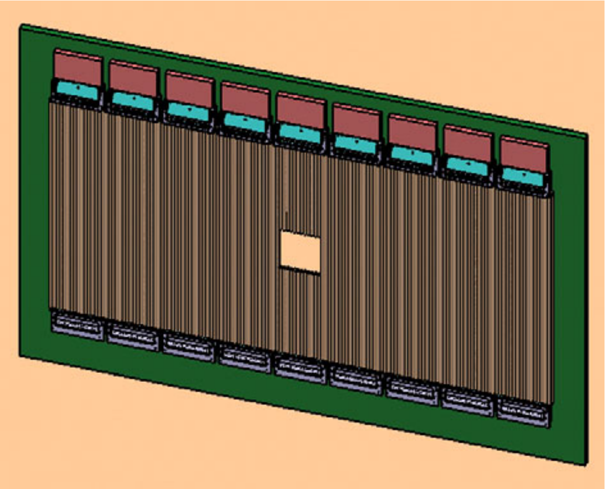

Fig. 14. Double layer of straw tubes with preamplifier cards and gas manifolds mounted on rectangular support frame. The opening in the middle of the detector is foreseen for the beam pipe.

Forward electromagnetic calorimeter

For the detection of photons and electrons a Shashlyk-type calorimeter with high resolution and efficiency will be employed. The detection is based on lead-scintillator sandwiches read out with wave-length shifting fibres passing through the block and coupled to photo-multipliers. The lateral size of one module is 110 mm × 110 mm and a length of 680 mm ($= 20X_0$). A higher spatial resolution will be achieved by sub-dividing each module into 4 channels of 55 mm × 55 mm size coupled to 4 PMTs. To cover the forward acceptance, 351 such modules, arranged in 13 rows and 27 columns at a distance of 7.5 m from the target, are required. With similar modules, based on the same technique as proposed for $\overline{\text{P}}$ANDA, an energy resolution of $4\%/\sqrt{E}$ [30] has been achieved.

Forward muon detectors

For the very forward part of the muon spectrum, a further range tracking system consisting of interleaved absorber layers and rectangular aluminium drift-tubes is being designed, similar to the muon system of the TS, but laid out for higher momenta. The system allows discrimination of pions from muons, detection of pion decays and, with moderate resolution, also the energy determination of neutrons and anti-neutrons. The forward muon system will be placed at about 9 m from the target.

Luminosity detector

The luminosity at $\overline{\text{P}}$ANDA will be determined by using elastic antiproton-proton scattering as a reference channel.

At very small transferred momentum, corresponding to small polar angles, the elastic cross section is dominated by the Coulomb component which is exactly calculable. Taking the beam divergence into account, the angular distribution of scattered antiprotons will be measured in the range of 3–8 mrad, corresponding to the Coulomb-nuclear interference region. The angle of each scattered antiproton will be measured by four tracking planes equipped with HV-MAPS [31] placed about 11 m behind the interaction point, behind the Forward Spectrometer. The planes are positioned as close to the beam axis as possible and separated by 10–20 cm along the beam direction. The current design foresees that every plane consists of 10 modules where one module contains 10 HV-MAPS glued on both sides of a CVD-diamond substrate. In this way, the whole azimuth angle is covered in order to suppress systematic effects from, *e.g.*, the forward dipole magnet and potential misalignment of the beam. The silicon sensors will be located in vacuum to minimize scattering of the antiprotons before traversing the tracking planes. With the proposed detector setup an absolute precision of 3% for the time integrated luminosity is expected.

1.2.3 Data acquisition

In $\overline{\text{P}}$ANDA, a data acquisition concept is being developed to be as much as possible matched to the complexity of the experiment and the diversity of physics objectives and the rate capability of at least $2 \cdot 10^7$ events/s. Therefore, every sub-detector system is a self-triggering entity. Signals are detected autonomously by the sub-systems and are preprocessed. Only the physically relevant information is extracted and transmitted. This requires hit detection, noise suppression and clusterisation at the readout level. The data related to a particle hit, with a substantially reduced rate in the preprocessing step, is marked by a precise time stamp and buffered for further processing. The trigger selection finally occurs in computing nodes which access the buffers via a high-bandwidth network fabric. The new concept provides a high degree of flexibility in the choice of trigger algorithms. It makes trigger conditions available which are outside the capabilities of the standard approach.

1.2.4 Infrastructure

The $\overline{\text{P}}$ANDA experimental hall will be located in the east straight section of HESR. The planned floor space in the hall will be of 43 m × 29 m. Within the cave, the $\overline{\text{P}}$ANDA detector, the auxiliary equipment, the beam steering magnets and the focusing elements will be housed. To allow for access during HESR operation, the area of the beam line and the detector will be shielded with movable concrete blocks. Controlled access will be provided via a properly designed chicane in the concrete wall. In addition, the experimental hall will provide additional space for components storage and detector parts assembly. The $\overline{\text{P}}$ANDA hall will feature an overhead crane, spanning the whole area and with a maximum load capacity of 25 *t*. The shielded space for the $\overline{\text{P}}$ANDA detector and the beam line will have an area of 37 m × 9.4 m and a height of 8.5 m. The beam line at a height of 3.5 m. The floor level in the HESR tunnel will be 2 m higher. The TS with its front-end electronics will be mounted on rails and movable from the on-beam position to outside the shielded area, to allow simultaneous detector and accelerator maintenance.

In the south-west corner of the $\overline{\text{P}}$ANDA hall, the experiment counting house complex is foreseen. It will be a complex made of five floors. At the first floor, the supplies for power, high voltage, cooling water, gases and other services will be housed. The second floor will provide space for the readout electronics and data processing and the online processing farm will be housed at the third floor. The hall electricity supply and ventilation will be hosted at the fifth floor, whereas at the fourth floor there will be the space for the shift crew: the control room and a meeting room, with some service rooms, will be at the same level of the surrounding ground. The $\overline{\text{P}}$ANDA experiment will need liquid helium for the TS solenoid and for the compensation solenoid. The refrigeration scheme will be similar to the one used for the BaBar magnet [32]. The cryogenic plant will be built and characterised at FZ

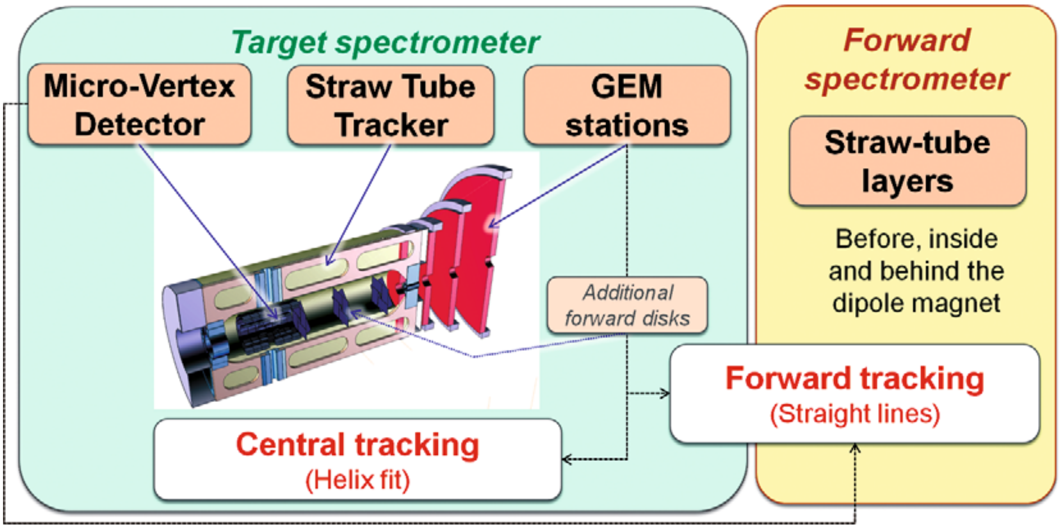

Fig. 15. Overview of the $\overline{\mathrm{P}}$ANDA tracking system, including the option of the additional forward disks.

Jülich and moved to FAIR with the magnet. In the natural convection refrigeration scheme that has been proposed, the storage-liquefaction Dewar close to the liquefier acts as buffer for the system. With the projected LHe consumption (safety factor on cryogenic losses included), a 2000 l storage will allow ∼ 10 h of operation in case of liquefier failure, giving ample time margin for the magnet discharge. The supply point will be at the north-east area of the building. From that point, the LHe will be delivered to the control Dewar, which can be chosen sufficiently small (∼ 30 l) to minimise the LHe inventory in the $\overline{\mathrm{P}}$ANDA hall. The helium gas coming out from the thermal shields would be recovered at room temperature and pressure in the low pressure recovery system.

All other cabling, which will be routed starting at the counting house, will join the LHe supply lines at the end of the rails system of the TS at the eastern wall. The temperature of the building will be moderately controlled. More stringent requirements with respect to temperature and humidity for the detectors have to be maintained locally. To facilitate cooling and avoid condensation, the Target Spectrometer will be kept in a tent with dry air at a controlled temperature.

1.3 The charged-particle tracking system

There are different tracking systems for charged particles at $\overline{\mathrm{P}}$ANDA (see fig. 15), positioned inside the target spectrometer and in the forward region around the dipole magnet. Main tasks of the global tracking system are the accurate determination of the particle momenta, a high spatial resolution of the primary interaction vertex and the detection of displaced secondary vertices. Therefore, measurements of different subdetectors have to be merged in order to access the full tracking information.

1.3.1 Basic approach

The magnetic solenoid field in the target spectrometer results in a circular transverse motion of charged particles with non-zero transverse momentum. The particle momentum then can be extracted via the determination of the bending radius. However, tracks with a small polar angle will exit the solenoid field too soon to be measured properly. For this case, the particle deflection induced by the subsequent dipole magnet is used to measure the particle momentum. Basically it can be deduced from a combined straight line fit before and after the dipole.

Due to the different analysing magnets, different track fitting algorithms have to be applied for central and forward tracks. Central tracks are reconstructed by combining hit points in the MVD layers with the hit information of the STT or the GEM stations. For the reconstruction of small angle tracks the straw tube layers in the forward spectrometer have to be used. In overlap regions the MVD, the additional forward disks or the GEM stations can contribute to the forward tracking because the delivery of an additional track point closer to the IP significantly improves the precision of the fitting results. After the global identification of individual tracks an event mapping have to be performed to match different tracks of the same event to a common vertex which either corresponds to the primary interaction vertex or a delayed decay of short-lived particles.

The luminosity monitor at the downstream end of the experiment is a tracking device of its own right. It was introduced to measure the time integrated luminosity, which is essential for the determination of cross sections for different physics processes. Therefore, elastically scattered antiprotons are measured under small angles corresponding to small momentum transfers. The associated differential cross sections are well known and thus provide an ideal reference channel. Additional information from the MVD will eventually improve the measurement by taking advantage of the reconstructed slow recoil proton at polar angles of around 90°, which is correlated with the highly energetic antiproton detected in the luminosity monitor.

1.3.2 Optimisation criteria

The different topics of the $\overline{\mathsf{P}}$ANDA physics program will impose specific optimisation criteria and requirements to design and performance of the tracking system. The optimum design thus depends on the relative weight which is given to the different physics aspects. Main criteria for the optimisation will be discussed in the following.

Acceptance

Full 2π azimuthal coverage is mandatory in order to allow identification of multi-particle final states and studies of correlations within the produced particles. In particular, the spectroscopy program of charmed and strange hadrons relies on the measurement of Dalitz plot distributions of three-body final states, which requires a smooth acceptance function across the full phase-space. Particular care has to be taken to avoid gaps in the acceptance function and to minimise the effect of discontinuities induced by the transition between adjacent sub-detector components, by detector frames or by mechanical support structures.

The fixed-target setup at $\overline{\mathsf{P}}$ANDA implies a Lorentz boost γ_{CM} of the centre of mass ranging from 1.20 to 2.92. This large dynamic range in the Lorentz boost corresponds to a large difference in the typical event topologies at low and at high antiproton momenta. At higher antiproton beam momenta the vast majority of the produced particles in the final state will be emitted into the forward hemisphere. However, light particles like $e^{\pm}$, $\mu^{\pm}$ or $\pi^{\pm}$ may well be emitted into the backward hemisphere even at highest beam momentum. As an example, pion backward emission is possible for a centre of mass momentum $p_{cm} > 93\,\mathrm{MeV}/c$ at $p_{\bar{p}} = 1.5\,\mathrm{GeV}/c$, and for $p_{cm} > 380\,\mathrm{MeV}/c$ at $p_{\bar{p}} = 15\,\mathrm{GeV}/c$.

Backward charged particle tracking is needed for various measurements foreseen at $\overline{\mathsf{P}}$ANDA. For instance, for the independent determination of the electric and magnetic parts of the time-like proton form factor in the reaction $\bar{\mathrm{p}}\mathrm{p} \to \mathrm{e}^+\mathrm{e}^-$ the full angular distribution has to be measured. At $q^2 = 14\,\mathrm{GeV}^2/c^2$, that is at $p_{\bar{p}} = 6.45\,\mathrm{GeV}/c$, a polar angle of 160° in the centre of mass frame corresponds to electrons with a momentum of $0.70\,\mathrm{GeV}/c$ at $\theta_{lab} = 113°$. Detection of pions in the backward hemisphere is important in studies of strange, multi-strange and charmed baryon resonances in $\bar{\mathrm{p}}\mathrm{p} \to Y^{\star}\bar{Y}'$ (+c.c.) reactions where the excited hyperon $Y^{\star}$ decays by single or double pion emission. Also higher charmonium states may emit pions with decay energies above the critical value for backward emission in the laboratory. The $\overline{\mathsf{P}}$ANDA tracking detectors therefore have to cover the full range of polar angles between 0° and about 150°.

Besides the solid angle of the detector also the acceptance in momentum space has to be considered. Often the final state contains charged particles with very large and with very small transverse momentum components which need to be reconstructed at the same time. Given the strength of the solenoid field of 2 T required to determine the momentum vector of the high transverse momentum particle, the radius of the transverse motion of the low transverse momentum particle may be small. Sufficient tracking capability already at small distance from the beam axis is therefore mandatory. As an example, one may consider the reaction $\bar{\mathrm{p}}\mathrm{p} \to \mathrm{D}^{*+}\mathrm{D}^{*-}$ close to threshold with $\mathrm{D}^{*+} \to \mathrm{D}^0\pi^+$ (+c.c.). Assuming $39\,\mathrm{MeV}/c$ momentum of the decay particles in the $\mathrm{D}^{*\pm}$ rest frame, particles of the subsequent decay $\mathrm{D}^0 \to \mathrm{K}^-\pi^+$ (+c.c.) have $61\,\mathrm{MeV}/c$ momentum in the $\mathrm{D}^0/\bar{\mathrm{D}}^0$ rest frame. In the solenoid field of the TS, the charged pions and kaons from the $\mathrm{D}^0/\bar{\mathrm{D}}^0$ decay may have helix diameters up to almost 1.5 m. The transverse motion of the charged pion from the $\mathrm{D}^{*\pm}$ decay stays within a distance of almost 7 cm from the beam axis and therefore need to be reconstructed based on the track information from the MVD only.

Delayed decay vertex detection

An important part of the $\overline{\mathsf{P}}$ANDA physics program involves final states consisting of hadrons with open charm or strangeness which decay by weak interaction and thus have macroscopic decay lengths. The decay length of charmed hadrons is of the order of $100\,\mu\mathrm{m}$ ($\approx 310\,\mu\mathrm{m}$ for $\mathrm{D}^{\pm}$, $\approx 150\,\mu\mathrm{m}$ for $\mathrm{D}_s^{\pm}$, $\approx 120\,\mu\mathrm{m}$ for D^0, $\approx 130\,\mu\mathrm{m}$ for Ξ_c^+, $\approx 60\,\mu\mathrm{m}$ for Λ_c^+, and $\approx 30\,\mu\mathrm{m}$ for Ξ_c^0). Therefore, the design of the tracking system aims on a detection of decay vertices of particles with decay lengths above $100\,\mu\mathrm{m}$. In order to achieve sufficient separation of the reconstructed decay vertex, the inner part of the tracking system has to be located very close to the interaction point, both in longitudinal and in radial direction. This requirement is fulfilled in the design of the MVD.

The identification of hyperons and K_S mesons requires the reconstruction of delayed decay vertices at much larger distances. Λ and Ξ hyperons have comparatively large decay lengths of about 8 cm and 5 cm, respectively. Due to the Lorentz boost this may result in vertices which are displaced by tens of centimetres from the interaction point mostly in the downstream direction. The considerations in the previous section concerning the required acceptance thus apply with respect to the shifted emission points of charged particles. The inner part of the $\overline{\mathsf{P}}$ANDA tracking system, therefore needs sufficient extension to the downstream direction in order to deliver sufficient track information for charged particle tracks originating from these displaced vertices.

Momentum and spatial resolution

The spatial resolution of the tracking detectors is important in two aspects. In the vicinity of the interaction point it directly determines the precision to which primary and displaced decay vertices can be reconstructed. Further on, based on the deflection of charged particles in both solenoid and dipole magnetic fields, it is an essential contribution to the momentum resolution of charged particles in all three coordinates.

The detection of displaced vertices of charmed hadrons imposes particular requirements to the spatial resolution close the interaction point. With a typical Lorentz boost $\beta\gamma \simeq 2$, D meson decay vertices have a displacement of the order of a few hundreds micrometres from the primary production point. Hence, to distinguish charged daughter particles of D mesons from prompt particles a vertex resolution of $100\,\mu$m is required. The position resolution is less demanding for the reconstruction of strange hadrons having decay lengths on the scale of centimeters. In this case a vertex resolution of a few millimetres is sufficient. Due to the significant Lorentz boost and the small opening angle between the decay particles of hyperons the resolution in transverse direction is required to be much better than the one for the longitudinal component.

The achievable momentum resolution is a complex function of the spatial resolution of the tracking subdetectors, the number of track-points, the material budget of active and passive components resulting in multiple scattering, the strength and homogeneity of the magnetic field, and of the particle species, its momentum and its emission angle. Due to the respective momentum dependence, it is generally expected that multiple scattering limits the momentum resolution of low energy particles, whereas for high-energy particles the smaller curvature of the tracks is the dominant contribution to the resolution.

The resolution in the determination of the momentum vectors of the final state particles directly determines the invariant or missing mass resolution of the particles that are to be reconstructed. Typically, the width of hadrons unstable with respect to strong interaction (except for certain narrow states like, *e.g.*, charmonium below the $\mathrm{D\bar{D}}$ threshold) is of the order of $10\,\mathrm{MeV}/c^2$ to $100\,\mathrm{MeV}/c^2$. As an instrumental mass resolution much below the natural width is without effect, a value of a few $10\,\mathrm{MeV}/c^2$ seems to be acceptable for the identification of known states or for the mass measurement of new states. With a typical scale of GeV/c^2 for the kinematic particle energy this translates to a relative momentum resolution σ_p/p of the order of 1% as design parameter for the $\overline{\mathsf{P}}$ANDA tracking detectors.

Count rate capability

The expected count rates depend on the event rate as discussed in sect. 1.1.4 and the multiplicity of charged particles produced in the events. While the total rate is of importance for DAQ design and online event filtering, the relevant quantity for detector design and performance is the rate per channel, which is a function of the granularity per detector layer and of the angular distribution of the emitted particles. The latter depends on the beam momentum and the target material.

The nominal event rate at $\overline{\mathsf{P}}$ANDA is given by $2\cdot 10^7$ interactions per second. In case of $\bar{\mathrm{p}}\mathrm{p}$ annihilations typically only a few charged particles are produced. Even if secondary particles are taken into account, the number of charged particles per event will not be much larger than 10 in most cases. Thus the detector must able to cope with a rate of $2\cdot 10^8$ particles per second within the full solid angle. Particular attention has to be paid to elastic $\bar{\mathrm{p}}\mathrm{p}$ scattering since this process contributes significantly to the particle load in two regions of the detector: scattering of antiprotons at small forward angles and the corresponding emission of recoil protons at large angles close to 90°. This affects primarily the inner region of the MVD disc layers and the forward tracking detector as well as the MVD barrel part and the central tracker.

The use of nuclear targets will not create significantly higher count rates than obtained with a hydrogen or deuterium target. This is due to single Coulomb scattering which dramatically increases with the nuclear charge ($\propto Z^4$) and results in $\bar{\mathrm{p}}$ losses with no related signals in the detector. In contrast to $\bar{\mathrm{p}}\mathrm{p}$ collisions in $\bar{\mathrm{p}}\mathrm{A}$ collisions no high rate of recoil particles close to 90° is expected. The emission angles of recoil protons from quasi-free $\bar{\mathrm{p}}\mathrm{p}$ scattering are smeared by Fermi momentum and rescattering, while recoil nuclei, if they at all survive the momentum transfer, are too low energetic to pass through the beam pipe.

Particle identification

Charged-particle identification over a wide range of momentum and emission angle is an essential prerequisite for the capability of $\overline{\mathsf{P}}$ANDA to accomplish the envisaged physics program. Charged particles with higher momenta will be identified via Cherenkov radiation by the DIRC detector in the Target Spectrometer and by the forward RICH detector in the Forward Spectrometer. For positive charged kaon-pion separation in the DIRC about $800\,\mathrm{MeV}/c$ momentum is required. While almost all particles emitted within the acceptance of the Forward Spectrometer are above the Cherenkov threshold due to the forward Lorentz boost, a number of interesting reaction channels have final states with heavier charged particles ($\mathrm{K}^{\pm}, \mathrm{p}, \bar{\mathrm{p}}$) at larger angles with momenta below the DIRC threshold. In order to separate these low energy kaons from the much more abundant pions, particle identification capability based on energy loss information has to be supplied by the central tracking detector.

Material budget

Any active or passive material inside the detector volume contributes to multiple scattering of charged particles, electron bremsstrahlung and photon conversion, and thus reduces the momentum resolution for charged particles in the tracking detectors, and detection efficiency and energy resolution for photons in the EMC. Therefore the material budget has to be kept as low as possible. Following the more demanding requirements to meet the performance criteria of the EMC, a total material budget of MVD and Central Tracker below 10% is still considered to be acceptable [28].

2 The Straw Tube Tracker - STT

2.1 General overview

This section describes the technical layout of the central Straw Tube Tracker (STT) of the $\overline{\mathrm{P}}$ANDA experiment. The STT is the main tracking detector for charged particles in the $\overline{\mathrm{P}}$ANDA target spectrometer and consists of 4636 single straw tubes, arranged in a large cylindrical volume around the beam-target interaction point. It encloses the Micro-Vertex-Detector (MVD) for the inner tracking and is followed in beam direction by a vertical setup of GEM disks for adding track points in the forward polar angle range, as discussed in the previous section.

The tasks of the STT are the precise spatial reconstruction of the helical trajectories of charged particles in a broad momentum range from about a few $100\,\mathrm{MeV}/c$ up to $8\,\mathrm{GeV}/c$, the measurement of the particle momentum by the reconstructed trajectory in the solenoidal magnetic field and the measurement of the specific energy loss ($\mathrm{d}E/\mathrm{d}x$) for particle identification (PID). The PID information from the STT is needed in particular to separate protons, kaons and pions in the momentum region below about $1\,\mathrm{GeV}/c$.

Since straw tubes are the basic detector elements of the STT, the next section describes first straw tubes and their properties in general. Then the specific straw tube design and chosen gas mixture for the $\overline{\mathrm{P}}$ANDA-STT are described. The technical layout of the STT, presented in the next sections, is based on the construction and development of several prototype systems. The main detector and electronic readout properties have been investigated by various test setups and measurements, including tests with high-rate proton beams, which will be discussed in a later chapter.

The presented layout and performance of the STT in the $\overline{\mathrm{P}}$ANDA target spectrometer environment has been checked by dedicated simulations, reconstruction and full analysis studies of certain $\mathrm{p}\bar{\mathrm{p}}$-reactions, identified as being benchmark tests for the whole $\overline{\mathrm{P}}$ANDA scientific program. These studies used the official $\overline{\mathrm{P}}$ANDA software framework (PandaRoot) with implemented track-finding, -fitting and analysis routines for primary and secondary tracks in the STT. The results are discussed in detail in a particular section.

The last section describes the project organization and summarizes the time lines of the STT construction.

2.2 Straw tube description

Straws are gas-filled cylindrical tubes with a conductive inner layer as cathode and an anode wire stretched along the cylinder axis. An electric field between the wire and the outer conductor separates electrons and positive ions produced by a charged particle along its trajectory through the gas volume. Usually the wire is on positive voltage of a few kV and collects the electrons while the ions drift to the cathode. By choosing thin wires, with a diameter of few tens of μm, the electric field strength near the wire is high enough to start further gas ionizations by electron collisions with gas molecules. Depending on the high voltage and the gas characteristics an amplification of about 10^4–10^5 of the primary charge signal is possible, which is large enough to read out the signal.

By measuring the drift time of the earliest arriving electrons one gets the information about the minimum particle track distance from the wire. The isochrone contains all space points belonging to the same electron drift time and describes a cylinder around the wire axis. The characteristic relation between drift time and isochrone is given by the electron drift velocity, depending on specific gas parameters, electric and magnetic field. Therefore, this fundamental relation has to be calibrated using reference tracks with known space and drift time information. The particle track is reconstructed by a best fit to the isochrones measured in a series of several straw tubes with the same orientation. Additional skewed straw layers provide a full stereo view of the particle trajectory.

The specific energy loss ($\mathrm{d}E/\mathrm{d}x$) of a charged particle in the straw gas volume can be used to identify the particle species and can be derived from the number of ionization electrons per track length ($\mathrm{d}x$) for the generated straw signal. Since the specific ionization in gas with about 100 ion-electron pairs per cm for minimum ionizing particles is quite low and shows in addition a strong fluctuation described by an asymmetric Landau distribution, a higher number of measurements is needed to get a sufficient precision for the particles' specific energy loss. The truncated mean method, which rejects from many samples those with the largest energy losses due to the fluctuations, can help to improve the resolution.

Straw detectors exhibit the most simple geometry of highly symmetrical, cylindrical tubes and have several advantages which are summarized in the following:

- Robust electrostatic configuration. The shielding tube around each high-voltage wire suppresses signal cross-talk and protects neighbor straws in case of a broken wire.
- Robust mechanical stability if the straws are arranged in close-packed multi-layers.
- High detection efficiency per straw for about 99.5% of the inner tube radius and minimal dead zones of a few mm at the tube ends.
- High tracking efficiency for multi-layers if thin-wall straws are close-packed with minimal gaps of about $20\,\mu$m between adjacent tubes.
- High spatial resolution, $\sigma_{r\varphi} < 150\,\mu\mathrm{m}$ depending on the tube diameter and gas characteristics.
- Simple calibration of the space-drift time relation due to the cylindrical isochrone shape.
- Small radiation length, $X/X_0 \sim 0.05\%$ per tube, if straws with thinnest ($\sim 30\,\mu$m) film tubes are used.
- The high rate capability can be improved by reducing the occupancy using smaller tube diameter and/or choosing a fast drift gas.

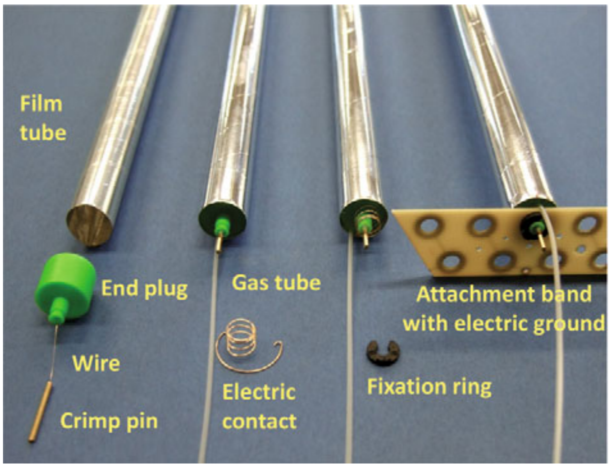

Fig. 16. Photograph of all straw components and the straw assembly steps. See the text for a description.

2.2.1 Straw materials

The straw tubes used for the $\overline{\text{P}}$ANDA STT have a length of 1500 mm, 10 mm inner diameter, and a total wall thickness of 27 μm. They are made of two layers of 12 μm thin aluminized Mylar [33] films by wrapping two long film strips around a rotating mandrel and gluing the two half-overlapping strips together. Then the cylindrical film tube is stripped off. The aluminization at the inner tube wall is used as the cathode whereas the aluminization of the second, outer strip layer is used to prevent light incidence.

A gold-plated tungsten-rhenium wire with 20 μm diameter is used as anode. Cylindrical precision end plugs made from ABS thermoplastic [34] with a wall thickness of 0.5 mm close the tube at both ends (see fig. 16). They are glued to the Mylar film leaving a small 1.5 mm film overlap on both ends. There, a gold-plated copper-beryllium spring wire is inserted to provide the electric cathode contacting. The springs allow a 2 mm tube elongation with a typical spring force equivalent to 10 g. The end plugs have a central hole with a 3 mm thick cylindrical nose to insert and glue a crimp pin for the wire. A micro PVC (medical-quality grade) tube is fed through another hole and glued in the end plugs to provide a gas flow through the tube. The total weight of a fully assembled straw is 2.5 g. The anode wire is stretched by a weight of 50 g and crimped in the copper pins at a gas overpressure in the straw tube of 1 bar.

Table 5 lists the different straw components and their thickness in radiation lengths. The chosen film tubes are the thinnest used for straw detectors, but still show sufficient mechanical stability for the assembly to self-supporting multi-layers. For the proposed $\overline{\text{P}}$ANDA straw tracker the total radiation length of the straw volume is 1.2% with a maximum number of 27 hit straw layers for a traversing particle track in radial direction.

2.2.2 Pressurized straws

Both, efficiency and resolution of a straw are best for a perfect cylindrical shape of the film tube and the wire being highly concentrically stretched along the cylinder axis. With a wire tension[1] of about 50 g inside a 1.5 m long horizontal straw tube the maximum sag due to gravitation at the middle of the tube is less than 35 μm. For the 4636 straws of the $\overline{\text{P}}$ANDA central tracker this adds up to a wire tension equivalent to about 230 kg which must be maintained. Usually, this is done by fixing the straw tubes inside a strong and massive surrounding frame or by adding reinforcement structures like CF-strips along the tubes to keep them straight. All methods inevitably increase the detector thickness given in radiation length by these additional materials.

Therefore a new technique based on self-supporting straw double layers with intrinsic wire tension developed for the COSY-TOF straw tracker [35] has been adopted and further developed for the $\overline{\text{P}}$ANDA STT. Single straw tubes are assembled and the wire is stretched by 50 g at an overpressure of 1 bar. Then a number of tubes are close-packed and glued together to planar multi-layers on a reference table which defines a precise horizontal tube to tube distance of 10.1 mm. At the gas overpressure of 1 bar the double layer maintains the nominal wire tension of 50 g for each tube, *i.e.* becomes self-supporting.

The precision of the tube and wire stretching method by the gas overpressure for the used thin film tubes was studied in detail for the COSY-TOF straw tubes. Figure 17 shows the measured tension with decreasing gas overpressure. A well-defined tension is seen, even down to vanishing overpressure where only the stiffness of the Mylar film tube maintains a wire tension of 28 g. The nominal tension for the COSY-TOF 1 m long straws was 40 g at 1.2 bar overpressure. For the $\overline{\text{P}}$ANDA 1.5 m long straws the nominal tension is 50 g at 1.0 bar overpressure.

2.2.3 Gas mixture

The need of high spatial resolution in the STT requires high amplitude anode signals even for the single electron clusters, thus requiring high gas gain. On the other side, a high gas gain significantly reduces the chamber lifetime. For the optimum gas amplification choice both these factors should be taken into account properly. Table 6 shows the main parameters of some of the most used gases and gas mixtures. In order to select the most suited gas mixture for the STT detector, it is useful to consider two essentially different situations. Some gas mixtures, if a low electric field is used, can effectively quench the electron kinetic energy, preventing them to gain enough energy between collisions. In this case, electrons are in thermal equilibrium with the surrounding medium and the drift velocity is proportional to the electric field. Such gases are usually called "cold" for that given electric field strength.

---

[1] Usually given as the mass weight used to stretch the wire.

Table 5. Mean thickness in radiation lengths of the different straw tube components. The number for the gas mixture is evaluated at 20 °C and 2 atm.

Element	Material	X[mm]	X_0[cm]	X/X_0
Film Tube	Mylar, 27 μm	0.085	28.7	3.0×10^{-4}
Coating	Al, $2 \times 0.03\,\mu$m	2×10^{-4}	8.9	2.2×10^{-6}
Gas	Ar/CO_2(10%)	7.85	6131	1.3×10^{-4}
Wire	W/Re, 20 μm	3×10^{-5}	0.35	8.6×10^{-6}
			$\sum_{straw}$	4.4×10^{-4}

Table 6. Properties of different gases and gas mixtures. Z and A are charge and atomic weight, for molecules the total number has to be taken, N_p and N_t are the number of primary and total electrons per cm, respectively, E_x and E_i are the excitation and ionization energy, respectively, W_i is the average energy required to produce one electron-ion pair in the gas, $(\mathrm{d}E/\mathrm{d}x)_{mip}$ is the most probable energy loss by a minimum ionizing particle and X_0 is the radiation length. For gas mixtures, the weighted average value has been taken.

Gas or gas mixture	Z	A	E_x [eV]	E_i [eV]	W_i [eV]	$\mathrm{d}E/\mathrm{d}x$ [keV/cm]	N_p [cm^{-1}]	N_t [cm^{-1}]	X_0 [m]
He	2	4	19.8	24.5	41	0.32	4.2	8	5299
Ar	18	40	11.6	15.7	26	2.44	23	94	110
CO_2	22	44	5.2	13.7	33	3.01	35.5	91	183
i–C_4H_{10}	34	58	6.5	10.6	23	5.93	84	195	169
Ar+10% CO_2	–	–	–	–	26.7	2.5	24.6	93	117
He+10% i–C_4H_{10}	–	–	–	–	39.2	0.88	12.7	26.7	1313
He+20% i–C_4H_{10}	–	–	–	–	37.4	1.44	20.6	45.4	749

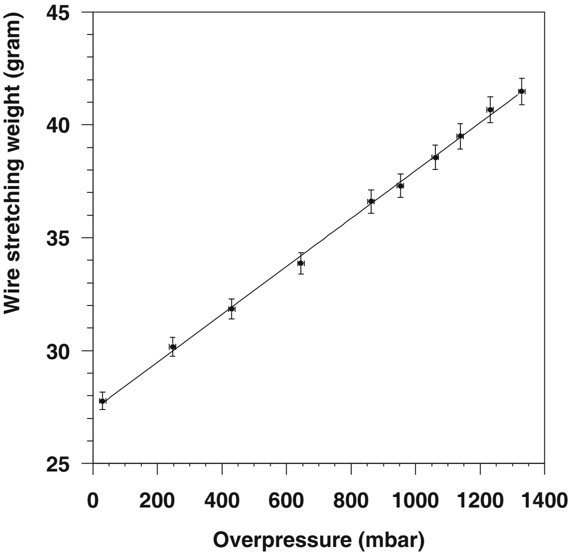

Fig. 17. Measured wire tension (weight equivalent) at different gas overpressures inside a straw. The nominal tension is 40 g at 1.2 bar overpressure for the COSY-STT straws.

On the contrary, if the electron average kinetic energy differs from the thermal energy, the drift velocity behavior becomes more complicated. In many gas mixtures the drift velocity becomes saturated and does not depend strongly on the electric field strength. That makes the reconstruction of the track coordinates easier. However, it is difficult to get high spatial resolution in these "hot" gas mixtures, in principle due to the large diffusion. The standard choice of many experiments is to have a "hot" or "warm" gas mixture, that has a weak dependence of the drift velocity on the applied electric field. In this case, the electric field inhomogeneities do not play a significant role, which makes the calibration simpler. An overpressure can be used in these cases to reduce the diffusion.

The main requirements, that should be taken into account for the choice of the most suited gas mixture, are:

- good spatial resolution;
- rate capability;
- radiation hardness;
- radiation length;
- chemical inactivity;
- working voltage;
- working pressure;
- accessibility on the market and price.

For the $\overline{\mathrm{P}}$ANDA CT the spatial resolution, the rate capability and the radiation hardness are the points of highest importance. Initially a "cold" gas mixture of He + 10% i–C_4H_{10} was proposed for the Conceptual Design Report [36]. Although this gas mixture has one undoubted advantage, the long radiation length X_0, it provides a relatively low drift velocity, which is a disadvantage more or less peculiar for all "cold" gases. As a result, a gas mixture based on Ar + 10%CO_2 has been suggested.

Figures 18 and 19 show the results of the simulation for the spatial resolutions achievable for the Ar + 10% CO_2 and He + 10% i–C_4H_{10} for 1 and 2 atm gas pressure. The simulations have been performed using the GARFIELD

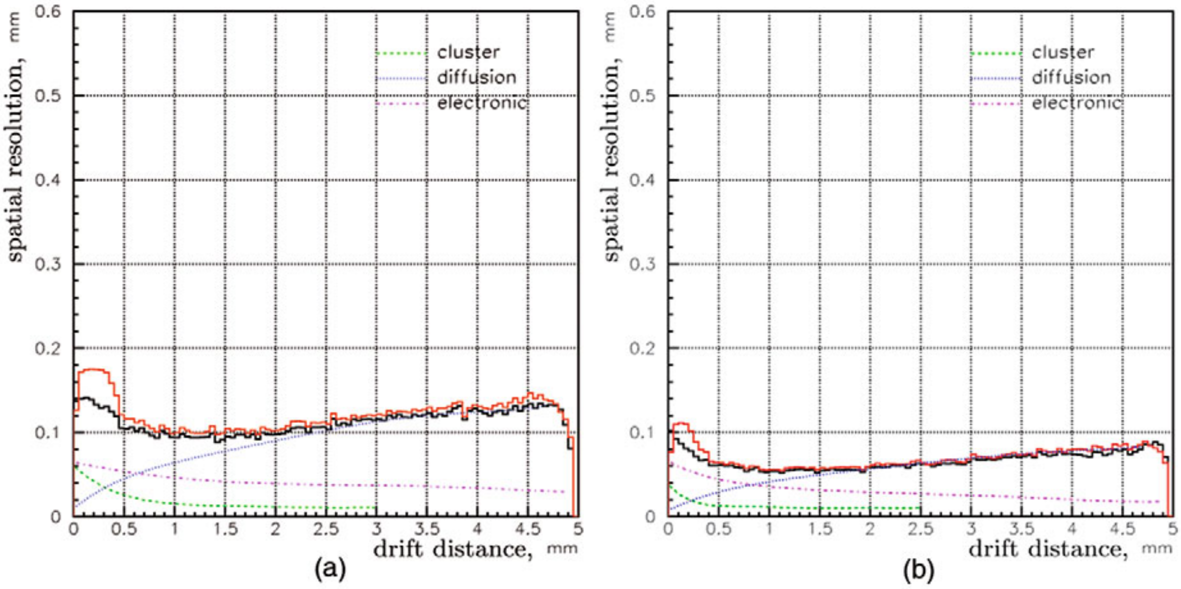

Fig. 18. The spatial resolution for the Ar+10% CO_2 gas mixture for 1 a) and 2 atm b) pressures. The red line corresponds to an ideal $r(t)$ relation, the black one to the measured. The main contributions to the resolution are also shown in different colors.

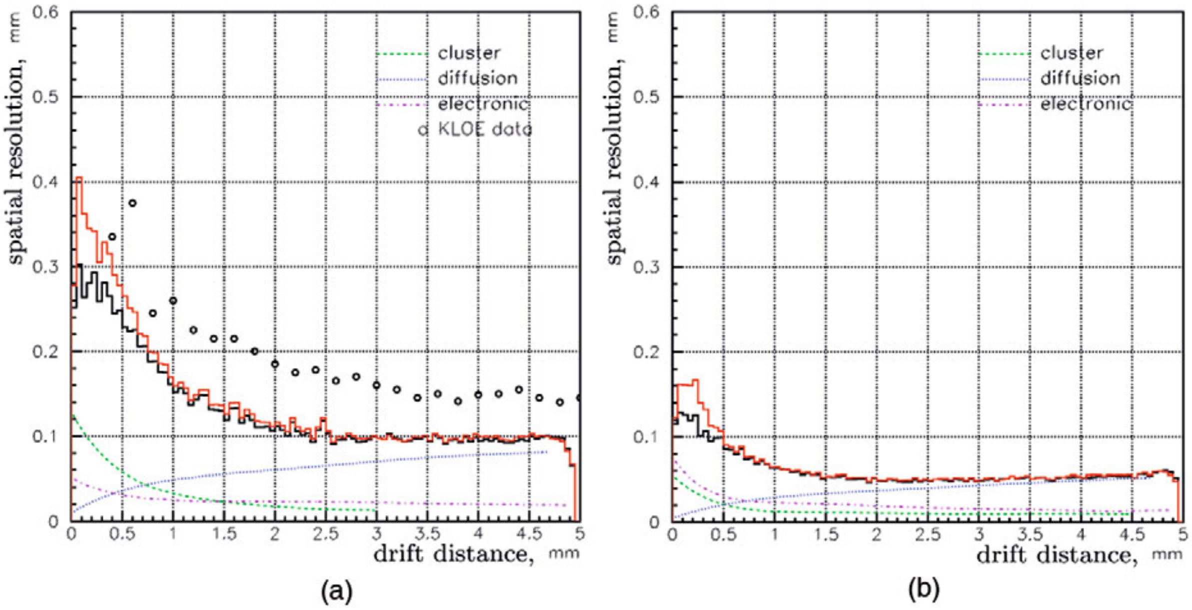

Fig. 19. Spatial resolution in He+10% i–C_4H_{10} with 1 a) and 2 atm b). The red line corresponds to an ideal $r(t)$ relation, the black one to the measured. The main contributions to the resolution are also shown in different colors. The experimental spatial resolution of the KLOE drift chamber, denoted by the open circles, is given for comparison [38].

program and the build-in MAGBOLTZ package [37]. The good agreement of these simulation data with the experimental results obtained by the KLOE drift chamber prototype [38], as shown in fig. 19, can be interpreted as a proof of the validity of the simulations of the straw tube parameters.

The spatial resolution of the Ar + 10% CO_2 mixture is satisfactory even at 1 atm pressure, while the spatial resolution in the He + 10% i–C_4H_{10} is worse than the required 150 μm, and only an increase of the pressure could improve this situation. The total drift time is also an important parameter. The Ar+10% CO_2 mixture has a drift time of 80 ns for a 4 mm drift path. The He+10% i–C_4H_{10} has double the drift time. Since the average time between two events in $\overline{\mathsf{P}}$ANDA will be ∼ 100 ns, when using the He+10% i–C_4H_{10} gas mixture, the information from consecutive events could be contained in the STT at any time. This event mixing in the tracker will result in a significant complication of the trigger logic and of the pattern recognition algorithm. By increasing the pressure two times,

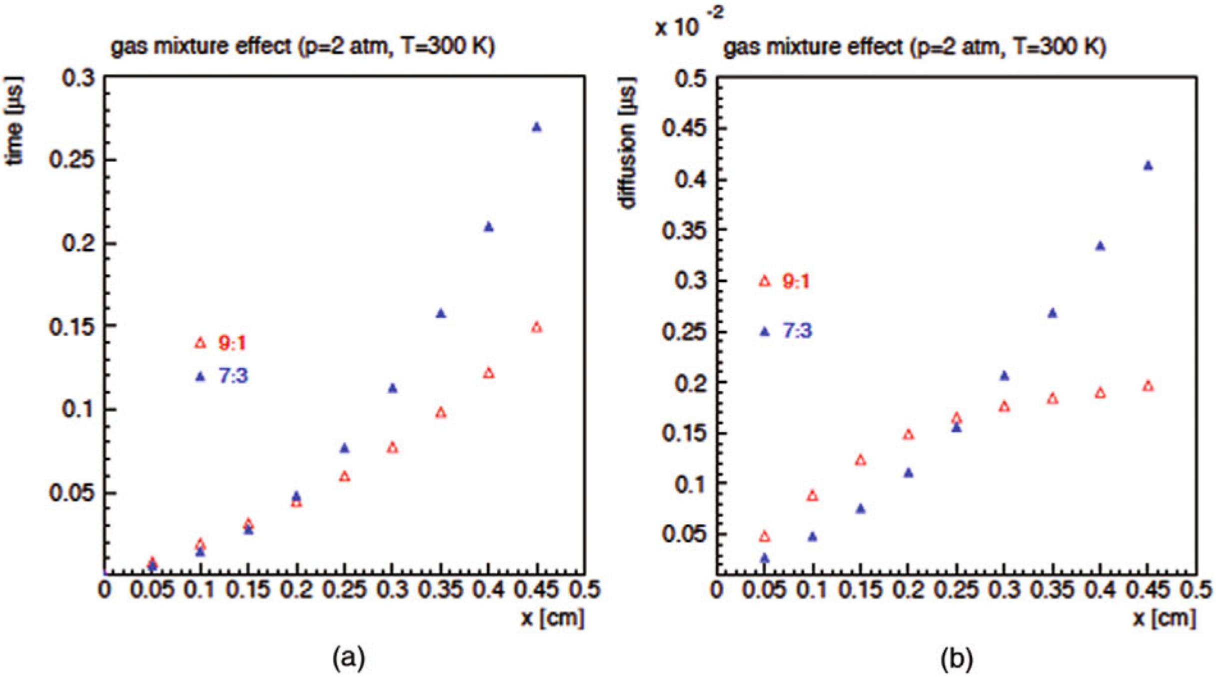

(a) (b)

Fig. 20. The graphs refer to two gas mixtures with different CO_2 percentage. Red points correspond to a percentage of 10% of CO_2, blue to 30%. (a) Space time relation. (b) Diffusion.

the drift time for the He+10% i–C_4H_{10} grows by 50 ns, while for the Ar + 10% CO_2 only by 10 ns. That makes the situation with the event mixing even more difficult.

The effect of the electronics threshold on the spatial resolution has also been studied. The average gas gain has been reduced by a factor two using the same electronic threshold. Figure 19 shows only a small deterioration of the Ar+10% CO_2 resolution and a strong worsening in the case of the He+10% i–C_4H_{10} gas mixture. This is one more argument in favor of the Ar + 10% CO_2 usage.

All these considerations show strong advantages for the Ar + 10% CO_2 gas mixture for the $\overline{\mathrm{P}}$ANDA STT compared to the He + 10% i–C_4H_{10} gas composite.

The possibility to use higher percentages of CO_2 has been investigated. Figure 20 shows the space-time relation with two different CO_2 percentages: 10% and 30%, respectively. A greater percentage of CO_2 produces an increase of the electron diffusion which worsens the achievable space resolution. For completeness, we notice that a greater fraction of the quench gas will reduce the effect of the magnetic field on the mixture (Lorentz angle). Therefore the final concentration of the CO_2 component can be defined only after tests with magnetic field.

The variations of the gas mixture performance due to changes of the absolute temperature have been studied. The space time relation for the Ar+10% CO_2 mixture at 1 atm for two different temperatures, 250 and 300 K, is shown in fig. 21. No significant differences are present between the two curves. Therefore, it will not be necessary to control the temperature variation very precisely.

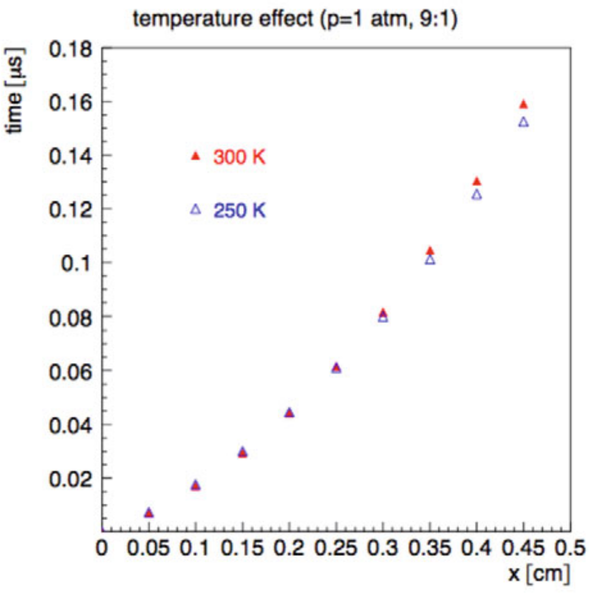

Fig. 21. Space-time relation for the Ar+10% CO_2 mixture at 1 atm for two different temperatures.

2.3 The STT detector

The surrounding detector systems define the available space for the $\overline{\mathrm{P}}$ANDA-STT as a cylindrical volume with an inner radius of 150 mm, outer radius of 420 mm and length of 1650 mm, at a position in the *z*-direction relative to the target from about $z = -550$ mm to $z = +1100$ mm. The space for the target pipe of the pellet beam at the vertical axis cuts this volume into two semi-cylinders with a gap of 42 mm in between. To facilitate access and maintenance the layout of the STT detector is split into two independent semi-cylindrical systems, with two separated mechanical frame structures, separated frontend electronic, gas and high-voltage supply. The two systems are mounted at the opposite sides of the vertical Central Frame (CF) structure which also supports the inner MVD detector system and the beam-target cross-pipe. The electronic frontend readout cards, supply and other services of the STT are placed at the upstream end of the detector within a space of 150 mm in the z-direction. The remaining active detection volume with a length of 1500 mm is filled by layers of straw tubes, each tube with a diameter of 10 mm and a length of 1500 mm. A few dedicated tubes have shorter lengths to fill some rest gaps in the volume.

2.3.1 The straw layout in the STT

The solenoid magnetic field is parallel to the beam axis and forces charged particles to helical trajectories, which are described by the helix circle in the projection on the xy-axis and by the helix slope in the perpendicular projection in the z-direction. For the spatial reconstruction of the trajectory the STT consists of a number of straws precisely aligned parallel to the beam and magnetic field, which measure the helix circle. Additional straws which are skewed by a few degrees to the axial direction provide a stereo view of the track and measure the z information of the track for reconstructing the helix slope.

The $\overline{\text{P}}$ANDA-STT uses the technique of pressurized straw tubes, closely packed and glued together to planar multi-layer modules. As discussed in the previous section such self-supporting straw modules show a high rigidity and mechanical precision and allow to reduce the weight and size of the mechanical frame structure to an absolute minimum. In addition, the close-packaging yields the highest straw density with a maximum number of straws per cross-sectional area. Therefore, the planar layer modules are arranged in a hexagonal layout which preserves the 60° position symmetry of close-packed, parallel straws.

Each of the two semi-cylindrical $\overline{\text{P}}$ANDA-STT volumes is filled by three sectors of straw tubes aligned in the z-direction and arranged in stacks of planar multi-layer modules. The hexagonal layout of both volumes together has an almost cylindrical shape with a 42 mm gap for the target pipe (fig. 22).

The arrangement of the straw layers in each of the six hexagonal sectors is as follows. In radial direction and starting from the inner radius in a sector there are 8 straw layers parallel to the beam axis, followed by a block of 4 stereo double layers, alternately skewed by ±2.9° relative to the axially aligned straw layers, and again a block of 4 layers parallel to the beam axis. Then, there are another 7 layers aligned parallel to the beam with a decreasing number of straws per layer to achieve the outer cylindrical shape of the STT. The inner cylindrical shape is reached by placing a few axially aligned straws in the inner corner region of each hexagon sector (see fig. 22).

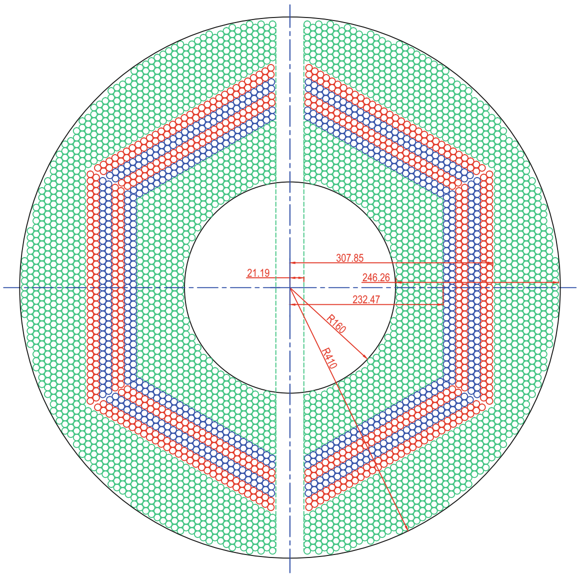

Fig. 22. Layout of the straw tubes in the STT in xy-view. The straws marked in green are parallel to the beam axis. The blue and red marked straw layers are skewed relative to the axially aligned straws in the same sector by a small angle of +2.9° and −2.9°, respectively.

In total, there are 4636 straws in the layout. All straws have the same inner diameter of 10 mm and length of 1500 mm, except a few outer straws in the border region of each skewed layer, which have different, reduced lengths (see fig. 24). The film wall thickness of all straws is 27 μm Mylar, aluminized on the inner side and outer side of the tube.

The close-packaging of the straws with less than 20 μm gaps between adjacent tubes yields the highest straw density with up to 27 layers in radial direction for the 3-dimensional track reconstruction. Up to 19 layers with axial straws parallel to the beam measure the helix circle in the xy-projection with a single (mean) isochrone resolution of better than 150 μm (σ_r). The association of the isochrone hits in the 8 stereo layers to the helix circle provides the z-coordinates of the track with a single hit resolution of slightly better than 3 mm (σ_z), which is determined by the isochrone resolution and the skew angle (α) of ±2.9° ($\sigma_z = \sigma_r / \sin(\alpha)$). The tracking efficiency for a single layer is 98.5% and only slightly reduced compared to the single tube radial efficiency (99.5%) by the thin tube wall (27 μm) and minimal spacing (20 μm gaps) between adjacent tubes.

Since the momentum resolution is dominated by the transverse momentum reconstruction and the stereo layers distort the close-packed cylindrical geometry their skew angle should be kept as small as possible to a few degrees. As can be seen in fig. 22 the chosen value of 2.9° creates only minor gaps between two hexagon sectors.

Due to the technique of the self-supporting straw modules no support or reinforcement structures in the tracking

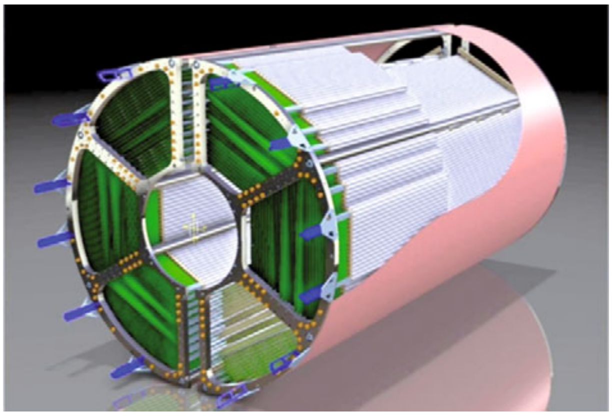

Fig. 23. Three-dimensional view of the STT with the mechanical frame consisting of light-weight profiles at both ends to attach and support the straw modules.

volume are needed. Figure 23 shows a three-dimensional view of the STT including the light-weight mechanical frame which consists of end flange profiles with precision holes to attach and support the straw modules. The inner and outer semi-cylinder surfaces will be covered by a thin wall of a light-weight composite material, consisting of a 1 mm Rohacell layer with a 0.17 mm thin carbon fiber skin, to protect the straw film tubes against a mechanical hazard from outside.

The low material budget of 1.23% (X/X_0) in the radial direction is the sum of the 24 average straw layers in the STT (1.06%) and the two protection walls ($2 \times 0.084\%$). It is dominated by the film wall thickness of the straw layers (0.72%) and the gas (0.31%). As discussed in the previous section the chosen film thickness of 27 μm Mylar is at a minimum and can not be further reduced. The resolution of the reconstructed momentum from the spatial trajectories is about 1–2% (σ_p/p) for simulated charged particles originating from the beam-target interaction point and including the track hits in the MVD. The material budgets of the straw layers and the walls have been taken into account in the simulation.

At the 2 tesla solenoid magnetic field the minimum transverse momentum for charged particles to reach from the interaction point the innermost straw layer in the STT is about 50 MeV/c. A minimum transverse momentum of about 100 MeV/c is needed to reach enough straw layers for a complete three-dimensional reconstruction of the helical trajectory. The STT covers a polar angle range from about 10° to 140°. The azimuthal coverage is only limited by the gap for the target pipe at ±90°.

The high number of up to 27 hit straws in radial direction is important to achieve a high resolution for the specific energy loss measurement (dE/dx). The high sampling number per track allows to truncate such hits with large deviations from the mean energy loss per tube. This so-called truncated mean method for the measured Landau-distributed energy losses improves the resolution significantly. From prototype measurements an energy resolution of better than 8% ($\sigma(E)/E$) is expected for the $\overline{\mathsf{P}}$ANDA-STT (see sect. 5.2).

2.3.2 Layout considerations

The specific straw layout described in the previous section has been optimized to achieve highest geometrical efficiency and spatial resolution for the track reconstruction in the $\overline{\mathsf{P}}$ANDA target spectrometer environment. By choosing a hexagonal geometry the straw tubes can be arranged in close-packed layers and the number of straws per cross-sectional area is largest. Then the main parameters for the STT layout determination are the straw diameter, number and position of the axial and skewed stereo layers, and the stereo angle which are discussed in the following.

The inner straw diameter of 10 mm is the same for all tubes which avoids different end plug designs, assembly tools and techniques. Therefore the cost and time for the mass production of the 4636 straws are strongly reduced. The expected highest particle rates of the single straws in the innermost layers scale roughly with the straw diameter and are about 5–8 kHz/cm, corresponding to 800 kHz per tube. These rates are still tolerable concerning signal distortion and aging properties. In a closed-packed geometry smaller tube diameters would increase the number of readout channels and reduce the available cross-sectional space for the electronic readout and gas supply per channel. In addition the material budget would be higher. All these aspects together favor the 10 mm tube diameter.

The tracking properties of the STT are mainly defined by the number and radial position of the axial and stereo straw layers. The axial straws are used for the measurement of the helix curvature and transverse momentum with high resolution. Then the hits in the stereo layers are associated to the found circular trajectory in the xy-projection and determine the helix slope in the z-direction. Instead of choosing a layout with many alternating axial and stereo layers in radial direction, the specific requirements for a highly efficient and high-resolution reconstruction of charged particle tracks in the $\overline{\mathsf{P}}$ANDA environment favors a different layout.

The chosen layout with a larger inner block of close-packed, axial straws, central block of stereo layers, followed again by an outer block of close-packed axial straws has the advantage of an almost continuous tracking, which is important for the particular $\overline{\mathsf{P}}$ANDA tracking environment with a high $\mathrm{p\bar{p}}$ interaction rate of $2 \times 10^7\,\mathrm{s}^{-1}$ and a mean particle multiplicity of about 4 charged tracks per event. The close-packing of many layers of axial straws yields the highest possible number of straw layers in the radial direction.

An important task is the recognition and reconstruction of the decay vertices of the Λ ($\bar{\Lambda}$) by the tracks of the charged decay particles. Up to a few 10% of the Λ ($\bar{\Lambda}$) can decay inside or even outside the region of the outer MVD layers. Then the vertex finding and reconstruction can only be done by the STT and needs a larger number (≥ 6) of inner axial straw layers for the precise track reconstruction in the xy-plane with a single hit resolution of about 150 μm. Although a complete secondary track finder program should combine the information of all the tracking detectors of the target spectrometer, the STT capability in this respect has been checked an preliminary

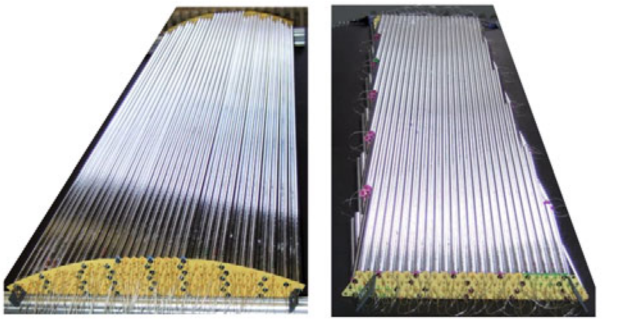

Fig. 24. Photograph of an axial straw layer module for the outer cylindrical shape and module with two double layers with opposite skew angle.

results are described in sect. 6.2.4. The resolution in the z-direction by the skewed layers is about 3 mm for single hits. As discussed in the previous section larger stereo angles which would improve the z resolution are not favorable because they distort the cylindrical geometry, cause larger gaps in the close-packed layout and have a higher material budget. For forward emitted decay tracks which hit only the inner axial layers and then leave the STT the hits in the vertical GEM tracker are associated to the found trajectories and add the z information.

In general the large inner and outer blocks of axial layers in the STT provide a continuous tracking in the xy-plane with high resolution for tracks entering the STT from the target interaction point or for background tracks entering the STT from outside. This is important to recognize a distortion of the helical trajectory by interactions with the MVD material or secondary background production inside the MVD volume or the outer DIRC and EMC volumes.

In summary, the STT layout combines a large acceptance and high momentum resolution for charged-particle tracks originating from the beam-target interaction point and a high efficiency for the reconstruction of displaced vertices, even outside the MVD. The detailed properties and performance results for the STT are described in the chapter about the physics analyses.

2.3.3 Straw layer modules

The layers of a sector are grouped into multi-layer modules, consisting of four close-packed axial layers or two close-packed double layers with opposite skew angle. The outermost module in a sector consists of 7 close-packed axial layers with a varying number of straws per layer to reach an outer cylindrical shape (see fig. 24). For the innermost straw module a few single straws are added in the corners to reach the inner cylindrical shape.

The close-packed layer modules show a strong rigidity when the straws are pressurized to the nominal overpressure of 1 bar. No stretching from a mechanical frame structure to sustain the wire tension or reinforcements for the tube shape are needed. Due to the high overpressure the thin-wall tubes have a perfect and strong cylindrical shape and the modules are self-supporting. At both ends of a module dedicated strips made of 0.7 mm thin glass fiber are attached and fixed to the end plugs by thermoplastic snap rings (see fig. 16). The strips provide the electric grounding of the individual straws and the mechanical support and positioning of a module by two additional thermoplastic mounting brackets per strip. Figure 25 shows all modules of one full hexagon sector together.

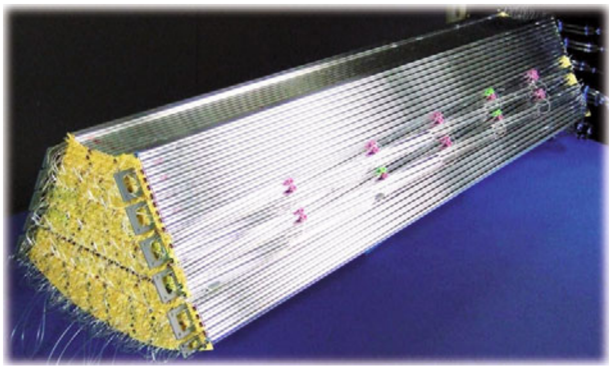

Fig. 25. Photograph of all straw modules of one STT hexagon sector. Two thermoplastic mounting brackets at both ends of a module are used for its support and positioning in the mechanical frame.

The modules consisting of two stereo double layers with opposite ±2.9° skew angle have several straws with different, shorter lengths at the corners to adopt the hexagonal sector shape. For the gas supply and the electric connection of these tubes the shorter straws in the lower double-layer are connected to the corresponding, at the same z-position attaching straws in the upper double layer. About 2 cm space in the z-direction is foreseen for connecting the gas tubes, sense wires and electric ground. The electric connection scheme was tested by illuminating two connected straws with an ^{55}Fe radioactive source and comparing the shape of their analog signals. No obvious distortions of the signals were observed due to the short length of the electric connection.

For all modules the electronic readout, gas and high-voltage supply are at the upstream end of the detector to reduce the material budget for tracks going in forward direction through the downstream end of the STT.

2.3.4 Assembly of straw modules

The construction of the straw modules consists of several assembly steps, starting with the production of the single straw tubes and ending with a final, self-supporting straw module, consisting of several straw layers. Such a module is then mounted in the mechanical frame structure which is discussed in detail in the next section. In the following, the main steps of the assembly procedure of the single straws and modules are described.

- Mylar film tubes are cut to the nominal length of 1500 mm and gas pipes are glued to the end-plugs using a plastic glue (Pattex plastik [39]).

Fig. 26. Gluing of straw tubes to multi-layers.

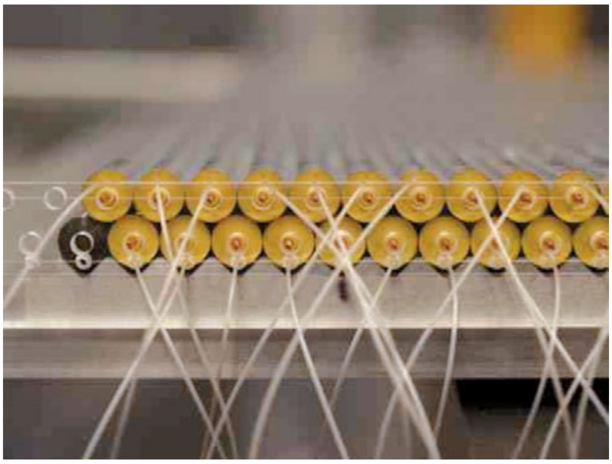

Fig. 27. A straw tube double layer on the reference plate.

- The anode wire is fed through a crimp pin, end-plug, Mylar film tube, next end-plug and crimp pin. The crimp pins are then glued in the end-plugs, and afterwards the end-plugs are glued inside the Mylar film tube leaving a small ∼ 1.5 mm film overlap at both ends. In the film overlap, later a dedicated spring with an outer snap-ring contact is inserted, which provides the electric grounding and can compensate the elastic elongation of the film tube under overpressure. The glue used for gluing the end-plug and crimp pin is a 2-component epoxy adhesive (UHU endfest 300 [40]) with 2 h working time, and 12 h setting time.
- After glue hardening, a single straw is placed in a long v-shaped profile and at one end the wire is crimped. At the other end the wire is stretched by a weight of 50 g. The straw is then connected to a gas supply and the gas pressure inside is raised smoothly to the nominal overpressure of 1 bar. Then, the wire is crimped in the second end-plug.
- After having produced a sufficient number of straws each of them is tested for gas leakage and correct wire tension. The wire tension is measured by placing the pressurized tube in a strong magnetic field and applying an AC current to the wire. The tension can be calculated by measuring the first harmonic of the oscillating wire. Tubes showing deviations from the nominal 50 g wire tension or gas leakage and tubes with broken wires are rejected.
- After this selection a number of straws is placed as a mono-layer onto a reference groove plate, connected to a gas supply and pressurized to the nominal pressure of 1 bar. The individual tubes are aligned with high precision also from the top by smaller reference plates (see fig. 26). Then, each tube is glued to the two adjacent ones at several defined points along their length. The glue used here is an instant cyanoacrylate adhesive (Loctite 408 [41]). After that, the second layer of straws is precisely positioned on top of the first one, pressurized to the nominal pressure and the single tubes are then glued to the adjacent ones in the same layer and in the lower layer (see fig. 27).

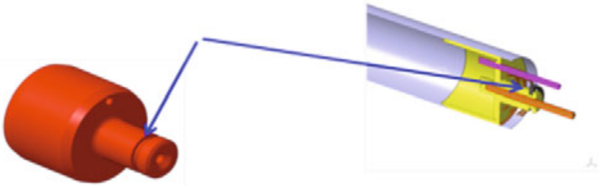

Fig. 28. Straw end-plug with a groove (indicated by the arrows) for a thermoplastic snap-ring to attach it to the side-band.

- This procedure is repeated depending on the number of layers in the straw module.
- Springs at both straw ends are inserted and finally side-bands are fixed to both ends of the straw module by thermoplastic snap-rings attached to the end-plugs (see figs. 28 and 16).

2.4 Mechanical structure

The STT layout is split into two independent semi-cylindrical detector volumes with two separated mechanical frames. The symmetrical, mirrored layout of the two detector volumes is also adopted for the frame system. The mechanical frame structure for each volume has to support and precisely position the straw layer modules at both ends. In addition the structure has to support all the electronic readout and supply elements, which are connected and placed at the detector front-end: the electronic readout cards, all readout and supply cables, the gas manifolds and supply pipes.

After the detector assembly, the two mechanical frames are mounted at the opposite sides of a vertical structure which has the additional task to support and align the beam-target cross-pipe and the MVD detector system. This vertical Central Frame (CF) is mounted on rails to move the entire system in and out of the $\overline{\text{P}}$ANDA target spectrometer. The CF system is described in sect. 2.4.3.

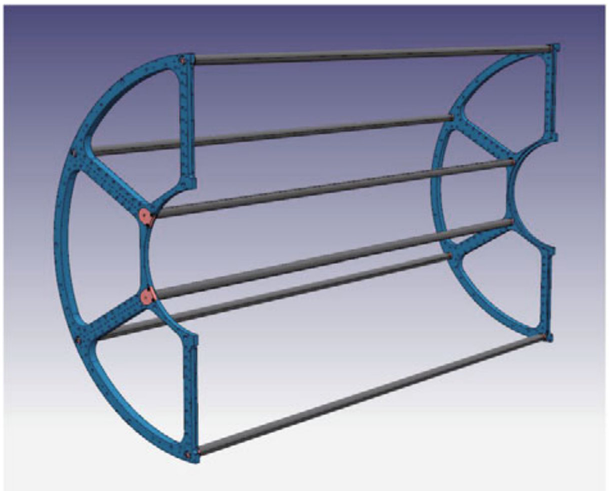

Fig. 29. Pictorial drawing of one of the two frame structures of the STT.

Table 7. Data used for the FEA (KinonRisic@ Finite Element Analysis) of the support structure.

2 End plates	60 N
6 Connecting bars	30 N
2100 Straw Tubes	80 N
Electronics, gas, services	110 N
Total weight	**280 N**
Density	2.7 g/cm^3
Youngs modulus	70 GPa
Thermal expansion	24 ppm/°C

2.4.1 The STT mechanical frame

In order to obtain a structure with high mechanical accuracy and rigidity, but being extremely light-weight, we have conceived a simple and easy to realize solution using aluminum or carbon fiber. Following the experience gained in previous experiments [42,43], the solution shown in fig. 29 has been designed.

The structure consists of two identical flanges, shaped and drilled individually, connected by screws to six precise tubular spacers. The two inner ones are only necessary during the mounting phase and could be removed after the installation of the straw modules (see fig. 29). The two flanges with semi-cylindrical shape are mounted to the central frame structure and are separated by 42 mm to leave space for the target pipe.

High-precision boreholes on the spokes of the flanges are used to mount the straw layer modules with the required position accuracy of ±0.05 mm. In order to check the solution, a thorough finite element analysis (FEA) of the whole structure has been performed. The results confirm the validity of the frame design, both from the functional and the structural point of view. The input parameters of the FEA analysis are listed in table 7 for aluminum. Figure 30 shows the calculated stress on the structure. The maximum value of the deflection on the frame is 0.03 mm.

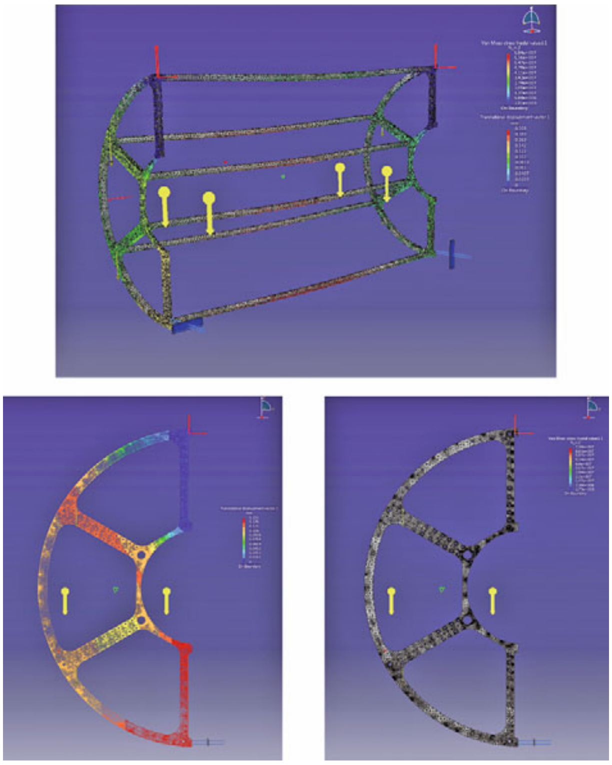

Fig. 30. Results of the FEA of the STT support structure. The maximum deflection of the frame is 0.03 mm.

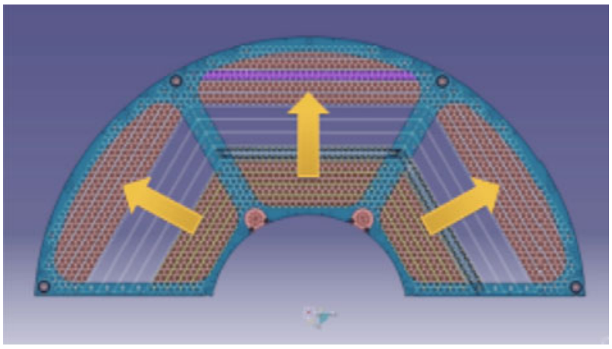

Fig. 31. Mounting scheme of the straw tube layer modules in the support structure. The free space in the middle is filled by the skewed layer modules.

The biggest stress is suffered at the backward flange, which also has to support the weight of the electronics and supply services of the detector (see fig. 30, bottom left panel).

2.4.2 Mounting of the straw layer modules in the support structure

The assembled straw layer modules will be mounted in the mechanical frame structure, starting with the inner axial ones. Figure 31 shows a scheme of the mounting procedure. As described in sect. 2.3.3 each module is precisely positioned by two mounting brackets at both ends, which are fixed by special pins to the reference boreholes on the

Fig. 32. Full-size prototype of the mechanical frame structure of the STT.

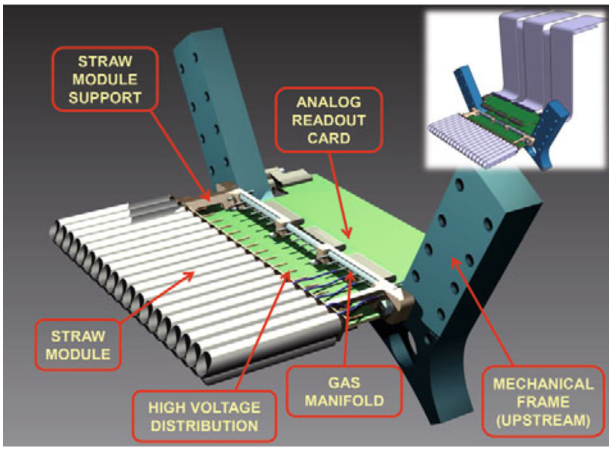

Fig. 33. CAD drawing of the STT front-end part with the analog readout boards, high-voltage and gas supply. The cabling scheme is shown in the upper right corner.

spokes of the frame flanges. A full-size prototype of the mechanical frame structure made of aluminum is shown in fig. 32 and is used to check the mechanical precision and complete mounting scheme of the straw layer modules.

A very limited space of only 15 cm in the z-direction upstream of the detector is foreseen for the readout electronics, high voltage supply, gas manifold lines, and distribution of all cables and supply pipes. The electronic readout scheme of the STT is split into the analog part, consisting of an Application Specific Integrated Circuit (ASIC) for each individual straw, and the digital readout part, which is located close to the $\overline{\text{P}}$ANDA spectrometer and connected by 5–6 m long cables. The STT readout is described in detail in the next chapter.

As can be seen in fig. 33 the readout part, high-voltage and gas supply are located at the same upstream end of the detector. Thus, the material budget at the downstream end of the STT can be kept very low, which is important for the particle tracking in the forward direction.

Fig. 34. First prototype of the central frame (see text for more details).

2.4.3 The central frame structure

The inner central region of the $\overline{\text{P}}$ANDA target spectrometer consists of the beam-target cross-pipe, the Micro Vertex Detector (MVD) and the STT detector, which are supported and precisely positioned by a common mechanical Central Frame (CF) structure (fig. 34). In addition, the CF structure has to support all services, readout components, cable routing, gas pipes, and cooling pipes in case of the MVD.

The mounting procedure of this system will start with connecting the beam-target cross-pipe to the CF structure. Next the MVD detector and all related services will be mounted to the CF and precisely positioned to the cross-pipe. Finally, the two semi-cylinders of the STT will be attached to both sides of the vertical CF structure, including the cable routing. Then the completed system will be inserted in the target spectrometer using two top and bottom rails, which are installed in the apparatus parallel to the spectrometer axis. Three skates on top of the CF structure and two skates at the CF bottom move the system on the two rails in and out of the target spectrometer.

The CF frame has a total thickness of 20 mm and consists of a sandwich made with a central core of honeycomb covered on both sides with pasted skins of carbon fiber. By this the structure is very thin and light-weight. The most massive parts are those necessary to fix the beam-target cross-pipe. In fact, on top and bottom, the fixing pads must be able to support the torque of 1 Nm that will be applied when the pipe is connected. Moreover, the backward support of the beam pipe must leave sufficient space for the cable routing of the MVD. Therefore, it has two rectangular housings, located top and bottom. The attachment point of the beam pipe in the forward region is less critical. Figure 35 shows the CF after the mounting of the beam-target cross-pipe and an enlarged cut-out of the target pipe support at the top and bottom of the CF.

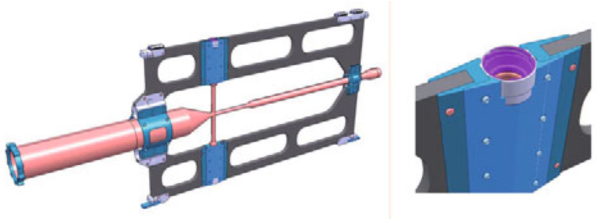

Fig. 35. CAD drawing of the Central Frame (CF) structure with the mounted beam-target cross-pipe (left figure). The right figure shows an enlarged cut-out of the target pipe support in the CF.

Table 8. Input data used for the FEA analysis of the central frame structure.

Straw tube tracker	700.0 N
Beam-target cross-pipe	45.0 N
Micro vertex detector	300.0 N
Gas pipes, electronics, cables, others	100.0 N
Safety load	250.0 N
Total load	**1395.0 N**

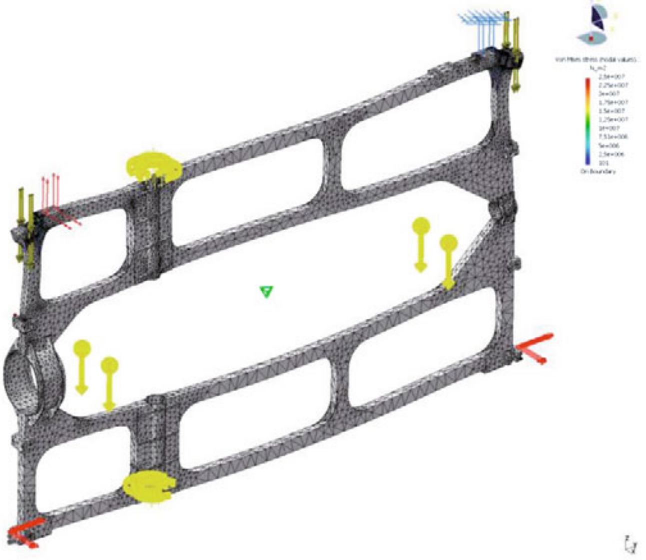

Fig. 36. Results of the Finite Element Analysis (FEA) performed on the central frame.

Table 8 lists the input data for a FEA analysis of the mechanical stress of the CF structure. A maximum equivalent stress of 25 MPa and maximum deflection (sag) of 0.5 mm has been calculated (see fig. 36), which is far below the stress limit of the structure of 95 MPa.

In order to test the solution and the mounting sequence, a prototype of the CF has been constructed. Figure 37 shows a CAD drawing of the CF structure with the target-beam cross-pipe, the micro vertex detector and one semi-cylinder of the STT mounted at the backside of the CF.

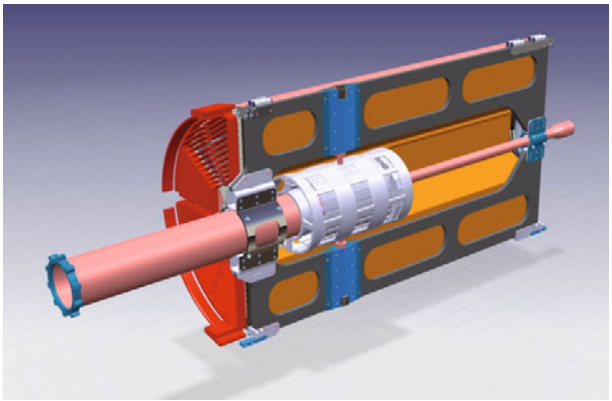

Fig. 37. CAD drawing of the central frame with the target-beam cross-pipe, the MVD detector and one semi-cylinder of the STT at the backside of the CF.

2.4.4 Positioning and alignment

As described in sect. 2.4.1 the position accuracy of the mounted straw layer-modules relative to the precision boreholes in the end flanges of the STT mechanical frame is within 50 μm. Due to the close-packaging of the glued straws in a module with a precise 10.1 mm tube-to-tube distance, deviations in the position of a single straw larger than about 40 μm are not possible.

After the complete assembling of each STT chamber, they will be attached to the CF by means of a set of precise positioning pins. This solution ensures that the two semi-cylindrical STT volumes are placed with the correct relative position to each other. It is worth to remind here that the CF not only holds the STT but also the MVD and the target-beam cross-pipe. Therefore it will house a complete set of reference marks so that the three systems can be aligned relative to each other with a precision of about 100 μm. This is also the reason why the attach points on the CF for each detector are made as hardened-titanium inserts, embedded in the carbon fiber structure. They will be precisely machined to allow a high dimensional and geometrical accuracy.

The relative alignment of the three components (cross-pipe, MVD, STT) of the $\overline{\mathsf{P}}$ANDA target spectrometer will be done during the installation, outside of the solenoid magnet. Afterwards, only the Central Frame structure must be precisely positioned inside the magnet by means of the sliding rail system. Reference marks will be placed on the CF to allow an external survey to define its position with respect to the general $\overline{\mathsf{P}}$ANDA reference frame. The overall mechanical precision in the x, y-plane will be below 150 μm.

2.5 The gas system

The preferred gas mixture for the $\overline{\mathsf{P}}$ANDA-STT is argon with an admixture of about 10–20% CO_2 as the quenching component. The details that brought to this choice are illustrated in sect. 2.2.3. This gas mixture has also good capability to tolerate high irradiation levels (see sect. 5.3)

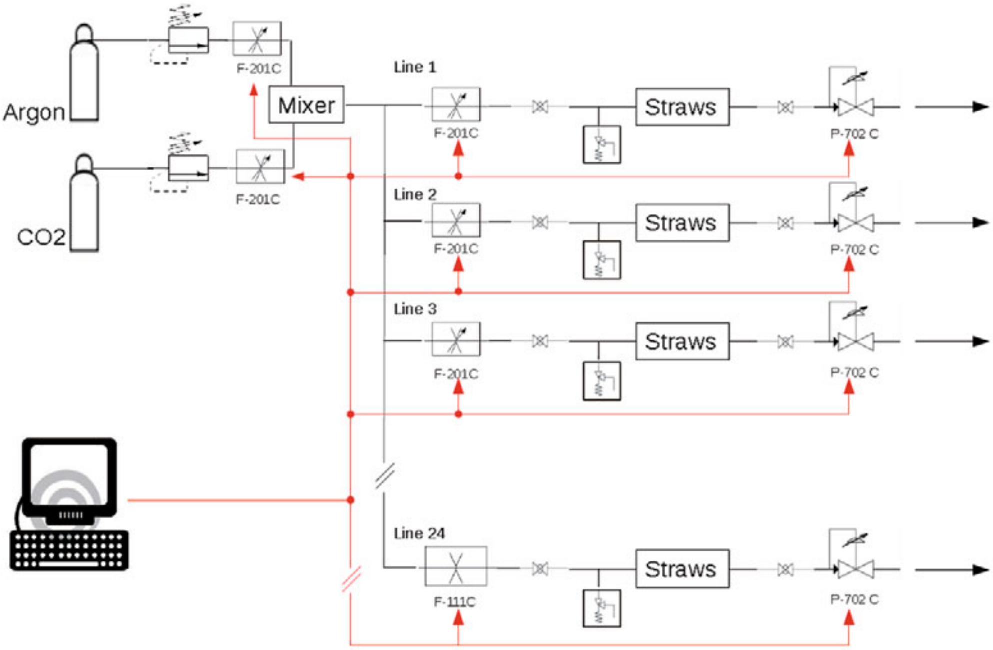

Fig. 38. Scheme of the gas system.

since no deposits on the straw tube electrodes from polymerisation reactions occur, provided that there is a clean gas environment including all materials and parts of the detector and gas supply system in contact with the gas. For both gas components a high purity grade is required (argon with grade 5.0, CO_2 with 4.8). The supply lines consist of polished stainless-steel pipes and thermoplast (PA) tubings where a higher flexibility is needed. Since argon and CO_2 are non-flammable, not expensive, and components of the atmosphere, no recirculation and containment of the gas mixture is needed, and the gas supply of the detector is done in flushing mode. The STT will be operated at a gas pressure of about 2 bar (absolute) and preferably at room temperature. The total STT gas volume of about 1040 l is exchanged typically every six hours with a flow rate of about 3 l per minute to refresh the gas mixture and to prevent an accumulation of contaminants in the detector and gas system.

The gas system of the STT consists of supply gas bottles for each mixture component, cleaning filters in the gas lines, a mixing section with ratio-based mass flow controllers, regulated by a pressure transducer inserted in the STT volume to set a constant absolute pressure of about 2 bar in the detector, the supply lines in and out of the detector and outlet valves to a dedicated exhaust line at the $\overline{\mathrm{P}}$ANDA experimental area. The scheme of the gas distribution system is shown in fig. 38. The mass flow controller and meter devices [44] are based on digital electronics. In these devices the analog sensor signal is sent directly to a micro processor. By doing so, optimum signal stability and accuracy is achieved. An integral alarm function continuously checks the difference between the set point and the measured value. If the supply pressure drops the instrument gives a warning. In addition the instrument runs a self diagnostics routine, and controller settings can be remotely adjusted with a hand terminal or a computer using an RS-485 busline. For the Ar/CO_2 gas mixture the required accuracies of the settings and control have to be better than 0.3% (absolute) for the mixture ratio, about 1–2 mbar for the pressure, and 1 K for the temperature.

The $\overline{\mathrm{P}}$ANDA straw tubes are arranged in six sectors forming a hexagon around the interaction point. Each sector can be further sub-divided in three regions in the radial direction: the inner and outer region ones, that are equipped with axially aligned straws, and the middle section which houses stereo straw tubes, see fig. 22 (more details of this arrangement can be found in sect. 2.3). To flush the straws with the required two-components gas mixture, the following guidelines have been adopted:

- reducing the redundancy of the system to lower the costs and the complexity of the system;
- assure a minimal redundancy to guaranty, in case of failure, the operation of at least parts of any sector;
- keeping the space needed for the system within reasonable boundaries (∼ few cm);
- automatization and remote control of the gas flow parameters, with the possibility to switch to manual/local operation for:
  - setting the ratio of the two components in the gas mixture;
  - quantifying the gas flow;
  - setting the gas pressure;
  - controlling the temperature.

Following these guidelines we decided to have 24 independent lines, organized as follows:

- a line per sector for each axial straw regions: $6 \times 2 = 12$;
- two lines per sector for each of the stereo straw groups: $6 \times 2 = 12$.

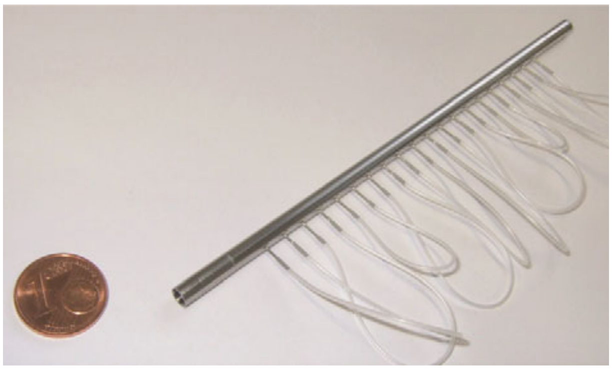

Fig. 39. Prototype of a gas distributor consisting of a stainless-steel pipe (4 mm diameter, 0.1 mm wall thickness) with small capillaries (0.55 mm diameter) for connecting the individual straws.

Table 9. Straw tube electrical properties.

Capacitance	8.9 pF/m
Sense wire resistance	258 Ω/m
Inductance	1.24 μH/m
Impedance	373 Ω
Analog cross talk	< 1%

With this selection of multiplicity and topology, in case of failure of one line, it is assured that at least one half of any sector remains operative. This is particularly important for the stereo tubes that allow to determine the z-coordinate of particle trajectories. The gas lines are connected to gas manifold pipes which supply each individual straw. Figure 39 shows a first prototype of such a gas manifold. It consist of a stainless-steel pipe having a wall thickness of 0.1 mm and a diameter of 4 mm. On it, small capillaries (diam. 0.55 mm) are welded and will be connected to the individual straws. By connecting two straws in series it is possible to place the in- and outlet gas manifolds together at the upstream end of the detector.

3 The readout and control systems

The input characteristics of the front end electronics have to match the electrical properties of the straw tubes, which are listed in table 9. From the point of view of the pulse propagation, the straw tube acts as a coaxial transmission line with loss, with an impedance given by the formula

$$Z = \sqrt{\frac{R + i\omega L}{i\omega C}}\,, \tag{5}$$

where R is the electrical resistance, L is the inductance, C is the capacitance and ω is the angular frequency. For high frequencies (> 100 MHz), the impedance of the straw tubes tends to the limit $Z \to \sqrt{\frac{L}{C}} = 373\,\Omega$ (see fig. 40).

The basic requirements for the straw tube front-end electronics are listed in table 10.

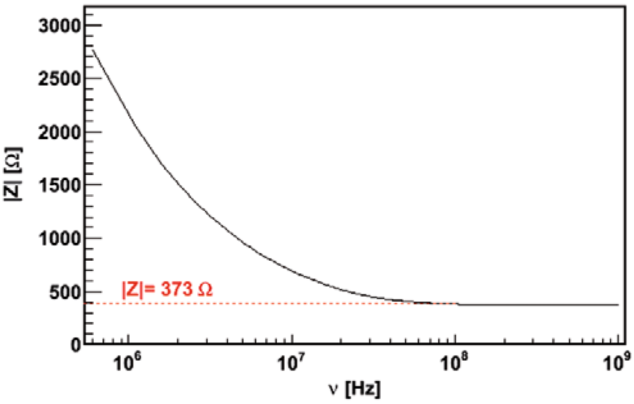

Fig. 40. Straw tube impedance as a function of frequency $\nu = \omega/2\pi$ (solid black line). The high frequency limit is indicated with the red dashed line.

Table 10. Front-end electronics requirements.

Peaking time	≤ 20 ns
Double pulse resolution	∼ 100 ns
Intrinsic electronic noise	< 1 fC
Discrimination threshold	≈ 5 fC
Max. drift time	200 ns
Max. occupancy	< 10%
TDC resolution	∼ 1 ns

3.1 General concept

The STT detector consists of 4636 tubes arranged in 27 layers (see sect. 2.3). The maximum counting rate of 800 kHz is expected for straws in the innermost layer for the $\bar{p}p$ annihilations at the highest energy and 2×10^7 interactions/s. The maximum drift time of a straw is 200 ns which results in an average double-hit probability less than 10% for the innermost layers. The requested electronic time resolution should be around 1 ns and the intrinsic noise level below 1 fC. The maximum analog pulse duration should be comparable to the maximum drift time of 200 ns. Furthermore, an energy loss measurement with all straws is requested for particle identification.

To fulfill all these requirements, the proposed straw tube readout organization comprises 3 stages:

1. Analog Front End Electronics (FEE) cards hosting, depending on radial distance from the beam, 36–80 channels. FEE is composed of preamplifier, amplifier with analog signal shaping and discriminator unit with differential output.
2. Digital Board (DB) for time and amplitude (or charge) measurements, local logic resources for noise suppression, fast hit detection, memory buffer for hit storage, serial Gbit optical links for the data transmission and slow control.
3. Detector Concentrator Board (DCB) (optional) receiving and merging inputs from several DB in local memory buffer and sending it to the $\overline{\text{P}}$ANDA DAQ system.

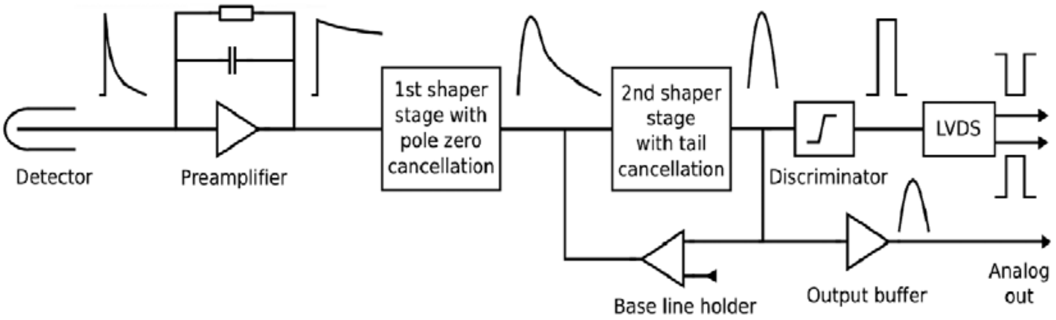

Fig. 41. Block diagram of the ASIC under development for the straw tube readout.

The data from the DCBs will be transferred via fast optical links to Compute Nodes for the on-line track reconstruction and subsequently, after merging with the information from other $\overline{\mathsf{P}}$ANDA detector systems, for the event selection. It will be possible to perform some local correlations on the data inside the single DB to suppress noise and reduce the amount of data sent from the board.

The $\overline{\mathsf{P}}$ANDA data acquisition and filtering systems will implement a trigger-less architecture. Instead of having a hardware trigger signal, which indicates the occurrence of a valid event, each DB will receive a precise clock signal distributed centrally from a single source: the Syncronization Of Data Acquisition (SODA). The DB boards will continuously monitor the detector channels and will generate data packets whenever the number of the input signals exceeds programmed thresholds. These data will be tagged with time stamps obtained from the SODA.

The data acquisition system will profit from the structured running mode of the HESR operation. Periods of 2 μs with antiproton interactions will be interleaved with periods of 400 ns of idle time. The information on the accelerator activity will be distributed to DCBs via the Clock and Timing Distribution System. The data recorded during the interaction intervals will be grouped together in DCB to form a burst which will be then uniquely tagged. Grouping of data from many bursts into predefined epoques (*e.g.* 500 μs) inside DB is also considered in order to reduce network traffic. Data from all $\overline{\mathsf{P}}$ANDA detectors tagged with the same burst identification number will be grouped together and will be made accessible to filtering algorithms implemented in the Compute Nodes (CN). Decisions produced by these algorithms will thus be based on the complete detector data with full granularity.

3.2 Analog front-end electronics

An Application Specific Integrated Circuit (ASIC) is being developed in order to read out the straw tube pulses. The main specifications of this chip are summarized in table 11.

The ASIC's channel comprises a charge preamplifier stage, a pole-zero cancelation (PZC) network, a shaper stage, a tail cancelation network, a discriminator circuit, a baseline holder (BLH), a fast differential LVDS output and an analog output. The block diagram of the designed readout channel is shown in fig. 41.

Table 11. Main parameters of the new straw tube front-end readout chip (see text for more details).

Technology	0.35 μm CMOS
Number of channels	16
Input Resistance	$\sim 120\,\Omega$
Default gain	~ 10 mV/fC
Peaking time (for delta)	20 ns
Timing resolution	1–2 ns
Equivalent (delta) input range	0–200 fC
Noise ENC	< 0.4 fC
Output standard	LVDS and analog
Power consumption	~ 30 mW

The solution for the FEE should provide both, the timing and the amplitude information. Since it is still under study whether the Time Over Threshold (TOT) technique or the analog amplitude information will be used for the energy-loss measurement, the first ASIC prototype provides both the amplitude and TOT information.

A typical simulated analog response of the amplifier for straw tube pulses (generated with GARFIELD [45]) for different charge depositions is shown in fig. 42. The charge depositions are expressed both as equivalent charges of "delta-like" pulses and as integrated charge carried by the pulses. The tail cancelation network assures that the pulse length is shorter than about 150 ns.

The design of the first version of the ASIC channel was completed and a first prototype containing 4 readout channels has been fabricated and delivered in the second part of 2011. Signals from an ^{55}Fe source measured with the ASIC prototype connected to the illuminated straw tube, for different settings of the ion cancelation network, are shown in fig. 43. It is seen that, with optimized parameters of the network, the long tail can be eliminated.

Preliminary measurements of the front-end gain and noise are shown in figs. 44 and 45. The gain characteristics have been measured with a step-like voltage pulse injected into the ASIC channel via a capacitance ("delta-like" pulse).

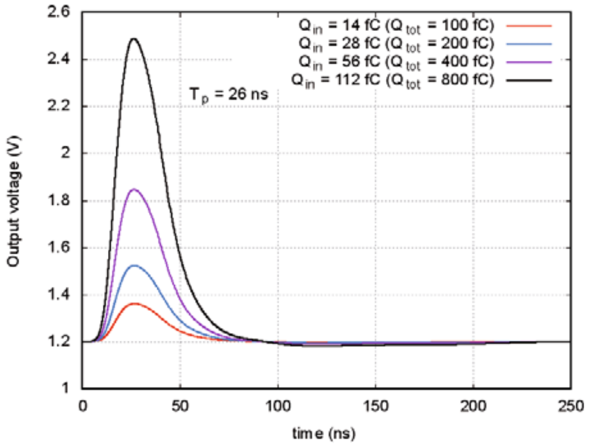

Fig. 42. Examples of the simulated analog responses for different input charges.

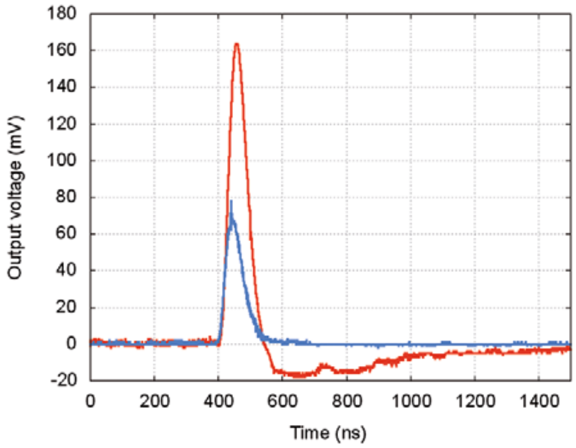

Fig. 43. Examples of front-end pulses for not optimized (red) and optimized (blue) settings of the ion cancellation network.

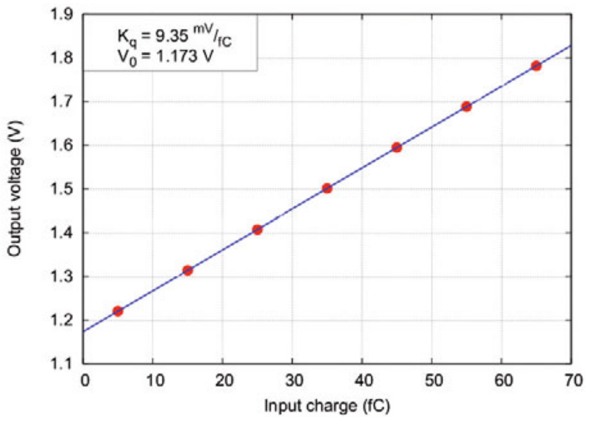

Fig. 44. Examples of the front-end gain measurement for default settings with "delta-like" current pulses.

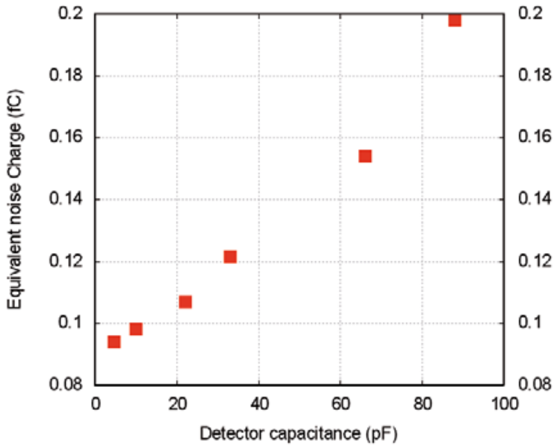

Fig. 45. Example measurement of the front-end noise *vs.* input capacitance.

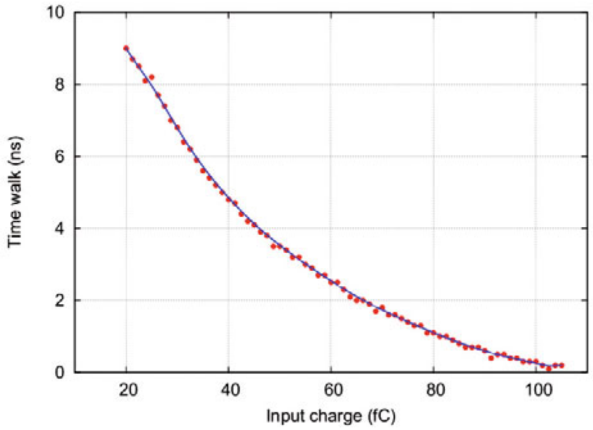

Fig. 46. Example measurement of the discriminator time walk.

Both results stay well within the requested specifications. The discriminator circuit uses a simple leading edge configuration. A preliminary measurement of the discriminator time walk, shown in fig. 46, shows the typical leading-edge behavior.

The charge *vs.* Time-Over-Threshold (TOT) behavior of the ASIC is shown in fig. 47. It has been measured with "delta-like" pulses for an input charge range of 10–80 fC. It shows a non-linearity which is typical for Gaussian-like pulses. It can be optimized in a future version by implementing a linear discharge of the front-end output capacitance. A discharging capacitance by a constant current provides a linear shape of the analog pulse and then the width of the discriminator response may be proportional to the collected charge. A similar idea was successfully used in previously reported designs [46,47].

However, it should be noted that already with the present design, the amplitude spectrum measured with an ^{55}Fe source exhibits two clearly separated peaks corresponding to the characteristic 2.9 keV and 5.8 keV energy deposits of the source, as shown in fig. 48. Further simulations are needed to answer the question whether the

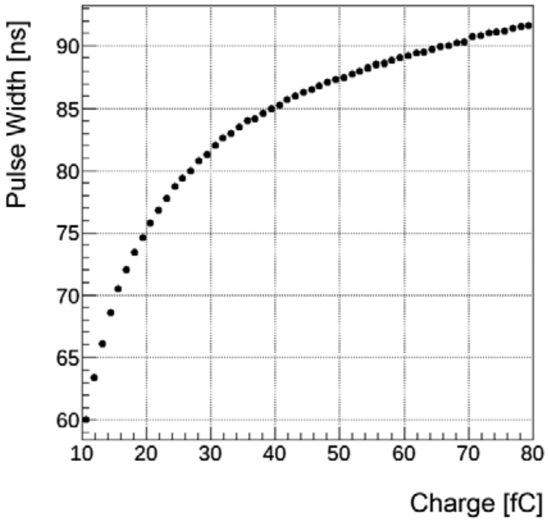

Fig. 47. Time over threshold *vs.* charge measured with "delta-like" current pulses.

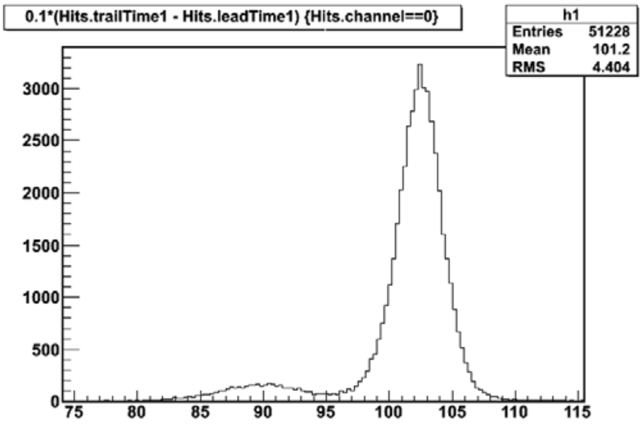

Fig. 48. Time-over-threshold spectrum measured with an ^{55}Fe source and the straw tube at HV = 1750 V.

present non-linearity is acceptable for particle identification without losing too much performance.

Despite the expected large counting rate and long time constant related to the ion propagation it is very crucial to demonstrate that the ion tail cancelation and the base holder circuits work according to the design. Recently, first measurements with a high-intensity proton beam were performed in Jülich in order to verify the signal readout at high rates. As an example, fig. 49 shows the analog output of the ASIC recorded by an oscilloscope. No baseline distortion and a clear separation of the four individual signals can be seen within a time window of about 700 ns, which corresponds roughly to a proton rate of 6 MHz in the single straw.

A further optimization of the ASIC with a systematic study of the design parameters is still going on. In addition, a thorough analysis of the two different methods of the signal amplitude measurement will be done by comparing the TOT information with the analog signal shape, which are both provided by the ASIC. Depending on the result, the final architecture of the ASIC chip including the specific method for the amplitude measurement will be determined.

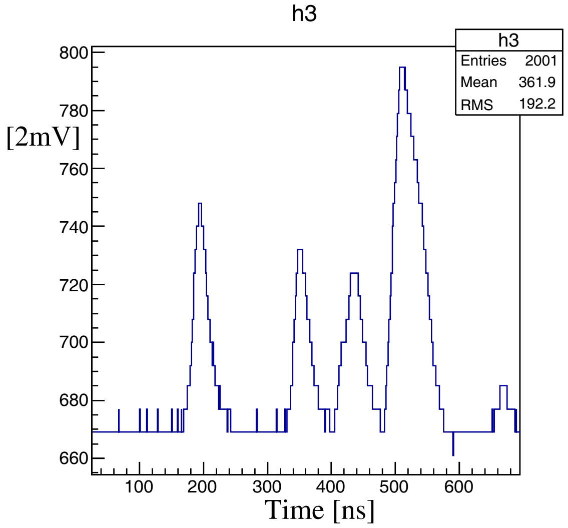

Fig. 49. Example of the ASIC analog signal output measured at a high (few MHZ) hit rate.

Apart from the not yet decided method for the amplitude measurement, some other design aspects have to be considered. In particular the DAC converters need to be designed and added to each channel in order to tune independently the discrimination threshold of each channel, the reference voltage source needs to be designed and added, the digital part of the ASIC needs to be implemented. Although the present ASIC was designed in 0.35 μm technology, the final technology choice has not yet been done. The final ASIC will probably contain 16 channels.

The multi-layer printed circuit board (PCB) for the FEE will contain 2 to 5 ASICs (for 16 channels each), a dedicated logic for the ASIC configuration and connectors for flat twisted-pair cables with signal inputs (for slow control) and outputs to the DB. The inputs from the single straws will be provided by thin single-ended, coaxial cables. Since the mechanical frame structure of the STT has two support flanges with a six-fold symmetry, a back plane with the analog readout will be composed out of six independent sectors, each serving 768 straws. Thus, 13 FEE boards with a varying number of channels, from 36 (innermost) to 80 (outermost), are needed for the readout of one complete sector.

During the design phase of the new ASIC several FEE prototypes, based on CARIOCA chips, have also been tested with prototype chambers and showed satisfactory performance.

The CARIOCA is an 8 channel, radiation hard (up to 20 Mrad dose) ASIC, featuring preamplifier, shaper, base line restorer and discriminator. One single FEE board consists of four CARIOCA chips for the readout of 32 chan-

Table 12. Basic technical parameters of the CARIOCA-10 chip.

General parameters	Number of channels	8
	Radiation resistance	20 Mrad
	Technology	IBM CMOS 0.25 μm
Input parameters	Input impedance	45 Ω
	Range of input charge	$2.5 \div 300$ fC
	Peaking time	14 ns
	Sensitivity with detector capacitance 220 pF for	
	positive input	8.21 mV/fC
	negative input	7.7 mV/fC
	Width of output pulse for charge < 300 fC at	
	positive input	55 ns
	negative input	65 ns
	Minimum charge	
	positive input	2.4 fC (rms 0.37 fC)
	negative input	2.4 fC (rms 0.24 fC)
Output parameters	Standard of pulses	LVDS

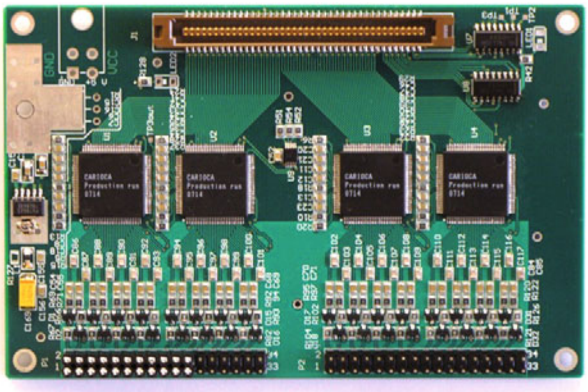

Fig. 50. Prototype board of a 32-channel preamplifier/discriminator based on CARIOCA-10 chips.

Table 13. Technical characteristics of the prototype preamplifier/discriminator board - version-2.

Supply voltage	$+4.5 \div +12$ V DC
Supply current	560 mA
Power consumption	3.3 W
Number of channels	32
Dimensions of board	124 mm × 80 mm × 16 mm

nels. The FEE board provides an LVDS differential output which is connected by a flat cable to the DB. The threshold for the CARIOCA's leading-edge discriminators is set by the on-board DAC, which is controlled by dedicated lines in the cable connection to the DB. The total power consumption per channel of the CARIOCA chip is 25 mW (table 12).

The second version of the preamplifier/discriminator board is shown in fig. 50. Its basic parameters are given in table 13.

The main limitation of the CARIOCA chip is the lack of the signal amplitude information which is crucial for the STT for the dE/dx measurement. However, it is still considered as a back-up solution for the $\overline{\text{P}}$ANDA Forward Tracker (FT) where a dE/dx measurement is not required.

3.3 Digital electronics

The DB readout will be located outside the $\overline{\text{P}}$ANDA target spectrometer in a distance of 5–6 meters to the STT. The DB will contain a multi-hit TDC measuring the signal arrival time with respect to the external clock provided to the DB by the $\overline{\text{P}}$ANDA SODA. For the amplitude measurement and depending on the test results, either the TDC will provide the sufficient pulse length information (TOT) or the DB will contain an additional fast sampling ADC for the analog signal.

A time measurement system based on FPGA is foreseen for the STT. Recently, a time measurement board (TRBv3 see below) based on the Lattice ECP3 family, has been developed at GSI, University of Frankfurt and Jagiellonian University. The implementation of a TDC in FPGA allows for a large flexibility in the selection of main measurement parameters like time range, binning etc., and makes this approach very attractive for a broad range of applications. The implementation of the TDC functionality in FPGA is achieved by using its internal architecture elements - carry chains [48–50].

As presented in fig. 51, the time measurement is based on the information (from the carry chain - START signal in fig. 51) saved in the flip-flops ($Q_1 - Q_n$) on the rising edge of the system clock (STOP signal in fig. 51). Each carry chain element delays the signal in average by 30 ps. Time measurements done at GSI demonstrate a $\sim$ 17 ps resolution. For the STT detector, a TDC binning of 0.5 ns

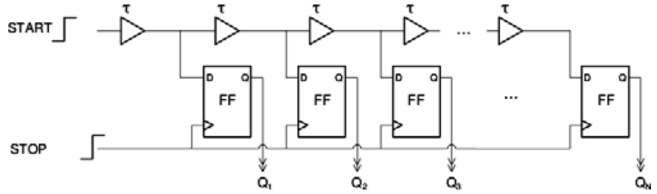

Fig. 51. Scheme of TDC-FPGA implementation with carry chain usage.

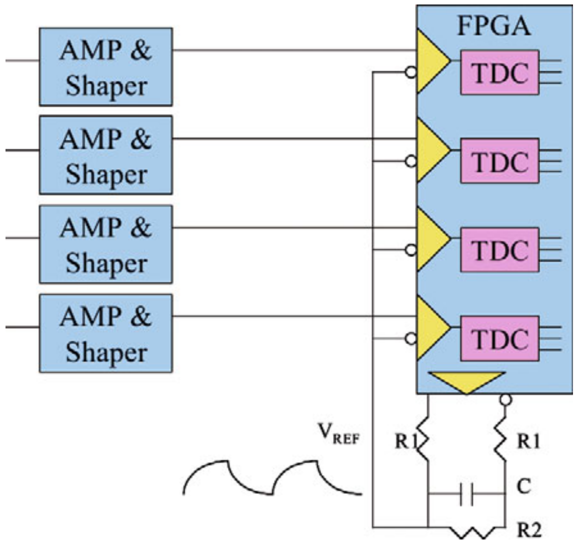

Fig. 52. ADC-FPGA implementation [51].

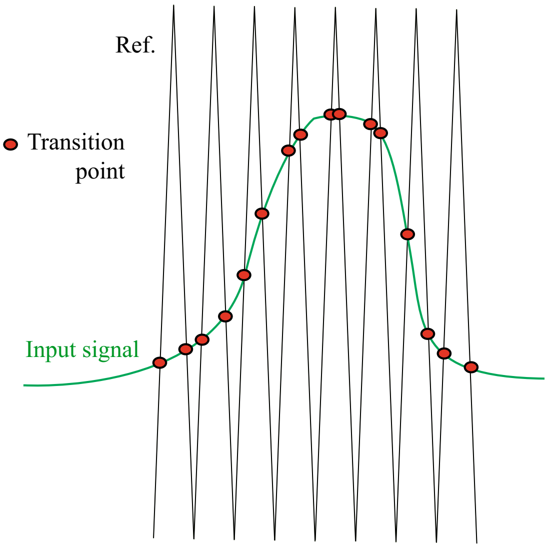

Fig. 53. Example of the input and reference signals. The red points mark the transition point when the FPGA should see a change from the logical 0 (1) to the 1 (0) level.

will be sufficient. To have all needed information about the signal from the detector it will be required either to measure the amplitude/charge of the straw signal via TOT or even, if it turns out to be necessary, sample its shape. This is possible since the FEE-ASIC can provide both, the digital (time and TOT) and analog signals.

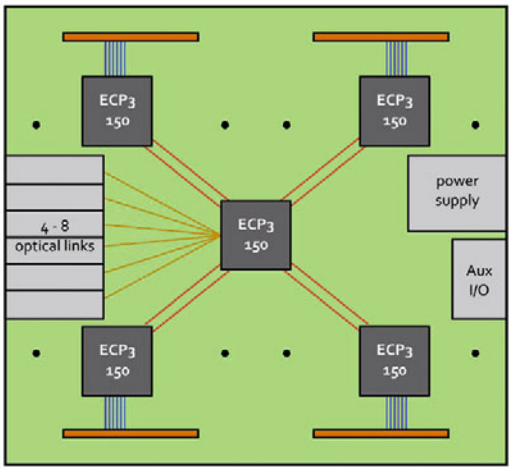

Fig. 54. Block diagram of the TRBv3.

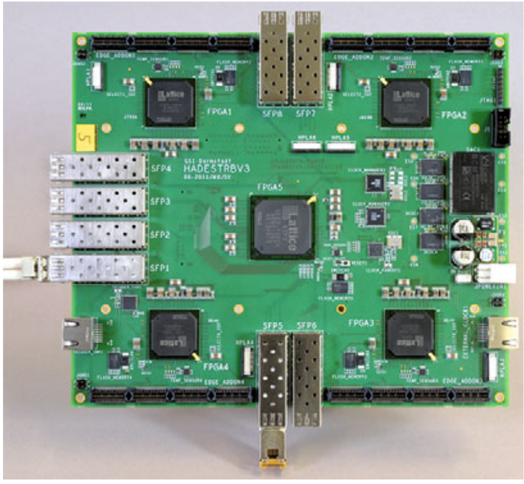

Fig. 55. Produced TRBv3 board.

Therefore, along with the development of the TDC-FPGA measurement techniques the utilization of the ADC functionality into the FPGA is under investigation. The TDC implementation together with just a few components (resistors and capacitors) allows to perform an additional ADC measurement. Figure 52 shows a scheme of such an approach. The differential input of the FPGA is used as a comparator. If a defined signal generated by the FPGA (V_{ref} in figs. 52 and 53) is larger than the input signal, the FPGA logic sees a 0, otherwise a 1 level. The transitions from the 0 to the 1 level are again saved in the flip-flop chain (see fig. 51). At the end the time measurement of the transition can be translated to a voltage. The advantages of this solution compared to the usage of a standard sampling ADC are the smaller power consumption and lower price. The decision about the final method of the ADC measurement will be taken after thorough tests. Consequently, appropriate mezzanine cards will be build. Such mezzanine cards can be added as an add-on to the basic Time Readout Board (TRB, see below) containing the TDC.

The block diagram and a recently produced TRBv3 board are shown in figs. 54 and 55, respectively. Four out of five FPGAs on the TRBv3 are located along the edges of the board. Each of them has a 208 pin input/output connector assigned. The fifth FPGA is located in the center of the board and coordinates the work of the edge FPGAs as well as communicates with the data acquisition system. The TRBv3 board is equipped with eight optical SFP connectors. The maximum transmission speed of each optical connector is 3.2 Gbit/s. The input/output connectors are used to plug in mezzanine cards. The connector contains 188 general purpose lines and 6 high-speed serial connections between edge FPGA and a mezzanine board. Eight lines are connected to the central FPGA from each connector. The design of the mezzanine card is left for future TRBv3 users. It may range from a simple flat cable adapter to a sophisticated board (*e.g.* multichannel ADC). A set of two connectors is placed on the bottom side of the TRBv3 allowing for yet another mezzanine card connection. All 160 general purpose lines from the bottom connectors are controlled by the central FPGA. Both top and bottom connectors provide a power and ground for mezzanine cards.

The edge FPGA may contain up to 64 time measurement channels. The DB based on TRBv3 for the STT will have 48 TDC channels in FPGA, giving the total number of 192 channels per board. Thus, four TRBv3 boards will be sufficient to collect data from one STT sector.

The former version of the TRB (TRBv2), containing four HPTDC chips is presently used for straw detector tests (as, for example, shown above). It has been built for the HADES experiment at GSI [52] (schematics and photograph of TRBv2 are shown in figs. 56 and 57, respectively). The HPTDC chip (32 channels) has been developed at CERN for LHC experiments. The HPTDC can operate with a maximum trigger rate of 1 MHz and a maximum of 2 MHz hit rate per channel. Four TDC binning widths (25, 100, 195 or 785 ps) can be selected by software during the chip initialization. For the straw tubes, a binning of 785 ps has been selected. The measured hit times together with the trigger time stamp are stored in the local TDC memory (up to 256 hits/shared by 8 channels can be stored) and read out from the TDC readout FIFO (also 256 hits deep) with 40 MHz clock (8 bit parallel bus). Noise suppression and a fast hit detection on single wires is performed in FPGA located on the board. The HPTDC allows also to measure the time over threshold which is used for a noise suppression. The FPGA controls also the data flow. The data are transmitted from the DB via 8b/10 serial 2.5 Gbit optical link driven by TLK2501 transceiver from Texas Instruments.

For tests an external trigger (clock) was connected to the TRBv2 by a dedicated line, not shown in the schematics. The slow control is provided by the Etrax FS CPU running a LINUX OS and an EPICS client [53].

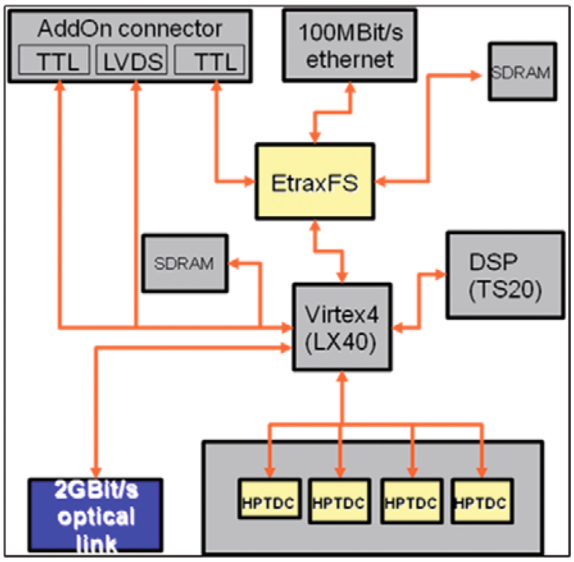

Fig. 56. Schematics of the HADES TRBv2 board used for the time-of-flight measurements.

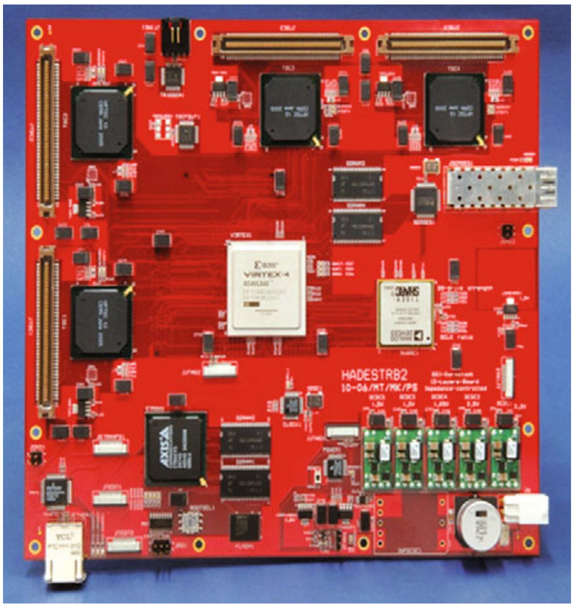

Fig. 57. HADES TRBv2 board.

3.4 Data rate

An average maximum hit rate of 800 kHz per channel is expected for the innermost straws when operating at an interaction rate of 2×10^7 proton-antiproton annihilations per second. One DB, with 196 channels, will provide on average 157 Mhits/s. The TDC will require 11 bits in order to measure a 1 μs range with a 0.5 ns binning with. The time over Threshold will require 8 bits to cover a range up to 200 ns. The channel number (1–48) will require 6 bits and the encoding of the time stamp (1–500) will require 9 bits. The latter assumes that epoques of 500 μs are stored in the DB buffer. Sufficient memory (400 kB) for one epoque can be easily implemented in the FPGA.

Altogether 34 bits represent one TDC channel result in a given TDC on the DB. Two more bits are necessary to distinguish the FPGA. Thus a 5 byte word is generated for each hit on the DB. Assuming 800 khits per second a data rate of 4 MB/s is generated in each TDC channel.

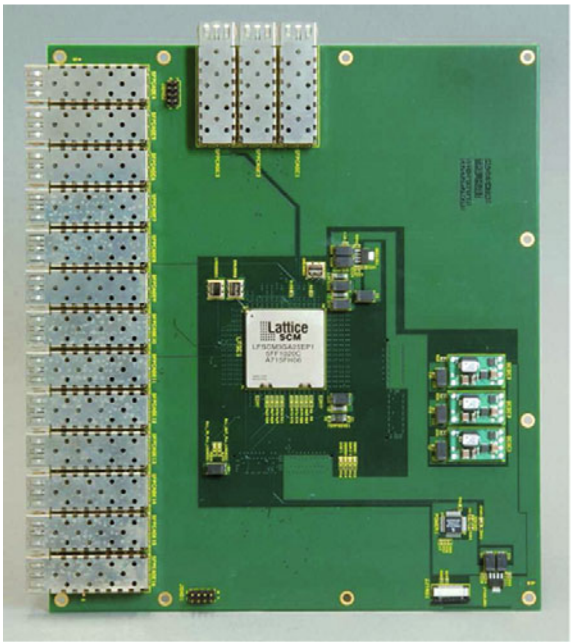

Fig. 58. Optical HUB board for the HADES experiment.

This results in a 784 MB/s data rate from one DB. This data rate can be handled by four 3.2 GBit/s optical serial links. Twenty four 196-channel DBs will be necessary for the full CT readout.

It seems reasonable to merge the data from the straw layers belonging to one STT sector and sent them to a common DCB. Such a layout can be more favorable for a cluster search but is not mandatory since the DB have also features of the Detector Concentrator (grouping of bursts in epoques).

A board which could be considered as a prototype of the $\overline{\textsf{P}}$ANDA DCB has also been developed by the HADES DAQ group, fig. 58 (optical HUB module), and is currently installed in the Krakow straw tube test set-up. The prototype is equipped with several Small Form-factor Pluggable Transceivers (SFPT) serving as optical connectors and FPGAs controlling the data transfer. An attractive feature of this unit is the possibility to create groups of links (4 in the present prototype) into one protocol standard. This is provided by the FPGA controlling the data flow (*i.e.* Lattice SCM 50 chip) which currently supports 8b/10b and GBit Ethernet format. The optical links used on this prototype can send data with a maximal speed of 3.8 Gbit/s.

3.5 Detector control system

The Detector Control System (DCS) of the STT is one branch of the general $\overline{\textsf{P}}$ANDA Experiment Control System (ECS). The control system has to continuously collect the actual parameters from the supply and electronic readout systems and compare them with their set values and predefined tolerances. In addition, parameters of the detector environment, like, for instance, temperatures and humidities at several locations must be monitored.

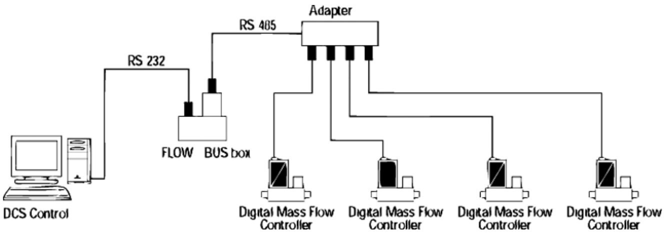

Fig. 59. Layout of the STT gas control system.

In case of certain deviations a specific alarm message should be generated to inform the detector operators. Some of the data must be stored on disk and added to the experiment event data for possible offline corrections of the detector measurements. The DCS system will manage the database with the mapping of the physical channel source (voltage, current, temperature, aso.), the label and the relevant calibration constants.

The parameters which have to be considered for the STT are listed below:

- gas supply system: gas mixture composition, pressure and temperature at several locations in the in- and outlet lines, gas flow;
- high-voltage supply system: high voltage, current and status (trip, ramp, on, off) values for every supply line, temperature of the supply boards;
- electronic readout system: discriminator thresholds for every readout channel, supply and reference voltage of every readout board, temperature of the readout boards;
- detector environment: temperature and humidity at several locations at the detector.

For the Ar/CO_2 gas mixture in the STT the control of the fraction of the two components will be done within a level of 0.3% (*i.e.* within $10.0 \pm 0.3\%$), while the mixture pressure and temperature will be kept stable at the level of 1 mbar and 1 °C, respectively. This will be done using components, for the gas system, with digital communication capability controlled by the user via Graphical User Interfaces (*e.g.* LabVIEW). An example of the DCS implementation for the gas system is shown in fig. 59. For the high- and low-voltage distribution, multichannel power supply systems like the CAEN SY1527 will be used. This system consists of a main frame allowing the housing of a wide range of boards providing high and low voltages. For the high voltage, the straw tubes will require boards which are able to provide up to 3 kV with a current per channel of about 100 μA. The straws will be grouped to sectors, which will be fed in parallel by a single system channel each. High voltage supplied, current, ramp up and down times, will be the parameters to be controlled by the DCS system using a dedicated bus or Ethernet connection.

For the front-end electronics a few channels of low voltages can be housed in the same main frame. This system allows an easy communication with the mainframe through ethernet using an OPC server software which can be easily integrated in the user DCS.

For a stable STT operation, remote access and monitoring of the front-end electronics (FEE) cards is mandatory. Therefore, the DCS will be connected to the STT FEE via a dedicated bus. The software will permit adressing, via read-write operations, the status and control registers of the FEE ASIC chips. Moreover, through the slow control software interface, various test and/or calibration pulses will be generated.

4 Calibration method

The calibration of the STT includes a determination of the position in space of the straw tubes and the characteristic relation between the measured drift time and the isochrone radius. In principle, both calibrations have to be done for each single straw, but the layout and properties of the pressurized tubes simplify the calibration method to a large extend.

The calibration of the isochrone radius and drift time relation benefits from the mechanical properties of the pressurized, thin-wall ($27\,\mu$m) straw tubes, having a perfect cylindrical shape and precise diameter. The experience from the COSY-STT with 2700 straw tubes, also pressurized and with a similar thin film wall ($32\,\mu$m), showed that a global isochrone calibration for all straws together is sufficient. The isochrone relation only depends on the specific gas and electric field parameters. The individual time offsets from the electronic readout system have to be corrected only once.

In the following, algorithms for the isochrone calibration are described, which can be easily adapted for the $\overline{\text{P}}$ANDA-STT. The methods presented were checked with experimental data from different straw test systems. In particular the COSY-STT detector is considered as an ideal test system for the whole calibration method and the performance results can be extrapolated to the $\overline{\text{P}}$ANDA-STT due to the similar technique of close-packed straw layer-modules. The test systems and measurements are described in detail in sect. 5.

4.1 Drift time spectra

Figure 60 shows an example of a measured time spectrum for a uniformly illuminated straw tube, with some particular noise contribution from the electronic readout system. In this figure, the time is expressed in TDC counts and runs from the right to the left. In order to get the time spectrum, the TDC counts are converted into seconds and the time is reversed; finally, the spectrum shown in fig. 61 is obtained. The analysis of the time distributions of individual straws allows the monitoring of the data quality: the minimum and the maximum drift times, t_0 and t_{max}, correspond to a track traversing the tube close to the wire and close to the cathode wall, respectively. The value of t_0 depends on the signal cable length, discriminator threshold, high voltage setting and delays in the readout electronics. Nearby tubes sharing the same front-end electronics are expected to have a similar value of t_0; on the contrary, the drift time $\Delta t = t_{max} - t_0$ depends only on the drift properties of the tubes. The number of events outside the drift time window gives an estimate of the random, constant noise level over time range (see fig. 60) [54]. For each tube, the parameters of the drift time distribution are derived from a fit performed with

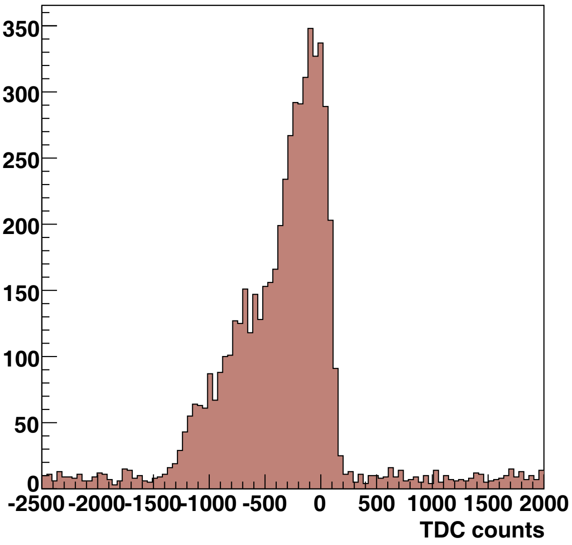

Fig. 60. Example of a measured raw TDC spectrum with some particular noise contribution from the electronic readout system. On the x-axis, the time is expressed in TDC counts (in this case, one TDC channel corresponds to 130 ps) and runs from right to left.

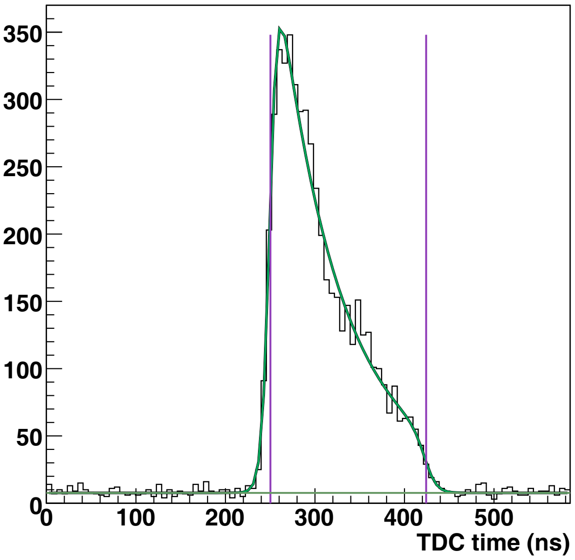

Fig. 61. Example of a fitted TDC spectrum. The light green line is the fit of the distribution; the violet vertical lines correspond to the t_0 and t_{max} values determined by the fit. The dark green horizontal line indicates the noise level.

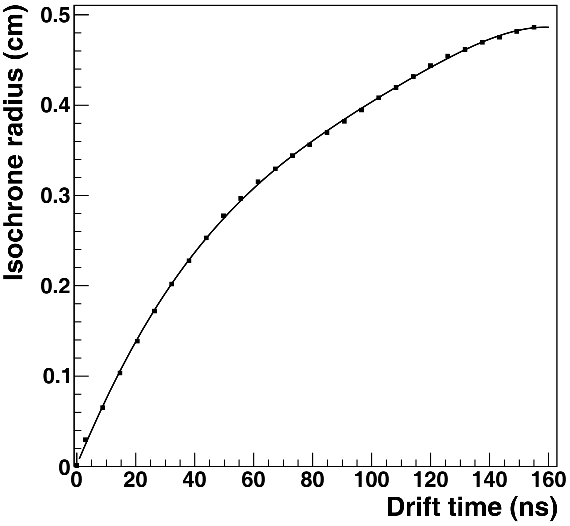

Fig. 62. Isochrones radius-drift time relation ($r(t)$), parametrised using a combination of Chebyshev polynomials of the first kind, up to the fifth order.

the following empirical function [54–56]:

$$\frac{\mathrm{d}n}{\mathrm{d}t} = P_1 + \frac{P_2\left[1 + P_3 \exp((P_5 - t)/P_4)\right]}{\left[1 + \exp((P_5 - t)/P_7)\right]\left[1 + \exp((t - P_6)/P_8)\right]}, \tag{6}$$

where P_1 is the noise level, P_2 is a normalisation factor, P_3 and P_4 are related to the shape of the distribution, P_5 and P_6 are the values of t_0 and t_{max}. P_7 and P_8 describe the slope of the leading and trailing edge of the distribution, so they are indicators of the drift tube resolution close to the wire and to the tube wall, respectively. The fit result of fig. 61 shows as an example the fit of the function (green line) to a measured TDC spectrum. In order to do a common calibration for all the tubes, their time spectra must have approximately the same shape and the same maximum drift time Δt. A quality check on the uniformity of the tubes, as well as on the quality of the fit, can be done by looking at the distributions of the fit parameters.

4.2 r(t) calibration curve

After the selection of the similar spectra, their specific time offset t_0 is corrected and their noise level is subtracted; then, they are added into a sum spectrum, each in its Δt range. Under the hypothesis of a uniform illumination of the tube and a constant efficiency over the tube volume, the isochrone radius-drift time relation ($r(t)$ relation in the following) can be obtained by the following integration:

$$r(t) = \frac{R_{\mathrm{tube}}}{N_{\mathrm{tot}}} \int_0^t \frac{\mathrm{d}n}{\mathrm{d}t'} \mathrm{d}t', \tag{7}$$

where n is the number of tracks, N_{tot} is the total number of tracks and R_{tube} the tube radius.

Taking into account the finite TDC resolution (bin size) and the wire radius R_{wire}, eq. (7) becomes

$$r(t_i) = \frac{\sum_{i=1}^{i_t} N_i}{N_{tot}} \cdot (R_{tube} - R_{wire}) + R_{wire}. \tag{8}$$

R_{wire} is the wire radius and N_{tot} is the sum of all bin entries N_i. The obtained space–time relation is then parametrised as a polynomial function.

An example of the $r(t)$ curve is shown in fig. 62; in this case, the space-time relation has been parametrised with a combination of Chebyshev polynomials of the first kind up to the fifth order[2],

$$\begin{aligned} r(t) &= p_0 + p_1 t + p_2(2t^2 - 1) + p_3(4t^3 - 3t) \\ &\quad + p_4(8t^4 - 8t^2 + 1) + p_5(16t^5 - 20t^3 + 5t). \end{aligned} \tag{9}$$

Once the space-time relation is known, the isochrone radius of a certain tube is computed by substituting in eq. (9) the measured drift time. This is calculated by subtracting from the measured drift "raw" time the time offset t_0 of that tube, obtained from the fit of eq. (6).

4.3 Autocalibration

Once the calibration curve has been derived, it is possible to proceed with the track reconstruction. In order to perform a good track fitting, it is necessary to know with high precision the relation between the measured drift time and the distance of closest approach of the particle trajectory to the wire. This implies an accurate knowledge of the $r(t)$ relation, that can be achieved with an iterative procedure called *autocalibration*, since it makes use of just the information from the tubes under investigation.

The autocalibration works as follows: at each step of the procedure, the $r(t)$ relation derived in the previous iteration is used to convert the measured drift times into drift radii, which will be used in the track fitting. At the first step, the $r(t)$ relation obtained directly from the integration of the drift time spectra (sect. 4.2) is used. Once a track candidate has been identified through dedicated pattern recognition algorithms, the track is reconstructed by using a track fitting algorithm. It allows to extract the (x, y) hit coordinates from the drift times and the (x, y) coordinates of the firing wires, which are the observables measured by the straw tubes. The fitting algorithms implemented for the $\overline{\text{P}}$ANDA-STT will be described in detail in sect. 6.2; the tracking procedure used for the test systems will be briefly presented in sect. 5. In this last case, in general tracks are reconstructed as straight lines

---

[2] The Chebyshev polynomials of the first kind are defined by the recurrence relation

$$\begin{aligned} T_0(x) &= 1, \\ T_1(x) &= x, \\ T_{n+1}(x) &= 2xT_n(x) - T_{n-1}(x). \end{aligned}$$

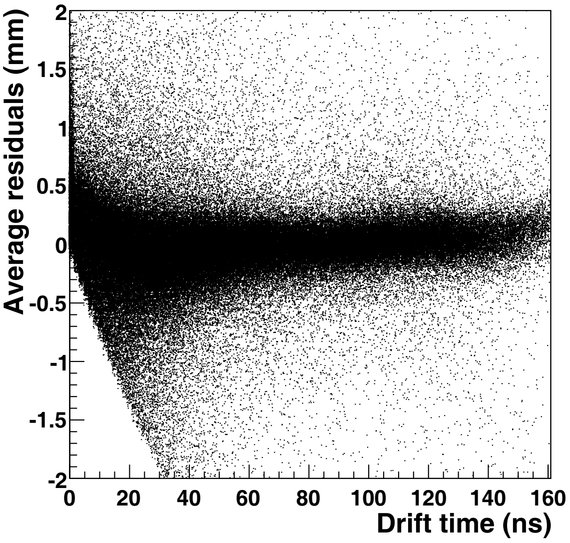

Fig. 63. Distribution of the average residuals as a function of the drift time at the first iteration.

$y = a + bx$, where the parameters a and b are obtained by a least squares fit (χ^2) that minimizes the track residuals, *i.e.* the difference of the distances of closest approach of the best fit lines to the centers of the firing tubes and the corresponding isochrones calculated from the measured drift times using the $r(t)$ relation. For each tube of the pattern associated with a track, the residuals are then computed and represented as a function of the N bins the drift time interval is divided into. If the $r(t)$ relation was exact, the average residuals would be zero at all radii.

An example of a residual distribution is shown in fig. 63: at this step, the mean value of the residuals varies from a minimum of $\sim -160\,\mu$m to a maximum of $\sim 320\,\mu$m for small radii. These deviations from zero indicate a miscalibration in the $r(t)$ relation, which is then corrected by taking the average deviation. The track reconstruction and the $r(t)$ calibration with the residuals as input are then repeated until the corrections become negligible and the mean value of the residuals is close to 0, as shown in fig. 64.

To study the speed and stability of the convergence of the method, the following quantity (mean square correction):

$$\Delta_k^2 = \frac{\sum_{i=0}^{N} \delta_{ik}^2}{N}\,, \qquad (10)$$

where δ_{ik} is the mean value of the residuals in the i-th time bin and N is the total number of bins, can be used as figure of merit (fig. 65).

The recalibration procedure is iterated until the mean square correction has converged to a stable solution [57].

5 Prototype tests

5.1 Test systems

The experience from different straw test systems and dedicated test measurements has been taken into account in the design of the $\overline{\text{P}}$ANDA-STT. The Straw Tube Tracker (COSY-STT) of the COSY-TOF experiment is considered to be a global test system, due to the similar mechanical layout of close-packed, self-supporting straw modules and its operation in the experimental environment of proton-proton collisions with a proton beam momentum around 3 GeV/c. COSY-TOF is a non-magnetic spectrometer (see fig. 66) and the tracks are reconstructed as straight lines instead of the helical trajectories in the solenoid magnetic field at $\overline{\text{P}}$ANDA. Nevertheless, the calibration method of the COSY-STT, the obtained spatial resolution and the mechanical precision of the detector, which consists of 2700 straw tubes, are of interest for the $\overline{\text{P}}$ANDA-STT design and expected performance. The COSY-STT is operated in the large ($25\,\text{m}^3$) evacuated time-of-flight barrel of the spectrometer since about 3 years. The surrounding vacuum is a strong test of all straw materials and assembly

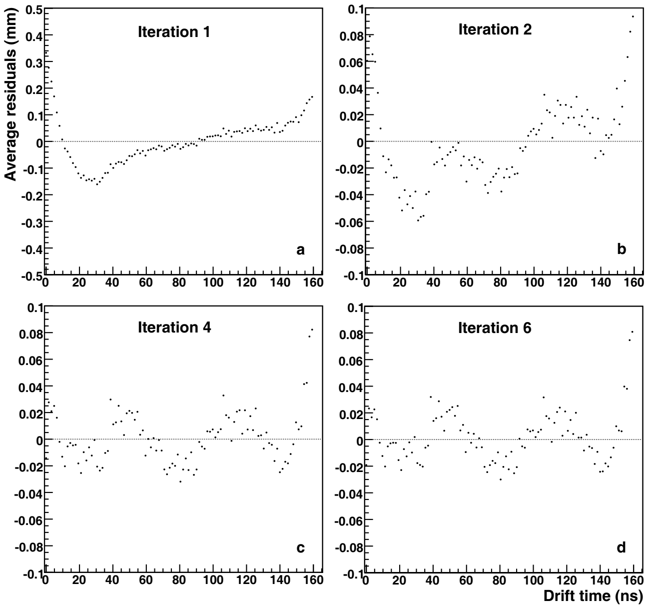

Fig. 64. Distribution of the average residuals as a function of the drift time after one (a), two (b), four (c) and six (d) iterations of the autocalibration procedure.

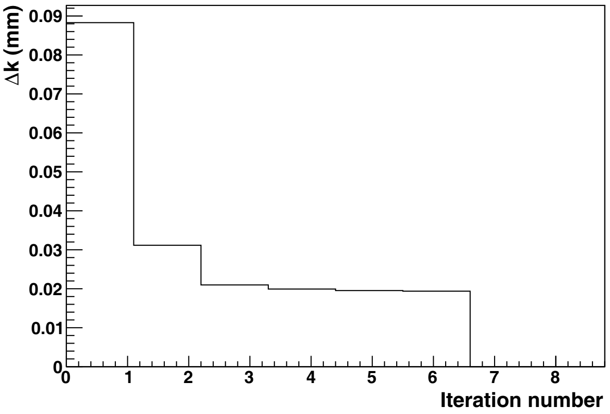

Fig. 65. Root mean square correction from the autocalibration procedure.

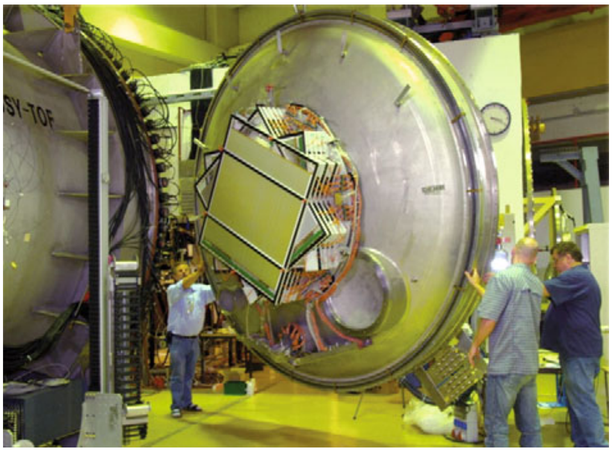

Fig. 66. Mounting of the COSY-STT in the time-of-flight barrel of the COSY-TOF spectrometer.

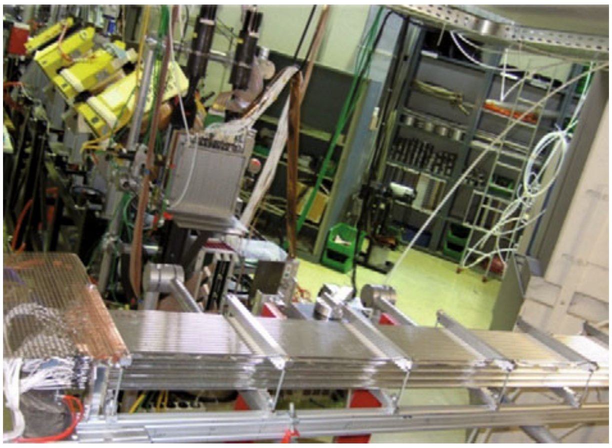

Fig. 67. Straw setup (in front) for the energy loss test measurements. The proton beam is coming from the back.

techniques, which are the same or similar to the $\overline{\text{P}}$ANDA-STT. Section 5.4 describes the properties and results of the COSY-STT.

A dedicated straw system consisting of a close-packed double layer of 32 tubes was used for specific aging tests. The setup was installed behind the COSY-TOF apparatus and exposed to the residual proton beam with a momentum of about 3 GeV/c during about 2 weeks. Except of their shorter length of 1 m the straw design and materials are similar to the $\overline{\text{P}}$ANDA type straws. The aging test and obtained results are summarized in sect. 5.3.

The measurement of the energy loss of a charged particle with high resolution is a non-standard task for a straw detector. It requires a novel electronic readout design, as well as a dedicated layout of the straw tubes in the $\overline{\text{P}}$ANDA-STT. A specific test system consisting of 128 straws, arranged in 8 close-packed layers, has been set up and measurements with high-intensity proton beams have been carried out (see fig. 67). The next section describes in detail the tests and developments concerning the energy loss measurement for the $\overline{\text{P}}$ANDA-STT.

5.2 Energy loss measurements

The STT has to measure, in addition to the trajectory reconstruction with high resolution, the specific energy-loss of the charged particle for an identification of the particle species. In particular, an efficient separation of pions, kaons and protons in the momentum region below 1 GeV/c is needed. Section 6.2 shows the results from a simulation analysis of the energy loss measurement with the STT and the expected separation power of the particle species.

Charged-particle identification with drift chambers of comparable size and channel numbers to the $\overline{\text{P}}$ANDA-STT has been performed in experiments like BABAR [58], BESIII [59] and HADES [60] and are very encouraging. In all gaseous detectors with segmented readout, there are factors which limit the precision of the energy loss measurements:

- the statistical nature of the ionization process that results in an extended and asymmetric energy loss distribution (Landau-curve shape);
- the limited numbers of sampling points used for the energy loss estimation;
- the long range of the drift time;
- the compromises necessary on the readout electronics, which should provide, at the same time, a “fast” time information for an efficient tracking, and which have to integrate for a sufficiently “extended” time interval the charge necessary for energy loss measurements.

The experimental investigations to evaluate the achievable energy resolution of the $\overline{\text{P}}$ANDA-STT are described in the following sections and aim at:

- fixing of the requirements for the readout electronics;
- selecting and optimizing the method of signal processing and data treatment;
- optimizing the detector performance, the electronics coupling and the noise suppression.

5.2.1 Experimental setup

The test setup consists of 128 $\overline{\text{P}}$ANDA-type straw tubes which are arranged in four double layers of 32 straws each (see fig. 67). The tubes, with an aluminized Mylar wall of 30 μm thickness, are 150 cm long and have an inner diameter of 10 mm. Several scintillators are placed in front and after the straw setup in the proton beam and are used to trigger on a coincident event and start the data-acquisition.

The electronic readout of the straw signals consists of front-end transresistance amplifiers with about 8 ns rise time and a gain factor of about 360, and flash-analog-to-digital converters (FADC) which sample the analog signal amplitude with a frequency of 240 MHz. FPGAs (Field Programmable Gate Array) controlling the readout of an FADC module are programmed for high flexibility to permit also the total readout in the “oscilloscope mode” and to record single spectra in a self-triggering mode for calibration measurements with an ^{55}Fe β^+ source.

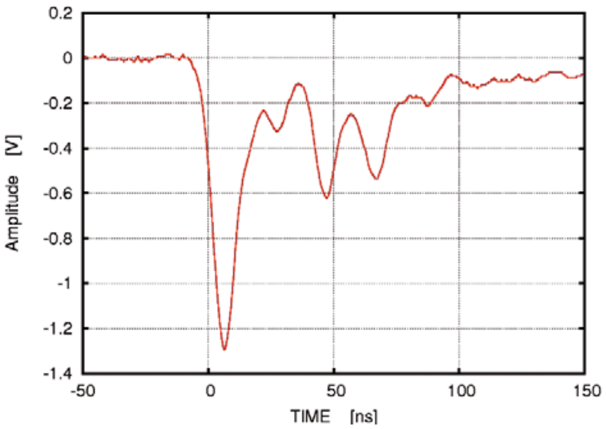

Fig. 68. Example of an analog output signal of the amplifier from a straw irradiated by a ^{90}Sr β-source.

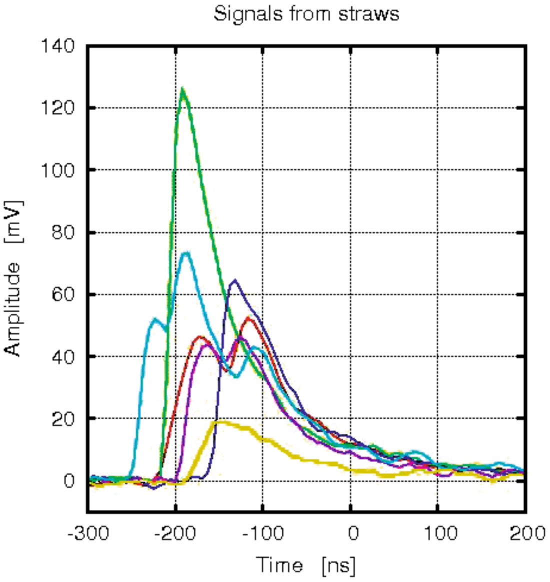

Fig. 69. Analog signals from the straw tubes as recorded by the 240 MHz FADC.

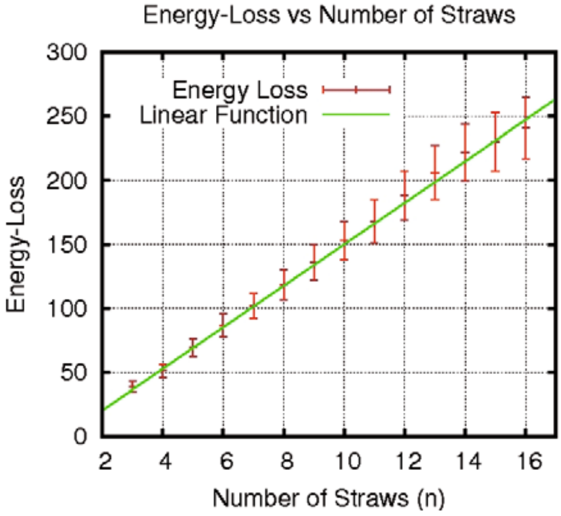

Fig. 70. Dependence of the energy loss for minimum ionizing β-particles on the number of the traversed straws. The energy loss is given in arbitrary units.

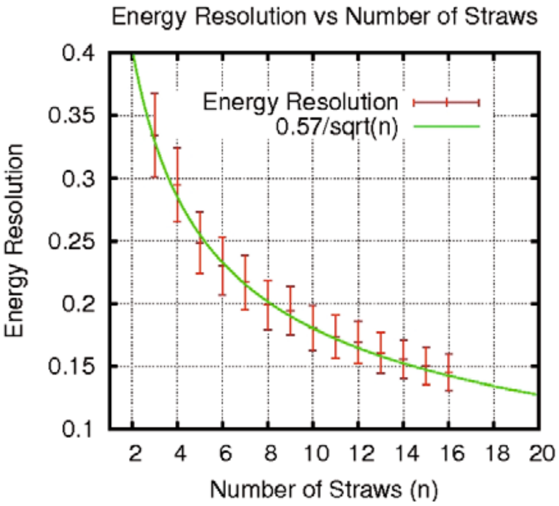

Fig. 71. Dependence of the energy resolution for minimum ionizing β-particles on the number of traversed straws.

In order to test different analysis methods of the signal shape, the analog output signals were recorded as a sampled waveform.

Figure 68 shows an example of a straw tube signal from a ^{90}Y/^{90}Sr β-particle processed by the transresistance amplifier. Due to the fast risetime of the amplifier several ionization clusters are resolved as distinct peaks in the output signal.

The amplified signals are fed into the FADCs with a sampling time interval of 4.17 ns (240 MHz). An example of the recorded straw signals is shown in fig. 69. As can be seen the limited precision of the sampling and the additional integration deteriorates the shape of the initial signals to some extent. Nevertheless, the envelopes of the groups of clusters are still visible. Since the straws are operated in proportional mode and the response of the electronics is almost linear, the area of the signal is directly proportional to the primary ionization in the straw tube, and therefore proportional to the energy loss of the traversing particle.

Initial checks of the detector response were performed by using β-particles from a ^{90}Y/^{90}Sr source. The geometry and the trigger conditions were optimized in order to select only the highest energy fraction of the β-decay spectrum containing minimum ionizing electrons. Figure 70 shows the dependence of the energy loss of the β-particles on the number of traversed straws. The relation between the energy resolution and the number of traversed straws has also been tested and the result is presented in fig. 71. In this case the energy loss spectra have been built integrating the area of the recorded signals. No further cuts were applied. The resolution is calculated as the ratio between the width and the mean value derived from the fit with a Landau curve. As expected, the energy dependence

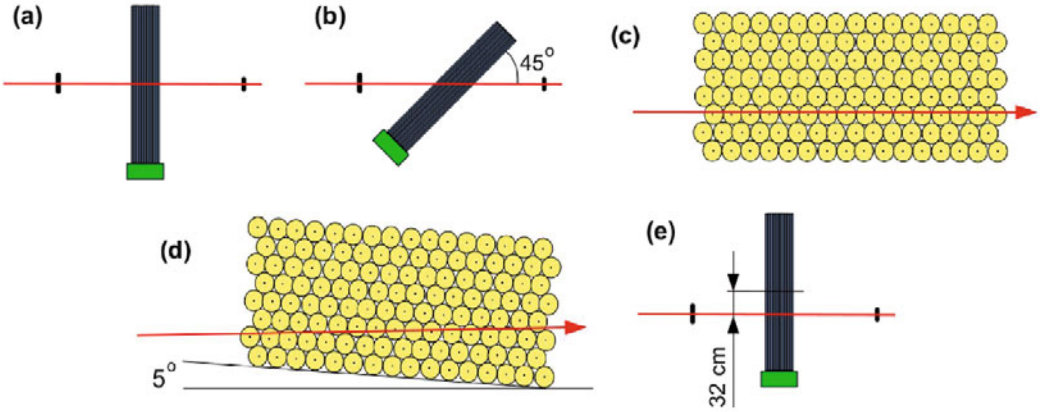

Fig. 72. Configurations of the straw prototype detector during the tests with the proton beam: (a) protons hit the straw tubes perpendicularly; (b) protons hit at 45° with respect to the straw axis; (c) the beam direction is parallel to the layers of straw tubes; (d) the prototype is rotated by 5°; (e) the prototype is displaced horizontally by 32 cm. The red lines indicate the beam.

is perfectly linear and the resolution follows an inverse square-root relation to the number of fired straws.

Further tests were performed using a monoenergetic proton beam of the COSY accelerator. A low-intensity beam (up to $1 \cdot 10^4$ protons/s) was selected and focussed directly onto the straw prototype.

During the measurements the detector was first oriented perpendicular to the beam axis (see fig. 72 a) to have the protons impinging at 90° with respect to the straw axis. Then, it was turned by 45° as it is shown in fig. 72 b. In vertical direction the straw tracker was positioned allowing the beam to pass parallel to the layer structure or with an angle of 5° in order to increase the number of crossed straw tubes and to enhance the merit of the isochrone calibration method: figs. 72c and 72d, respectively. All these measurements were done with the beam hitting the straw in the middle. In order to test possible amplitude differences along the straw length, the prototype was finally displaced by 32 cm. In this case, the beam entered the detector closer to the straw end equipped with the readout electronics (fig. 72 e).

The trigger signal was generated by the coincidence of the signals of two small ($\sim 10 \times 10$ cm) and thin (5–10 mm) scintillation detectors situated upstream and downstream the straw prototype. The beam was defocused in the vertical direction in order to cover a broad range of straws. The small size of the triggering scintillators assured a negligible horizontal angular spread of the beam.

The detector was filled with an Ar/CO$_2$ (9/1) mixture at 1 bar overpressure. The high voltage was set to keep the gas gain factor at a moderate level of about 5×10^4.

5.2.2 Analysis method

The shapes of the recorded signals (see figs. 68 and 69) do not allow to estimate the particle energy losses from the numbers and the distributions of the initial ionization clusters. The energy losses can be deduced only from the integrated charge of the output signal, or from any other parameter which is linear or related through an other known function to the collected charge. Two different methods have been tested: the so called *Truncated Mean* and the *Time over Threshold*. The methods and their results are described in the following.

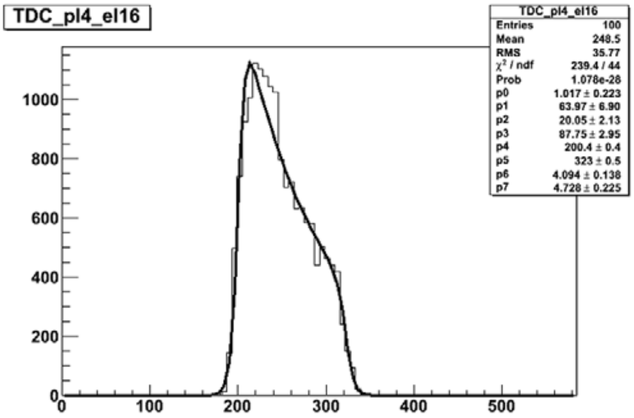

Fig. 73. Drift time distribution for a straw irradiated by the proton beam with a momentum of 2.95 GeV/c. The fit function to the time distribution is described in sect. 4.

Selection of events

The sampling frequency of the used FADC provides a drift time precision of 4.17 ns. Figure 73 shows a typical drift time spectrum. The isochrone calibration was performed as it is described in sect. 4. The gas mixture in the straws was Ar/CO2 (9/1) at a pressure of 2 bar. The tracking procedure allowed the selection of the fired straws belonging to an event and the calculation of the particle path length (fig. 74). The signals from the fired straws were then used to build the energy loss distribution. The energy-loss distribution for 2.95 GeV/c momentum protons is shown in fig. 75. As expected, it shows a Landau distribution shape.

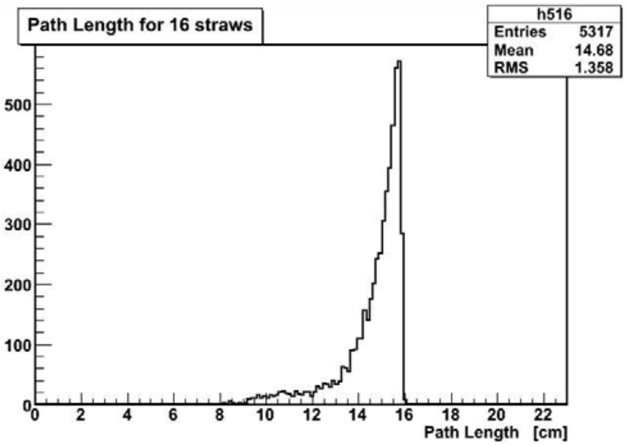

Fig. 74. Path length distribution for reconstructed tracks where 16 straw tubes were hit.

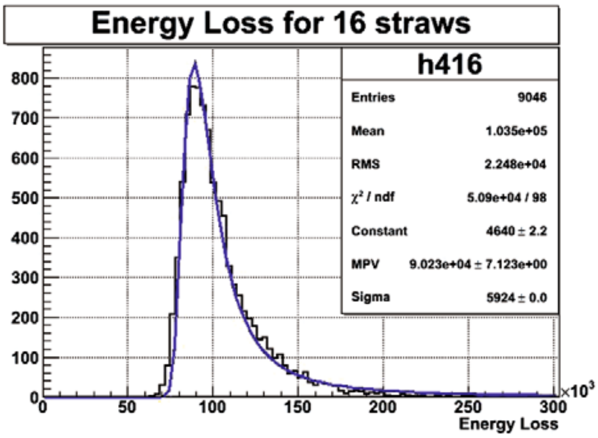

Fig. 75. Energy loss distribution for 2.95 GeV/c protons for reconstructed tracks hitting 16 straw tubes. The energy loss is given in arbitrary units, and the distribution is fitted with a Landau function.

The tail of the distribution extends to higher energies deteriorating the separation between the neighbouring ionization curves. In order to avoid the tail of the energy distribution a conversion of the Landau function into a symmetric Gaussian-like function by means of the so called *Truncated Mean* is performed.

Truncated Mean method

The probability of a certain mass assignment to a charged track may be determined by means of the observed ionization values. The average of all n measurements performed in a gaseous detector, is a bad estimator of the particle energy since it fluctuates a lot from track to track, because the underlying mathematical ionization distribution has no finite average and no finite variance. A good estimator is either derived from a fit to the shape of the measured distribution or from a subsample excluding the very high measured values [61]. By taking a fixed fraction r of the signals with the smallest amplitudes and evaluating their mean one finds a shallow minimum of this quantity as a function of r for values between about 0.35 and 0.75. This procedure has been deeply studied in the field [61–63] finding that in this range of r it is an empirical fact that the truncated mean values are distributed almost like a Gaussian. Figure 76 shows energy loss distributions obtained with the straw tube signals when different truncation factors f ($f = 1 - r$) are applied. The most suitable truncation factor has been determined by optimizing the resolution for the truncated mean distribution of the specific energy loss. For the analyzed data the best truncation fraction is 30% (see fig. 85).

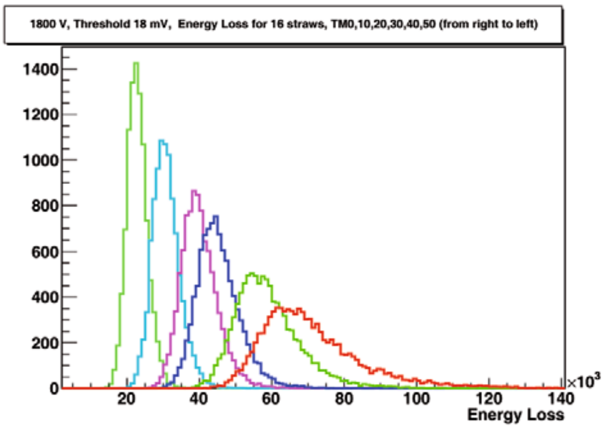

Fig. 76. Modification of the experimental Landau distribution by the so called *Truncated Mean* method. From right to left: original distribution, truncated by 10%, 20%, 30%, 40% and 50%. The energy loss is given in arbitrary units.

The energies of the truncated distributions have then to be divided by the appropriate reconstructed path lengths. The energy loss distribution 30% truncated, corrected for the path length for protons of 2.95 GeV/c momentum, is shown in fig. 77. The distribution has a shape well resembling the normal distribution and the fit with a Gaussian curve permits to derive the parameters of the distribution biased only with minimal uncertainties.

Time over threshold

Another technique that can be used to determine particle energy-loss, avoiding two electronic-readout branches (time and amplitude), is the so called *Time over Threshold* (ToT). This method postulates that the energy deposit inside the drift cell could be related to the time duration of the output signal and has been exploited by the ATLAS experiment [64–66].

Utilizing the recorded signal shapes from the straw prototype, it was checked that the direct measurement of the signals duration does not give a satisfactory relation with the specific energy loss for any reasonable threshold value. Only a coarse relation between the time width and the deposited charge is observed. Moreover, for high counting rates it is not affordable to follow the output signal over the whole drift time.

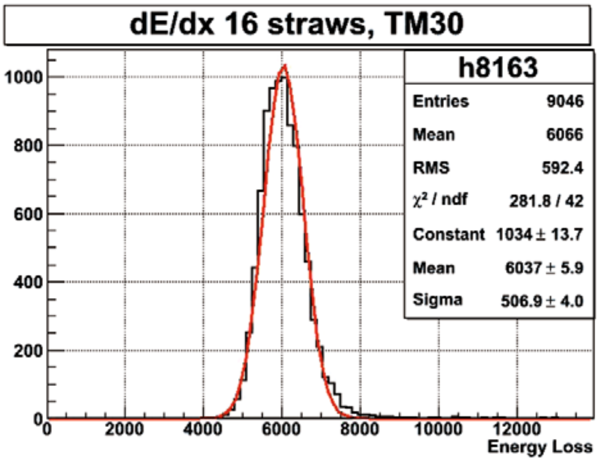

Fig. 77. dE/dx distribution for 2.95 GeV/c protons fitted with a Gaussian curve. The protons hit 16 straw tubes, and a truncation of 30% has been applied.

A most successful compromise solution, utilizing only a sensible fraction of the output signals, has been worked out and applied in the HADES experiment [60]. Unfortunately, due to the lack of a proper readout electronics, this method could not be checked in the tests we performed. However, since the characteristics of the signals of the HADES drift chambers are similar to those of the $\overline{\mathrm{P}}$ANDA-STT, the method and the results obtained by the HADES Collaboration are recalled here as an example of what could be achieved with the use of timing electronics only.

In HADES the ToT method was used for particle discrimination by means of dE/dx measurements in Mini-Drift Chambers (MDC), a four sections gaseous tracker. Each section of the detector consists of 6 separate drift chambers forming in total a 24 layer structure. Hence, particles traversing the tracking system may induce up to 24 individual output signals per track. The drift cells of each section have different dimensions and alternates from 5×5 mm for the first section, up to 14×10 mm for the chambers in section IV. The chamber windows are made of 12 μm aluminized Mylar foils. Aluminum, tungsten, bare and gold-plated wires are used for anodes, cathodes and field shaping. Diameters of the wires vary from 20 to 100 μm. The detector is filled with an helium/isobutane gas mixture (6/4) at atmospheric pressure.

The outputs of the sense wires are connected to analog boards [67] allowing for differential amplification, shaping and discrimination. The signals are digitized by means of an ASD8-B chip [68], which delivers a logical (LVDS) signal whose width is proportional to the time that the shaped signal remain above a fixed threshold value. Logical signals are then fed to multi-hit TDCs allowing both the time stamping with a 0.5 ns precision (from the leading edge of the signal), as well as the ToT evaluation (from the signal width). The method is illustrated in fig. 78. In order to extract the energy loss from the measured ToT a careful calibration has been performed. For each particle species the non-linear correlation function has been determined by means of a fitting procedure taking into account various incident angles and drift distances (in bins of 5° and 100 μm, respectively). Finally, the Truncated Mean method, similar to that already described, has been applied.

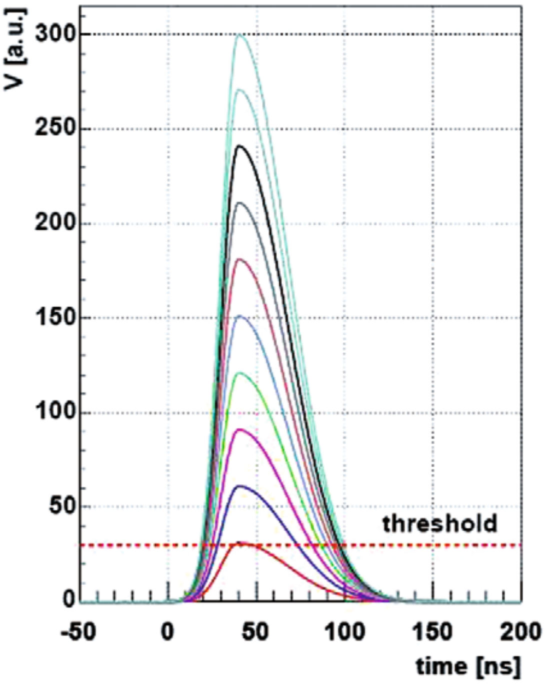

Fig. 78. Illustration of the *Time over Threshold* dependence on a preshaped fraction of the initial signals from the MDC-drift cells of the HADES experiment [60].

Eventually, an energy resolution of the order of 7% has been obtained for minimum ionizing particles, whereas for higher ionizing particles the achieved resolution was about 4% [60].

5.2.3 Results

In this subsection the results obtained with the use of the Truncated Mean method are reported.

Truncated energy loss distributions for different proton beam momenta and for selected tracks of high statistics are shown in fig. 79, for 2.95 and 1.0 GeV/c and in fig. 80 for 0.64 GeV/c. A Truncated Mean cut of 30% of the hits has been applied. The Gaussian fits are superimposed and the fit parameters are given in the figures. The results for the 0.64 GeV/c protons cannot be presented on the same energy scale of the results of 1.0 and 2.95 GeV/c due to a slightly different orientation of the setup (5° inclination and 18 hit straws instead of 16 for the latter two momenta). Also a higher threshold was used during the analysis of this data set. This was necessary since a higher pick-up noise was observed during this measurement created by an insufficient shielding of the scintillator bases. The selected threshold was two times higher than that set for the other tests. In all cases the applied HV was the same: 1800 V (gas gain of about $5 \cdot 10^4$).

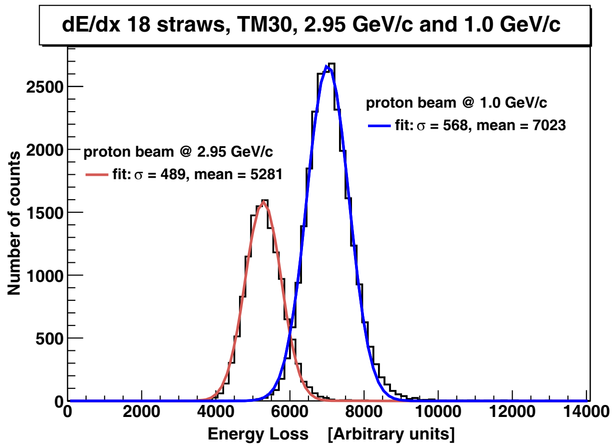

Fig. 79. dE/dx distributions for monoenergetic protons of 2.95 GeV/c (left one) and 1.0 GeV/c (right one) with Gaussian fits. The proton beam hit a maximum of 18 tubes for the 5° inclined straw setup.

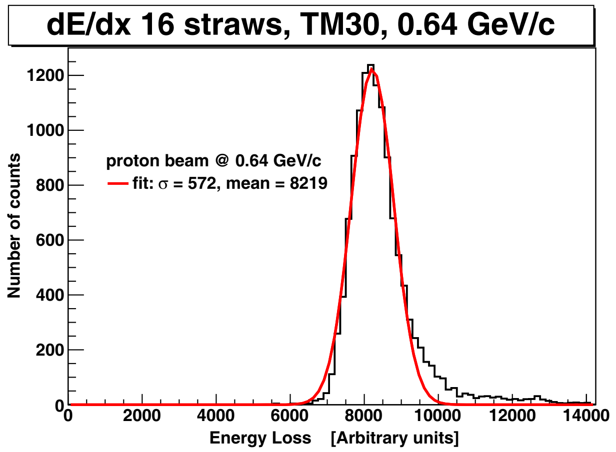

Fig. 80. dE/dx distribution for monoenergetic protons of 0.64 GeV/c with Gaussian fit. The protons hit a maximum of 16 straw tubes.

Figures 81 and 82 present the energy resolution dependence on the number of straws used to reconstruct the track for various geometrical configurations of the detector for 2.95 and 1.0 GeV/c proton momentum, respectively. The dependence of dE/dx on the number of hit straws for protons at 0.64 GeV/c momentum is shown in fig. 83. Due to technical problems, for this beam momentum the inclined tracks could not be registered. In this case the beam passed parallel to the detector layers and the highest statistics was obtained for reconstructed tracks with only 16 hits. Results for two different values of HV: normal one (1800 V) and decreased by 50 V (1750 V) are given. No significant difference in resolution for the lower voltage is observed. The presented results show that within the geometrical constrains of the laboratory test and in the kinematical momentum range of interest, the achievable energy resolution is equal to 8% for 1.0 GeV/c proton momentum and improves at lower momenta with the increase of the particle energy deposit. At 0.64 GeV/c, with only 16 straws in the track, the resolution is equal to 7%. For tracks inclined by 45° a systematical deterioration of the resolution of 1% is observed. For minimum ionizing protons of 2.95 GeV/c the energy resolution is about 9%, and for tracks at 45° it is worse of 1.5%. No significant effect on the energy resolution is observed for tracks hitting the straws at different longitudinal positions.

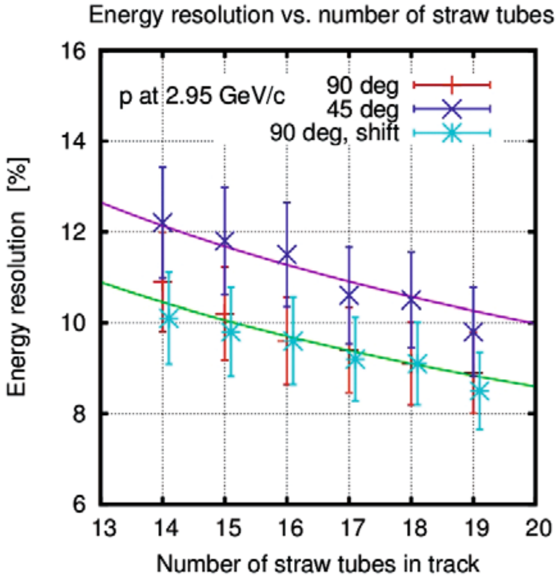

Fig. 81. Dependence of the energy resolution on the number of hit straws for protons with 2.95 GeV/c momentum. The different measurement setups are marked by different colors (see also fig. 72). Red: straw set-up perpendicular to the proton beam. Dark blue: setup skewed horizontally by 45°. Light blue: setup shifted by 32 cm in straw direction. The superimposed curves are functions $\propto (n)^{-1/2}$, where n is the number of hits.

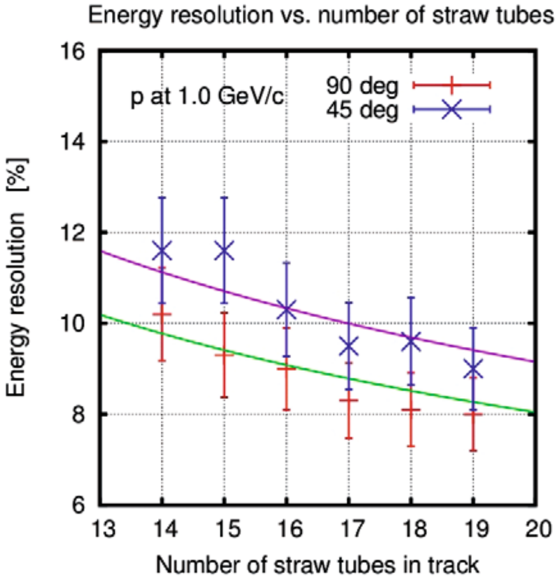

Fig. 82. Dependence of the energy resolution on the number of hit straws for protons with 1.0 GeV/c momentum. For the setup inclined by 45° the resolution is slightly worse, from about 8% to 9% at 19 hit tubes.

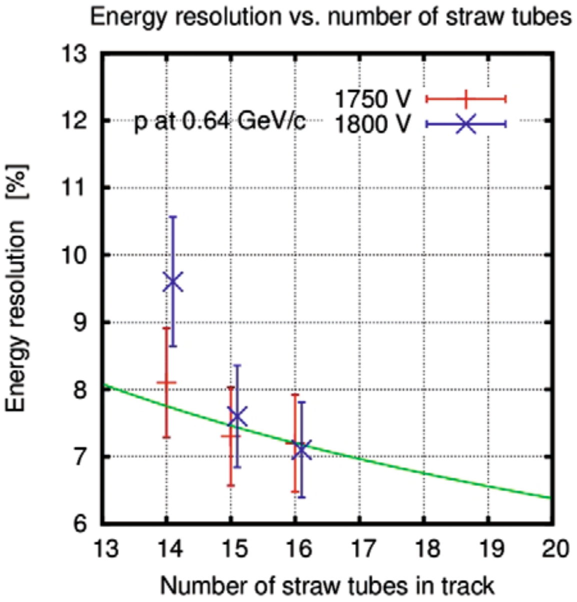

Fig. 83. Dependence of the $\mathrm{d}E/\mathrm{d}x$ on the number of hit straws for protons at 0.64 GeV/c momentum for two different high-voltage settings.

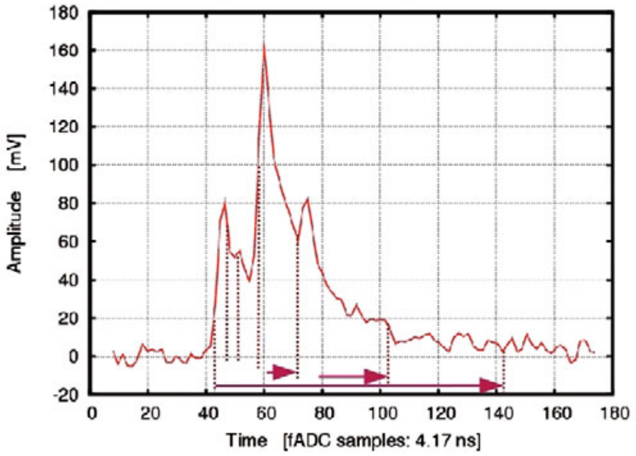

Fig. 84. Straw tube signal recorded by the FADC. The integration range indicated by the lines are 4, 8, 16, 30, 60, and 100 times the 4.17 ns sampling time.

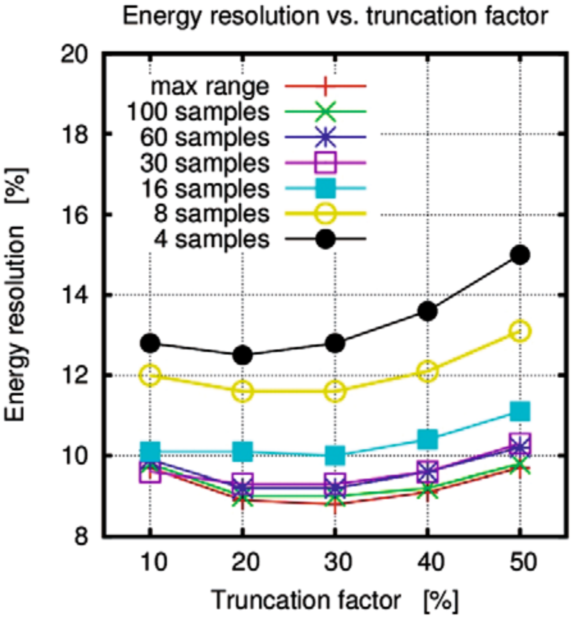

Fig. 85. Energy resolution as a function of the truncation factor for various fractions of the deposited charge.

In order to check the possibility to perform $\mathrm{d}E/\mathrm{d}x$ measurements also for high particle rates, which are expected in the innermost layers of the $\overline{\mathrm{P}}$ANDA-STT, and the possibility to use the ToT method for the energy-loss determination, we explored the possibility of shortening the signal integration time.

By using the recorded analog signals of protons of 1.0 GeV/c momentum, an analysis changing the fractions of the integrated signals has been performed. The concept of this analysis is shown in fig. 84. The signals have been integrated over 4, 8, 16, 30, 60 and 100 FADC samples (sample width is equal to 4.17 ns). The resulting energy-loss distributions have been truncated and a Gaussian fit has been performed. The results for events with 18 hit straws per track are shown in fig. 85. For this analysis, the path length correction has been applied before making the tail truncation (this was not done for the results shown above). A significant deterioration of the energy resolution is observed when the integration range is reduced to less then 16 samples (time interval 16×4.17 ns). "max range" means that the integration is done over the whole time window of the FADC. A small deterioration of the resolutions is obtained in comparison with that presented in fig. 82.

Since almost the whole charge of the signals is contained within the first 40–60 samples, there is not a significant decrease of the energy resolution measured, when the integration range extends beyond 30 samples. On the other hand, the 16 sample resolution is worse by 1% with respect to that obtained with the whole integration, and any further reduction of the integration range causes big worsening of the resolution. For the shortest integration time, only 4 samples, the energy resolution increases by an additional 3–4%. This result is shown in fig. 86. Here the energy resolution and its dependence on the number of hit straws is presented. The energy resolution is evaluated with a truncation factor of 30% only, which gives the best results.

The presented analysis, indicates that in order to obtain a satisfactory energy resolution with the $\overline{\mathrm{P}}$ANDA-STT, there is no need to integrate the signal charges over the whole drift time. A preshaping over 65 ns would be sufficient in order to keep the energy resolution below 10%, if the amplitude is used to measure the energy loss. On the other hand, if ToT is used, in the version developed in the HADES experiment, the integration time could be even shorter. In HADES the charge is integrated over few

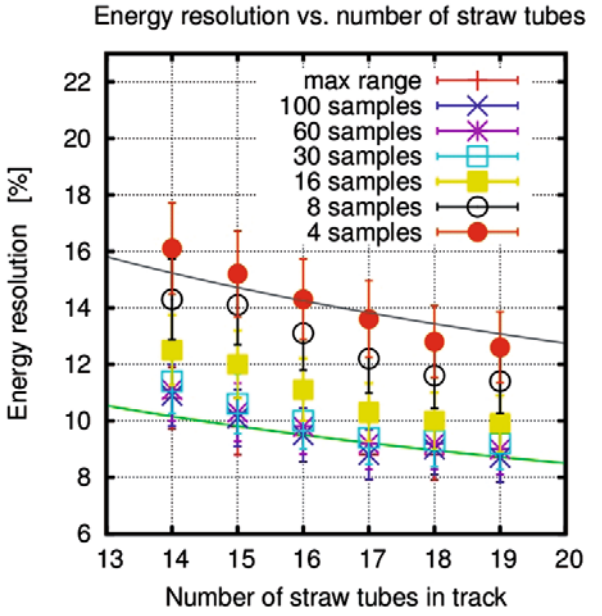

Fig. 86. Deterioration of the energy resolution by decreasing the fraction of the integrated charge. For the superimposed curves refer to fig. 81.

tens of ns. Further test exploring the possibility of using this technique will be done.

5.2.4 Detector performance at high counting rates

The results described above were obtained with monoenergetic beams of protons of intensity up to 10^4/s. At $\overline{\text{P}}$ANDA the experimental conditions foreseen predict for the innermost layer of $\overline{\text{P}}$ANDA-STT a particle rate of up to 0.8 MHz/straw. The rather long ion tail of the signals with this heavy particle flux calls for very efficient baseline restoration circuits, furthermore it could produce space charge distortions that can cause gas gain reduction with loss in resolution. In order to start addressing these problems the experimental setup was exposed to a proton beam of a momentum of 2.7 GeV/c of intensity up to 2.4 MHz. The actual beam intensity was monitored by counting the signals of each of the first straw in the layer. Due to the high beam divergence a stable high-intensity beam could not be kept on the whole detector. Therefore, a variation of the instantaneous beam intensity was observed, that can even better simulate the experimental conditions at $\overline{\text{P}}$ANDA. Examples of the spreads of the beam intensity are given in fig. 87.

The short integration constant of the front-end electronics permits to observe an almost undistorted shape of the anode current signal of the straws. These shapes were recorded by the FADC in time windows of 5 μs length. Figure 88 shows the signals recorded for one complete layer (16 straws) of the straw prototype. The individual groups of the signals may consist of up to 16 components.

Even at a very high beam intensity of 2.2 MHz, which is significantly beyond the expected rate during the operation of the $\overline{\text{P}}$ANDA-STT, the signal's baseline was stable and no onset of space-charge effects were recognized as well. At the normal operational voltage with particle fluxes of the order of 0.8 MHz/straw, both space as well as energy resolution of the tracker will not be deteriorated.

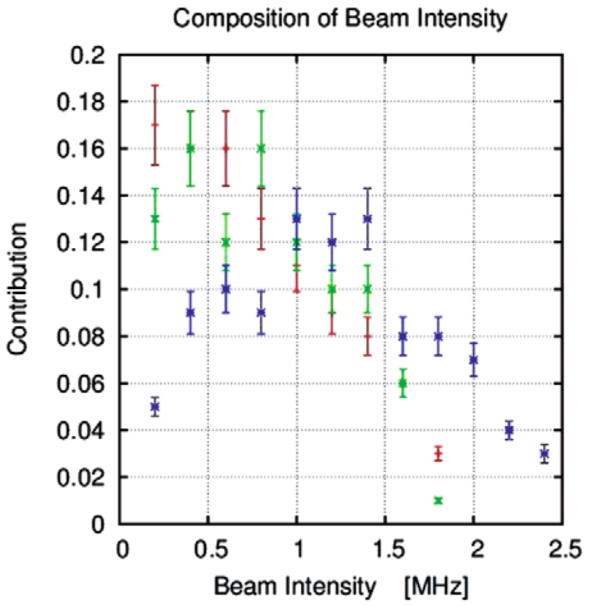

Fig. 87. Examples of the beam intensity variation during the high-rate test of the straw prototype. The different colors give the distributions of the measured beam intensity in different straws.

5.3 Aging tests

A degradation of the straw tube properties like a specific gas gain reduction or high voltage instabilities during operation caused by irradiation is expressed as aging. In general, aging is induced by the plasma-chemical processes during the gas amplification processes with a high density of ions, electrons, excitation photons, free radicals and possible molecular dissociations and polymerizations. A complete overview and description of the aging phenomena in gaseous detectors can be found in [69] which is a summary of a dedicated workshop with about 100 detector experts, held at DESY (Hamburg, Germany) in 2001. In the following, the main aspects relevant for the $\overline{\text{P}}$ANDA-STT are discussed.

Two main sources of aging have been identified in wire chambers. A growth of polymeric deposits on the electrodes which can change the electric field, create sparking, produce dark- or even self-sustaining (Malter) currents. At high irradiation densities and high gas gains already trace contaminations on the sub-ppm level in the gas can lead to such deposits. Another aging source is a possible oxidation of the sense wire. Usually the wire is protected by an outer gold-plating layer which makes the wire highly inert to chemical reactions. If oxygen produced in the amplification avalanche penetrates through the gold layer to the inner wire by permeation or at imperfection spots (holes)

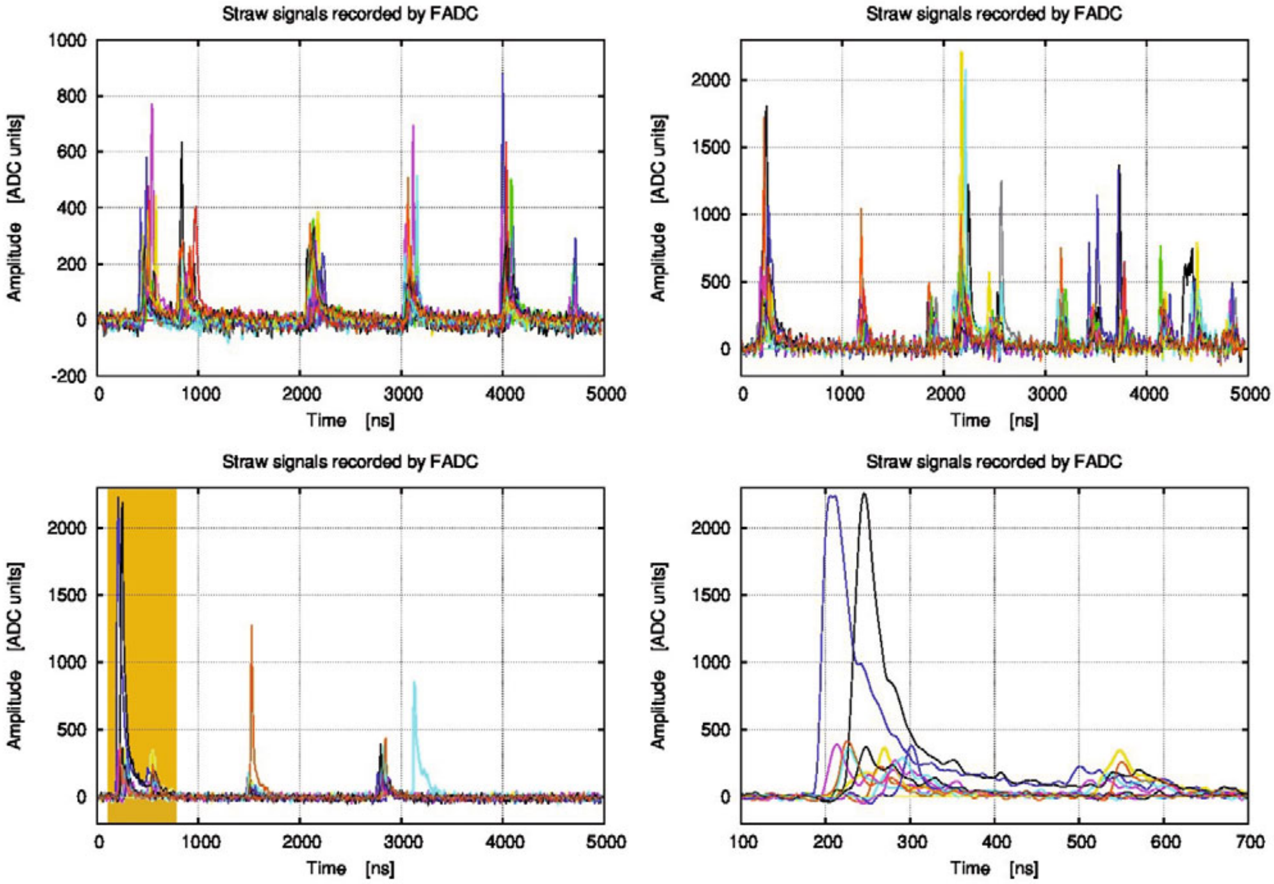

Fig. 88. Signals from different straw tubes recorded in $5\,\mu$s time windows by the 240 MHz FADC at high beam intensities. Top left: 6 particles crossings within the time window are visible, equiv. to $\simeq 1.2$ MHz rate. Top right: Beam intensity of about 2.2 MHz. Bottom left: Example of signals pileup. The colored region is shown enlarged in the bottom right panel of the figure. No baseline shift or signal shape deterioration is visible.

it can oxidize the wire with a swelling of the inner wire diameter and a cracking of the gold-plating layer [70]. The increased wire diameter reduces the gas gain at a given voltage by the lower electric field strength on the wire surface. A quantitative description of the aging process is difficult due to the high complexity with an influence for instance of the gas mixture and purity, trace contaminations, construction materials, gas flow, irradiation area and intensity, ionization density, high-voltage setting, particle type and energy.

The proposed Ar/CO_2 gas mixture is known as being one of the best gas mixtures for high-rate hadronic environments due to the absence of polymerization reactions of the components. Contaminations of the gas or detector materials with silicone, *e.g.* from lubricants must be avoided, since they produce a strong growth of non-volatile SiO_2 crystals on the wire. An admixture of CF_4 to the gas can remove such SiO_2 deposits, but due to its high additional wire etching capability special care is needed. Hydrocarbons are better quenching agents compared to CO_2, but not considered for the $\overline{\text{P}}$ANDA-STT because of their high polymerization rate, which can lead to deposits on the electrodes. In particular deposits on the cathode can produce self-sustaining currents with a possible high voltage breakdown (Malter effect) [69]. In general a moderate gas gain of about 5×10^4 is recommended which reduces the occurrence of limited streamer mode pulses with an increased avalanche size and possible accelerated aging [71].

The behaviour of the straw tubes under very high irradiation was studied at COSY with a proton beam. The goal was to check the influence of the beam exposure and charge deposition on the straw gas gain, high-voltage operation stability and to verify that all assembled materials including the gas system do not create harmful pollution, *e.g.* by out-gassing. Within the short time of about 10 days beam irradiation it was possible to collect a charge deposition in single tubes up to about 1.2 C/cm equivalent to more than 5 years in 99.7% of the STT volume when operated in the $\overline{\text{P}}$ANDA detector at full luminosity.

The straw setup consisted of a planar double layer of 32 close-packed tubes installed behind the COSY-TOF apparatus and exposed to the residual proton beam with a momentum of about 3 GeV/c. The straw design and all materials were the same as used for the COSY-TOF straw tracker assembly, *i.e.* $30\,\mu$m thick Mylar film tubes with 10 mm diameter and a length of 105 cm. For the $\overline{\text{P}}$ANDA detector the same straw tube design is proposed, but with

Table 14. List of straw settings and charge load during the beam test. The last column shows the normalized gas gain reduction in the irradiated straw region with a measurement resolution of about 2%. The aging intervals give the minimum and maximum gain reductions, *e.g.* 0–7% means that at least one straw showed no gain reduction and one a maximum of 7%.

Straw no.	Gas mixture	Voltage (V)	$\sum Q$ (C/cm)	Aging $\Delta G/G_0$
1–8	Ar/CO_2 (10%)	1750	0.72	0–3%
9–16	Ar/CO_2 (10%)	1700	0.58	0–7%
17–20	Ar/CO_2 (30%)	2200	1.23	no
21–24	Ar/CO_2 (30%)	2100	0.79	no
25–32	Ar/C_2H_6 (10%)	1550	0.87	no

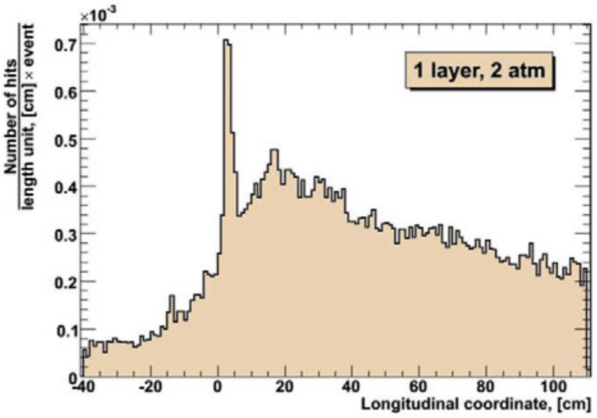

Fig. 89. Simulation of $\bar{\mathrm{p}}\mathrm{p}$ reactions giving the number of hits per event and per cm along the tubes in the innermost layer of the $\overline{\mathsf{P}}$ANDA straw tube tracker. The target position is at $z = 0\,\mathrm{cm}$.

a length of 150 cm. Due to the horizontal placement of the double-layer and a beam spot of about $2 \times 2\,\mathrm{cm}^2$ the particle rate through all tubes was almost the same. The surrounding alignment frame consisted of sandwich bars with a Rohacell core reinforced by Carbon fiber skins [35]. Therefore, interaction of the beam with this low-density foam material ($\rho = 0.05\,\mathrm{g/cm}^3$) was negligible.

The gas supply was divided into four parallel gas lines, each serving eight straws. Thus, it was possible to test at the same time straws filled with four different gas mixtures and gas gains with the same particle rates. The chosen gas mixtures were argon based, with different fractions of CO_2 (10% and 30%) and one mixture with 10% ethane. The gas pressure for all mixtures was 1650 mbar. The typical gas flow was one volume exchange per hour. In total, 16 high-voltage supply channels (one channel per two straws) allowed to operate the straws at different voltage levels and gas gains. The current of every voltage channel was monitored with a resolution of 2 nA. All straws were equipped with preamplifiers and 30 m long signal cables ending in the counting room. Therefore, it was possible to check analog signal shapes and signal rates during beam irradiation for every straw. Table 14 lists the straw settings during the beam test.

The expected particle rates for the individual tubes in the $\overline{\mathsf{P}}$ANDA central tracker volume were derived from a simulation of $\bar{\mathrm{p}}\mathrm{p}$ interactions and assuming an event rate of $2 \times 10^7\,\mathrm{s}^{-1}$ (see fig. 89). The mean particle flux for straws in the innermost layer was $\simeq 800\,\mathrm{kHz}$ per 1500 mm long tube and about $\simeq 7\,\mathrm{kHz/cm}$ in the forward region ($z > 0\,\mathrm{cm}$). The maximum flux of $\simeq 14\,\mathrm{kHz/cm}$ in the tube was concentrated within $z = 2 \pm 1\,\mathrm{cm}$ (target position at $z = 0\,\mathrm{cm}$) coming from $\bar{\mathrm{p}}\mathrm{p}$ elastic interactions with a laboratory scattering angle $\theta \simeq 90°$ and relatively low momentum. These particles crossing the tubes around $z = 2 \pm 1\,\mathrm{cm}$ were highly ionizing and produced a high charge load of $\simeq 1\,\mathrm{C/cm}$, if one assumed a typical gas gain inside the tubes of 5×10^4. At all other positions, which represent 99.7% of the STT volume, the mean charge load was about 0.2 C/cm. All quoted charge loads were equivalent to an expected typical beam time for $\overline{\mathsf{P}}$ANDA of one year with 50% live-time.

The total live-time with beam on the straws was 199 hours after correcting the COSY spill time structure and beam breaks. All straws were exposed to the proton beam at the same longitudinal position, in the middle of each tube. The beam rate and cross section profile was measured by a scintillating fiber hodoscope placed behind the COSY-TOF apparatus and in front of the straw setup. The derived proton intensity per straw diameter during extraction was about $2.3 \times 10^6\,\mathrm{s}^{-1}$. The slightly lower pulse rate of $\simeq 2.0 \times 10^6\,\mathrm{s}^{-1}$ measured for the single straws could be explained by losses of low amplitude signals due to the damping inside the 30 m long cables.

During the beam time no high voltage failures, dark currents or broken wires due to the high charge load were observed. A high maximum current of a single straw wire of up to $2.3\,\mu\mathrm{A}$ was measured.

A possible gas gain reduction due to the proton beam irradiation was checked after the beam time by exposing all straw tubes to a ^{55}Fe radioactive source with 5.9 keV γ-emission. In the argon-based gas mixtures the photo-absorption produces a localized ionization spot with a characteristic number of about 220 electrons. Therefore, the recorded signal amplitude height was a direct measure of the gas gain. The amplitude heights were checked for each straw at different longitudinal positions around the beam irradiation spot and normalized to the ampli-

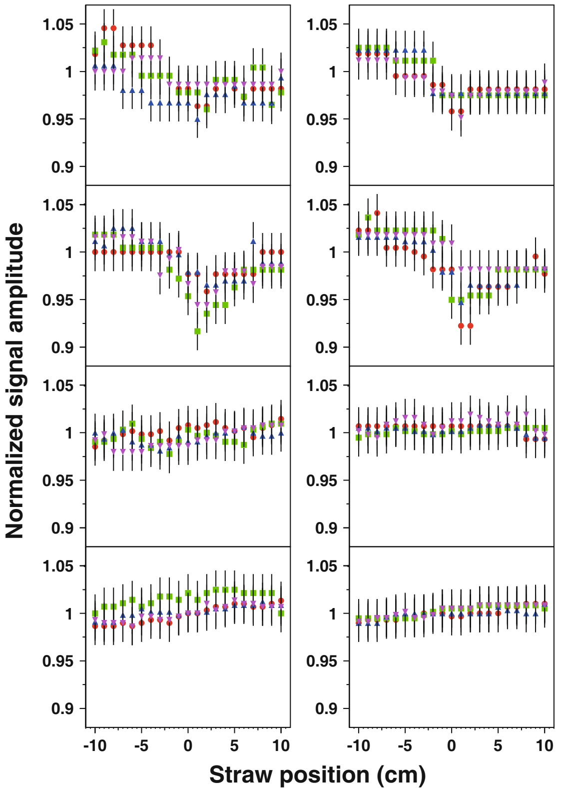

Fig. 90. Measured normalized gas gain reduction ($\Delta G/G_0$) along the tube for all 32 straws, shown in groups of 4 straws. Straw no. 1–4 (upper left), straw no 29–32 (lower right). The beam hits all tubes around 0 cm longitudinal position.

tude heights far from the irradiation spot (see fig. 90). A lower amplitude height indicates a reduction of the gas gain ($\Delta A/A_0 = \Delta G/G_0$). The estimated resolution error of the measurement was about 2% of amplitude height.

It can be seen that for all straws filled with 30% CO_2 or 10% ethane in argon no gas gain reduction was measured, even for the highest charge loads up to 1.2 C/cm. Some but not all straws filled with 10% CO_2 in argon showed a small gas gain loss of up to 7% at the beam irradiation spot. A clean spatial correlation between the reduced gas gain and beam intensity distribution, measured by the scintillating fiber hodoscope in front of the straws, was observed. The results of the gas gain measurement together with the total charge loads for all 32 straws are summarized in table 14.

The absence of any aging in the straws filled with ethane or the higher CO_2 percentage in argon indicated no general problem with the gas purity, and a pollution by the used straw materials or gas system could be excluded. The small gas gain reduction observed only for some of the straws operated with the lower 10% CO_2 admixture might be explained by the known poor quenching capabilities of CO_2, together with the very high irradiation perpendicular to the wire and concentrated at a small spot of about 2 cm along the wire during the beam test. Due to the incomplete avalanche quenching the occurrence of limited streamer mode pulses, with the characteristic double-peak signal shape, was higher for that gas mixture. The high ionization density with a large number of produced oxygen ions and radicals increased the probability of oxygen permeation through the gold layer to the inner wire. The oxidation of the inner tungsten-rhenium wire caused a swelling of the wire diameter, and as a result the electric field strength at the wire surface was reduced ($E \propto 1/r$) which lowered the gas gain at the same high voltage setting. Since the observed gas gain reduction was very small the occurring aging processes were rather weak. To clearly identify the sources of aging, dedicated investigations with a higher charge load over a much longer time period would be needed.

Ar/CO_2 is the preferred gas mixture for the $\overline{\text{P}}$ANDA-STT since it is highly tolerant to highest irradiation, not expensive, and non-flammable. The measurements confirm that the straw design and all used materials are suited and will not limit the life time of the detector. No aging in the straws is expected at moderate gas gains of about 5×10^4 for 99.7% of the STT volume during more than 5 years of $\overline{\text{P}}$ANDA operation at full luminosity. A small aging on the low percent level may start first in the region at $z = 2 \pm 1$ cm (= 0.3% of the STT volume) after about 2 years of operation, caused by low energy protons from elastic scattering. The modular mechanical design of the $\overline{\text{P}}$ANDA-STT allows to replace even single straws showing aging or other failures inside the layer modules after some years of operation during the $\overline{\text{P}}$ANDA maintenance time.

5.4 The COSY-TOF Straw Tube Tracker

The technique of pressurized, self-supporting straw tube layers was first developed for the Straw Tube Tracker of the COSY-TOF experiment (COSY-STT) at the COSY accelerator (Jülich, Germany). The used straw tube materials and dimensions, and the geometry of planar, close-packed multi-layers are the same or quite similar as for the $\overline{\text{P}}$ANDA-STT. Although the COSY-STT is a non-magnetic spectrometer, the calibration methods for the straw tube positions and isochrone radius-drift time relation are similar for both detectors. The operation of the COSY-STT with about 275 l gas volume in surrounding vacuum is an outstanding technical challenge. The required minimal leakage of the detector in vacuum is a strong and sensitive proof of all straw materials, glueing and assembly techniques, which are also crucial for the $\overline{\text{P}}$ANDA-STT. The COSY-STT is considered to be a global test system for the $\overline{\text{P}}$ANDA-STT and its properties and performance results are summarized in the following.

The COSY-STT was installed in 2009 as an upgrade of the COSY-TOF spectrometer, which consists of a large 25 m^3 vacuum barrel with a liquid-hydrogen target cell at the entrance, followed by a start detector, silicon-microstrip detector, the straw tube tracker (STT), and scintillator hodoscopes covering the barrel walls and end cap. The apparatus allows to measure kinematically complete the time-of-flight and space directions of the reaction particles of hyperon production in proton-proton and proton-deuteron collisions with polarized proton beam. The vacuum ensures lowest background produced by beam and reaction particles with up to 3.5 m track lengths. More

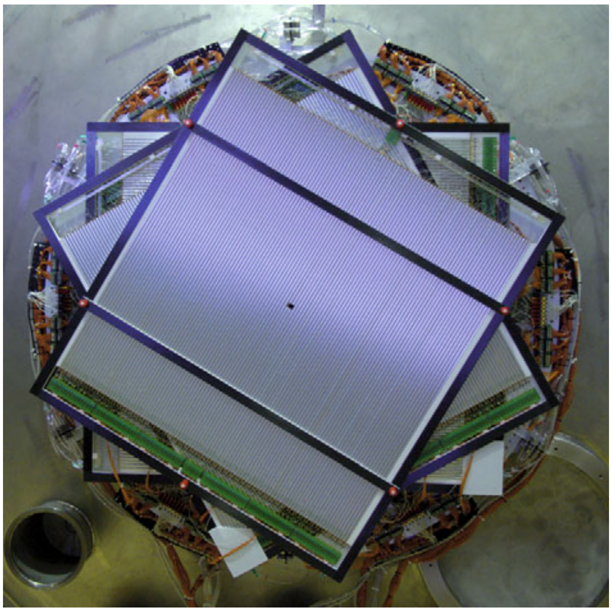

Fig. 91. The COSY-STT mounted at the front cap of the COSY-TOF spectrometer. The detector consists of 2704 straw tubes of 1 m length and 10 mm diameter, arranged as a vertical stack of 13 close-packed double layers at three different orientations.

details about the experimental program and the STT installation can be found in [72] and [73]. A first experiment beam time of hyperon production with polarized proton beam was carried out in 2010.

The COSY-STT consists of 2704 straw tubes, each with a length of 1050 mm, inner diameter of 10 mm, and 32 μm wall thickness of aluminized Mylar film. The tubes are arranged as a vertical stack of 13 close-packed double layers with three different orientations ($\phi = 0°, 60°, 120°$) for a 3-dimensional track reconstruction. A $15 \times 15\,\mathrm{mm}^2$ beam hole in the center of every double layer is realized by splitting the 4 central straws into 8 straws with about half length (see fig. 91). The straws are filled with a gas mixture of Ar/CO_2 (80/20%) at a pressure of 1.25 bar. The typical operation voltage is 1840 V. The electronic readout consists of low-power trans-impedance preamplifiers directly connected to each straw in vacuum and feeding the signals through 13 m coaxial signal cables to ASD8B-discriminators and TDCs, which are located outside the vacuum barrel.

The COSY-STT is now since about three years in surrounding vacuum and no real leakage sources of the detector, caused by dissolving glue spots, brittle materials, or loose gas connections, have been observed. The gas leakage stays on the permeation level, which is caused by the flow of the gas molecules inside the straws through the thin Mylar film wall to outside vacuum. Figure 92 shows the gas loss by measuring the pressure drop inside the straws in surrounding vacuum if the STT is filled with pure argon and pure CO_2. The difference in the gas loss rate for argon and CO_2 of about a factor of 10 is characteristic for the different permeation of the specific gas molecules through the Mylar film and in accordance with reference measurements by the manufacturer (DuPont Teijin Films, USA). For the used gas mixture of Ar/CO_2 (80/20%) the total leakage is about 2% of the STT volume per day. The typical gas flow during the high voltage operation is about four times the STT volume per day (= 1000 l/day).

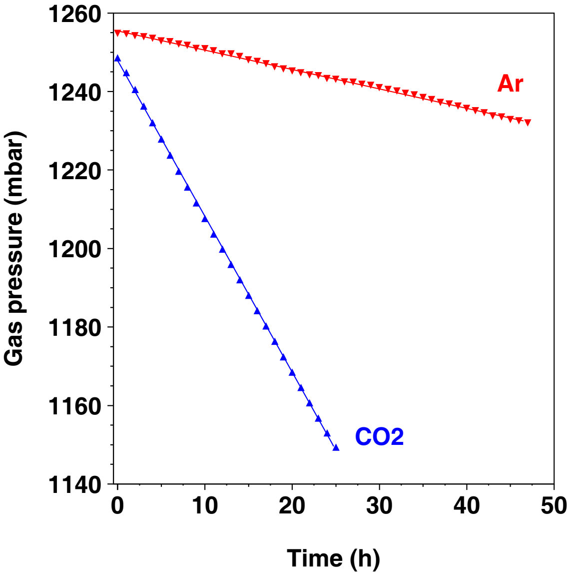

Fig. 92. Gas leakage of the COSY-STT filled with pure argon (red) and pure CO_2 (blue), measured by the gas pressure drop of the straws in surrounding vacuum.

The calibration of the STT consists of the determination of the isochrone radius-drift time relation and the adjustment of the straw positions and is performed as an iterative procedure. At first, the isochrone-drift time relation ($r_{iso}(t)$ in the following) is parametrized as a polynomial function of 4th order and obtained by an integration of the time offset corrected drift time spectrum (see sect. 4.2),

$$r_{iso}(t) = \sum_{i=0}^{4} P_i \times t^i. \tag{11}$$

Then, tracks are reconstructed as straight lines with a least squares fit (χ^2) to the isochrones calculated from the measured drift times using the defined $r_{iso}(t)$-relation. Figure 93 shows the distances to the fired straw wires *versus* the measured drift times for all reconstructed tracks. A systematic deviation in the track distance for single straws or straw groups from the expected $r_{iso}(t)$-relation is corrected by adjusting the straw position accordingly. Here, the assembly technique of the STT simplifies the position calibration to a large extent. Individual deviations of single tubes in the close-packed double-layers are not possible and only the vertical position of the 13 double layers have to be adjusted. The track reconstruction is repeated using the new straw layer positions, the distances are checked and the positions are corrected again until the systematic deviations vanish. Finally, also the $r_{iso}(t)$-relation is verified by a new parameter fit of the reconstructed track to wire distances to the measured drift times.

The distribution of the finally obtained residuals of the reconstructed tracks to the isochrones is a measure of

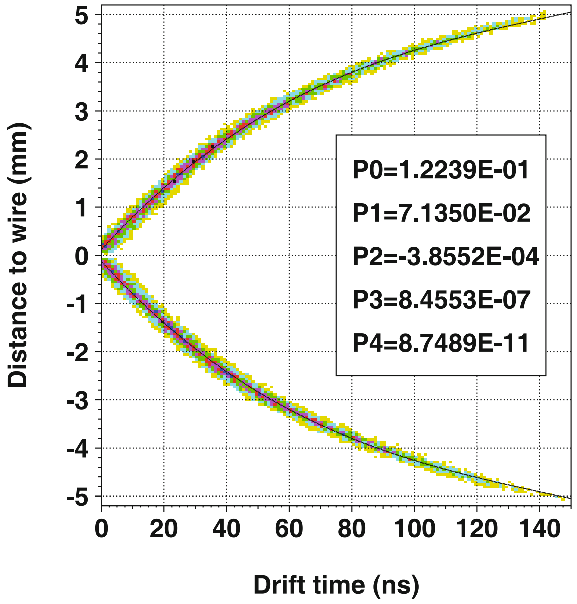

Fig. 93. Track to wire distances and measured drift times for the reconstructed tracks. The $r_{iso}(t)$-relation (black line) is parametrized as a polynomial function of 4th order with the parameters P_0–P_4.

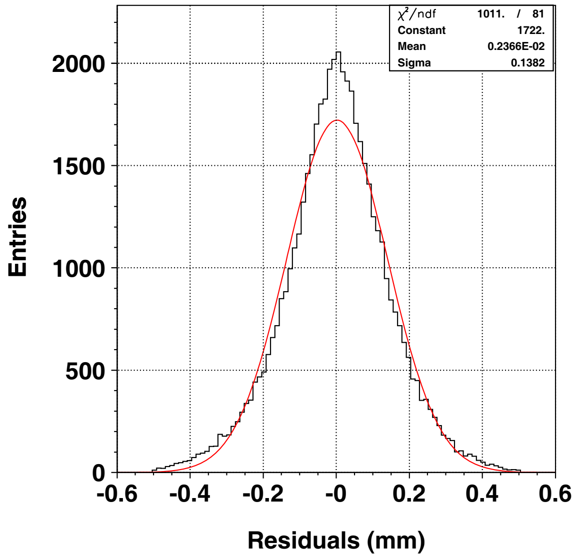

Fig. 94. Distribution of the residuals of all reconstructed tracks as a measure of the COSY-STT spatial resolution. The width of 138 μm (σ) and mean of 2 μm are the results from the Gaussian fit (red line).

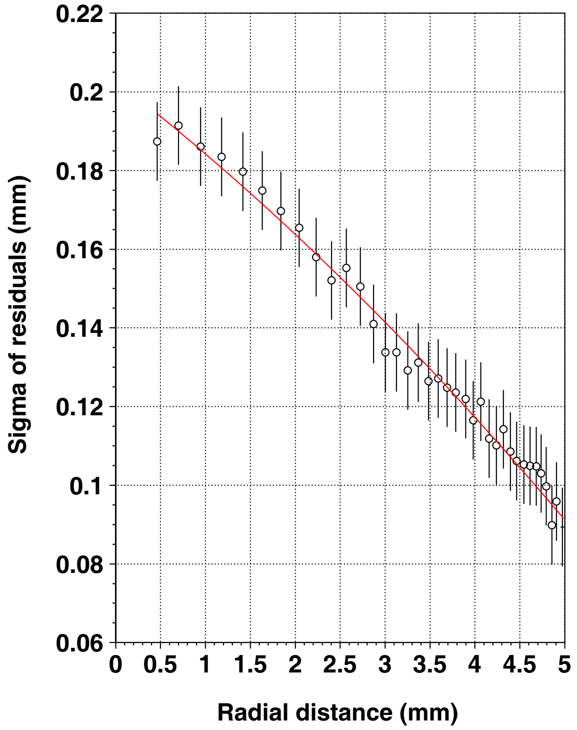

Fig. 95. Width (sigma) of the residual distributions for different intervals of the radial distances to the wire.

the spatial resolution of the STT and is shown in fig. 94. Only a simple filter for single hits from delta-electrons with large distortions to the fitted track has been applied. No drift time correction due to the signal propagation time along the wire and the particle time of flight have been made. The estimated drift time error is about $\Delta t = 2\,\mathrm{ns}$. Also the reconstruction of a straight line track does not take into account multiple-scattering inside the STT which contributes to a maximum of about 100 μm for the first and last layers. The spatial resolution of the STT is given by the width of the residual distribution, which is 138 μm (σ) for the gas mixture of Ar/CO$_2$ (80/20%) at an absolute pressure of 1.25 bar. The shape of the distribution is nicely symmetric with a low mean of 2 μm, showing no distortion by additional systematic errors.

The variation of the spatial resolution depending on the radial distance to the wire is shown in fig. 95. Close to the wire the resolution is about 190 μm, dominated by the primary ionization cluster spacing and time jitter together with higher drift velocities. Both effects are reduced more and more for larger distances to the wire and the resolution improves to about 100 μm close to the straw cathode, where the electron diffusion during their drift to the anode is the limiting factor.

Since the installation of the STT in the COSY-TOF spectrometer several experiments with different momenta of the polarized proton beam have been carried out to study the hyperon production in proton-proton collisions. The performance of the track reconstruction with the STT can be studied by the analysis of the pp → pp elastic scattering process, which is used for the calibration of the detectors and for a determination of the luminosity in the experiment. The pp → pp elastic scattering event kinematics can be calculated from the measured direction of the two reconstructed tracks ($\hat{p}_{1,2}$) and the known beam momentum (p_{beam}). Requiring momentum conservation, the violation of the energy conservation in the process is a strong selection criterion against physical background processes like pp → dπ^+ or final states with higher track multiplicities (*e.g.* uncharged π). The latter are also tested

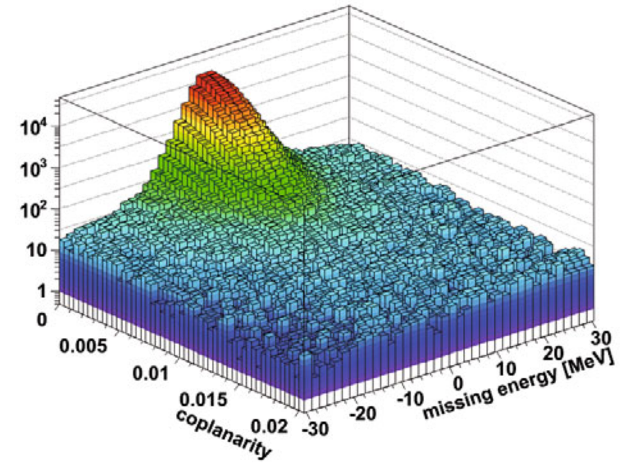

Fig. 96. The distribution of the missing energy in the primary vertex and the coplanarity (C) shows a clear peak from pp elastic scattering events.

by the coplanarity (C) defined as

$$C = |(\hat{p}_1 \times \hat{p}_2) \cdot \hat{p}_{\mathrm{beam}}|,$$

which measures how well the final-state particles are reconstructed back to back in the center-of-mass system. Figure 96 shows the coplanarity (C) *versus* the missing energy for an event sample of 7.6 million triggered events. Due to the high reconstruction precision of the STT the signal events are strongly peaked around $(0,0)$. A sample of 420 000 elastic scattering events can be selected with a circular cut around the peak center. From the surrounding bins a background contamination of the event sample from inelastic scattering can be determined to be lower than 0.45%

The results obtained from the COSY-STT can be extrapolated to the $\overline{\text{P}}$ANDA-STT. Both detectors have a similar material budget and number of straw layers for the tracking. The main differences are the operation of the $\overline{\text{P}}$ANDA-STT inside a solenoid field and at a higher straw gas pressure of about 2 bar. The additional Lorentz force will change the radial drift path for the electrons inside a straw to a longer, spiral drift path and increased drift times. Still the isochrones have a cylindrical shape, only the $r_{iso}(t)$-relation will be different. The higher gas pressure will increase the maximum drift times and the ionization density which improves the spatial resolution. Therefore, assuming a comparable resolution of the drift time measurement of about $\Delta t = 2\,\mathrm{ns}$ the spatial resolution of the $\overline{\text{P}}$ANDA-STT is expected to be better than $140\,\mu\mathrm{m}$.

6 Simulations

6.1 The single straw tube simulation

6.1.1 The charge released into the tube

We have performed a detailed simulation of the charge generation and collection process in a single straw tube.

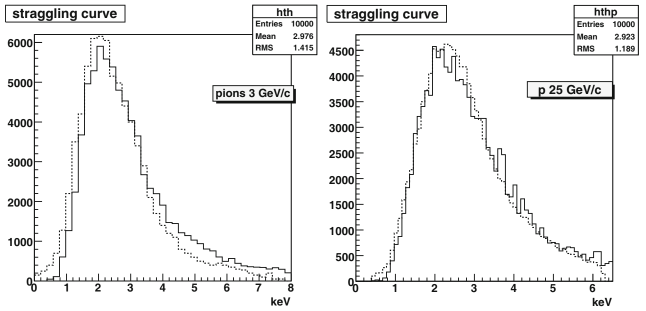

Fig. 97. Comparison between the simulated energy loss in a 1.5 cm Ar/CO_2 layer (line) and the experimental values of Allison *et al.* [77] (dotted line).

In correspondence of an incident charged particle, we sample from the exponential distribution the point where an electron cluster is generated and from the proper distribution (see below) the number of electrons in the cluster. By stopping when the particle leaves the tube, we have the number of free electrons generated from a Poissonian number of clusters. The mean number of clusters/cm is taken from [74] (25 for Ar and 35.5 for CO_2). For the reliability of the simulation, it is crucial to know the cluster size distribution, *i.e.* the number of electrons per cluster. We use the theoretical calculations of [75] for Ar and the experimental data on Ar and CO_2 from [76]. The comparison with some available results in gas has shown that this choice is in reasonable agreement with the data (see fig. 97). By knowing the mean value of the energy spent per free electron (*i.e.* to create an electron-ion pair), the overall energy loss of the projectile on the whole path can be calculated. The assumed values are 27 eV for Ar and 33.5 eV for CO_2 [74].

As a further check, we compared the energy lost in the tube, for a variety of projectiles and energies, with the Urban model [78], which is used in GEANT3 and GEANT4 in the case of gaseous thin absorbers [79,80]. The results, reported in fig. 98, show good agreement with our simulation.

6.1.2 The drift process from GARFIELD

The tube response has been studied in detail giving the tube size, wire radius, high voltage, gas mixture and magnetic field as input to the GARFIELD [45] code.

The mixture and the high voltage determine the behavior of a gas. In a weak electric field or in a mixture with high quenching, the electrons are in thermal equilibrium with the surrounding medium and the drift velocity is proportional to the electric field intensity. Such gases are usually called "cold".

On the contrary, if the electron average kinetic energy differs from the thermal energy, the drift velocity behaviour becomes saturated and tends to be constant and independent of the electric field strength, that is of the distance from the wire anode. In this way the main sources of systematic errors are removed and the track

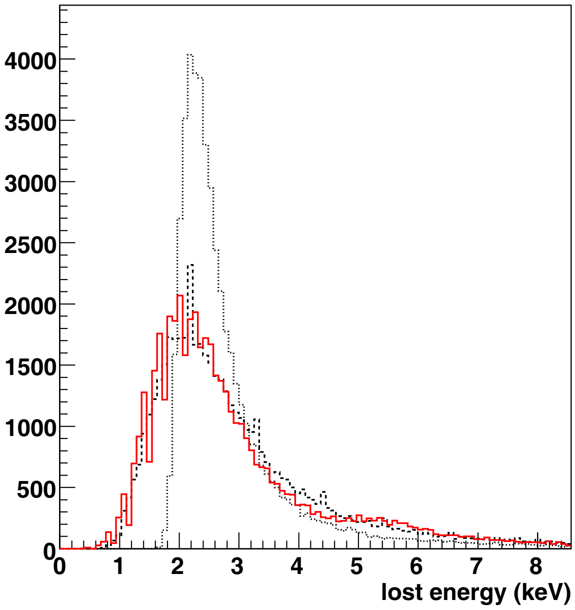

Fig. 98. Energy loss of 1 GeV pion traversing a 1 cm of 90% Ar, 10% CO_2 gas mixture at NTP. Solid line: Urban distribution; dashed line: specific simulation model; dotted line: Landau distribution.

reconstruction is easier. Such gases are called "hot". However, the spatial resolution in hot gas mixtures is limited by the large diffusion and cannot be better than 50 μm.

The drift velocity as a function of the wire distance is reported in fig. 99 showing that the increase of the CO_2 percentage tends to cool the gas, with a corresponding stronger dependence of the velocity from the wire distance. This effect could be recovered by an accurate self-calibration (see below), but makes the tube stability more critical, requiring a precision control of temperature and pressure.

The effect of the magnetic field transforms the path between two collisions of a moving charge into circular trajectories. With obvious notation, the electron Lorentz angle is [61]

$$\tan\alpha = \tan\omega\tau = \frac{eB}{m_e}\tau,$$

where τ is the average time between collisions and ω is the Larmor frequency of the electron. In cold gases the drift velocity tends to be linear with the electric field E and τ is almost constant, whereas in hot gases, where the drift velocity is more constant, τ is inversely proportional to E. Due to the much lower elastic cross section, τ in hot gases is about one order of magnitude higher. Estimations from experimental data show that for a 2 T magnetic field and a 5 mm drift distance, the drift time for a CO_2/C_4H_{10} (90/10) mixture increases by 15% in a magnetic field, that for an Ar/CO_2 (90/10) mixture increases up to 50% [81].

All these effects are reproduced in the GARFIELD results.

Typical time *vs.* distance curves for a hot gas mixture like Ar/CO_2 (90/10), with and without magnetic field, are reported in fig. 100, where the increase of the drift time due to the field is clearly visible.

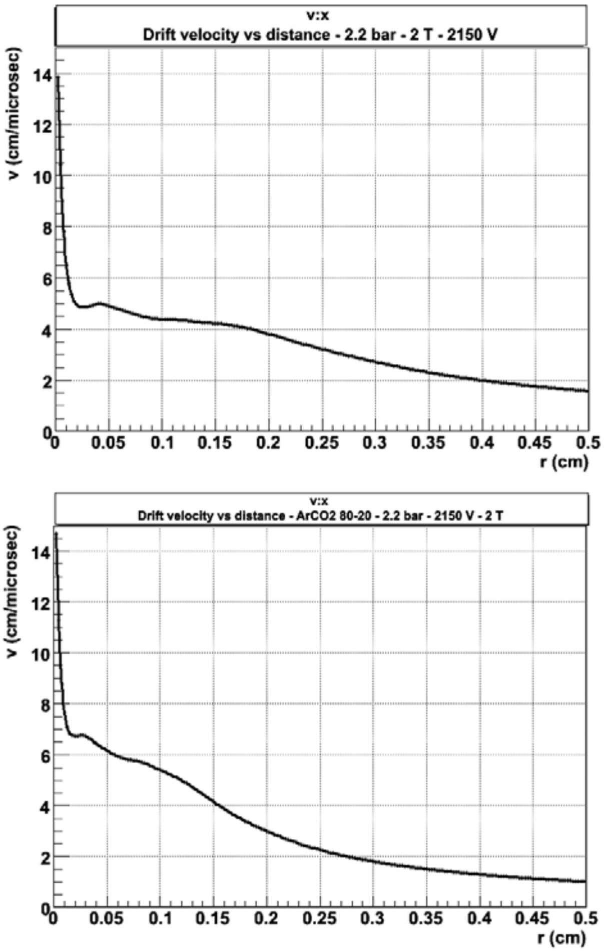

Fig. 99. Drift velocity *vs.* wire distance in a straw tube of 0.5 cm radius, 1850 V voltage, 2.2 bar pressure and 2 T magnetic field for different gas mixtures: 90/10% Ar/CO_2 (top), 80/20% Ar/CO_2 (bottom).

The increase in the drift time while increasing the CO_2 percentage is also clearly shown in fig. 101.

Another important input to the simulation are the transverse and longitudinal diffusion curves, due to the thermal spreading of the electron clouds during the drift. The GARFIELD results show that the high diffusion values of the hot gas (Ar/CO_2 = 90/10) are partially compensated by increasing the pressure. At 2 atm pressure the longitudinal and transverse diffusion coefficients, at 5 mm distance from the wire, are 100 and 140 μm, whereas at 1 atm pressure the same coefficients are 120 and 220 μm, respectively.

Finally, the necessary input to the simulation is the gas amplification, *i.e.* the multiplication factor of the avalanche which is formed in the last tens of microns of the primary electron path in its drift to the anode wire. This multiplication factor is given by [61]

$$G = \exp\left(\int_a^x \alpha(x)\mathrm{d}x\right),$$

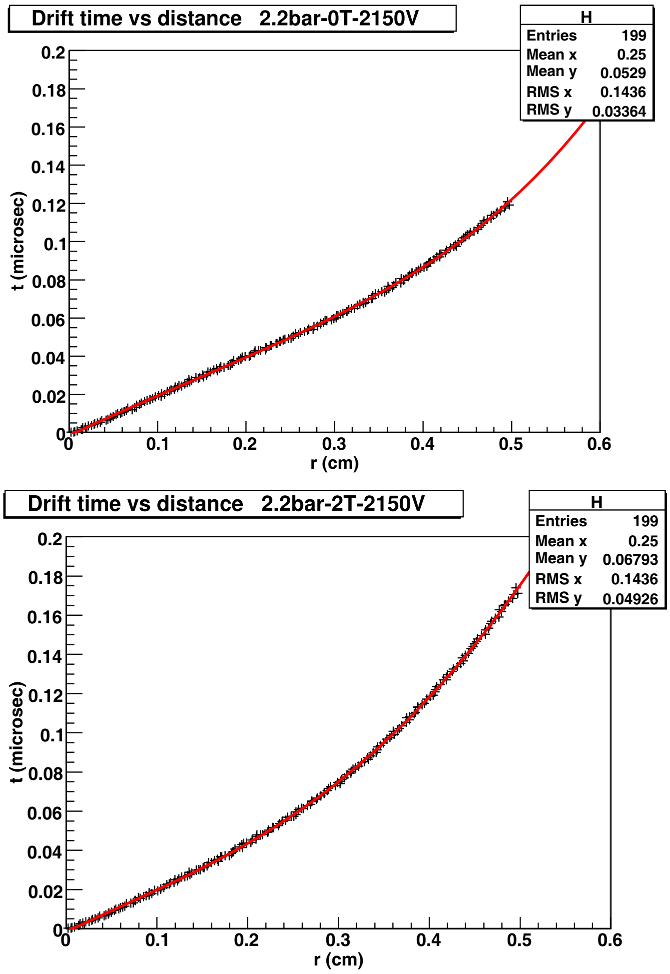

Fig. 100. Drift time *vs.* wire distance in a 90/10% Ar/CO$_2$ straw tube of 0.5 cm radius and 2.2 bar pressure: without magnetic field (top); with magnetic field of 2 T (bottom) (from GARFIELD).

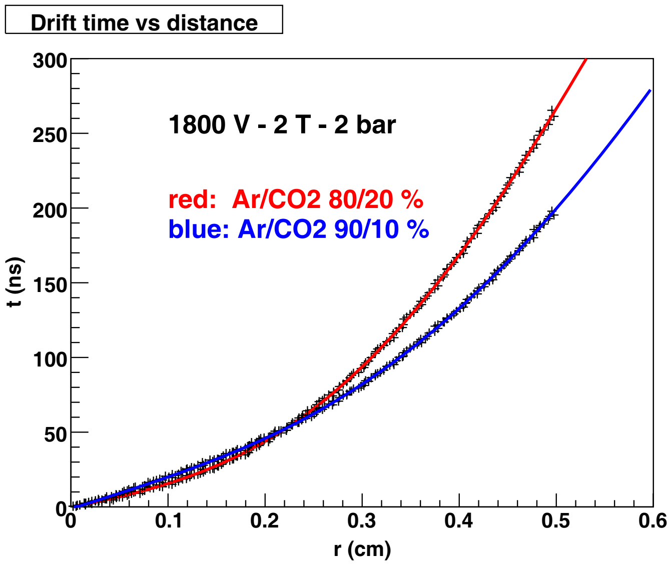

Fig. 101. Time *vs.* wire distance for two different Ar/CO$_2$ mixtures in the presence of magnetic field (from GARFIELD).

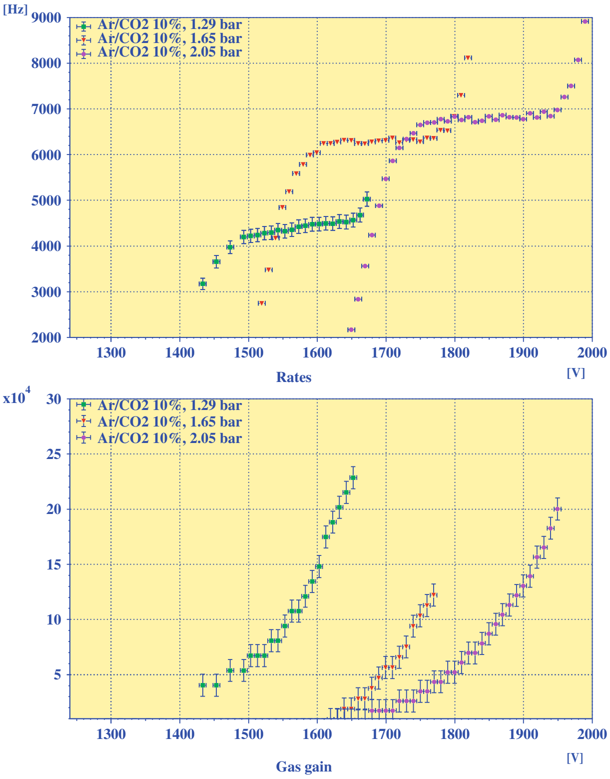

Fig. 102. Experimental plots of the tube rate and gas gain relative to a 90/10% Ar/CO$_2$ mixture.

where $\alpha(x)$ is the Townsend coefficient (inverse of the mean free path for ionization), a is the anode wire radius and the integral is taken along the whole drift path. A typical behaviour of the gas gain, measured for our mixtures of interest is shown in fig. 102, where one sees that in our case the tube remains in the region of direct proportionality.

6.1.3 Simulation of the drift process

Once the free electrons have been created in some points of the tube, their position is dispersed both longitudinally and transversally according to the GARFIELD diffusion curves and the time of arrival on the wire is calculated from the GARFIELD distance-time curves.

The movement of each electron gives rise to a charge, which is obtained by sampling from a Polya distribution [61] having as a mean value the gain or multiplication factor (around $5 \cdot 10^4$). Then, by summing this signal over the number of electrons we obtain the total charge, as shown in fig. 103.

6.1.4 The electrical signal

By taking into account the arrival time of each electron and assigning a Gaussian-shaped electrical response to each charge multiplication, we can reproduce also the shape of the electrical signal. We added also a white noise

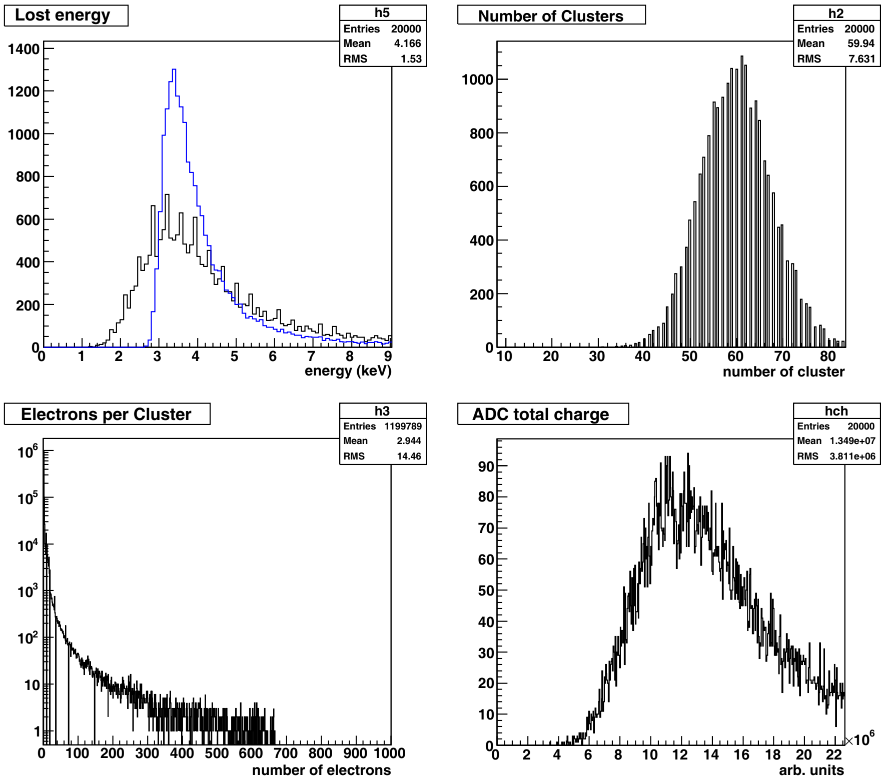

Fig. 103. Results of the single tube simulation for a 1 GeV pion in a 2 atm pressure straw tube with a 90/10 Ar/CO_2 gas mixture. Upper left: energy lost in a tube compared with the sharper Landau distribution. Upper right: Poissonian distribution of the number of clusters. Bottom left: cluster size distribution calculated as discussed in the text. Bottom right: charge collected on the wire assuming a multiplication mechanism from the Polya distribution. By multiplying the number of clusters with the mean number of electrons per cluster, a mean number of primary electrons of about 200 is obtained.

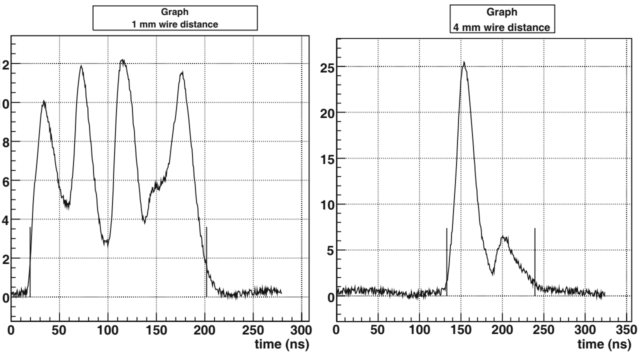

Fig. 104. Straw tube simulated signals for a track close to (left) and far from (right) the wire.

component equal to the 3% of the primary signal peak value.

Some examples are shown in fig. 104, where two typical signals are shown: the first one is generated from a track 1 mm near to the wire, the second one from a track 4 mm far from the wire. In the first case the clusters arrive dispersed in time, giving rise to an irregular structure of the signal. In this case the discrimination technique is crucial for a good time resolution. In the second case the cluster arrival is more concentrated and the signal structure appears more regular. These examples show the importance of the electronic treatment of the signal and of the discrimination technique to be used for obtaining the drift time.

We consider two discrimination techniques: fixed (F) and constant fraction (CF) thresholds. The F threshold is set to about 5% of the mean primary electron value, that is to 10 primary electrons in the 2 atm case (see fig. 103). This is compatible with previous studies [82,83]. The CF threshold is set to 5% of the peak value of the current signal.

In the following, unless specified otherwise, the displayed results are obtained with the standard F threshold.

6.1.5 Simulation of the self-calibration procedure

The primary information from the tube is the drift time distribution of the arriving signals, that is the number of tracks dN within the time interval dt. A typical distribution of this quantity, in the case of a parallel and uniform illumination of the tube is shown in fig. 105 and in fig. 106 (left) in the case of the absence and the presence of the magnetic field, respectively.

The self-calibration method exploits the properties of this distribution. Since the track density is constant over

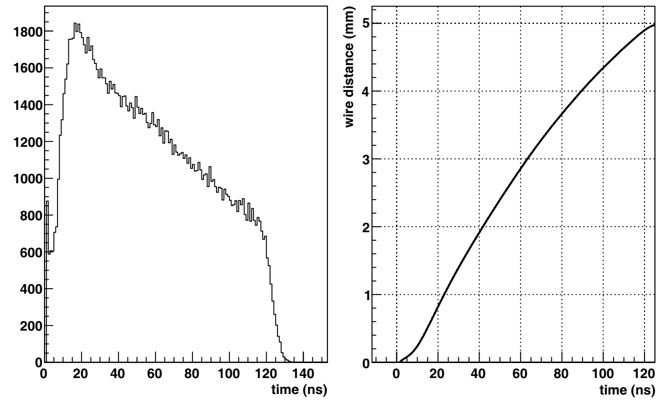

Fig. 105. Simulated TDC spectrum without magnetic field for a single tube uniformly illuminated (left) and space-time relation obtained with the self-calibration method of eq. (14).

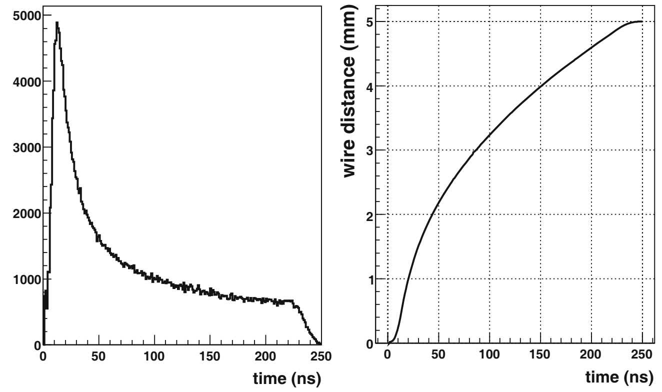

Fig. 106. Simulated TDC spectrum for a 2 T magnetic field for a single tube uniformly illuminated (left) and space-time relation obtained with the self-calibration method of eq. (14).

the tube diameter, one can write

$$\frac{\mathrm{d}N}{\mathrm{d}r} = \frac{N_{\mathrm{tot}}}{R}\,, \tag{12}$$

where N is the number of tracks, r is the wire distance, N_{tot} is the total number of tracks and R the tube radius. The number of tracks in a time interval can be obtained directly from the above relation

$$\frac{\mathrm{d}N}{\mathrm{d}t} = \frac{\mathrm{d}N}{\mathrm{d}r}\frac{\mathrm{d}r}{\mathrm{d}t} = \frac{\mathrm{d}r}{\mathrm{d}t}\frac{N_{\mathrm{tot}}}{R}\,. \tag{13}$$

After integration, one obtains the desired space-time relation $r(t)$ by integration of the time spectrum up to t

$$r(t) = \frac{R}{N_{\mathrm{tot}}}\int_0^t \frac{\mathrm{d}N}{\mathrm{d}t}\,\mathrm{d}t. \tag{14}$$

The time spectrum and the space time relation $r(t)$ are shown in fig. 105 (without magnetic field) and in fig. 106 (with magnetic field). The result of this method of calibration is shown in fig. 107. This simulated procedure corresponds, during the real calibration, to have an accurate knowledge of the relationship between the measured drift time and the minimum approach distance of the particle trajectory to the wire. The mean value of the residuals of tracks is then used to correct the measured drift times until the residual distribution is symmetric about zero.

To explore the effect of the electronic threshold, we also simulate the resolution obtained by applying the constant fraction discrimination technique, simulated as a fixed percentage (5%) of the peak of the current signal.

The improvement in the resolution, as shown in fig. 108, demonstrates the importance of the discrimination of the tube signals.

6.1.6 Full and fast simulation

The full simulation reproduces the time output from the drift tube and the ADC response on the charge collected starting from the primary cluster formation as discussed in the sections above. Since the time required for each event is long, we also implemented into the simulation software a fast simulation option.

The spatial resolution is simply obtained through the MC truth for the true wire distance, which is used as the abscissa in fig. 109 to extract the σ for the Gaussian smearing to obtain a realistic position determination of the tube.

The second important quantity, the charge collected on the wire, is simulated in a fast manner by sampling the energy lost from the Urban distribution as in fig. 98, avoiding in this case the charged cluster generation.

In this way the time spent in the tube response simulation results to be negligible when compared with the other part of the software.

6.2 Simulation and reconstruction software

The simulation and reconstruction code for the STT is fully integrated in the $\overline{\mathrm{P}}$ANDA code framework `PandaRoot` [84]. $\overline{\mathrm{P}}$ANDA shares the base classes of a wider framework called `FairRoot` [85] with other FAIR experiments (CBM [86], HADES [87], R3B [88]) and adds its own specific tasks. In this section, a quick overview of the software framework will be given, with particular attention to the STT related code. The software and the procedure used to perform the tests which will be reported in sect. 7.1 will be addressed.

6.2.1 The framework

The `FairRoot` framework is based on the Virtual Monte Carlo (VMC) [89,90], a tool developed at CERN by the ALICE Collaboration, which allows the user to change the engine for the transport of particles in matter (`geant3`, `geant4`) at run-time without the need to change the input/output structure and to adapt the geometry description of the detector. The VMC classes decouple the user classes from the Monte Carlo classes and act as an interface allowing the interchange of the Monte Carlo codes.

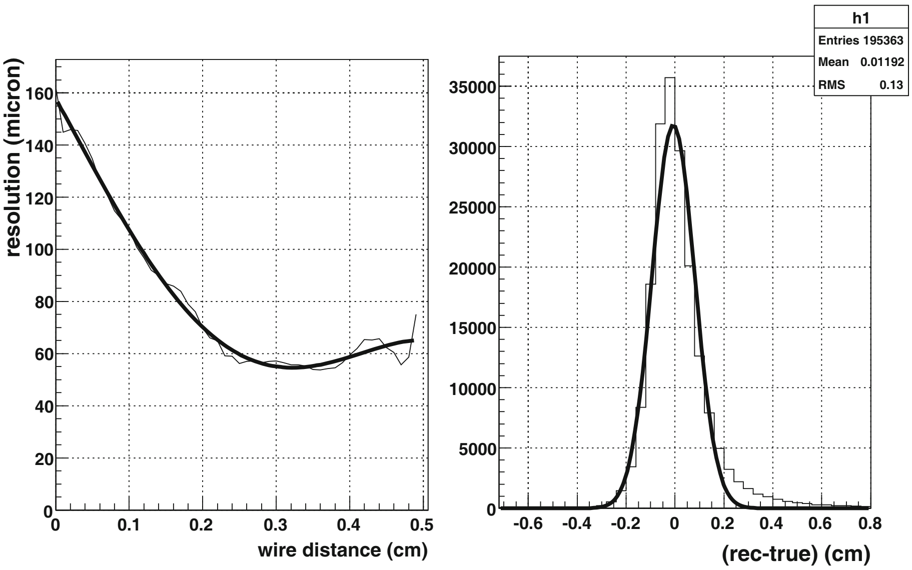

Fig. 107. Simulated average residual width as a function of the track distance from the wire (left) and residual distribution of (reconstructed-true) wire distance. The bold line is the smoothing polynomial.

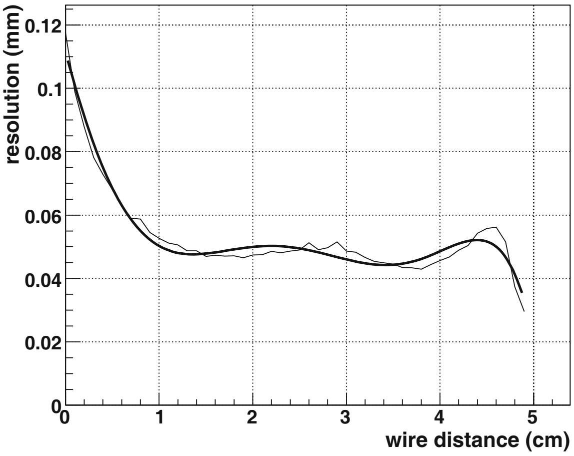

Fig. 108. As in fig. 107 with a constant fraction electronic discrimination.

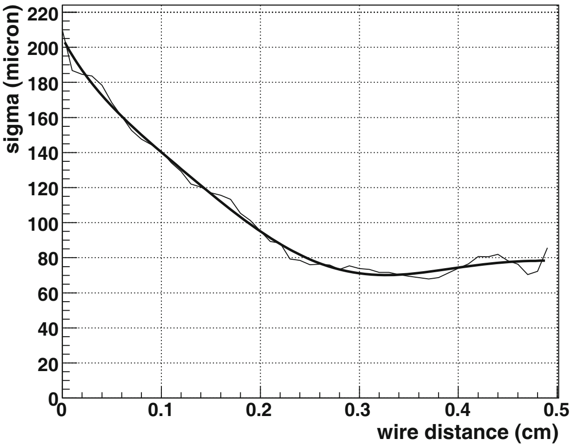

Fig. 109. Standard deviation corresponding to the residual width resolution of fig. 107 (left).

This grants high flexibility: the user can change the implementation of the detector and the algorithm of reconstruction and/or analysis independently from the core code.

The following tools are made available to the user by the framework, in addition to the VMC and ROOT specific tasks (see fig. 110):

- specific simulation and reconstruction classes for the detectors;
- I/O Manager based on ROOT TFolder, TTree and TChain;
- geometry readers: ASCII and ROOT (also CAD files converted to ROOT are usable);
- track follower (GEANE[3] [91]);
- event display based on TEve;
- database for geometry and parameters handling.

6.2.2 The STT simulation and reconstruction

A full simulation chain can be characterized by four main steps: simulation, digitization, reconstruction and analysis. In this section only the simulation and reconstruction code, which provides the tracks used for the analysis, will be addressed exhaustively, while the digitization will only be mentioned since it has already been described in sect. 6.1. The STT specific classes are all contained in the `stt` directory of `PandaRoot`.

---

[3] GEANE is a track follower distributed within the `geant3` package. It is written in FORTRAN and a C++ interface has been developed in `FairRoot` and is used also in the extrapolation step of the Kalman fit.

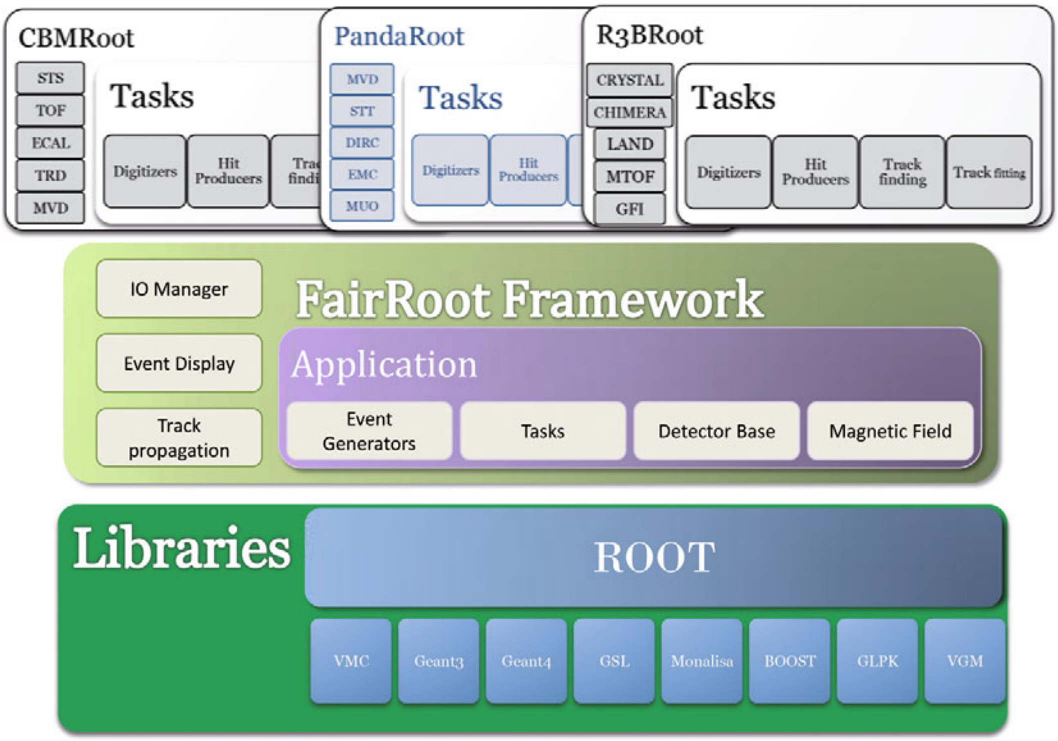

Fig. 110. Structure of the `FairRoot` framework with classes and applications.

Simulation and digitization

During this step, realistic data, resembling the ones that will be available from the operating system, are generated, ready for the reconstruction. It can be divided in two parts, concerning, respectively, the tracker setup and its response to the passage of the particles.

The *detector description* is contained in the `PndStt` class, where the geometry is loaded and the sensitive material is set to collect signals from charged particle transversing it. The straw tubes are built and positioned in an ASCII geometry file; for each tube, the coating, the filling gas mixture and the wire materials are implemented. The passive elements of the tube such as the plugs have not been implemented yet. On the other side, the passive support elements, which surround the central tracker, are present. It is however foreseen to insert all the information on passive elements in the future. Moreover, since the presence of many details will slow down the simulation, it is foreseen that the final geometry description will contain only *average* materials to take into account the correct material budget but be fast enough to grant good time performances. At the simulation stage the geometrical parameters of the tube are saved in the parameter file in order to be retrievable at any stage of the reconstruction.

After the collection of MC points from charged particles, the detector response of the STT is simulated as described in sect. 6.1 during the *digitization* step which provides the collection of realistic hits. These hits contain the information on the drift radius and the energy deposit: it must be pointed out that actual hits coming from the detector will contain only the time information together with the deposited energy, but in the present code the conversion from time to drift radius, which will be later part of the reconstruction, is inserted directly in the simulation of the single straw response (*i.e.* there is no separation between a “digi”, with the time information, and a“hit” with the reconstructed drift radius).

Reconstruction

In a tracking detector, the aim of the reconstruction is to collect the hits, assign them to the different track candidates and then fit the obtained track candidates to get the momentum of each particle. The STT does not provide the x, y, z spatial coordinates of the point where the particle passed. When a tube is hit by a particle, the only available information for the track reconstruction is the measured drift radius, together with the position and orientation in space of the tube itself. A specific track finding (described in sects. 6.2.3 and 6.2.4) and fitting (described in sect. 6.2.5) procedure has been developed relying only on this information. This procedure takes place through a chain of tasks, each one performing operations at event stage. Different packages devoted to the global tracking are available in `PandaRoot` [84,92–94]: only the procedure and the code used to obtain the results presented in sect. 7.1 will be described in sects. 6.2.3 and 6.2.5.

A dedicated pattern recognition for secondary tracks, *i.e.* tracks whose origin is far from the interaction point, is under development and will be described in sect. 6.2.4.

6.2.3 The pattern recognition for primary tracks

The track finder procedure for primary tracks crossing the STT detector is divided in several steps:

- track finding of the MVD stand-alone;
- track finding starting from the STT hits only;
- extension using also the MVD hits;
- extension in the forward region using the GEM hits;
- "cleanup" procedure to remove spurious tracks produced by the high interaction rate of $\overline{\text{P}}$ANDA.

MVD local track finding

The MVD stand-alone pattern recognition divides the problem in a circle fit (in the xy-plane) and a linear fit (in the arc length *vs.* z-coordinate plane). The circle fit is performed using the projection of the MVD hits to a Riemann sphere and fitting a plane through them. After this, the parameters describing the plane can be translated into the track parameters in the xy-plane [95].

Track finding starting from the STT hits

The pattern recognition for the track identification proceeds in two steps, using at first the axial straws, then the skewed straws.

In the first step only the hits of axial wires are used. The x and y position of the wires and the drift radius define a small circumference in the xy-plane (drift circles) to which the particle trajectory is tangent (see fig. 111), The following conformal transformation,

$$U \equiv \frac{x}{x^2+y^2} \qquad V \equiv \frac{y}{x^2+y^2},$$

is applied to the hit drift circles. New drift circumferences are obtained in the UV space. The particle trajectory, a circle passing through the origin in the xy-plane, transforms into a straight line in the UV-plane. A considerable mathematical simplification is obtained in this way since the problem reduces to finding straight line trajectories tangential to drift circles (see fig. 112). The Pattern Recognition proceeds by finding clusters of hits in the UV-plane belonging to a straight line. The search starts from hits belonging to the more external STT axial layers where the hit density is lower. A classical "road-finding" technique with a simple proximity criterion is used and a first fit to a straight line is attempted as soon as the cluster contains a minimum number of hits. The fit is performed minimizing a "cost function" which is the sum of the absolute values of the residuals (in the usual χ^2 it is the sum of the squares of them). This minimization is performed using a Mixed Integer Linear Programming (MILP) algorithm that is usually much faster than the normal χ^2 minimization. If a straight line is successfully fitted, a search among all unused STT axial hits is performed and hits close enough to it are associated and a new candidate track is formed. After this stage three of the five parameters of the track helix are known (the radius R, the position of the helix center in the xy-plane).

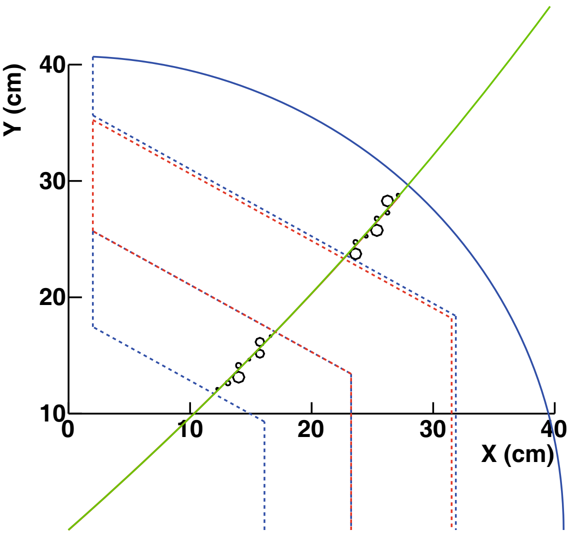

Fig. 111. Track generated with Monte Carlo at the interaction vertex; the small circles are the isochrone circles of the STT axial straws in the xy-projection; the track is the circle tangent to all drift circles. The green curve is the Monte Carlo truth, the red curve (almost not visible because essentially it coincides) is found by the pattern recognition.

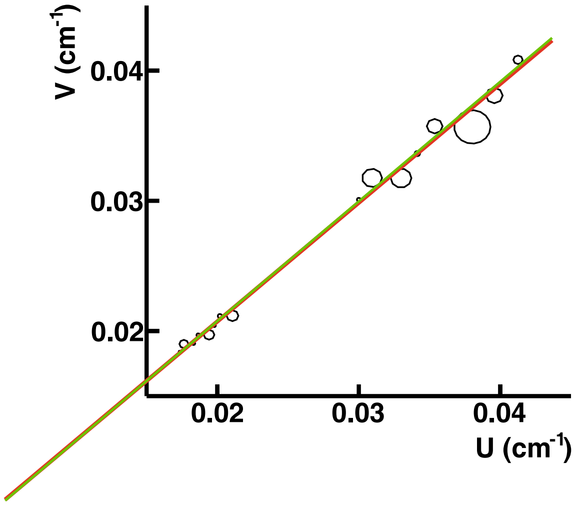

Fig. 112. The same track of fig. 111 plotted after the conformal transformation. The track circle transforms into a straight line, while the drift circumferences transform into circumferences. The track straight line is still tangent to all drift circles. The green line is the Monte Carlo truth, the red line (almost not visible because essentially it coincides) is found by the pattern recognition.

In the second step the remaining two parameters of the helix are determined by using the hits of the skewed STT straws. The "drift cylinder" is defined as an imaginary

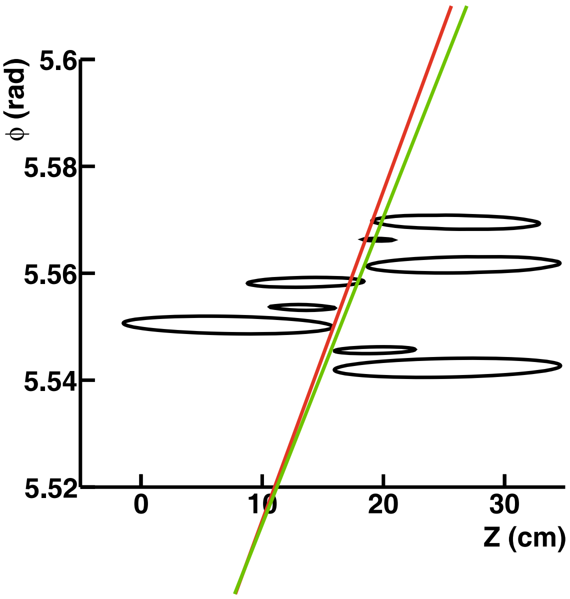

Fig. 113. The same track of fig. 111 plotted in the ϕ-Z plane. The approximate ellipses are the intersection of the skewed straws with the cylinder on which the helix trajectory lies. The track straight line is tangent to all skewed straw drift ellipses. The green line is the Monte Carlo truth, the red line is found by the pattern recognition.

cylinder coaxial to the straw wire and with radius equal to the drift radius. Only the hits of those skewed straws are considered whose drift cylinder intersects the cylinder on which the helix lies (see fig. 113). This intersection is approximately an ellipse. The helix trajectory is a straight line on the lateral surface of the helix cylinder ($\equiv$ ϕ-Z plane) with the equation

$$\phi = KZ + \phi_0,$$

and tangent to the ellipses of the skewed straws. K and ϕ_0 are the remaining two parameters of the helix. At this stage in the algorithm ϕ_0 is constrained with the requirement that the track originates from $(0, 0, 0)$ in the xyZ reference frame. A fit with with a MILP algorithm gives K. Possible spurious skewed straw hits are rejected if their distance from the fitted straight line exceeds a certain limit. Then a track candidate is constructed, consisting of all STT associated axial and skewed hits.

It should be mentioned here that an extension of this scheme is being written presently and although it is only in a preliminary stage it looks very promising and it will be included in the future pattern recognition. The peculiarity of the new scheme consists in the use of the SciTil hits at the very first stage of the algorithm. Since SciTil hits are very fast ($\approx 100\,\text{ps}$) the jitter of such pulses will be dominated essentially by the length of the trajectory of the charged particles from the interaction vertex to the SciTil detectors. This has been estimated to be of the order of 1 ns. Consequently such hits will be only very marginally affected by pileup of previous events and they will be very useful both in giving the time of production of an event and in signalling that the charged track associated to them is not spurious. That is why in the new scheme the pattern recognition algorithm starts clusterizing hits from the SciTil hits, in the conformal space. Significant CPU time gains and spurious track rejection are expected with this strategy.

STT + MVD track finding

In this stage all the track candidates of the previous step are considered. First the trajectory circle in the xy-plane, found as described above, is used to associate hits of MVD tracklets close to it. The MVD tracklets were previously found by the MVD standalone pattern recognition. The fit of the trajectory circle is performed again, including also the newly associated MVD hits and releasing the constraint that the trajectory goes necessarily through $(0, 0, 0)$. By using the improved helix parameters in the xy plane (better radius and center of the trajectory cylinder), skewed straw hits are associated to the candidate track in a similar way as in the previous step. The fit in the ϕ-Z plane is performed again using these skewed straw hits plus the MVD hits. The new trajectory parameters are used to eliminate some spurious skewed straw hits and/or to include some new axial straw hits not yet included before. In this way the final track candidates are obtained. Finally an attempt is made to find tracks starting from the MVD tracklets found by the MVD stand-alone pattern recognition. MVD tracklets not yet used in the previous steps and containing at least three MVD hits, are fitted with a straight line in the conformal UV-space first and then in the ϕ-Z plane with the fast MILP minimizer. A new track candidate is added only if the helix trajectory intersects the STT region. The found trajectory is used to collect straw hits, both axial and skewed, lying close to it.

The GEM extension

Once the MVD + STT track finder has been run and a track hypothesis is available, the GEM hit contribution can be exploited in the angular region where the tracks can cross both MVD/STT and the GEM detectors ($7° < \theta < 21°$). A simple extrapolation of the tracks using the track follower GEANE from the last point of the central tracker on each plane of the GEM detector is the starting point for adding the GEM hits to the tracks. For each extrapolation the distance between the propagated point and the error associated to it are calculated. The hit is associated to the track if the distance is within 5σ. The GEM detector is composed of three stations, with two sensors each. Every sensor has two views. When more than one track hits the GEM stations, combinatorial background is present and has to be suppressed. A specific test has been written to take care of this: the two sensors in each station are overlapped and only when a hit has its counterpart on the other sensor, within 1 cm, is considered *true*, otherwise it is flagged as *fake*. Once a true hit pair has been found, the GEM channels of such hits are excluded by further combinations, namely all the hits on the same sensors defined by the same channels are considered as combinatorial background. Only true hits are used in the next steps and possibly assigned to tracks. The tracks are eventually refined by requiring that each GEM hit is associated to at most one track and each track is associated to at most one hit on every measurement plane. Once the hits have been attached to a track, a dedicated Kalman filter, specifically implemented inside the GEM extension code, is applied on that track, using the measured GEM hits: this is necessary because the extrapolation with GEANE is always performed with the mass hypothesis of the muon and this could lead to an underestimation or overestimation of the energy loss between the GEM stations, causing the propagated point to be too far from the measured one. The application of the Kalman filter forces the track to stick to the measured hits and allows to retrieve some hits formerly missed due to the wrong mass hypothesis.

"Cleanup" procedure to remove spurious tracks

The average interaction rate of 20 MHz of $\overline{\mathsf{P}}$ANDA and the maximum drift time of the STT straws of 200 ns pose the problem of the presence of a large number of spurious hits in the STT system (spurious ≡ real hit belonging to a different event). To every interesting physics event there will be superimposed some STT hits belonging to previous or later events produced by the overwhelmingly large $\mathrm{p\overline{p}}$ total interaction. This will cause an increase of the number of spurious tracks found by the pattern recognition. A spurious track is formed by spurious hits and its characteristic, most of the times, is the absence of MVD hits and also gaps in the continuity of STT hits. The former happens because the time duration of a MVD hit is typically 10 ns and so those hits disappear when the spurious event is late or early by more than 10 ns. The latter happens because some STT (early) spurious hits have too small drift time or (for the late spurious hits) too large drift time and they fall out of the time window of the physics event leaving "holes" or gaps along the spurious track.

This section briefly describes the "cleanup" algorithm applied after the pattern recognition. This procedure is also useful to reject the (low percentage) ghost tracks inevitably produced by the pattern recognition even in the absence of spurious hits. The "cleanup" procedures has been used in the studies of the physics channels described in sect. 7.2.

The algorithm begins using the helix track parameters found by the pattern recognition. If there are no MVD hits associated to a track candidate going through the MVD system, this is a typical spurious or ghost track and the candidate is rejected. If gaps with more than 1 hit missing in the STT region are found, the track candidate is rejected.

In order to check the effectiveness of the cleanup procedure, a dedicated version of the $\overline{\mathsf{P}}$ANDA Monte Carlo was implemented, with the spurious hits superimposed at an average rate of 20 MHz. Presently the cleanup procedure is not in its final version yet. The geometric accuracy in the determination of how many hits should be in a track is still not refined and consequently it "cleans" too much, lowering the detection efficiency of the true tracks down to around 90%. In the near future this task will be refined and brought to conclusion.

6.2.4 The pattern recognition for secondary tracks

Events generated from the antiproton proton annihilation may produce neutral, long living particles, like Λ or K^0, which travel a while before decaying (for example the $c\tau$ value for the Λ is ~ 7.9 cm). The peculiarity of these decays is that the charged particles coming from them do not originate from the interaction point, but from a displaced position. Even though most of the secondary vertices will fall within the MVD, the neutral particles can as well decay outside it, thus demanding for good reconstruction capabilities of the other tracking detectors (STT, GEM). The secondary track finder is still under development.

General concept

At present, the secondary track finder uses only the STT hits, but it will be extended to include also the MVD and GEM information. The final version of the global pattern recognition of secondary tracks in the target spectrometer will resemble the one for primary tracks and will consist in the following steps:

- MVD local track finding,
- STT local track finding for secondary tracks,
- MVD + STT track finding,
- GEM extension.

Since the MVD + STT pattern recognition and the GEM extension for the primary tracks do not require that the particle comes from the interaction point they can also be used for secondary tracks, with minor modifications. The GEM extension code can be used also for tracks hitting only the STT and GEM, without MVD hits. Moreover, the secondary track finder will run over the hits which are left unassigned by the primary track finder and which most likely will belong either to secondary tracks or to background tracks. The main difference between the primary track finder and the secondary track finder is the inclusion of the interaction point as a constraint for the primary which cannot be used for the secondary tracks.

Secondary track-finding procedure

Currently, the procedure starts from the xy-plane to find the coordinates of the center of the track and its radius (x_c, y_c, R), and subsequently finds the remaining two parameters of the helix, $\tan(\lambda)$ and z_0. It is divided in several steps:

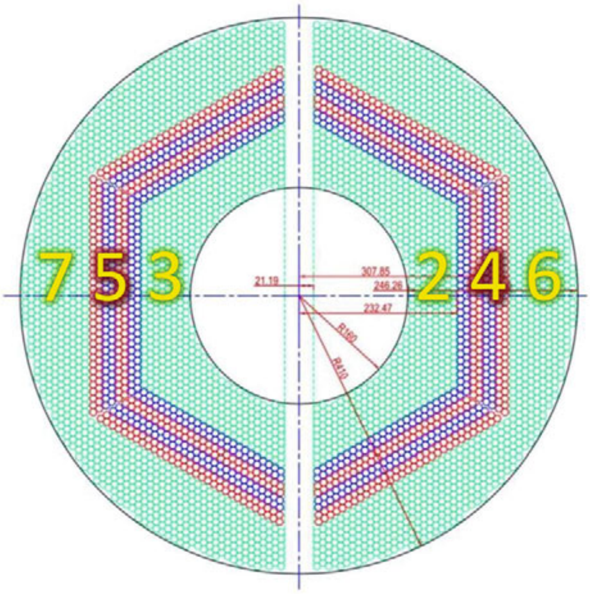

Fig. 114. The numbers correspond to the different sectors in which the STT is divided. 2 and 3 are inner parallel tubes, 4 and 5 are skewed tubes and 6 and 7 are outer parallel tubes.

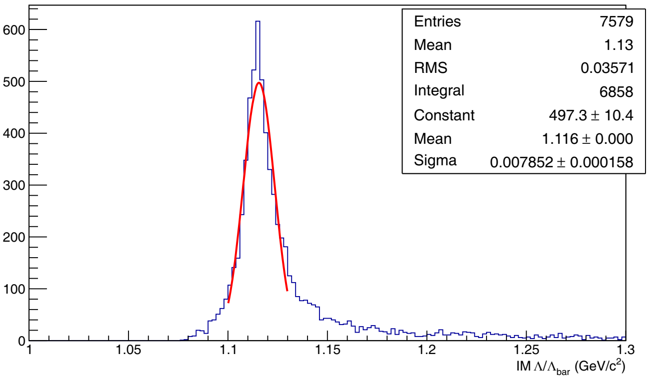

Fig. 115. Λ and $\overline{\Lambda}$ invariant mass for tracks which cover the inner parallel tube sector, the skewed sector and the outer parallel sector.

- *clustering:* the STT hits are assigned to different sectors of the detector depending on their position; a first division is between left and right hits (which refers to the two half cylinders of the STT) and a second separation is made among inner parallel tubes, skewed tubes and outer parallel tubes, as shown in fig. 114.
  The clusterization is performed directly on the tubes without taking into account the drift radius. If the xy distance between the centers of two tubes is less than 1.2 cm the hits are collected in the same cluster.
- *xy fitting:* when possible, the clusters are coupled in order to have one inner cluster and one outer cluster of parallel tubes and they are fitted in the xy-plane. The fit makes use of the conformal transformation, and considers the drift radii of the hits. Since the track cannot be assumed to go through the interaction point, the positions of the tubes are translated by the coordinates of the hit tube with the smallest drift radius. This is necessary since the conformal transformation maps circular tracks into straight lines only if they come from the origin and with the translation it is assumed that the track is passing through the center of the tube. When the association inner/outer cluster is impossible, the single cluster is fitted alone.
- *z fitting:* Once the xy parameters of the track are found, the wires of the skewed tube are projected onto the xy-plane. The ones which cross the trajectory circle are associated to the track. Their intersections are computed considering the drift radius and the left/right ambiguity: for this reason two solutions for each skewed tube are possible. For all the solutions the track length and the corresponding z-coordinate are computed and are plotted on a z *vs.* track length plane. Only the true intersections lie on a straight line. They are identified with a Hough transformation [96] and the two remaining helix parameters are found by means of a straight line fit.

First test and future developments

A test of this procedure has been made on 21500 $\mathrm{p\overline{p}} \to \Lambda\overline{\Lambda}$ events. They were generated with the `EvtGen` [97] generator with an antiproton momentum of $4\,\mathrm{GeV}/c$. All the Λ were forced to decay into $\mathrm{p}\pi^-$ and the $\overline{\Lambda}$ into $\overline{\mathrm{p}}\pi^+$. No forward peaking in the angular distribution was taken into account, but phase space was used as decay model. The tracks were simulated, digitized and finally reconstructed with the secondary track finder. Since this pattern recognition is still in its early stage, a full analysis of the channel was not possible. All the results were obtained without the MVD and GEM detectors, no Kalman filter was applied to the tracks and no kinematic fit was used. Further developments in the track finding and the use of the surrounding detectors will improve significantly the results. Once the information of these detectors will be used, a real event generator with the proper angular distributions will be adopted to evaluate the final event reconstruction efficiency.

The tracks reconstructed with the secondary pattern recognition were associated to pion and proton tracks using the MC particle identification. An algorithm to compute the distance among the two helices was then applied to each couple of $\overline{\mathrm{p}}\pi^+$ and $\mathrm{p}\pi^-$ tracks in order to find the point of closest approach. This point is used as the reconstructed vertex and the tracks are backtracked there. The invariant mass for the tracks traversing the inner parallel sector, the skewed sector and the outer parallel sector is shown in fig. 115. The corresponding $\Delta\mathrm{p}/\mathrm{p}$ for total, transverse and longitudinal momenta for both the protons and pions are plotted in figs. 116 and 117.

As already mentioned, the $\mathrm{p\overline{p}} \to \Lambda\overline{\Lambda}$ events have been generated a phase space distribution. The following considerations rely on this and thus the efficiencies and resolutions are not the ultimate ones. The number of Monte Carlo vertices which leave at least one track in the STT is

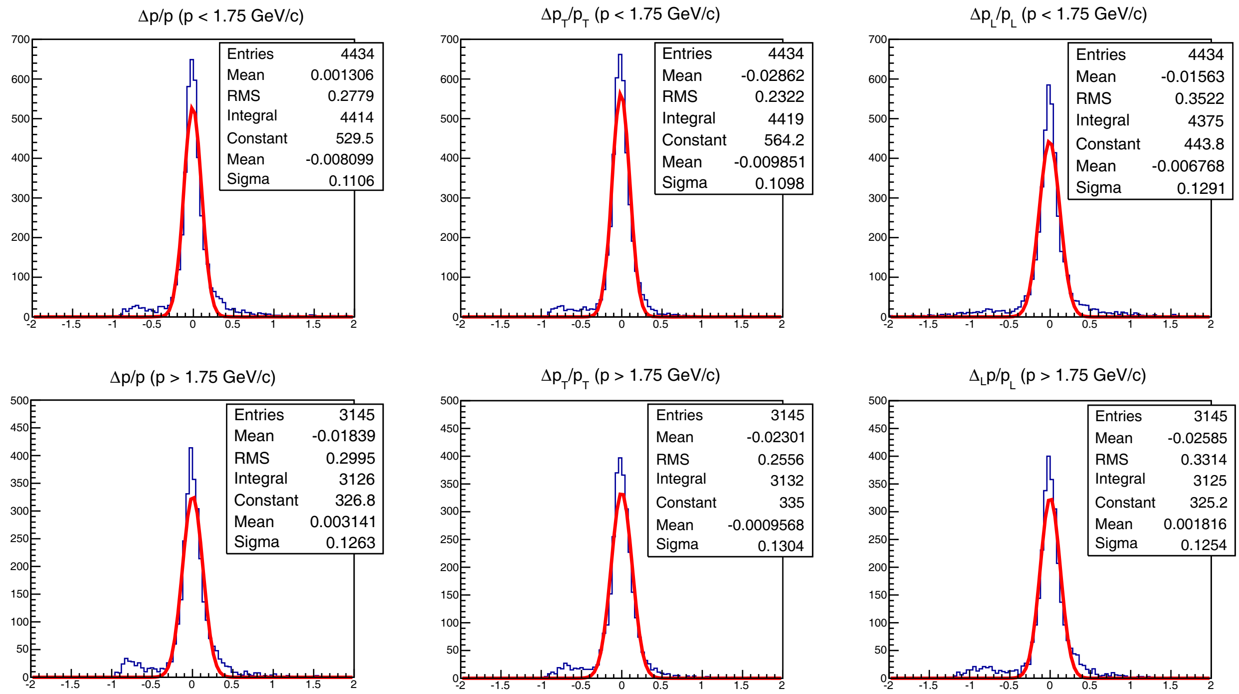

Fig. 116. $\frac{\Delta \mathrm{p}}{\mathrm{p}} = \frac{RECO_p - MC_p}{MC_p}$ for the protons and antiprotons which form the Λ and $\overline{\Lambda}$ of fig. 115. The first column plots the total momentum, the second column the transverse momentum and the third column the longitudinal momentum. The two rows represent the low-momentum (top) and high-momentum (bottom) particles.

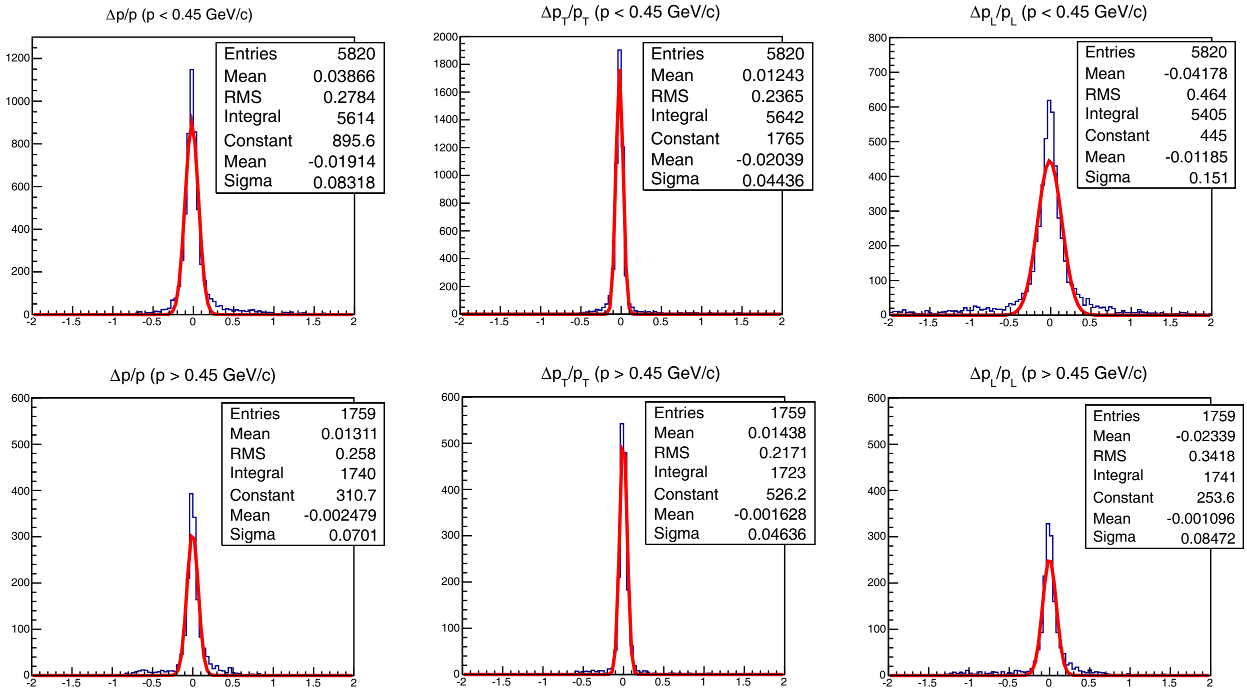

Fig. 117. $\frac{\Delta \mathrm{p}}{\mathrm{p}} = \frac{RECO_p - MC_p}{MC_p}$ for the negative and positive pions which form the Λ and $\overline{\Lambda}$ of fig. 115. The first column plots the total momentum, the second column the transverse momentum and the third column the longitudinal momentum. The two rows represent the low-momentum (top) and high-momentum (bottom) particles.

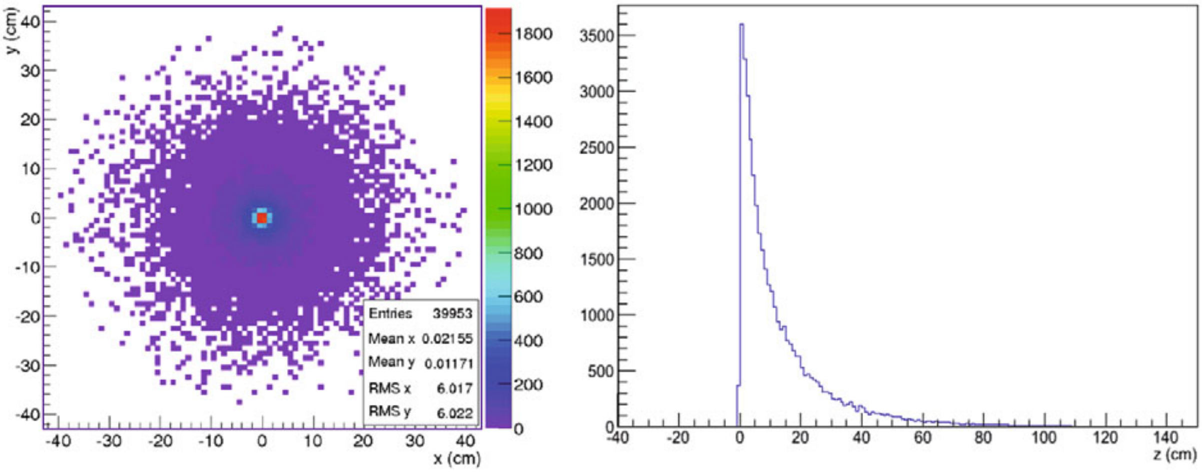

Fig. 118. Radial (left) and z (right) distribution of the MC vertices leaving at least one track in the STT.

39953 out of 43000 generated, with a geometrical distribution shown in fig. 118. Among these, 28303 vertices leave two tracks in the STT and thus their invariant mass can be reconstructed in the STT alone. The fraction of events where both Λ and $\overline{\Lambda}$ are reconstructable inside the STT is not considered here since the model used for the event generation does not correctly populate the phase space.

In fig. 115, 5433 entries fall within 3σ (corresponds to 19% of the $\overline{\Lambda}/\Lambda$ which leave two tracks in the STT). The use of *all sectors* tracks will increase the efficiency. It is clear that there is room for further improvements: starting from the *three sectors* tracks, for which a fine tuning of the cuts and the implementation of additional functions to assign the hits which are left unassigned from the present procedure will improve the efficiency. In addition to this, a lot of events also leave hits in the MVD and in the GEM. As a result, their contribution must be taken into consideration to refine the results. In particular the GEM will have great importance when the realistic events will be considered. The momentum resolution can be improved with the application of the Kalman filter and of the kinematic fit. The invariant mass resolution itself is not yet the best achievable. For example, the use of a kinematic fit will lower the tail in the invariant mass distribution. In conclusion: Improvements in both efficiency and resolution are expected for the secondary track finder from the inclusion of the contribution of the surrounding detectors and from the application of special fitting techniques.

6.2.5 The Kalman filter

The track fitting step is performed through the Kalman filter procedure, using the hits coming from MVD, STT and GEM where available and, as starting position and momentum, the values inferred by the pattern recognition backtracked to the point of closest approach to the interaction point in case of primary particles. In this section a short summary of the Kalman fit procedure [98, 99] is reported. A more detailed description of this topic can be found in [100] and [101] and references quoted therein. The package devoted to the Kalman fit procedure is `genfit` [102].

The Kalman fit is an iterative procedure which, unlike global methods such as the helix fit, takes into account the energy loss, the magnetic field inhomogeneities and the multiple scattering. The aim of the Kalman filter is to find the best estimation of the true track point f_i on the i-th detector plane by minimizing the χ^2,

$$\chi^2(\boldsymbol{f}) = \sum_i [(\boldsymbol{e}_i[\boldsymbol{f}_{i-1}] - \boldsymbol{f}_i)\boldsymbol{W}_{i-1}(\boldsymbol{e}_i[\boldsymbol{f}_{i-1}] - \boldsymbol{f}_i)] + (\boldsymbol{x}_i - \boldsymbol{f}_i)\boldsymbol{V}_i(\boldsymbol{x}_i - \boldsymbol{f}_i), \qquad (15)$$

where $\boldsymbol{e}_i[\boldsymbol{f}_{i-1}]$ is the extrapolated point on the i-th detector plane starting from the true point on the $(i-1)$-th plane and $\boldsymbol{x}_i$ is the measured one; $\boldsymbol{W}$ and $\boldsymbol{V}$ are the weight matrices containing, respectively, the tracking and the measurement errors. The Kalman filter is a method to minimize the χ^2 of eq. (15) to find the true points $\boldsymbol{f}_i$. Usually this is done through three steps [103,104]

- *Extrapolation*: the status vector on the i-th plane is predicted starting from the knowledge gained up to the $(i-1)$-th plane.
- *Filtering*: this is a preliminary evaluation of the track parameters on plane i, making a "weighted mean" between the measured and the predicted values on the same plane.
- *Smoothing*: on each plane, the Kalman point solution of the second step is refined to get the final estimate of its value. This last step is often substituted by an alternative option: the so-called "backtracking", which consists in repeating the first two steps while extrapolating in backward direction, from the last point of the track to the first one.

The Kalman filter algorithm is a standard tracking procedure, but its use in the case of the STT has some peculiarities: the extrapolation method, the use of virtual detector planes and the z reconstruction.

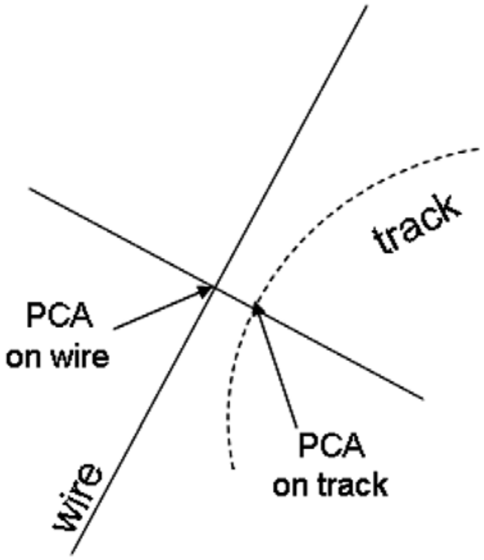

Fig. 119. Sketch of the positions of the point of closest approach (PCA) on the track and on the wire.

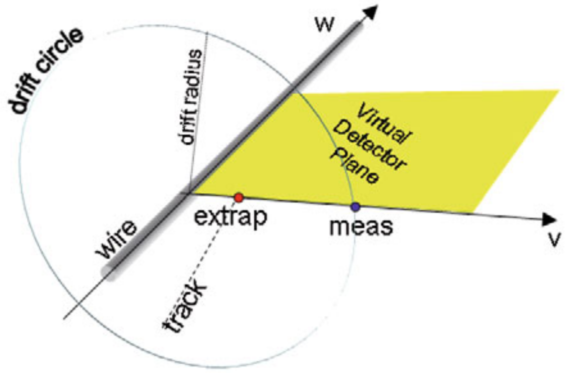

Fig. 120. Sketch of the virtual detector plane at the point of closest approach to the wire.

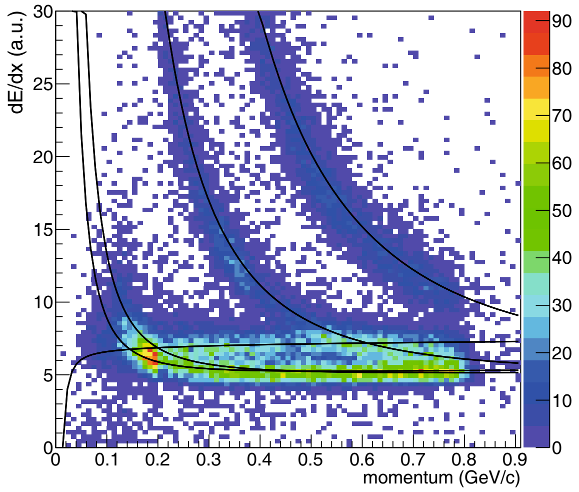

Fig. 121. Distribution of $\mathrm{d}E/\mathrm{d}x$ truncated mean values *vs.* reconstructed momentum for electrons, muons, pions, kaons and protons. The superimposed lines are the mean value of the bands of fig. 122. The procedure to find them is described in the text.

The track follower used during the extrapolation step is GEANE. The standard ways of extrapolation made available by this tool are the one to a volume, to a plane and to a track length. Though the extrapolation to a plane was useful and easily applied to planar detectors as MVD and GEM, it was not suitable for the STT. None of the standard functions was and so a fourth method has been developed: The propagation to the point of closest approach to a line or to a space point. In particular, for the STT, the propagation to the point of closest approach to the straw wire is used (see fig. 119). This method combines the propagation to a track length and to a plane: An extrapolation is performed, calculating the distance from the wire step by step, the minimum is found and a plane containing the wire and the point of closest approach is built there (see fig. 120). Eventually a standard extrapolation onto this plane is made. As already pointed out, the straw tube is not a planar device, thus no real measurement plane can be identified. The chosen detector planes are virtual and are built during the extrapolation step. Each plane is spanned by the axes v and w as shown in fig. 120: The w-axis is along the wire and the v-axis orthogonal to it, through the found point of closest approach. The z-coordinate of each single hit is unknown at this stage since no reconstruction of this coordinate has been done so far and it is not measured directly. It is reconstructed by the Kalman filter using the skewed tubes. In fact, given a starting position and direction (which contains also the z information) the extrapolation to the point of closest approach to the skewed tubes takes into account their position in tridimensional space and thus, indirectly, the z-coordinate. When performing the filtering step on the virtual planes associated to the skewed tubes, all the track parameters are modified at the same time, taking into account the z information provided by the skewed tubes themselves.

6.2.6 The $\mathrm{d}E/\mathrm{d}x$ simulation

The STT can also contribute to the particle identification in the low energy region, by means of the specific energy loss measurements. For gaseous detectors the particle identification is obtained from the simultaneous measurement of the $\mathrm{d}E/\mathrm{d}x$ and the momentum. For a $1\,\mathrm{GeV}/c$ track, the STT detector allows about 25 energy loss measurements. Although this is usually considered rather low for a good particle identification, some capability exists in the low energy range. Figure 121 shows the distribution of specific energy loss for different particles plotted *versus* the momentum. The various regions have been identified as bands, with a mean value and an amplitude, as shown in fig. 122, using a sample composed of five types of charged particles (electrons, muons, pions, kaons and protons). They have been simulated, digitized and fully reconstructed in a momentum range between $0.05\,\mathrm{GeV}/c$ and $0.8\,\mathrm{GeV}/c$.

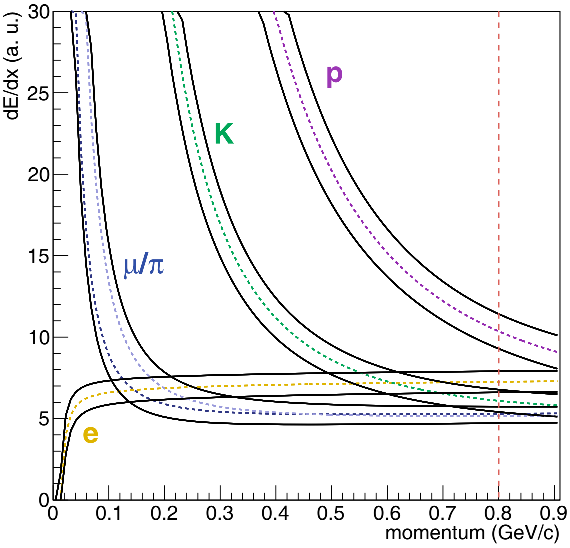

Fig. 122. The bands identifying the regions of dE/dx truncated mean values *vs.* momentum found for the different particles with the procedure described in the text are drawn (the tracks have been fitted by the Kalman filter with the mass hypothesis of muon). The muon and pion bands are highly overlapped due to the similarity in their masses: it is not possible to distinguish between these two particles in a reliable way with this method. The vertical line shows the chosen threshold value of 0.8 GeV/c.

In each tube, the deposited energy was reproduced with a fast simulation tuned to the real data results. The radial path has been reconstructed by the measured drift radius and by the dip angle resulting from the fit. The dE/dx truncated mean value has been calculated with the truncation at 30% in order to cut off the higher dE/dx tail. The momentum has been obtained by fitting the hits from MVD, STT and GEM detectors with the Kalman filter procedure. Since at fixed momentum the dE/dx truncated mean values are nearly Gaussian, the momentum range has been divided in many intervals $\sim$ 30 MeV/c large and for each interval the dE/dx distribution has been fitted (fig. 123): the obtained mean and sigma values as a function of the momentum, whose graphs are shown in fig. 124, have been fitted to obtain the bands. Actually the dE/dx truncated mean distribution at fixed momentum is not purely Gaussian, but has a small tail on the right side. To cope with this, the correct way of handling the fit procedure would be to consider the sum of two Gaussians, each one with its mean and sigma, conveniently weighted. To do so, the following function should be used:

$$p(x) = a \cdot p_1(x) + b \cdot p_2(x), \tag{16}$$

with $a + b = 1$, once $p(x)$ has been normalized. All the parameters $a, b, \mu_1, \mu_2, \sigma_1, \sigma_2$ must be fitted by functions similar to the ones in fig. 124. In the following only the results with the single Gaussian will be shown.

When a particle of unknown mass has to be identified with this method, the dE/dx and momentum are reconstructed and a point is identified in the plot of energy loss as a function of the momentum, where the bands are known. Then, for every particle hypothesis, the Gaussian corresponding to the reconstructed momentum of the track is chosen and it is evaluated at the measured track dE/dx truncated mean. The resulting value, which comes from a standard normalized Gaussian, is the value of the probability density function (p.d.f.) for that hypothesis. Since the momentum is the outcome of the Kalman filter procedure, for which a mass hypothesis has been used, two strategies can be followed: Either the Kalman fit is run on a track with all the mass hypotheses in parallel or the track is fitted with a unique mass hypothesis. In the first case, the particle identification from dE/dx is used just to give the probability that the Kalman mass hypothesis was correct. Only the couples of reconstructed track and particle identification output with the same mass hypothesis are then taken into account (*e.g.*, p.d.f. of the electron hypothesis for the momentum reconstructed with Kalman as an electron, p.d.f. of the muon hypothesis for the momentum reconstructed as a muon and so on as shown in fig. 125). They are normalized to their sum and the highest value gives the conclusive hypothesis. In the second case the track has only one reconstructed momentum and the particle identification is used to determine the mass hypothesis. After this the track should be refitted with the correct mass. Two different sets of bands have been identified.

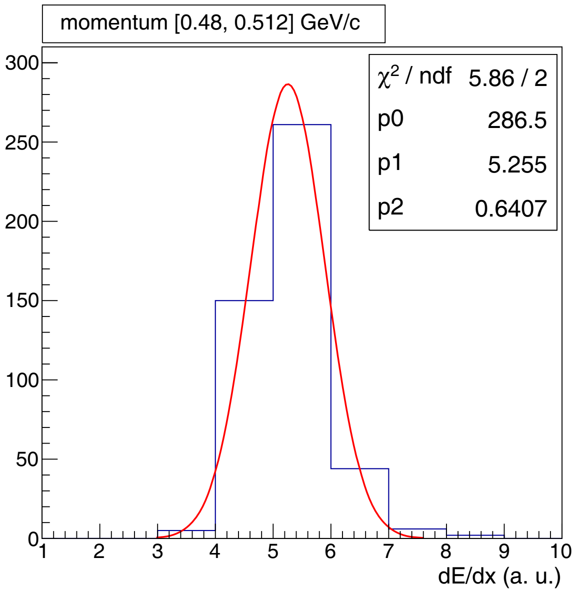

Fig. 123. Example of a dE/dx truncated mean distribution for muon tracks with momentum in the range [0.48, 0.512] GeV/c: it shows a Gaussian shape as expected.

To evaluate the performance of such a particle identification technique, a sample of particles of each kind, simulated with momenta between 0.05 GeV/c and 0.8 GeV/c, has been used. For higher momenta the p.d.f value is set equal to 1 for all the hypotheses, *i.e.* the procedure is not able to identify the particle mass. Each track has been reconstructed with the muon mass hypothesis (default in the code). For each reconstructed momentum, the p.d.f.

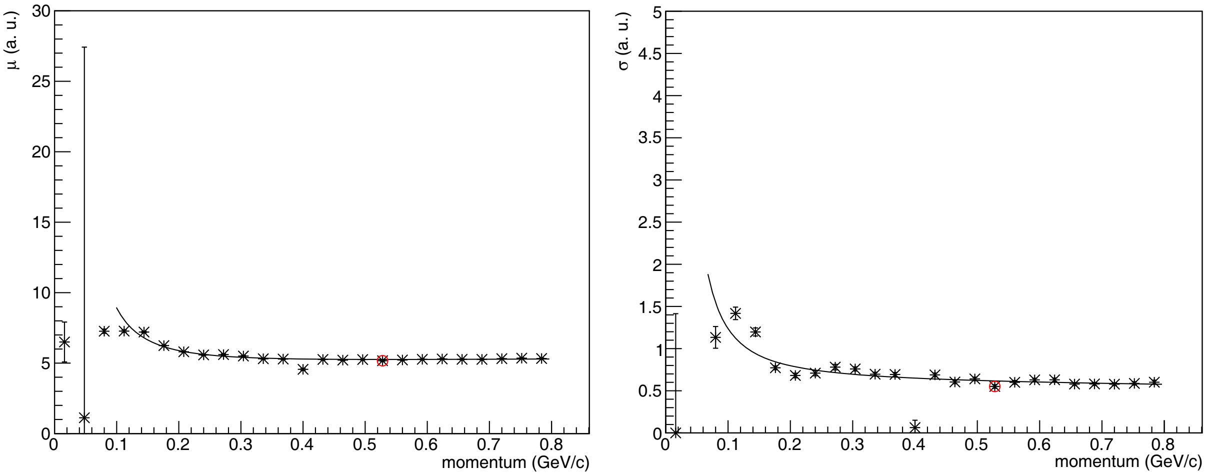

Fig. 124. Plot of the mean and sigma values of the Gaussians as a function of the momentum. The red circles correspond to the values for the momentum interval of figure fig. 123. From the fitting of these graphs the bands of dE/dx truncated mean *vs.* momentum are obtained. The points at the left extremity are not used since the statistics there is too low to perform a reliable fit.

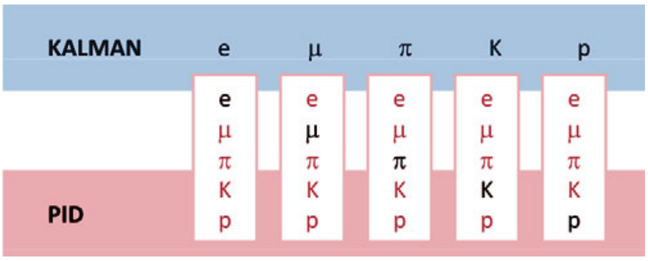

Fig. 125. Sketch of the association between the p.d.f. value from the particle identification (PID) procedure and the Kalman fitted track.

Table 15. Results of the performance test of particle identification: for each row the frequency, in percentages, with which the simulated particle is recognized as electron, muon, pion, kaon and proton is written. Each row percentages sum up to 100%. The correct association is the one on the diagonal. The muon and pion frequencies must be summed, since with this method muons and pions can be hardly distinguished.

		Frequencies of PID (%)				
		e	μ	π	K	p
true part.	e	78.9	5.2	5.6	10.1	0.2
	π	9.0	47.2	40.7	2.9	0.2
	K	22.3	8.0	1.6	65.1	3.0
	p	0.1	[0.01]	0.1	1.0	98.8

values for all the five particle hypotheses are extracted from the dE/dx truncated mean *vs.* momentum. The one with the highest value determines the identified particle: the obtained results are shown in table 15.

The separation power $S = 2\,\Delta E$ between two particles is defined as the distance between the centres of the two bands $\langle E_1\rangle$ and $\langle E_2\rangle$, measured in terms of the standard deviations σ_1 and σ_2 [105],

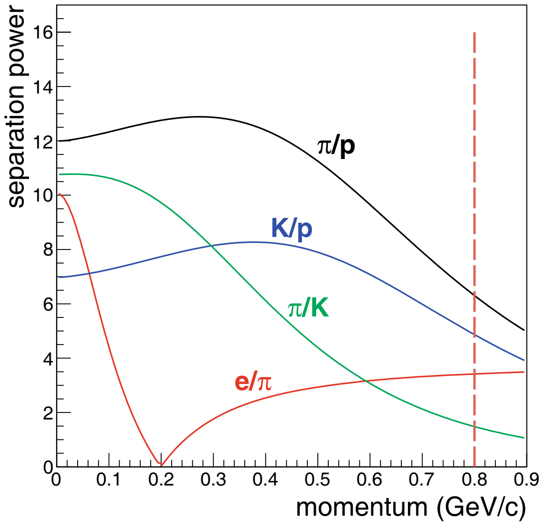

Fig. 126. Separation power in the STT for the bands built with particles all tracked with the same muon mass hypothesis. The vertical line at 0.8 GeV/c is the momentum threshold to perform the particle identification in the STT.

$$\Delta E = \frac{E - \langle E_1\rangle}{\sigma_1} = \frac{\langle E_2\rangle - E}{\sigma_2}\,. \tag{17}$$

Eliminating E from the previous equation and recalculating S, the following separation power is obtained:

$$S = \frac{\langle E_2\rangle - \langle E_1\rangle}{\sigma_1/2 + \sigma_2/2}\,, \tag{18}$$

when $\langle E_2\rangle > \langle E_1\rangle$ or

$$S = \frac{|\,\langle E_2\rangle - \langle E_1\rangle\,|}{\sigma_1/2 + \sigma_2/2}\,, \tag{19}$$

in general, which is shown in fig. 126. This plot demonstrates clearly the capability of the STT detector in the low-energy PID.

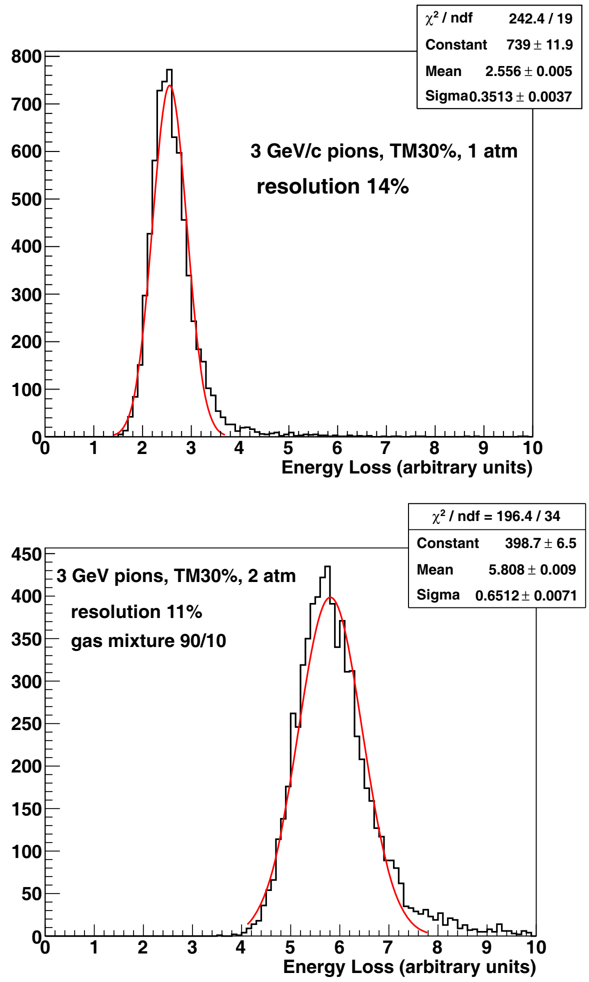

Fig. 127. Energy loss distributions for 3 GeV/c pions in 22 straw tubes. Truncated mean of 30% is applied. Upper figure shows the dE/dx resolution at 1 atm absolute pressure, lower figure at 2 atm: increasing the gas pressure a gain in resolution of about 20% is obtained. Both resolutions have been obtained with a gas mixture Ar (90%)/CO_2 (10%).

Effect of pressure and gas mixture

A simulation has been performed to investigate the relationship between gas pressure and dE/dx resolution, for two different gas mixtures. The test has been performed with a simple set-up, with 22 samplings of 3 GeV/c pions from a single straw tube and using the truncated mean at 30%. Figure 127 and 128 show the different dE/dx distributions with a gas mixture of Ar and CO_2 in different ratios and at different pressures. The change in CO_2 percentages does not produce observable effects, while the change in operating pressure improves the specific energy resolution by about 20%.

7 Straw tube tracker performance

7.1 Performance studies with single tracks

In order to study the performances of the designed $\overline{\text{P}}$ANDA Straw Tube Tracker in terms of geometrical acceptance of the layout, momentum resolution and reconstruction efficiency, systematic Monte Carlo studies have been performed with single track events.

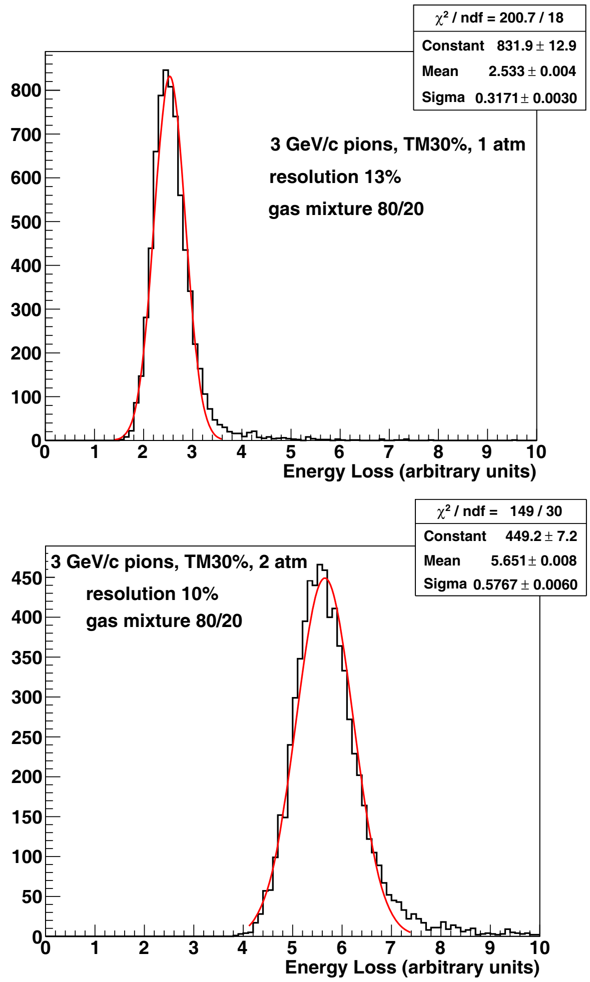

Fig. 128. The same plots of fig. 127, but with a gas mixture Ar (80%)/CO_2 (20%).

7.1.1 Simulation environment

A summary of the choices made to perform the tests is given here.

The target spectrometer was simulated to have a realistic material budget. Specifically, the list of the simulated subdetectors contains: MVD, STT, Electromagnetic Calorimeter, TOF detector, Muon Chambers, Cherenkov detectors and forward GEM stations. In addition also the passive elements have been placed in order to take the correct amount of material into account: The Solenoid Magnet, the Target and Beam Pipes.

The full magnetic field map has been used to account for magnetic inhomogeneities.

Different event generators are available in `PandaRoot`. For the single track tests, the `BoxGenerator` has been used, with the possibility to select ranges of momentum, both magnitude and direction, in addition to particle type and multiplicity.

The digitization step has been performed only for MVD, STT and GEM in order to save computation time, since the studies would have been dedicated only to the Central Tracker. It was performed in a realistic way to get a reliable detector response and the hits for the reconstruction.

All realistic pattern recognitions were used, with no information taken from the Monte Carlo truth. The full chain of track finders was adopted. After the track finding, the Kalman filter was applied to the tracks, using the package `genfit` [102] (see sect. 6.2.5). The starting point for the Kalman procedure was chosen by extrapolating the tracks fitted with the helix to the point of closest approach to the interaction point. The xy-plane was chosen as starting plane and only one iteration was performed in the fit procedure; this means that the filter step was performed on the plane corresponding to each measurement, both in the forward and in the backward direction.

7.1.2 Studies on the number of hits per track

In order to check the geometrical acceptance of the layout, the distributions of the number of hits coming from axial, skewed and short straws have been studied. 10^5 μ^- single track events have been generated in the interaction point I.P. ($x = y = z = 0$), with random azimuthal angle ϕ ($\phi \in [0°, 360°]$) and $\theta \in [7°,\ 160°]$, at fixed total momentum ($1\,\mathrm{GeV}/c$).

The plots in fig. 129 show the distributions of the hit numbers as a function of θ and ϕ. Moreover, if we distinguish between the contribution of the axial and the skewed straws, more detailed considerations can be drawn. In particular, the plots in fig. 130 show the number of hits per track in case of axial (left) and skewed (right) hit straws as a function of θ, and the ones in fig. 131 are the analogous as a function of ϕ.

As shown in the left plot of fig. 130, the minimum number corresponds to the STT edge at $\theta = 7.8°$; then the number of hits increases up to ~ 8 around $\theta = 11.6°$ and stays constant in the angular region where the skewed layers are placed. For larger values of θ, the number of hits for axial straws increases again, up to about 17–18, corresponding to the region where the tracks with $\theta \in [20.9°, 133.6°]$ hit all the straw layers. For tracks with a bigger θ value, the number of hits decreases down to 8 hits and again, after the plateau, down to 0 at $\theta = 159.5°$, corresponding to the backward lower edge of the STT.

The number of hits from skewed straws (right plot of fig. 130) increases, starting from 11.6°, since below this θ value only axial double layers are placed. The maximum number of skewed hits is 8, according to the fact that the STT layout foresees four double layers of tilted tubes. A higher number of hits from skewed straws can be due to the fact that, along their path, tracks may hit also the shorter tilted tubes placed in the corners of the hexagonal STT layout or more tubes due to the bending of their trajectory.

The hit distributions *vs.* ϕ are reported in fig. 131. The results are in agreement with the ones as a function of θ, showing that the maximum number of hits from axial straws is about 17–18 and that most tracks hit 8 skewed straws.

In addition, the left plot of fig. 131 shows a structure around 8 hits: This is due to the tracks which exit the front of the STT in the angular region of the skewed layers. This prevents them from reaching the outer axial straw layers: Thus, the maximum number of axial hits of these tracks is 8.

The hole at $\phi = 90°$ and the low number of hits around this ϕ value are due to the gap for the target pipe. The losses at $\phi = 30°$ and $\phi = 60°$ are caused by the fact that the short tubes placed in the hexagon corners do not completely fill the volume, leaving empty spaces. These losses are negligible: Only a small percentage of the total number of events hits less than 5 skewed straws. Nevertheless, there is a gain in efficiency when including in the reconstruction procedure also the information of the hits from the MVD and the GEM chambers.

As a summary, the distributions of the mean number of axial and skewed hit straws per track are shown in fig. 132.

7.1.3 Studies on momentum resolution and reconstruction efficiency

Studies with uniform $\cos\theta$

10^4 μ^- single track events have been generated in the interaction point I.P. ($x = y = z = 0$), with uniform azimuthal angle $\phi \in [0°, 360°]$ and uniform $\cos\theta$ ($\theta \in [7.8°, 159.5°]$) at fixed values of total momentum (0.3, 1, $5\,\mathrm{GeV}/c$).

The reconstructed momentum distributions are shown in fig. 133 for particles at (a) 0.3, (b) 1 and (c) $5\,\mathrm{GeV}/c$. The red dashed histograms show the prefit results (the outcome of the pattern recognition, sect. 6.2.3), while the blue histograms reproduce the Kalman fit result.

Each histogram has been fitted with a Gauss function in the range $[\mu - 3\sigma, \mu + 3\sigma]$, where μ is the mean value of the momentum distribution and σ has been calculated by dividing the FWHM of the histogram by 2.35.

Table 16 summarizes the obtained values of momentum resolution and efficiency. The resolution is calculated as σ/μ, using the μ and σ values from the Gaussian fit; it is then reported as relative resolution in percent. The efficiency is defined by the histogram integral divided by the number of generated tracks. In addition, the efficiency "in peak" is reported: it is the number of tracks in the fitted range ($\mu \pm 3\sigma$) with respect to the total number of tracks.

In all cases the Kalman fit results are better than the prefit ones (as expected), both in terms of mean value and sigma of the distributions. In fact the Kalman fit improves the helix fit results both reducing the width of the distribution (*i.e.* improving the resolution) and shifting the distribution mean value towards a more correct value. On the other hand, the helix fit introduces a systematic offset in the momentum determination giving an underestimated value.

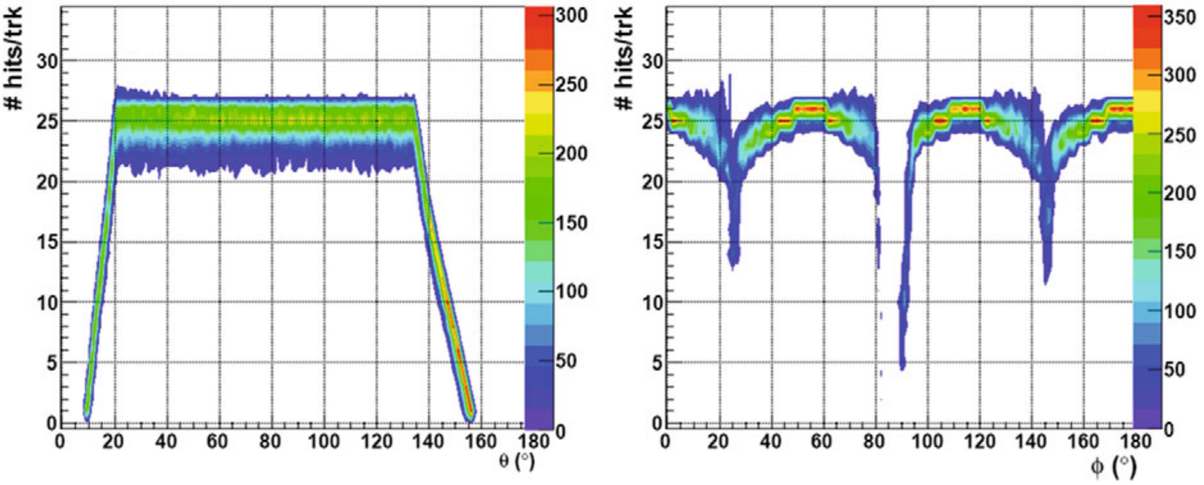

Fig. 129. Distribution of the number of hit straws as a function of θ (left) and ϕ (right) angles for 10000 μ^- generated with a momentum of $1\,\mathrm{GeV}/c$.

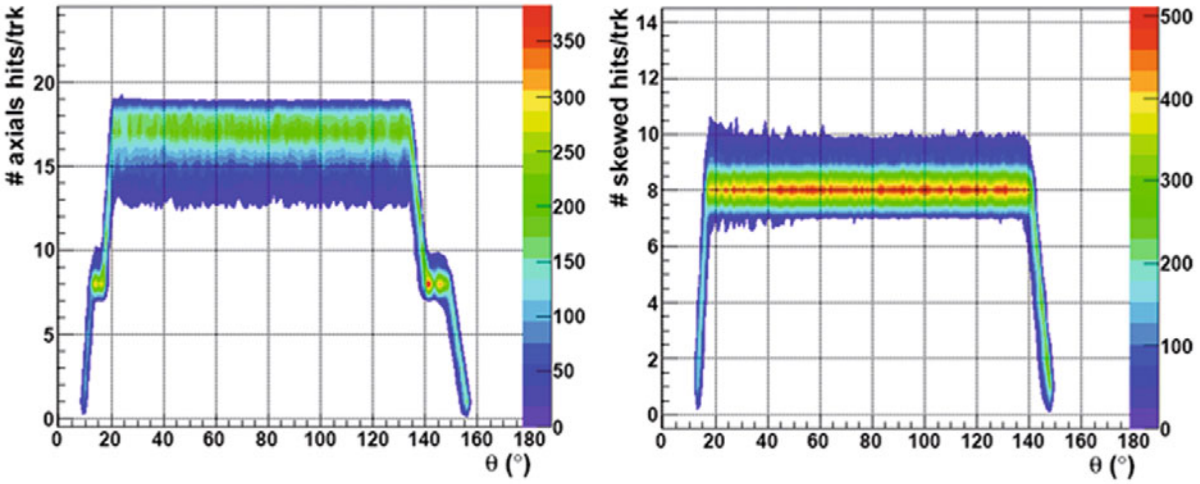

Fig. 130. Distribution of the number of hits per track as a function of θ angle for 10^5 μ^- generated with a momentum of $1\,\mathrm{GeV}/c$, in case of axial (left) and skewed (right) hit straws.

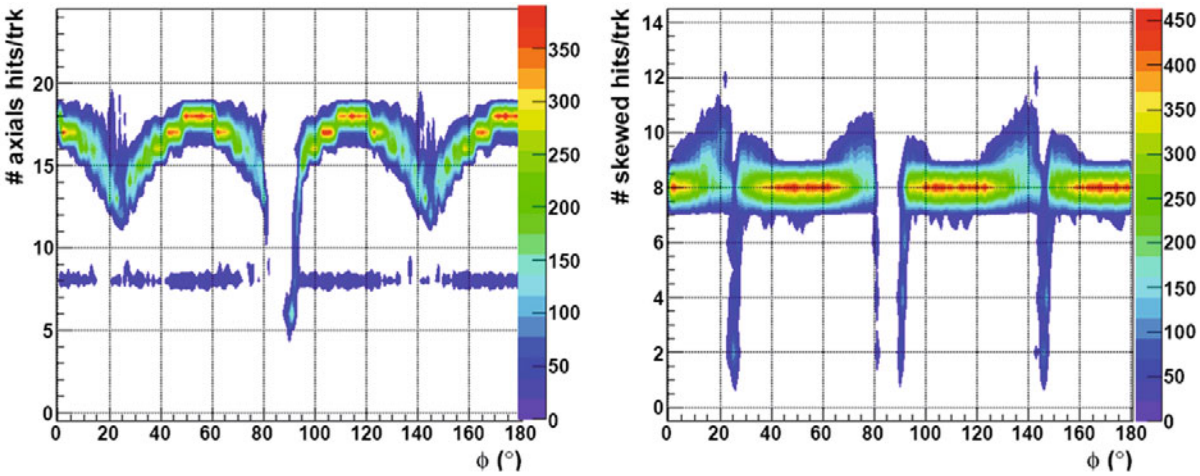

Fig. 131. Distribution of the number of hits per track as a function of ϕ angle for 10^5 μ^- generated with a momentum of $1\,\mathrm{GeV}/c$, in case of axial (left) and skewed (right) hit straws.

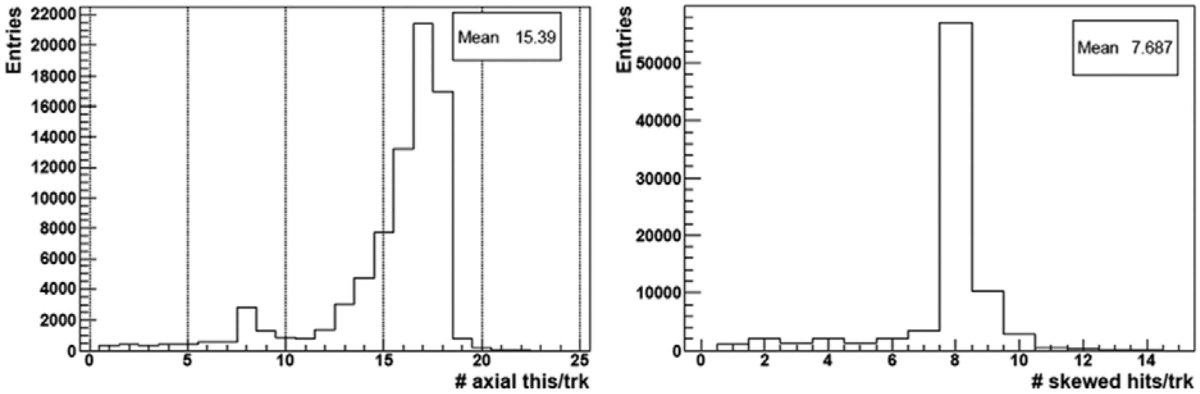

Fig. 132. Distribution of the mean number of axial (left) and skewed (right) hit straws per track.

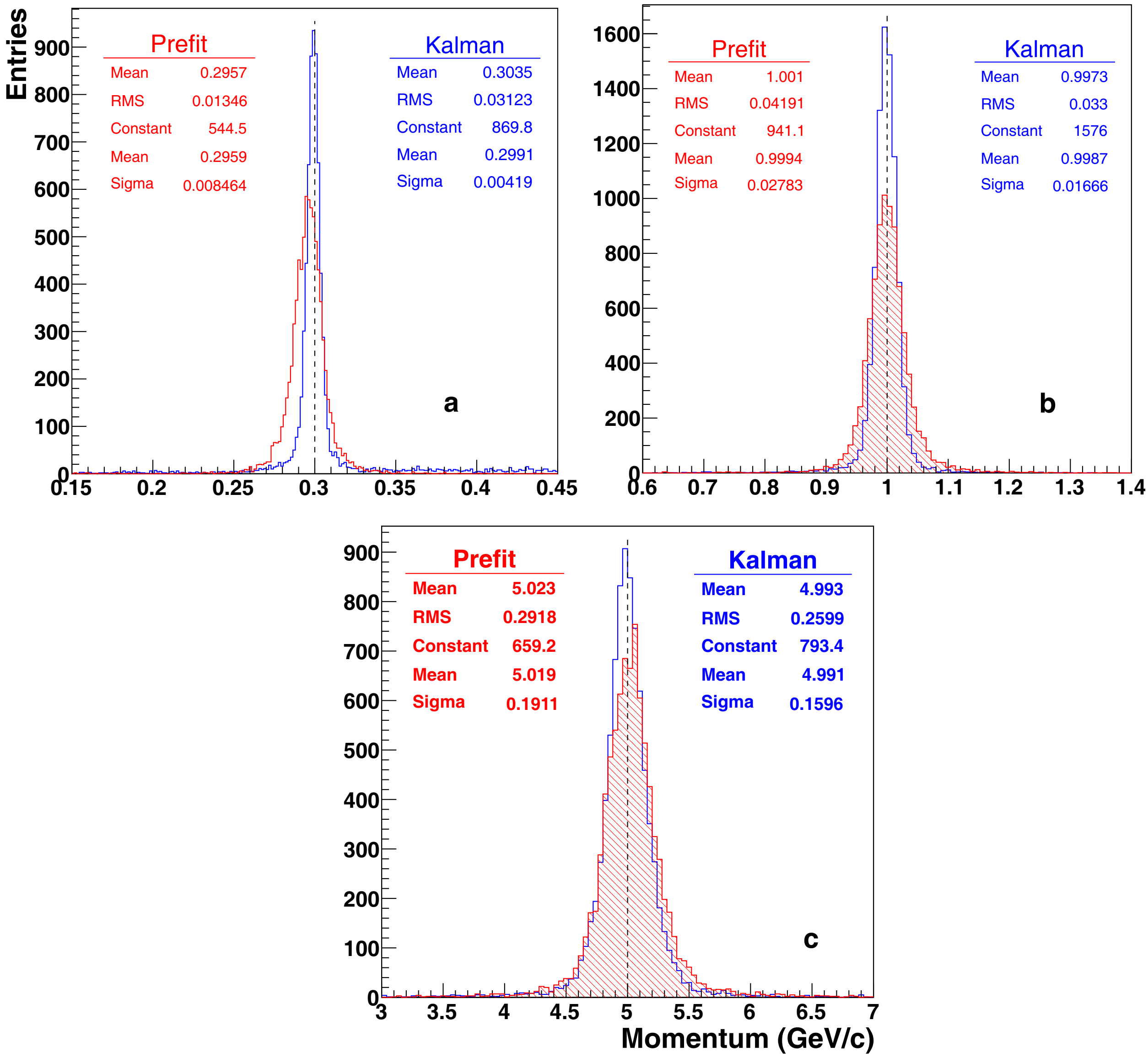

Fig. 133. Momentum distributions for (a) 0.3, (b) 1 and (c) 5 GeV/c μ^-, reconstructed with helix (red dashed) and Kalman (blue) fits. The statistic boxes report the mean values and RMS of the non-fitted histograms, as well as mean and sigma values of the Gaussian fits, before and after the Kalman fit.

Table 16. Momentum resolution and reconstruction efficiency for 10^4 μ^- (fig. 133). The resolution is calculated as σ/μ (with μ and σ values from the Gaussian fit); the efficiency is obtained as integral divided by the number of generated tracks and the efficiency "in peak" is the number of tracks in $(\mu \pm 3\sigma)$ divided by the total number of tracks (sect. 7.1.3).

Momentum	Resolution (%)		Efficiency (%)		Eff. in peak (%)	
(GeV/c)	Prefit	Kalman	Prefit	Kalman	Prefit	Kalman
0.3	2.86 ± 0.03	1.40 ± 0.02	82.75 ± 0.38	74.60 ± 0.44	77.64 ± 0.42	65.20 ± 0.48
1.0	2.78 ± 0.03	1.67 ± 0.02	86.89 ± 0.34	86.81 ± 0.34	81.64 ± 0.39	80.18 ± 0.40
5.0	3.81 ± 0.05	3.19 ± 0.04	84.91 ± 0.36	84.68 ± 0.36	79.07 ± 0.41	80.87 ± 0.39

An efficiency loss of about 13% from the prefit (78%) to the Kalman fit (65%) in the helix reconstruction is observed for the tracks with 0.3 GeV/c total momentum (see table 16, efficiency in peak values). This indicates a problem in the Kalman fit algorithm for these low momentum tracks, which has to be investigated in detail. For the tracks with higher momenta, the efficiencies of the prefit and Kalman fit are comparable and the differences are less than 2%.

Studies at fixed θ values

A systematic scan of the momentum resolutions and efficiencies has been performed with fixed angle generated particles. 10^4 μ^- single track events have been generated at the interaction point with fixed total momentum (0.3, 1, 2 and 5 GeV/c) and random ϕ ($\phi \in [0°, 360°]$). The θ angular range has been scanned as follows:

i) $\theta = 10°,\ 12°, \ldots, 24°$ in steps of 2° ($\pm1°$);

ii) $\theta = 30°,\ 40°, \ldots, 150°$ in steps of 10° ($\pm$ 5°).

Finally, the events have been reconstructed and the Kalman fit has been performed.

The values of momentum resolution and efficiency in peak (see sect. 7.1.3 for the meaning) are summarized in tables 17–20. The momentum resolution and efficiency plots as a function of the θ angle are shown in figs. 134–141.

Apart from the 0.3 GeV/c set of simulated events, for which a dedicated comment is needed, common conclusions can be drawn for the other event sets generated at 1, 2 and 5 GeV/c. Concerning the momentum resolution, a common behavior can be identified by looking at figs. 136, 138 and 140: the resolution improves for θ values up to $\sim 21°$, then starts to worsen again. The results can be interpreted on the basis of geometrical considerations, by looking at the sketch of the STT in the (z, r) plane shown in fig. 142. Tracks travelling with small θ values (but bigger than 7.8°) hit just few straw layers, in particular only the axial ones if $\theta < 11.6°$, preventing the reconstruction of the z-coordinate of the straw tube hits (sect. 6.2.3); this results in a bad spatial (and hence momentum) resolution of the STT hits. On the other hand, the tracking in this forward angular region is performed mainly with the hits produced in the MVD and in the GEM chambers. The very high precision of these two detectors improves the resolution, which becomes much better when including also the spatial information coming from their hits. As the θ value increases, tracks hit more and more straw layers, allowing a better track reconstruction in the tracker. This, combined with the good resolution of the MVD and GEM hits, results in a better global momentum resolution. Then, for $21° < \theta < 133°$, tracks traverse the MVD and all the straw layers; so the resolution obtained by the STT alone is improved with respect to that at lower θ values, but it suffers from the fact that there are no more hits in the GEM chambers. So the resolution is globally a bit worse.

Finally, for $\theta > 133°$ tracks are going in the backward direction and traverse a lower number of straw layers as the angle increases: Consequently, since the decreased number of hits is not compensated by any other outer tracking detector (like the GEMs in the forward direction), the resolution becomes worse.

The reconstruction efficiency, shown in figs. 137, 139 and 141, is quite low around $\theta = 10°$ because the tracking procedure fails when the number of reconstructed hits is too low. Then, it increases up to more than 90% in the central angular region. The efficiency presents a dip around $\theta = 90°$ due to the tracks that are lost because they go into the target pipe. Finally, for tracks travelling in the backward direction, the efficiency starts to decrease because of the reduced number of hits per track, that may cause problems in the reconstruction.

Concerning the events at 0.3 GeV/c, the results are not so reliable as at the others described above, in particular for small values of θ. The reason is that the Kalman fit produces long tails in the momentum distributions (see fig. 133 a), even if the outcome of the prefit does not present these tails.

This Kalman behaviour affects both the momentum resolution and the reconstruction efficiency, shown in figs. 134 and 135; it is probably due to a code bug, which has still to be deeply investigated and corrected.

Table 17. Momentum resolution and reconstruction efficiency for 10^4 μ^- single track events generated at 0.3 GeV/c and fixed θ angle.

$\theta\,(^\circ)$	Resolution (%)	Efficiency (%)	Efficiency in peak (%)
10	1.96 ± 0.21	2.17 ± 0.15	1.36 ± 0.16
12	2.26 ± 0.04	38.39 ± 0.49	33.61 ± 0.47
14	2.09 ± 0.02	88.45 ± 0.32	79.84 ± 0.40
16	1.98 ± 0.03	96.65 ± 0.18	73.56 ± 0.44
18	1.94 ± 0.03	89.58 ± 0.31	63.69 ± 0.48
20	1.53 ± 0.03	83.10 ± 0.37	49.42 ± 0.49
22	1.29 ± 0.02	79.11 ± 0.41	48.18 ± 0.49
24	1.34 ± 0.02	79.45 ± 0.40	47.87 ± 0.49
30	1.64 ± 0.03	83.25 ± 0.37	45.67 ± 0.49
40	1.47 ± 0.02	94.98 ± 0.22	65.35 ± 0.48
50	1.35 ± 0.01	95.56 ± 0.20	79.03 ± 0.41
60	1.29 ± 0.01	94.78 ± 0.22	84.34 ± 0.36
70	1.24 ± 0.01	95.61 ± 0.20	85.63 ± 0.35
80	1.23 ± 0.01	94.81 ± 0.22	85.15 ± 0.35
90	1.24 ± 0.01	92.38 ± 0.26	83.19 ± 0.37
100	1.25 ± 0.01	89.94 ± 0.30	78.18 ± 0.41
110	1.22 ± 0.01	89.48 ± 0.31	70.69 ± 0.45
120	1.27 ± 0.01	84.53 ± 0.36	57.24 ± 0.49
130	1.33 ± 0.02	85.52 ± 0.35	43.10 ± 0.49
140	2.16 ± 0.05	82.51 ± 0.38	43.24 ± 0.49
150	6.47 ± 0.17	36.34 ± 0.48	21.48 ± 0.41

Table 18. Momentum resolution and reconstruction efficiency for 10^4 μ^- single track events generated at 1 GeV/c and fixed θ angle.

$\theta\,(^\circ)$	Resolution (%)	Efficiency (%)	Efficiency in peak (%)
10	2.19 ± 0.05	20.51 ± 0.40	19.55 ± 0.39
12	2.05 ± 0.02	88.94 ± 0.31	85.93 ± 0.35
14	1.67 ± 0.02	93.53 ± 0.25	87.81 ± 0.33
16	1.46 ± 0.01	93.74 ± 0.24	90.35 ± 0.30
18	1.27 ± 0.01	94.25 ± 0.23	87.90 ± 0.33
20	1.09 ± 0.01	98.65 ± 0.12	94.27 ± 0.23
22	1.50 ± 0.01	99.23 ± 0.09	94.70 ± 0.22
24	1.60 ± 0.01	98.72 ± 0.11	93.33 ± 0.25
30	1.56 ± 0.01	97.57 ± 0.15	92.31 ± 0.27
40	1.58 ± 0.01	96.05 ± 0.19	90.58 ± 0.29
50	1.57 ± 0.01	95.45 ± 0.21	90.82 ± 0.29
60	1.59 ± 0.01	95.76 ± 0.20	91.62 ± 0.28
70	1.58 ± 0.01	94.66 ± 0.22	89.13 ± 0.31
80	1.60 ± 0.01	93.57 ± 0.24	87.67 ± 0.33
90	1.62 ± 0.02	93.82 ± 0.24	87.10 ± 0.33
100	1.63 ± 0.02	94.01 ± 0.24	88.00 ± 0.32
110	1.58 ± 0.01	95.34 ± 0.21	90.24 ± 0.30
120	1.60 ± 0.02	95.21 ± 0.21	92.13 ± 0.27
130	1.57 ± 0.01	95.63 ± 0.20	90.59 ± 0.29
140	2.47 ± 0.03	92.54 ± 0.26	88.01 ± 0.32
150	7.81 ± 0.15	39.69 ± 0.49	34.62 ± 0.48

Table 19. Momentum resolution and reconstruction efficiency for 10^4 μ^- single track events generated at 2 GeV/c and fixed θ angle.

$\theta\,(^\circ)$	Resolution (%)	Efficiency (%)	Efficiency in peak (%)
10	2.30 ± 0.05	23.53 ± 0.42	22.26 ± 0.42
12	2.02 ± 0.02	89.51 ± 0.31	84.84 ± 0.36
14	1.73 ± 0.02	92.66 ± 0.26	88.46 ± 0.32
16	1.50 ± 0.01	93.07 ± 0.25	89.58 ± 0.31
18	1.29 ± 0.01	93.59 ± 0.24	89.59 ± 0.31
20	1.20 ± 0.01	95.87 ± 0.20	92.62 ± 0.26
22	1.60 ± 0.02	95.90 ± 0.20	91.04 ± 0.29
24	1.67 ± 0.02	94.84 ± 0.22	89.68 ± 0.30
30	1.71 ± 0.02	94.43 ± 0.23	89.84 ± 0.30
40	1.92 ± 0.02	94.78 ± 0.22	92.07 ± 0.27
50	1.99 ± 0.02	94.84 ± 0.22	91.82 ± 0.27
60	2.14 ± 0.02	94.91 ± 0.22	92.73 ± 0.26
70	2.15 ± 0.02	94.34 ± 0.23	91.13 ± 0.28
80	2.15 ± 0.02	92.76 ± 0.26	88.01 ± 0.32
90	2.16 ± 0.02	93.19 ± 0.25	86.76 ± 0.34
100	2.20 ± 0.02	93.75 ± 0.24	88.92 ± 0.31
110	2.19 ± 0.02	94.44 ± 0.23	91.37 ± 0.28
120	2.16 ± 0.02	94.80 ± 0.22	92.28 ± 0.27
130	2.11 ± 0.02	95.04 ± 0.22	92.63 ± 0.26
140	3.18 ± 0.04	92.98 ± 0.26	87.23 ± 0.33
150	8.90 ± 0.16	37.86 ± 0.49	34.11 ± 0.47

Table 20. Momentum resolution and reconstruction efficiency for 10^4 μ^- single track events generated at 5 GeV/c and fixed θ angle.

$\theta\,(^\circ)$	Resolution (%)	Efficiency (%)	Efficiency in peak (%)
10	2.61 ± 0.05	23.93 ± 0.43	22.68 ± 0.42
12	2.25 ± 0.02	88.87 ± 0.31	85.07 ± 0.36
14	1.89 ± 0.02	91.93 ± 0.27	87.63 ± 0.33
16	1.55 ± 0.02	92.87 ± 0.26	88.33 ± 0.32
18	1.38 ± 0.01	93.13 ± 0.25	89.82 ± 0.30
20	1.28 ± 0.01	94.80 ± 0.22	90.95 ± 0.29
22	1.91 ± 0.02	94.33 ± 0.23	90.23 ± 0.30
24	2.01 ± 0.02	94.04 ± 0.24	90.10 ± 0.30
30	2.27 ± 0.02	94.27 ± 0.23	89.74 ± 0.30
40	2.88 ± 0.03	94.51 ± 0.23	91.22 ± 0.28
50	2.97 ± 0.03	94.71 ± 0.22	90.97 ± 0.29
60	3.30 ± 0.03	94.20 ± 0.23	90.96 ± 0.29
70	3.45 ± 0.03	92.57 ± 0.26	89.03 ± 0.31
80	3.41 ± 0.03	91.49 ± 0.28	85.56 ± 0.35
90	3.38 ± 0.03	90.85 ± 0.29	84.28 ± 0.36
100	3.44 ± 0.03	91.67 ± 0.28	85.46 ± 0.35
110	3.32 ± 0.03	93.48 ± 0.25	88.76 ± 0.32
120	3.26 ± 0.03	94.02 ± 0.24	91.12 ± 0.28
130	3.04 ± 0.03	94.33 ± 0.23	91.41 ± 0.28
140	4.53 ± 0.05	92.06 ± 0.27	87.17 ± 0.33
150	11.36 ± 0.23	34.84 ± 0.48	32.70 ± 0.47

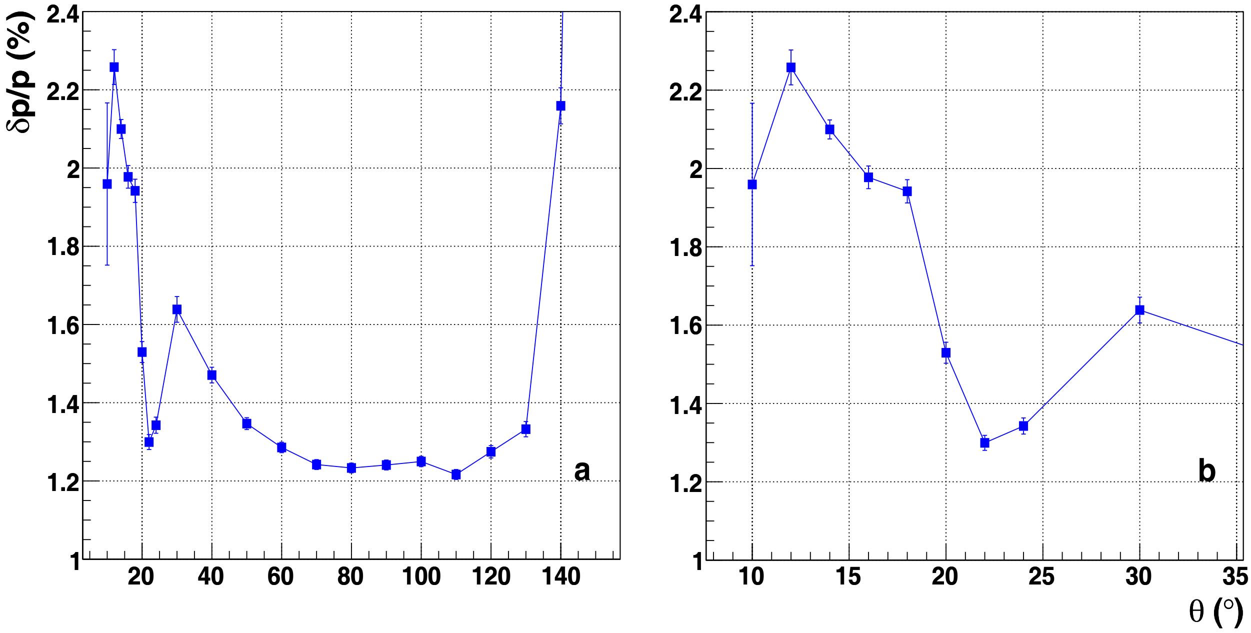

Fig. 134. Momentum resolution *vs.* θ starting angle for 0.3 GeV/c μ^- single track events, in the full angular range $\theta \in [9°, 160°]$ (a) and in the forward region $\theta \in [9°, 35°]$ (b) (see table 17).

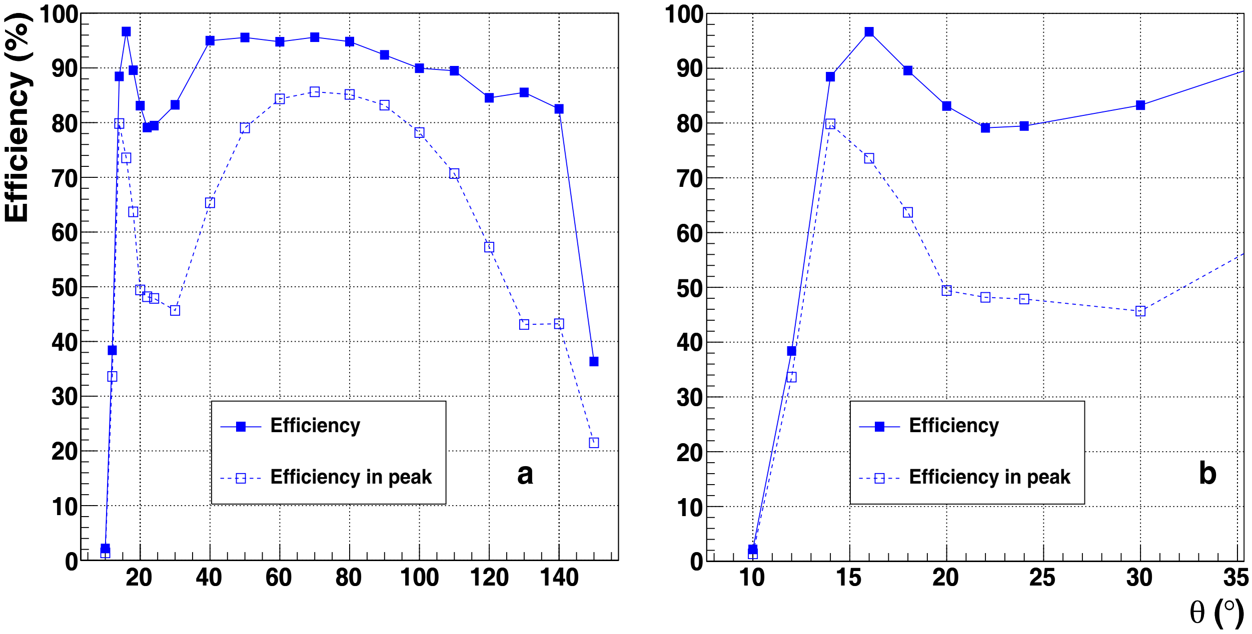

Fig. 135. Track reconstruction efficiency *vs.* θ starting angle for 0.3 GeV/c μ^- single track events, in the full range $\theta \in [9°, 160°]$ (a) and in the forward region $\theta \in [9°, 35°]$ (b) (see table 17).

Studies at fixed transverse momentum

The performances of the Straw Tube Tracker in terms of momentum resolution and reconstruction efficiency have been studied also through simulations of 10^4 μ^- single track events generated at the interaction point I.P., with $\phi \in [0°, 360°]$ and $\theta \in [7°, 160°]$. The tracks have been generated at the following values of fixed p_T: 0.2, 0.4, 0.6, 0.8, 1.0, 1.5, 2.0 and 2.5 GeV/c. The momentum resolution and efficiency plots as function of the p_t values are shown in figs. 143 and 144; the obtained values are reported in table 21. The momentum resolution is almost linear with p_T, as expected.

Summary of the results

The performance of the STT has been investigated through the simulation of different sets of single track

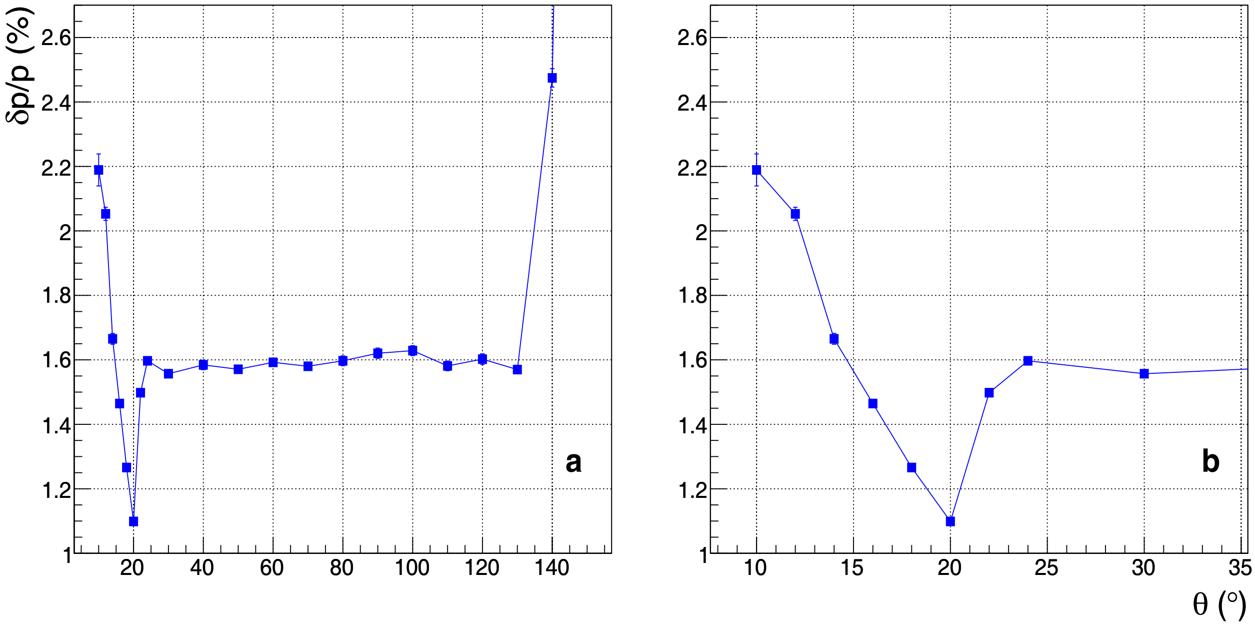

Fig. 136. Momentum resolution *vs.* θ starting angle for $1\,\mathrm{GeV}/c$ μ^- single track events, in the full angular range $\theta \in [9^\circ, 160^\circ]$ (a) and in the forward region $\theta \in [9^\circ, 35^\circ]$ (b) (see table 18).

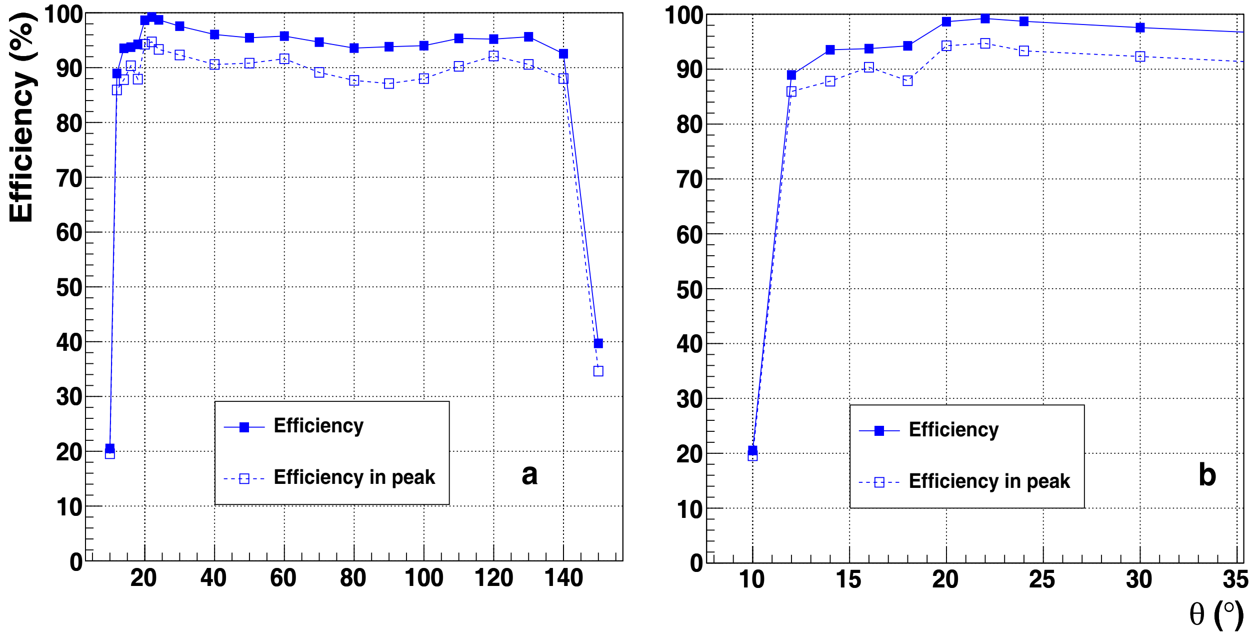

Fig. 137. Track reconstruction efficiency *vs.* θ starting angle for $1\,\mathrm{GeV}/c$ μ^- single track events, in the full range $\theta \in [9^\circ, 160^\circ]$ (a) and in the forward region $\theta \in [9^\circ, 35^\circ]$ (b) (see table 18).

(muon) events, generated at the interaction point at different momentum values, polar angle θ and uniform azimuthal angle ϕ. The tracks have been fitted by applying the procedure summarised in sect. 6.2. The attention has then been focused on the momentum resolution of the generated particles and on the tracking efficiency. In all the sets of simulations, the improvements due to the Kalman filter is evident, in particular in terms of momentum resolution: The mean values of the momentum distributions after the Kalman fit are more centered around the correct value than the ones obtained after the global helix fit. In addition, the Kalman distributions are narrower than the helix ones, resulting in better resolution values. Tests with tracks generated with random θ and ϕ show that the momentum resolution ranges from $\sim 1.32\%$ in case of $0.3\,\mathrm{GeV}/c$ tracks, to $\sim 3.61\%$ for $5\,\mathrm{GeV}/c$ tracks (fig. 133, table 16).

A more detailed investigation has been performed through the simulation of tracks scanning the whole CT angular region in fine steps. The results are shown in

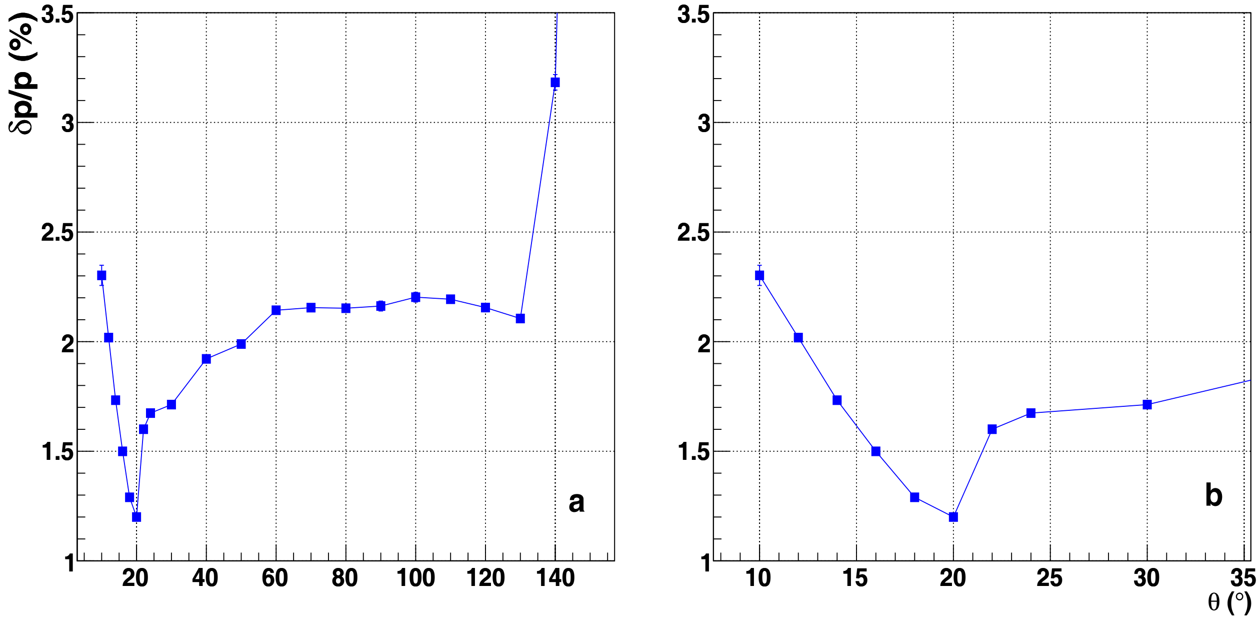

Fig. 138. Momentum resolution *vs.* θ starting angle for $2\,\mathrm{GeV}/c$ μ^- single track events, in the full angular range $\theta \in [9^\circ, 160^\circ]$ (a) and in the forward region $\theta \in [9^\circ, 35^\circ]$ (b) (see table 19).

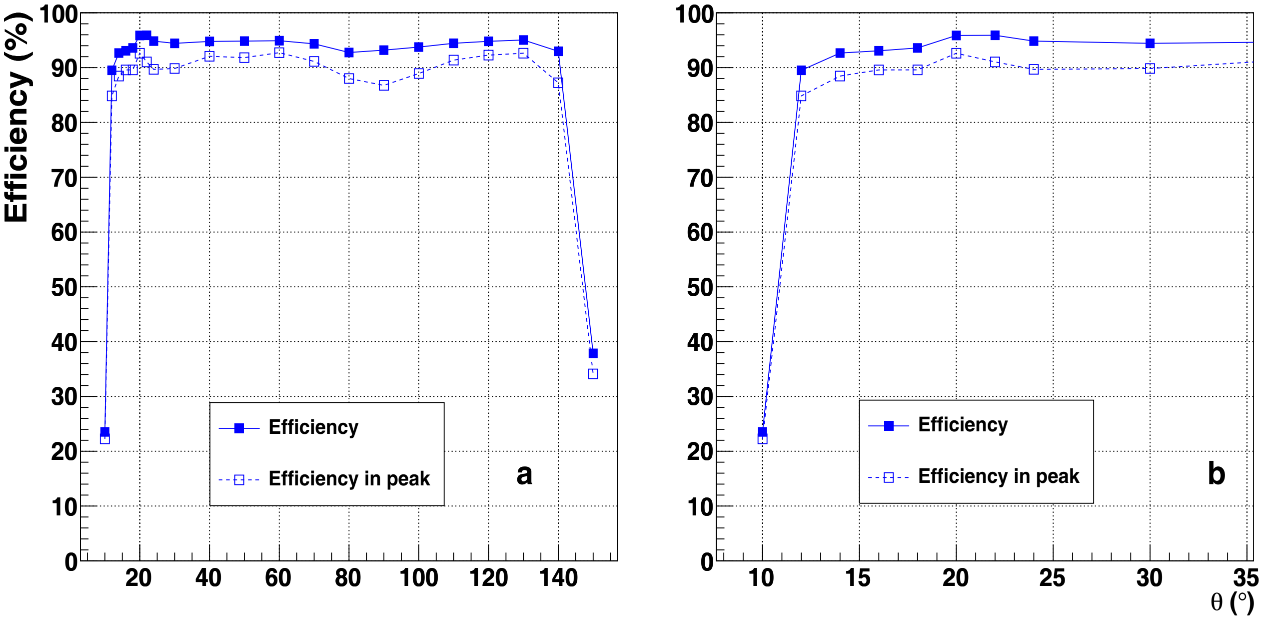

Fig. 139. Track reconstruction efficiency *vs.* θ starting angle for $2\,\mathrm{GeV}/c$ μ^- single track events, in the full range $\theta \in [9^\circ, 160^\circ]$ (a) and in the forward region $\theta \in [9^\circ, 35^\circ]$ (b) (see table 19).

figs. 134–141 and reported in detail in tables 17–20. As shown also in the summary fig. 145, the resolution improves up to $\sim 21^\circ$, due to the increasing number of straw layers traversed by the tracks and to the high precision of the MVD and GEM hits. In the central angular region, the resolution is almost constant, ranging from 1.3% at $0.3\,\mathrm{GeV}/c$, to 1.6% at $1\,\mathrm{GeV}/c$, 2.2% at $2\,\mathrm{GeV}/c$ and 3.3% at $5\,\mathrm{GeV}/c$.

In addition, a set of simulations at fixed values of transverse momentum has been performed. The obtained resolution is reported in table 21 and in figs. 143 and 144. As shown in the plots, the resolution presents an almost linear behaviour as a function of the p_T values, as expected.

7.2 Physics channels analysis

In order to test that the proposed central straw tube tracker fulfills the requirements of the $\overline{\mathrm{P}}$ANDA experiment, appropriate physics channels have been identified to test the detector performance. The set of channels proposed (see table 22) aims to test the detector's capability to

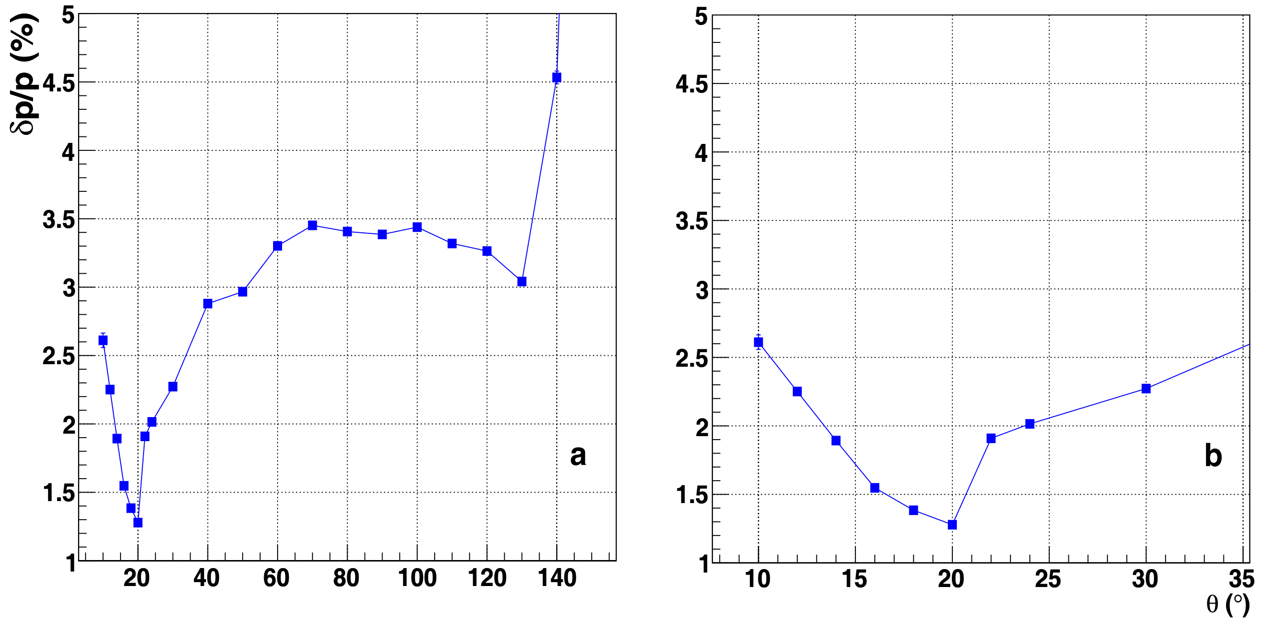

Fig. 140. Momentum resolution *vs.* θ starting angle for 5 GeV/c μ^- single track events, in the full angular range $\theta \in [9°, 160°]$ (a) and in the forward region $\theta \in [9°, 35°]$ (b) (see table 20).

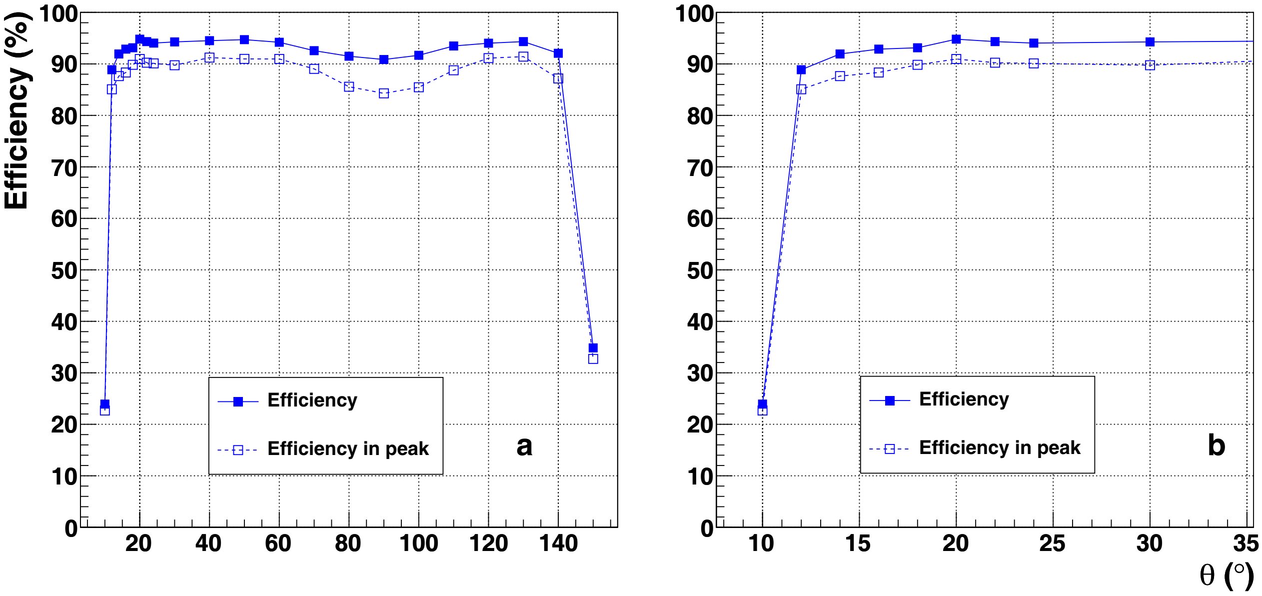

Fig. 141. Track reconstruction efficiency *vs.* θ starting angle for 5 GeV/c μ^- single track events, in the full range $\theta \in [9°, 160°]$ (a) and in the forward region $\theta \in [9°, 35°]$ (b) (see table 20).

measure tracks and momenta of charged particles in an energy region from 100 MeV up to 15 GeV with high precision. A special emphasis is also given to the capability to detect secondary vertices for hadrons with c- and s-quark content. In the following sections the results of the performed data analyses are reported. For the $\bar{\Lambda}\Lambda$ channel preliminary results are shown in sect. 6.2.4 using the STT stand-alone pattern recognition. A complete analysis of this channel will be possible only when the information of the forward tracking system will be included in the tracking code.

7.2.1 Simulation environment

The analysis is performed within the `PandaRoot` framework using the EvtGen event generator for the event production, Virtual Monte Carlo with Geant3 for the simulation, dedicated digitization and reconstruction code, and the rho analysis tool for high-level analysis. Event generation and analysis are performed on the `PandaGrid`. In the Monte Carlo simulations the primary vertex was generated according to the expected target beam interaction region, with 0.1 cm size in transverse direction and distributed

Table 21. Momentum resolution and reconstruction efficiency for 10^4 μ^- single track events generated at fixed transverse momentum.

p_t (GeV/c)	Resolution (%)	Efficiency (%)	Efficiency in peak (%)
0.2	1.48 ± 0.02	70.82 ± 0.45	58.48 ± 0.49
0.4	1.36 ± 0.02	79.01 ± 0.41	72.53 ± 0.45
0.6	1.48 ± 0.02	86.41 ± 0.34	80.24 ± 0.40
0.8	1.58 ± 0.02	85.82 ± 0.35	81.12 ± 0.39
1.0	1.76 ± 0.02	86.41 ± 0.34	79.38 ± 0.40
1.5	1.97 ± 0.03	86.28 ± 0.34	79.45 ± 0.40
2.0	2.25 ± 0.02	85.70 ± 0.35	81.27 ± 0.39
2.5	2.56 ± 0.03	84.70 ± 0.36	80.28 ± 0.40

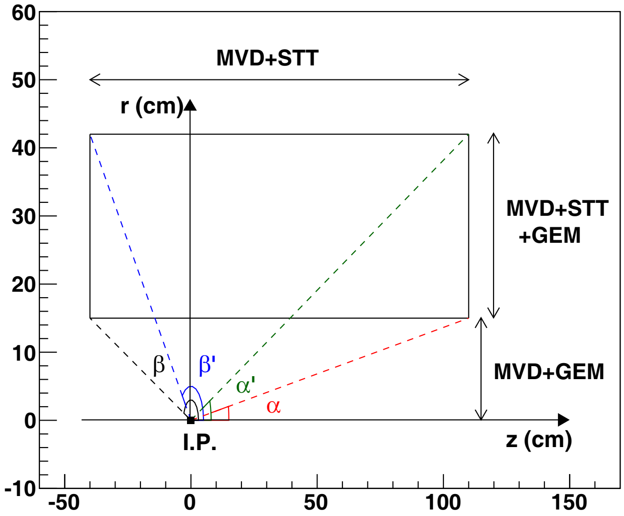

Fig. 142. Sketch of a section of the STT in the (z, r)-plane. The marker corresponds to the interaction point (I.P.); the angle values are: $\alpha = 7.8°$, $\alpha' = 20.9°$, $\beta = 133.6°$ and $\beta' = 159.5°$.

Table 22. Benchmark channels used to evaluate the performance of the central straw tube tracker.

Channel	Final state
$\bar{\mathrm{p}}\mathrm{p} \rightarrow (n)\pi^+\pi^-$	$(n)\pi^+\pi^-$
$\bar{\mathrm{p}}\mathrm{p} \rightarrow \psi(3770) \rightarrow D^+D^-$	$2\mathrm{K}\,4\pi$
$\bar{\mathrm{p}}\mathrm{p} \rightarrow \bar{\Lambda}\Lambda$	$\mathrm{p}\pi^-\bar{\mathrm{p}}\pi^+$
$\bar{\mathrm{p}}\mathrm{p} \rightarrow \eta_c \rightarrow \phi\phi$	4K

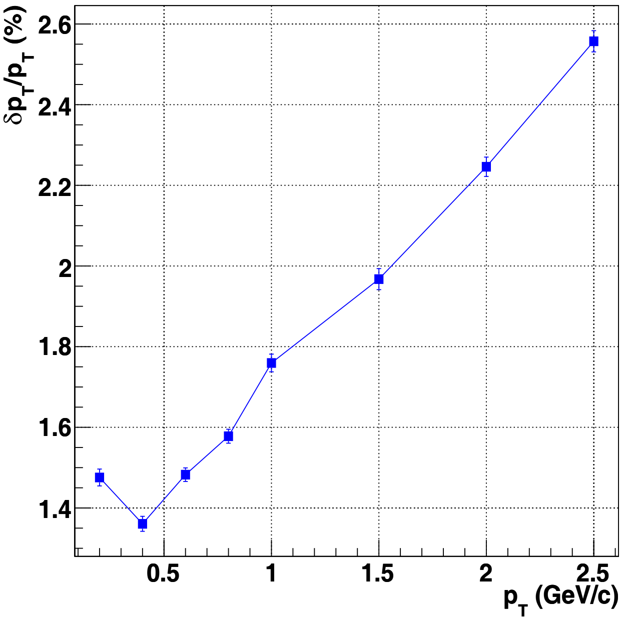

Fig. 143. Momentum resolution *vs.* p_T for μ^- single track events, in the angular ranges $\phi \in [0°, 360°$ and $\theta \in [7°, 160°]$ (see table 21).

by a Gaussian function with FWHM = 0.5 cm along the z-axis. The full $\overline{\mathrm{P}}$ANDA geometry has been included in the simulation, and for the tracking, the MVD, STT and GEM detectors have been used. An important remark here is that the analysis is performed with ideal particle identification, *i.e.* for each reconstructed track its particle type is associated using the Monte Carlo information, in order to avoid possible bias from the detectors used for PID. At first only the reconstruction of the signal itself is considered without study of background suppression. Final results of this study take mixing of the signal with generic background produced by the DPM event generator into account. The number of pile-up events is defined by the Poisson statistics. In this case complete tracks from the background events can be reconstructed as well as single hits from the background events can contribute to the tracks from the event of interest.

7.2.2 $\bar{\mathrm{p}}\mathrm{p} \rightarrow (n)\pi^+\pi^-$

In the $\bar{\mathrm{p}}\mathrm{p}$ annihilation process charged pions are the most abundant particles produced. Therefore, $\bar{\mathrm{p}}\mathrm{p} \rightarrow (n)\pi^+\pi^-$, with $n = 2, 4$, are the basic channels to test the STT performance. At an energy of 3.07 GeV in the center-of-mass system (CMS), the cross section of the channel $\bar{\mathrm{p}}\mathrm{p} \rightarrow \pi^+\pi^-$ is $\sigma = 0.007$ mb while at a CMS energy of 2.954 GeV the cross section of the $\bar{\mathrm{p}}\mathrm{p} \rightarrow \pi^+\pi^-\pi^+\pi^-$ final state is $\sigma = 0.43$ mb [106]. The interesting figures of merit for these benchmark channels are:

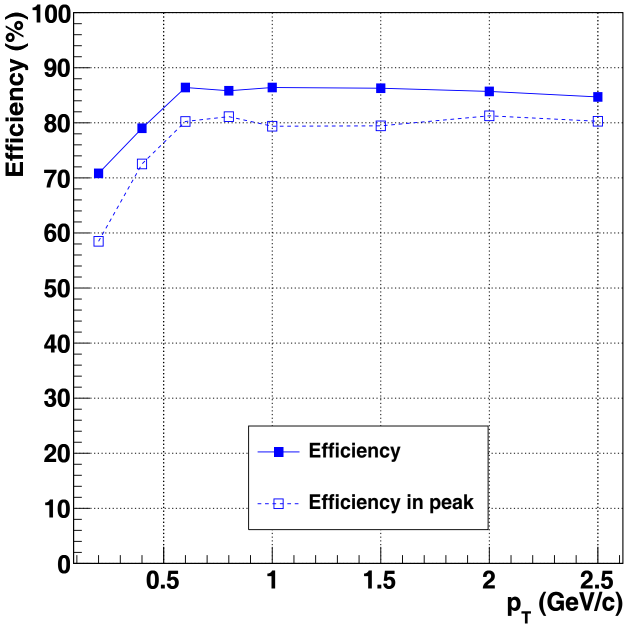

Fig. 144. Reconstruction efficiency *vs.* p_T for μ^- single track events, in the angular ranges $\phi \in [0°, 360°$ and $\theta \in [7°, 160°]$ (see table 21).

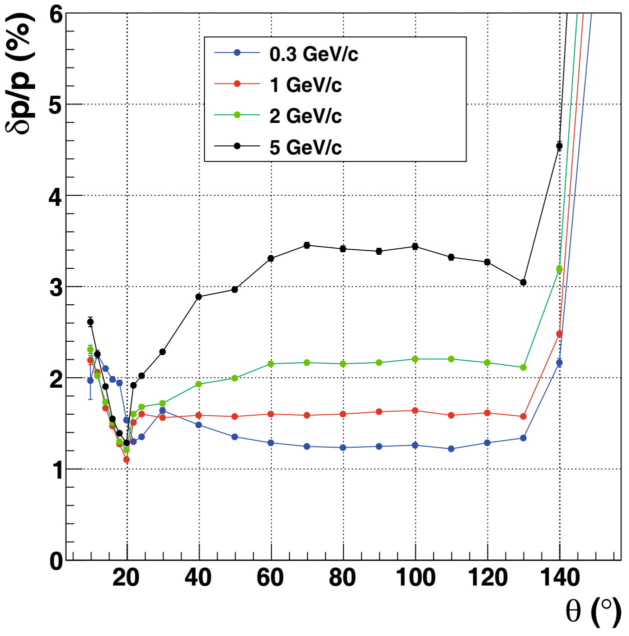

Fig. 145. Momentum resolution *vs.* θ starting angle for 0.3, 1, 2 and 5 GeV/c μ^- single track events, in the full angular range $\theta \in [9°, 160°]$ (figs. 134, 136, 138 and 140).

- single pion track resolution,
- momentum and invariant mass resolutions,
- vertex resolution,
- reconstruction efficiency.

The benchmark channel is simulated at a CMS energy of 3.07 GeV corresponding to an antiproton beam momentum along the z-direction of 4.0 GeV/c.

$\bar{\mathrm{p}}\mathrm{p} \to \pi^+\pi^-$

The distribution of the momentum of the pions as a function of θ and ϕ angles are shown in fig. 146. The majority of the pions has a momentum between 1 GeV/c and 4 GeV/c and they are found within a polar angular range between 0.4 rad and 1.1 rad.

In the first step of the analysis we require that all reconstructed track candidates have at least one STT hit. Events with $2.07\,\mathrm{GeV}/c^2 < m(\pi^+\pi^-) < 4.07\,\mathrm{GeV}/c^2$ are selected, then a vertex fit is performed and the best candidate in each event is selected using the minimal χ^2 criterion.

Figure 147 shows the difference between the reconstructed and the Monte Carlo generated momentum divided by the Monte Carlo one for the pion tracks. The distribution is fitted with a Gaussian function in order to extract the single pion track resolution which is 1.9%.

Figure 148 shows the distribution of the difference between the reconstructed azimuthal (polar) angle and Monte Carlo azimuthal (polar) angle of the single pion track. The distributions are fitted with a Gaussian function in order to extract the resolution of the two angles, which are 1.829 mrad for the azimuthal angle and 0.943 mrad for the polar angle.

The two reconstructed pions are combined in order to reconstruct their invariant mass. The result is shown in fig. 149; the distribution is fitted with a Gaussian function from which the estimation of the resolution is 42 MeV/c^2 and the global reconstruction efficiency, calculated as the ratio between the number of reconstructed events divided by the number of generated ones, is (70.9 ± 0.3)% and it comprises both reconstruction efficiency and geometrical acceptance.

A vertex fit has been performed during the reconstruction of the final state, and the best candidate in each event has been selected by a minimal χ^2 criterion. Figure 150 shows the resolution in x, y and z coordinates of the fitted decay vertex (*e.g.*, difference between reconstructed vertex and Monte Carlo truth vertex position). The distributions are fitted with the Gaussian function in order to extract the resolutions which are: $\sigma_x = 56\,\mu$m, $\sigma_y = 56\,\mu$m and $\sigma_z = 53\,\mu$m.

For the pattern recognition in the presence of pile-up from the mixed background events, the clean-up procedure is applied to remove spurious hits. Figure 151 shows the two pions invariant mass distribution after the clean-up procedure; the global reconstruction efficiency is (65.9 ± 0.3)% and the resolution is 42 MeV/c^2. The single pion track resolution after the clean-up procedure is again 1.9%.

Taking mixing of the signal with generic background into account, fig. 152 shows the difference between the reconstructed and the Monte Carlo generated momentum divided by the Monte Carlo one for the pion tracks. The single pion track resolution obtained from the Gaussian fit is 2.1%. Figure 153 shows the two pions invariant mass distribution which is fitted with a double Gaussian function plus a polynomial to take the background into

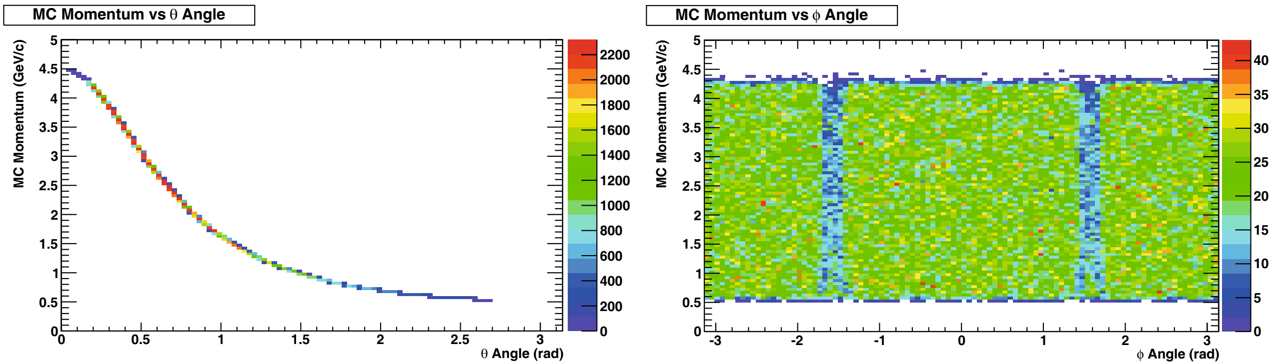

(a) (b)

Fig. 146. $\bar{\rm p}{\rm p} \to \pi^+\pi^-$: Pion momentum distributions *vs.* θ (a) and ϕ (b) angles.

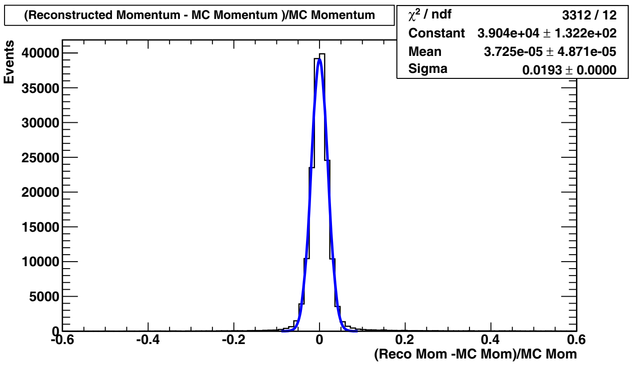

Fig. 147. $\bar{\rm p}{\rm p} \to \pi^+\pi^-$: Momentum resolution of the pion tracks, without event mixing. The fit is done with a Gaussian function (see text for more details).

account. From the fit, the global reconstruction efficiency is $(50.6 \pm 0.2)\%$ and the resolution is $47\,{\rm MeV}/c^2$.

An additional study is to check to which extent the Monte Carlo based PID is relevant for this benchmark channel. To do this, the two pions are reconstructed without any PID. The invariant mass is shown in fig. 154 and it looks unaffected. The two pions reconstruction efficiency is $(49.0 \pm 0.2)\%$; the resolution is $48\,{\rm MeV}/c^2$.

$\bar{\rm p}{\rm p} \to \pi^+\pi^-\pi^+\pi^-$

The distribution of the momentum of the pions as a function of θ and ϕ angles are shown in fig. 155. The majority of the pions has a momentum between $0.5\,{\rm GeV}/c$ and $2.5\,{\rm GeV}/c$ and they are found within a polar angular range between 0.4 rad and 1.1 rad. In the first step of the analysis we require that all reconstructed track candidates have at least one STT hit. Events with $2.57\,{\rm GeV}/c^2 < m(\pi^+\pi^-) < 3.57\,{\rm GeV}/c^2$ are selected, thena vertex fit is performed and the best candidate in each event is selected using the minimal χ^2 criterion.

Figure 156 shows the difference between the reconstructed and the Monte Carlo generated momentum divided by the Monte Carlo one for the pion tracks. The distribution is fitted with a Gaussian function in order to extract the single pion track resolution which is 1.7%. Figure 157 shows the distribution of the difference between the reconstructed azimuthal (polar) angle and Monte Carlo azimuthal (polar) angle of the single pion track. The distributions are fitted with a Gaussian function in order to extract the resolution of the two angles, which are 2.881 mrad for the azimuthal angle and 1.430 mrad for the polar angle.

The four reconstructed pions are combined in order to reconstruct their invariant mass. The result is shown in fig. 158; the distribution is fitted with a Gaussian function from which the estimation of the resolution is $31\,{\rm MeV}/c^2$ and the global reconstruction efficiency, calculated as the ratio between the number of reconstructed events divided by the number of generated ones, is $(43.1 \pm 0.2)\%$, and it comprises both reconstruction efficiency and geometrical acceptance.

A vertex fit has been performed during the reconstruction of the final state, and the best candidate in each event has been selected by the minimal χ^2 criterion. Figure 159 shows the resolution in x, y and z coordinates of the fitted decay vertex (*i.e.* difference between reconstructed vertex and Monte Carlo truth vertex position). The distributions are fitted with the Gaussian function in order to extract the resolutions which are: $\sigma_x = 47\,\mu{\rm m}$, $\sigma_y = 46\,\mu{\rm m}$ and $\sigma_z = 60\,\mu{\rm m}$.

For the pattern recognition in the presence of pile-up from the mixed background events, the clean-up procedure is applied to remove spurious hits. Figure 160 shows the four pions invariant mass distribution after the clean-up procedure; the global reconstruction efficiency is $(31.7 \pm 0.2)\%$ and the resolution is $31\,{\rm MeV}/c^2$. The single pion track resolution after the clean-up procedure is again 1.7%.

After mixing with background events, fig. 161 shows the difference between the reconstructed and the Monte Carlo generated momentum divided by the Monte Carlo one for the pion tracks. The single pion track resolution obtained from the Gaussian fit is 1.8%. Figure 162 shows the four pions invariant mass distribution which is fitted with a double Gaussian function plus a polynomial to take the background into account. From the fit, the global reconstruction efficiency is $(17.2 \pm 0.2)\%$ and the resolution is $39\,{\rm MeV}/c^2$.

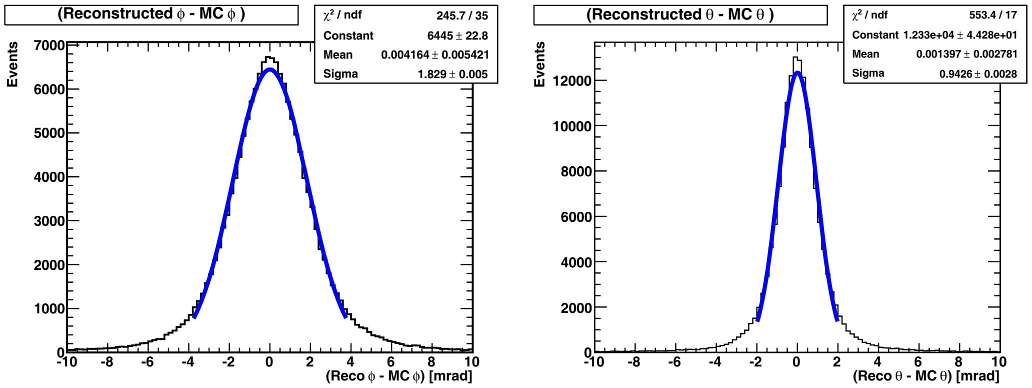

Fig. 148. $\bar{\mathrm{p}}\mathrm{p} \to \pi^+\pi^-$: Difference between the reconstructed and the Monte Carlo azimuthal angle (left) and polar angle (right), without event mixing. The fit is done with a Gaussian function (see text for more details).

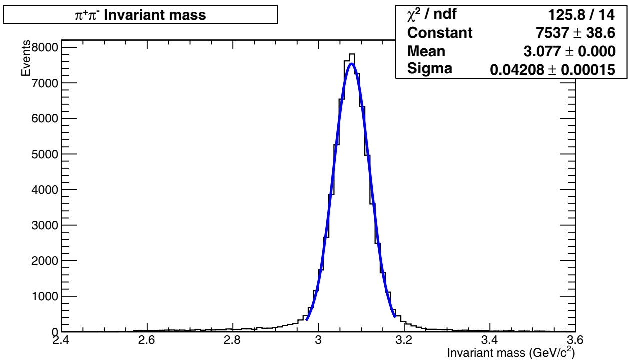

Fig. 149. $\bar{\mathrm{p}}\mathrm{p} \to \pi^+\pi^-$: Pions invariant mass distribution, without event mixing. The fit is done with a Gaussian function (see text for more details).

An additional study is to check to which extent the Monte Carlo based PID is relevant for this benchmark channel. So the four pions are reconstructed without any PID. The invariant mass is shown in fig. 163 and it looks affected, infact the four pions reconstruction efficiency is $(37.4 \pm 0.2)\%$; the resolution is $39\,\mathrm{MeV}/c^2$.

7.2.3 $\bar{\mathrm{p}}\mathrm{p} \to \eta_c \to \phi\phi$

Physics of charmonium is one of the main parts of the $\overline{\mathsf{P}}$ANDA experimental programme. To study the performance of the central tracker with respect to charmonium physics the η_c state has been selected. The $\eta_c(1^1S_0)$ state of charmonium with the mass $2980.4 \pm 1.2\,\mathrm{MeV}/c^2$ (according to the Particle Data Group (PDG)) was discovered more than thirty years ago. Being the ground state of charmonium it represents an interest as a final state in decays of other charmonium states but the resonance scan for precise determination of mass and width of η_c is a separate important task for the $\overline{\mathsf{P}}$ANDA experiment. The η_c can be detected through many exclusive decay channels, neutral or hadronic. For the study of the central tracker performance the following decay mode has been selected: $\eta_c \to \phi\phi$ with the branching ratio $2.7 \cdot 10^{-3}$ with the subsequent decay $\phi \to \mathrm{K}^+\mathrm{K}^-$. This decay mode has a very particular kinematics which simplifies its separation from the general hadronic background. The small Q value of $31\,\mathrm{MeV}$ of the decay $\phi \to \mathrm{K}^+\mathrm{K}^-$ results in directions of the two kaons close to the direction of the ϕ meson. On the other hand $\eta_c \to \phi\phi$ is a two-body decay and as a consequence the directions of the two ϕ and therefore of $\mathrm{K}^\pm$ are correlated. The kinematics of the final state kaons is shown in fig. 164. The distribution of kaons covers a wide range of the central tracker acceptance peaking between 20° and 40° and the covered momentum range is mainly from $200\,\mathrm{MeV}/c$ to $2\,\mathrm{GeV}/c$. The figures of merit of this analysis, which have to check the performance of the central tracker, are the efficiency of the η_c reconstruction and the resolution of the invariant mass for the η_c and the intermediate ϕ states. In addition, the vertex resolution is quoted, however this is not of primary interest for the given channel. The analysis is performed in the following steps:

- Charged candidates with opposite charge are combined to ϕ candidates with ϕ mass preselection $1.02 \pm 0.1\,\mathrm{GeV}/c^2$.
- A vertex fit is performed and the best η_c candidate in each event is selected by minimal χ^2.
- Events with ϕ candidates within a mass window $1.00\,\mathrm{GeV}/c^2 < m(\mathrm{K}^+\mathrm{K}^-) < 1.04\,\mathrm{GeV}/c^2$ are selected.
- η_c is considered as reconstructed if it falls into the mass window $[2.90; 3.06]\,\mathrm{GeV}/c^2$.

It is important to note here that the parameters used in this analysis, such as the cut ranges for the invariant mass, in the real experiment will be optimized for a best signal to background ratio while here they are based on educated guess.

The following results are presented without mixing the signal with background and results including mixing come later. Before estimating the reconstruction efficiency it was studied how many η_c events have final-state kaons within the central tracker acceptance. The study is based on Monte Carlo information and a kaon is considered within detector acceptance if it creates there at least one Monte Carlo hit. Results are summarized in fig. 165, where

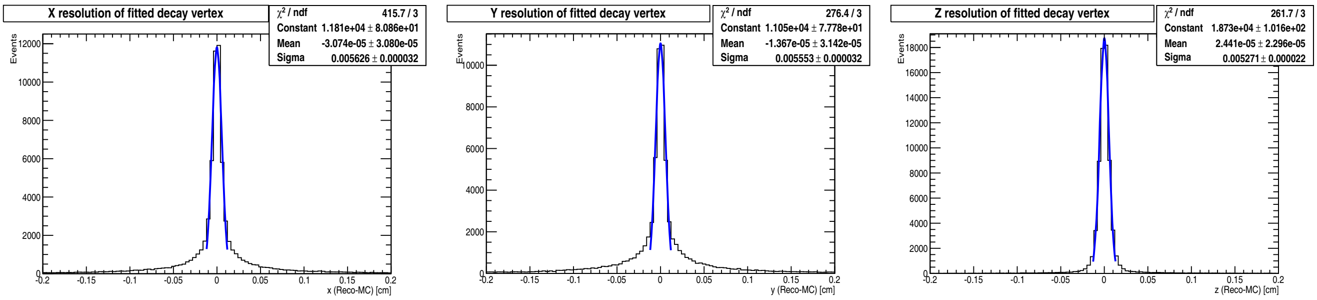

Fig. 150. $\bar{p}p \to \pi^+\pi^-$: Vertex resolution, without event mixing (see text for more details).

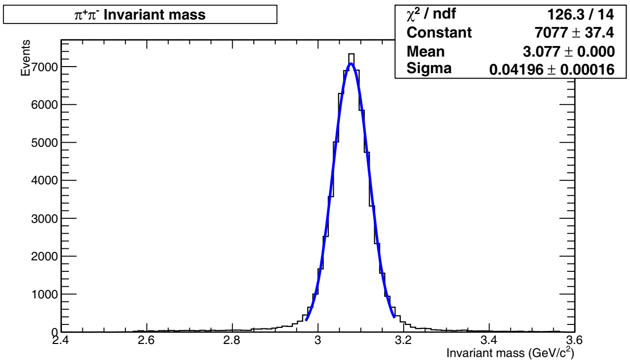

Fig. 151. $\bar{p}p \to \pi^+\pi^-$: Pions invariant mass distribution after clean-up procedure. The fit is done with a Gaussian function (see text for more details).

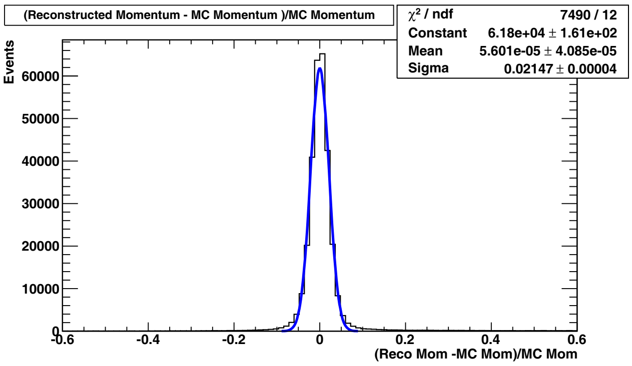

Fig. 152. $\bar{p}p \to \pi^+\pi^-$: Momentum resolution of the pion tracks with event mixing. The fit is done with a Gaussian function (see text for more details).

the multiplicity of kaons within the detector acceptance is presented. According to this plot 45% of events have all 4 kaons within the acceptance which defines an upper limit for the detector efficiency for η_c reconstruction.

At the beginning of the analysis the number of reconstructed charged tracks was studied (fig. 166). From this plot a tail in distribution is observed with a high number of reconstructed tracks which arises due to secondaries and to ghost tracks from the STT pattern recognition. In addition ghost tracks result in 72% of events having 4 or more reconstructed tracks which is higher than the 45% of estimated detector acceptance.

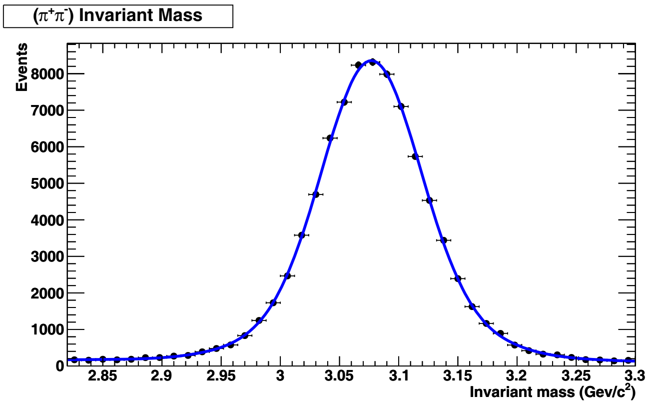

Fig. 153. $\bar{p}p \to \pi^+\pi^-$: Pions invariant mass distribution with event mixing. The fit is done with a double Gaussian function plus a polynomial (see text for more details).

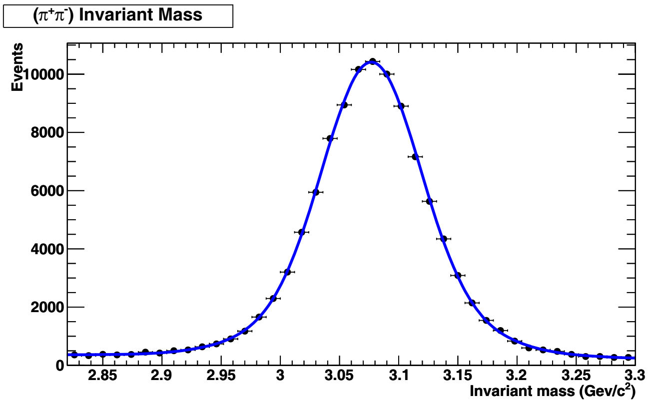

Fig. 154. $\bar{p}p \to \pi^+\pi^-$: Pions invariant mass distribution with event mixing and without Monte Carlo truth PID. The fit is done with a double Gaussian function plus a polynomial (see text for more details).

Invariant mass distributions of K^+K^- pairs of two ϕ candidates are presented in fig. 167. In the upper plot a cut is indicated for the ϕ candidate's invariant mass which is used for η_c construction. The plot of the $\phi\phi$ invariant mass has a significant tail on the left, which however is reduced after requiring ideal PID. Applying a vertex fit to four kaons combined to an η_c candidate the best η_c in each event is selected from the minimum χ^2 and those results are presented in fig. 168. To extract the invariant mass

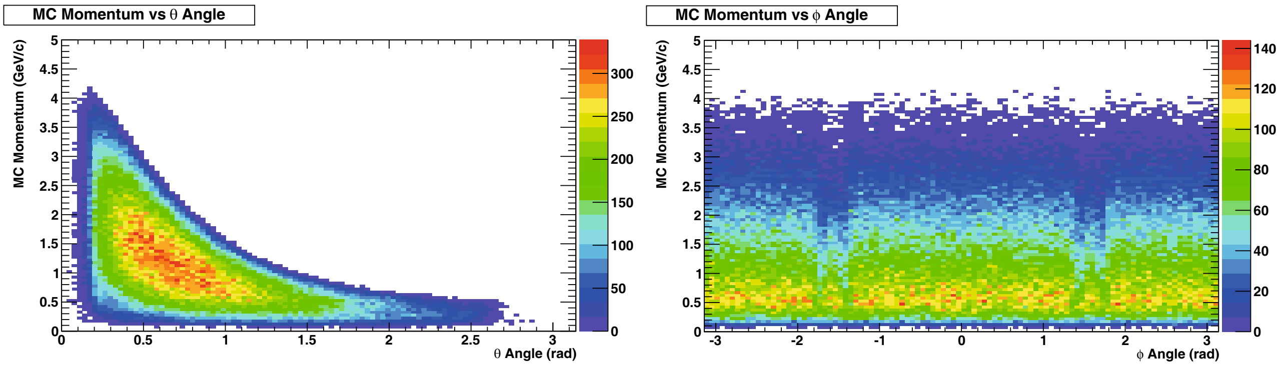

Fig. 155. $\bar{p}p \to 2(\pi^+\pi^-)$: Pion momentum distributions *vs.* θ (a) and ϕ (b) angles.

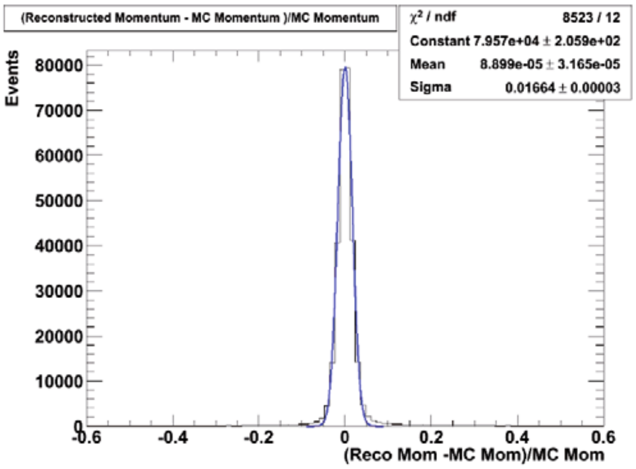

Fig. 156. $\bar{p}p \to 2(\pi^+\pi^-)$: Momentum resolution of the pion tracks, without event mixing. The fit is done with a Gaussian function (see text for more details).

resolution of η_c and ϕ the following two-step approach was applied. At the beginning each plot was fitted with a Gaussian function and the extracted parameters μ_1 and σ_1 were used at the second step where a fit with a Gaussian function was performed in the range $[\mu_1 - 1.6\sigma_1; \mu_1 + 1.6\sigma_1]$. The used range satisfies that the full width of half maximum of the fitted peak is a well defined quantity and the extracted width parameter of the Gaussian σ_2 is quoted. The given approach allows to avoid interference of the tails of the distribution with the extracted width parameter. The obtained resolution for ϕ and η_c are $3.9\,\mathrm{MeV}/c^2$ and $18\,\mathrm{MeV}/c^2$ correspondingly. Also, the given plot allows to extract the η_c reconstruction efficiency as a number of η_c candidates within the mass range $[2.90; 3.06]\,\mathrm{GeV}/c^2$ and it is $27.3 \pm 0.2\%$. In addition the space resolution of the primary η_c vertex in x, y, z coordinates is presented in fig. 169. The given plot represents the difference between reconstructed vertex and Monte Carlo truth vertex position. The obtained resolutions in all coordinates are $\sigma_x = 51\,\mu\mathrm{m}$, $\sigma_y = 51\,\mu\mathrm{m}$, $\sigma_z = 86\,\mu\mathrm{m}$.

For pattern recognition in the presence of pile-up from background events the clean-up procedure is applied to remove spurious hits. For the case of signal without mixing with background this leads to a deterioration of the η_c reconstruction efficiency because some real hits are removed by this procedure. The following change in the number of reconstructed tracks is observed (fig. 170), *i.e.* the number of events with more than 4 reconstructed tracks is reduced significantly. The η_c reconstruction efficiency after the clean-up procedure is $19.1 \pm 0.2\%$, the resolution for ϕ and η_c are slightly changed to $3.9\,\mathrm{MeV}/c^2$ and $17\,\mathrm{MeV}/c^2$ correspondingly.

Final results of this study take into account the mixing of signal with generic background produced by the DPM event generator, where the number of pile-up events is defined by the Poisson statistics. In this case all tracks from background can be reconstructed as well as single hits from background can contribute to the tracks from events of interest. The number of reconstructed tracks in one event becomes higher than for signal only (fig. 171).

Invariant mass distributions for ϕ and η_c are presented in fig. 172. Here the η_c peak appears on the top of a large combinatorial background. However after the whole selection procedure invariant mass plots look very similar to the case of signal only (fig. 173). The reconstruction efficiency for η_c however is lower in this case (11.6%), but the presence of “mixed” background does not affect much the resolution of the reconstructed invariant mass of η_c and ϕ, which are $19\,\mathrm{MeV}/c^2$ and $4.2\,\mathrm{MeV}/c^2$, respectively.

An additional important point of this study was to check how Monte Carlo based PID was relevant here. For this case the η_c reconstruction was performed without any PID as worst case scenario. The corresponding invariant mass distributions for ϕ and η_c are presented in fig. 174. Here, more pronounced tails from combinatorics arise in the ϕ mass distribution but the η_c mass distribution looks not much affected (ϕ mass resolution is $6.2\,\mathrm{MeV}/c^2$ and η_c mass resolution is $20\,\mathrm{MeV}/c^2$), however η_c reconstruction efficiency drops down to 9.6%.

7.2.4 $\bar{p}p \to \psi(3770) \to D^+D^-$

With the $\psi(3770)$ benchmark channel, the STT's performance in the reconstruction of particles with short decay lengths is evaluated. The figures of merit are the spatial resolution of the secondary vertices as well as the invariant mass resolution of the reconstructed D mesons.

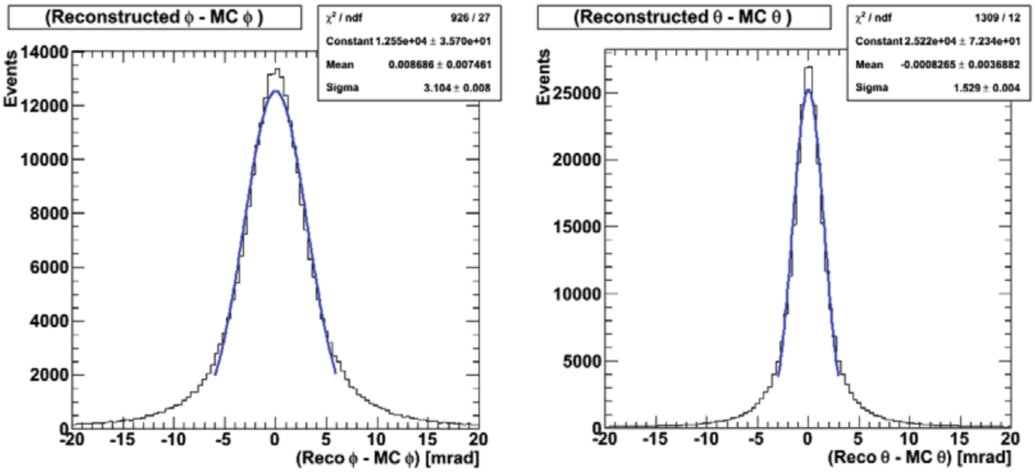

Fig. 157. $\bar{\mathrm{p}}\mathrm{p} \to 2(\pi^+\pi^-)$: Difference between the reconstructed and the Monte Carlo azimuthal angle (left) and polar angle (right), without event mixing. The fit is done with a Gaussian function (see text for more details).

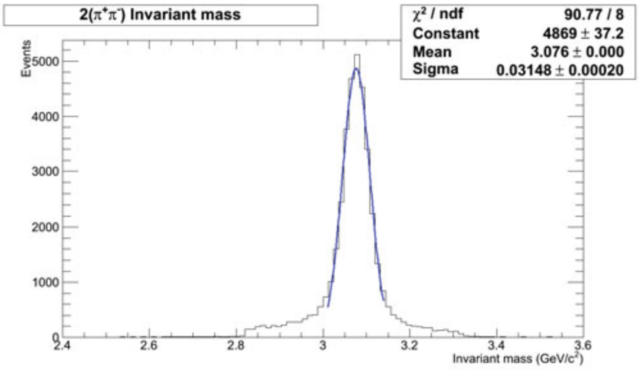

Fig. 158. $\bar{\mathrm{p}}\mathrm{p} \to 2(\pi^+\pi^-)$: Pions invariant mass distribution, without event mixing. The fit is done with a Gaussian function (see text for more details).

Channel description

The reaction

$$\bar{\mathrm{p}}\mathrm{p} \to \psi(3770) \to \mathrm{D}^+\mathrm{D}^- \to \mathrm{K}^-\pi^+\pi^+\mathrm{K}^+\pi^-\pi^-$$

at a beam momentum of 6.5788 GeV/c has a typical signature which is common for several of the channels within the scope of the $\overline{\mathsf{P}}$ANDA physics program.

Within the scope of this benchmark, its following key features are of particular interest:

- Secondary vertices with a short decay length (312 μm for the charged D mesons).
- A relatively large number of ejectiles (6 for this channel) to be reconstructed in an exclusive analysis.

The distribution of momentum and polar angle is shown for the positive kaons and pions (fig. 175) The distribution of the negatively charged particles is identical and thus not shown here. For both types the majority of particles have a momentum between 0.5 GeV/c and 3 GeV/c. While the kaons are only found in the forward hemisphere, the pions are also ejected at backwards angles due to their lower mass. However, the majority is found within a polar angle range between 5° and 60° in both cases. There is a high probability that at least one of the decay particles is strongly forward peaked.

Reconstructing this class of events requires a good interplay of the central tracking detectors MVD and STT as well as additional information from the forward tracking to detect also those particles which are ejected at shallow angles below 10°.

Resolution study

For the study of the achievable invariant mass and vertex resolutions, we simulate a large sample of signal events which have to pass an analysis chain similar to the procedure which would be used in a real experiment.

In the first step of the analysis all reconstructed track candidates which have at least one STT hit are considered for further processing. The distribution of polar and azimuthal angle of the reconstructed particles which pass the STT volume is shown in figs. 176 and 177. The presence of the target pipe is clearly visible in these plots as well as the ±10° shift in the observed ϕ position due to the bending of the oppositely charged particles' tracks in the magnetic field.

The decay particles are then combined to D^+ and D^- meson candidates. A first selection is done by requiring that the reconstructed D meson mass values differ by no more than 750 MeV/c^2 from the nominal D mass. After that, a vertex fit to the D meson decay vertices is carried out.

In the case of multiple D meson candidates of the same charge within one event, the best one is selected based on the χ^2 result from the vertex fit. Additionally, an absolute maximum limit of $\chi^2 < 18$ has been applied as quality cut (compare fig. 178).

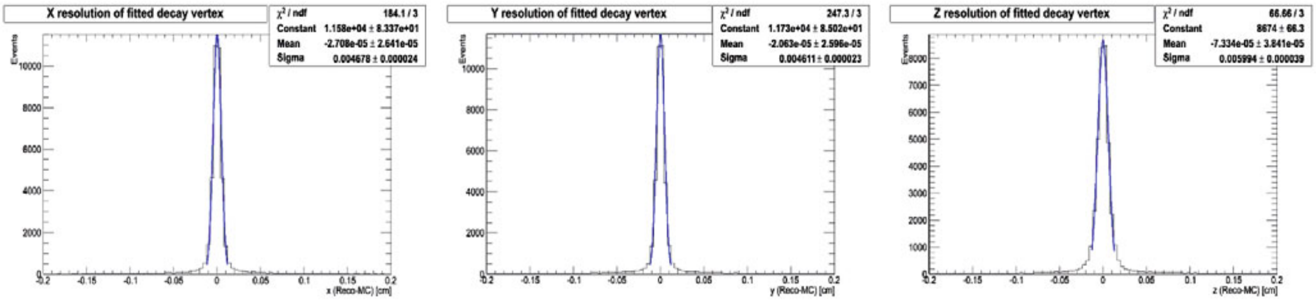

Fig. 159. $\bar{\mathrm{p}}\mathrm{p} \to 2(\pi^+\pi^-)$: Vertex resolution, without event mixing (see text for more details).

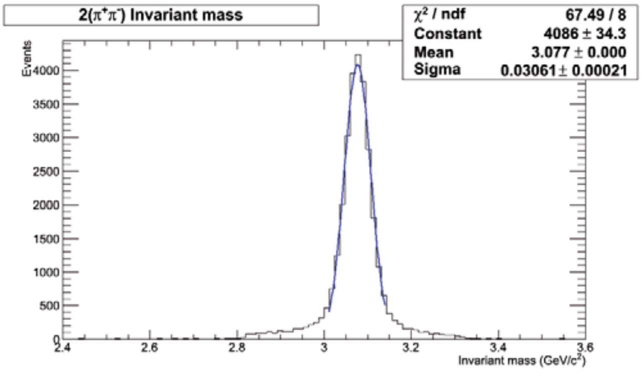

Fig. 160. $\bar{\mathrm{p}}\mathrm{p} \to 2(\pi^+\pi^-)$: Pions invariant mass distribution after clean-up procedure. The fit is done with a Gaussian function (see text for more details).

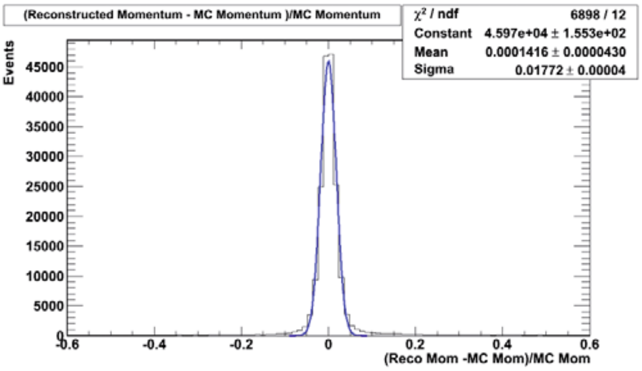

Fig. 161. $\bar{\mathrm{p}}\mathrm{p} \to 2(\pi^+\pi^-)$: Momentum resolution of the pion tracks with event mixing. The fit is done with a Gaussian function (see text for more details).

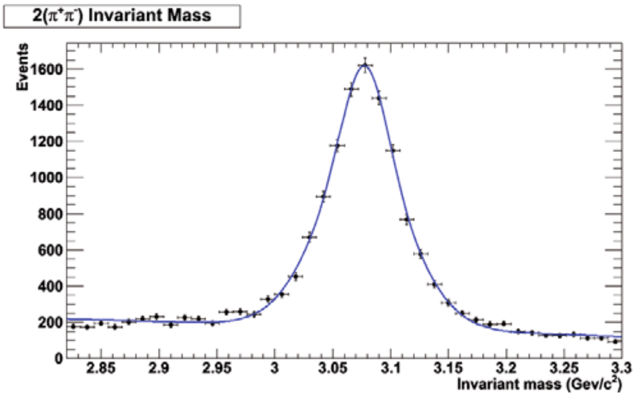

Fig. 162. $\bar{\mathrm{p}}\mathrm{p} \to 2(\pi^+\pi^-)$: Pions invariant mass distribution with event mixing. The fit is done with a double Gaussian function plus a polynomial (see text for more details).

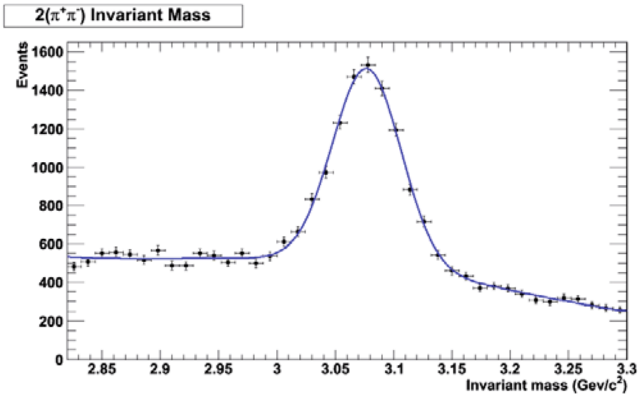

Fig. 163. $\bar{\mathrm{p}}\mathrm{p} \to 2(\pi^+\pi^-)$: Pions invariant mass distribution with event mixing and without Monte Carlo truth PID. The fit is done with a double Gaussian function plus a polynomial (see text for more details).

Results

The obtained vertex resolution is in the order of $55\,\mu$m in *xy*-direction and $104\,\mu$m in the *z*-direction (compare fig. 179). The mass resolution is in the order of $16\,\mathrm{MeV}/c^2$ after the vertex fit (compare fig. 180). The final reconstructed event sample consists of 5.9% of the initially simulated signal events, *i.e.* this fraction of the events has all tracks within the STT's geometrical acceptance and also passes all quality cuts of the analysis resulting in both D mesons of the event being successfully reconstructed. Thus, this number is a convolution of geometrical acceptance, reconstruction software performance and the settings of the quality cuts.

In addition to the pure signal, also mixed events where each signal event is overlayed with additional background events (compare sect. 7.2.1), have been analyzed

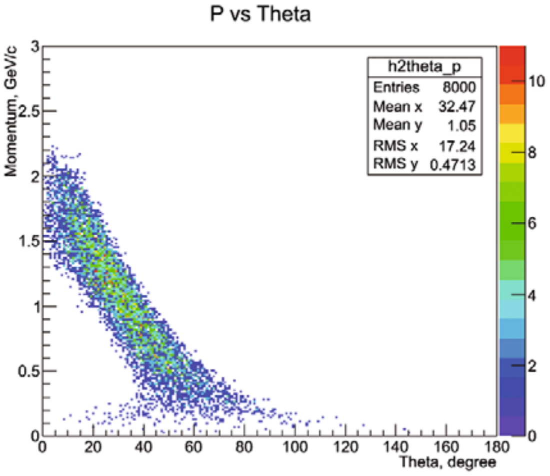

Fig. 164. Momentum *vs.* polar angle for the kaons from the reaction $\eta_c \to \phi\phi \to \mathrm{K^+K^-K^+K^-}$.

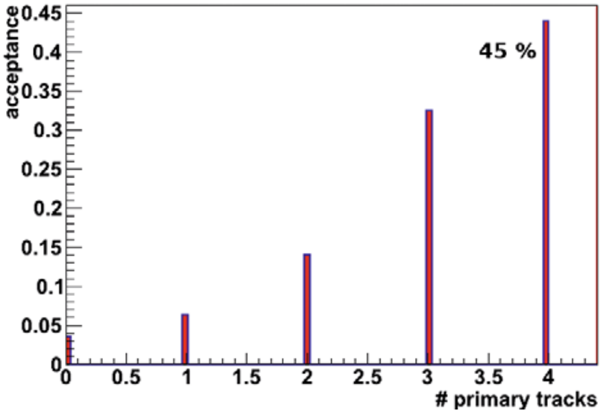

Fig. 165. Multiplicity of the kaons from the reaction $\eta_c \to \phi\phi \to \mathrm{K^+K^-K^+K^-}$ within central tracker acceptance.

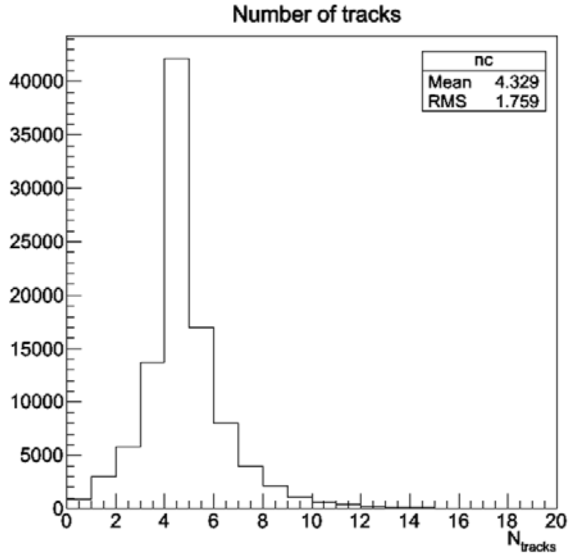

Fig. 166. Multiplicity of the reconstructed charged tracks from the reaction $\eta_c \to \phi\phi \to \mathrm{K^+K^-K^+K^-}$.

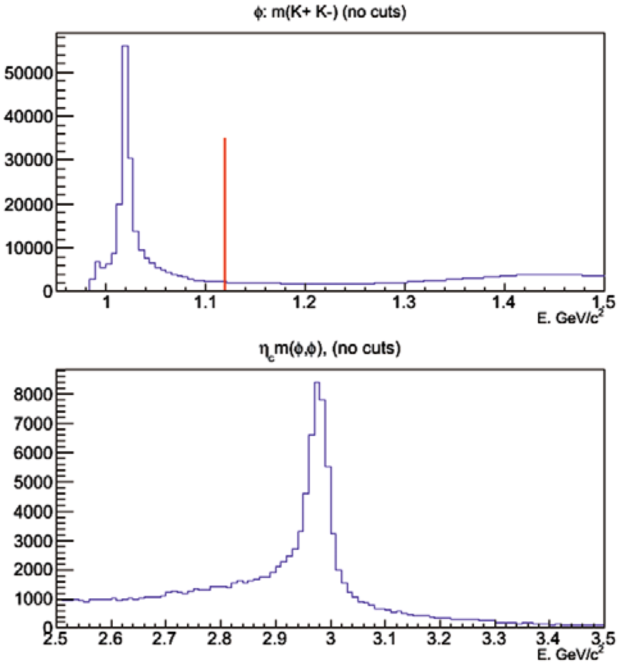

Fig. 167. Reconstructed invariant mass of $\mathrm{K^+K^-}$ pairs and $\phi\phi$ pairs with preselection on ϕ invariant mass.

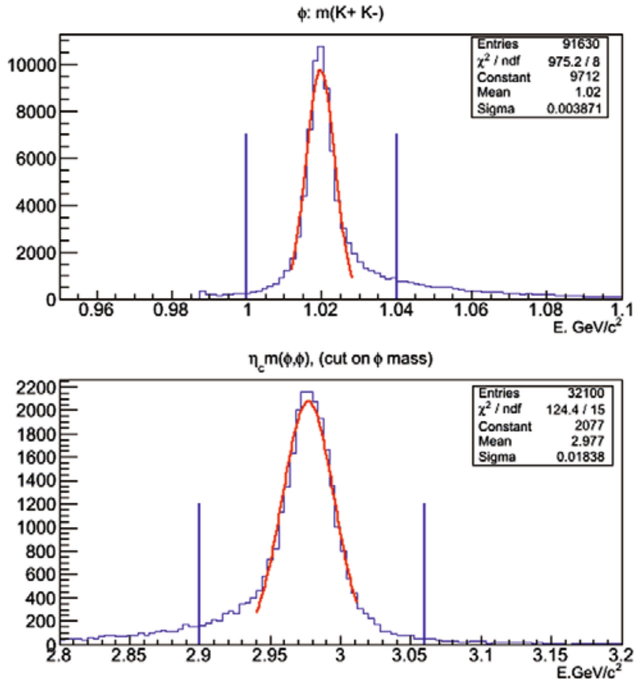

Fig. 168. Reconstructed invariant mass of $\mathrm{K^+K^-}$ pairs and $\phi\phi$ pairs after full selection chain.

to study the behavior of the reconstruction software under the influence of the additional particle tracks. The main influence of the mixed events is on the reconstruction software's efficiency which reduces the final reconstructed event sample to 3.3% of the initially simulated signal events. The resulting vertex resolutions are in the order of 61 μm (xy-direction) and 109 μm (z-direction).

The mass resolution is in the order of $17\,\mathrm{MeV}/c^2$. These resolutions are virtually the same as those obtained during the analysis of the pure signal and also the shapes of the distributions do not show any significant differences (compare fig. 181).

8 Online tracking

Effective online track finding and reconstruction is crucial for fulfilling the goals of the $\overline{\mathrm{P}}$ANDA experiment. Charged particles are used in most trigger objects, and robust, accurate charged particle reconstruction is essential for triggering on states, like J/ψ and D^0, and on interesting topologies such as displaced vertices.

8.1 Comparison with existing experiments

The challenge for $\overline{\mathrm{P}}$ANDA is to determine track parameters from the charged particles produced in $p\bar{p}$ collisions with an effective interaction rate of 20 MHz. The parameters for $\overline{\mathrm{P}}$ANDA are compared to other comparable recent experiments in table 23. The e^+e^- experiments have higher bunch crossing rates, but a lower rate of physics events due to the lower cross sections of those collisions. However, even the older CLEO III experiment performs pattern recognition over its entire drift chamber at a $\sim 20\,\mathrm{MHz}$ rate. The high-energy $p\bar{p}/pp$ experiments at the Tevatron and LHC have rates comparable to those expected for $\overline{\mathrm{P}}$ANDA, and so are a better comparison. CDF and DØ both perform track finding and fitting in their trigger systems, and upgrades for CMS and ATLAS are being planned that would allow for full online track reconstruction and fitting, in much larger detectors and at twice the rate of $\overline{\mathrm{P}}$ANDA. A simple order-of-magnitude comparison is illustrative of the challenges $\overline{\mathrm{P}}$ANDA faces. The $\overline{\mathrm{P}}$ANDA STT has roughly the same number of channels as DØ's fiber tracker, and an order of magnitude fewer channels than CDF's main drift chamber. Although $\overline{\mathrm{P}}$ANDA's expected event rate is 2–3 times that seen at the Tevatron, the expected track multiplicities are an order of magnitude smaller. Since the hardware used for online tracking in $\overline{\mathrm{P}}$ANDA is of similar or faster speed than CDF and DØ's systems, we fully expect that accurate online track reconstruction is possible at $\overline{\mathrm{P}}$ANDA.

8.2 Online strategy for $\overline{\mathrm{P}}$ANDA

The online track reconstruction will take advantage of the "Compute Nodes", which each contain several modern FPGAs with large associative memories that run at high clockspeeds. For example, track finding is easily parallelizable by segmenting the detector so multiple nodes can simultaneously search for tracks over the entire geometry. The low track multiplicity further simplifies the problem, and should allow for a simplified fitting algorithm.

Traditional trigger systems have a well-defined heirarchy of levels. However, with $\overline{\mathrm{P}}$ANDA's "triggerless" design, it makes more sense to describe the series of tasks that are performed. An example of such a flow is: Track Segment Finding → Track Linking → Track Fitting. The algorithms used by the experiments given in table 23 are all generally similar, with tracks being found by algorithms such as a Hough transformation or road following algorithm, and then fitted by a simple χ^2 fit. The determining factor, then, is how these algorithms perform for the topologies that $\overline{\mathrm{P}}$ANDA will eventually trigger on. Several algorithms are being implemented, and will be tested for their efficiency and robustness against pathologies such as displaced vertices and low-momentum tracks that curl in the magnetic field of the detector, and will be benchmarked using the physics channels given in sect. 7.2.

9 Organization

9.1 Production logistics

The $\overline{\mathrm{P}}$ANDA-STT is a modular detector. It consists of a set of individual detector components which can be produced and tested independently before the final installation. The construction procedure (see sect. 2.3.4) is such that the realization of the whole detector can be easily split on different sites. First of all, single tubes are assembled and tested individually; then multi-layer modules are realized; finally, the modules are mounted in the mechanical support. This will be extremely useful to reduce the time needed for the detector construction.

Even if the straw tubes are operated with an overpressure of about 1 bar of the gas mixture, they still have sufficient strength to maintain the 50 g wire tension without overpressure. Therefore, single tubes can be constructed and stored in appropriate places to be ready for the multilayer assembling later on.

At present, both the Forschungszentrum Jülich and the LNF laboratories are equipped with the necessary tools to start the production of straw tubes and modules. They both have a clean room (10000 class), a v-shaped reference plane (fig. 182) and the same expertise for starting a mass production. However, a clean room is not absolutely necessary. The straw tube components (cathodes, pins, end-plugs, etc.) have to be cleaned before starting the assembly procedure. Thus, if this work is realized in an environment where the dust concentration is under control, this could be done in one step before starting the single tubes production. If a clean room is not available, greater care has to be placed in this cleaning phase, which has to precede the straw tube assembly. The only required tool to produce straw tube modules is the v-shaped reference plane. This object is a precisely manufactured mechanical plate that guarantees that the spacing of the straw wires within a multi-layer meets the specifications ($\pm 50\,\mu\mathrm{m}$).

9.2 Safety

The design details and construction of the STT including the infrastructure for operation will be done according to the safety requirements of FAIR and the European and

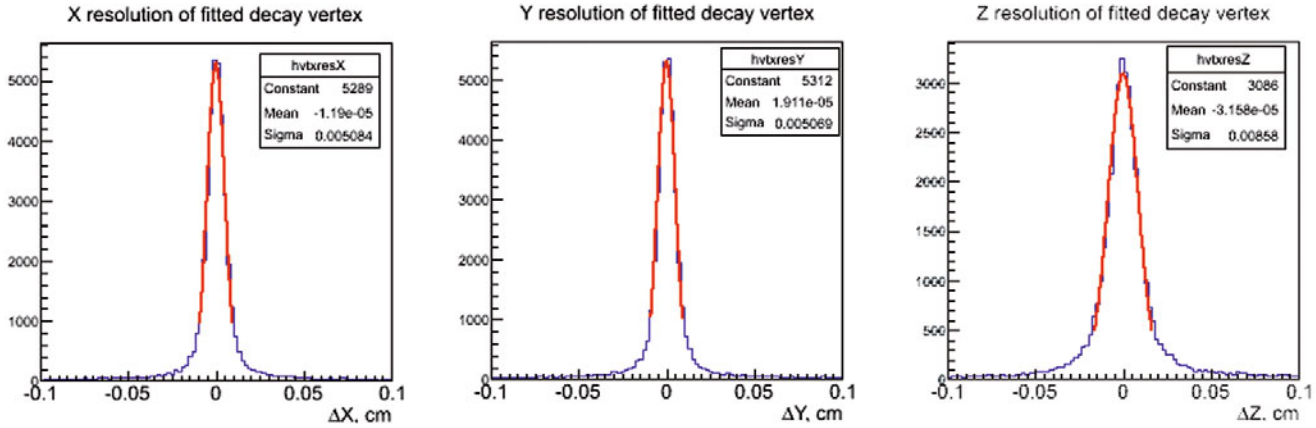

Fig. 169. Resolution of the reconstructed primary vertex of η_c from the reaction $\eta_c \rightarrow \phi\phi \rightarrow \mathrm{K}^+\mathrm{K}^-\mathrm{K}^+\mathrm{K}^-$.

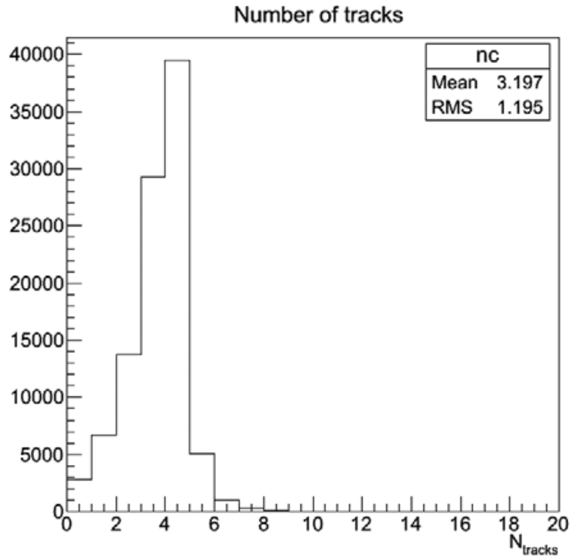

Fig. 170. Multiplicity of the reconstructed charged tracks from the reaction $\eta_c \rightarrow \phi\phi \rightarrow \mathrm{K}^+\mathrm{K}^-\mathrm{K}^+\mathrm{K}^-$ after applying clean-up procedure.

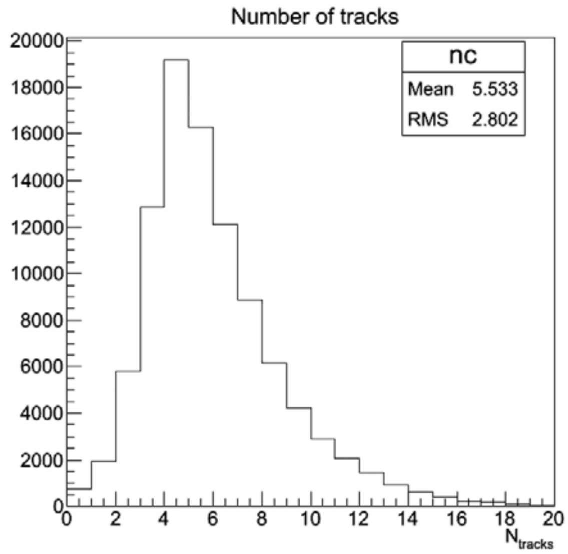

Fig. 171. Multiplicity of the reconstructed charged tracks from the reaction $\eta_c \rightarrow \phi\phi \rightarrow \mathrm{K}^+\mathrm{K}^-\mathrm{K}^+\mathrm{K}^-$ with background mixing.

German safety regulations. All electrical equipment and gas systems will comply with the legally required safety code and concur to standards for large scientific installations to ensure the protection of all personnel working at or close to the components of the $\overline{\mathrm{P}}$ANDA experimental facility. Hazardous voltage supplies and lines will be marked visibly and protected from damage by any equipment which may cause forces to act on them. All supplies will be protected against over-current and over-voltage and have appropriate safety circuits and fuses. All cabling and connections will use non-flammable halogen-free materials according to up-to-date standards and will be dimensioned with proper safety margins to prevent overheating. A safe ground scheme will be employed throughout all electrical installations of the experiment. Smoke detectors will be mounted in all appropriate locations. The gas system is based upon non-flammable gases and thus does not pose a fire hazard. The maximum pressure of the gas will be regulated, and the system is designed such that a sudden failure of one tube (operating at maximally 2 bar) cannot damage the adjacent tubes (that have equal or higher pressure than the escaping gas), and thus a chain reaction is ruled out. Appropriate measures will be taken during installation and maintenance to avoid damage to or by the STT. The outer foil will protect the device against potential condensation risks from other components of $\overline{\mathrm{P}}$ANDA. More specific safety considerations are discussed in the respective sections throughout this document.

9.3 Timeline

The projected timeline of the STT construction is based on the experience gained during the R&D and prototyping phase of the STT project and similar, former detector

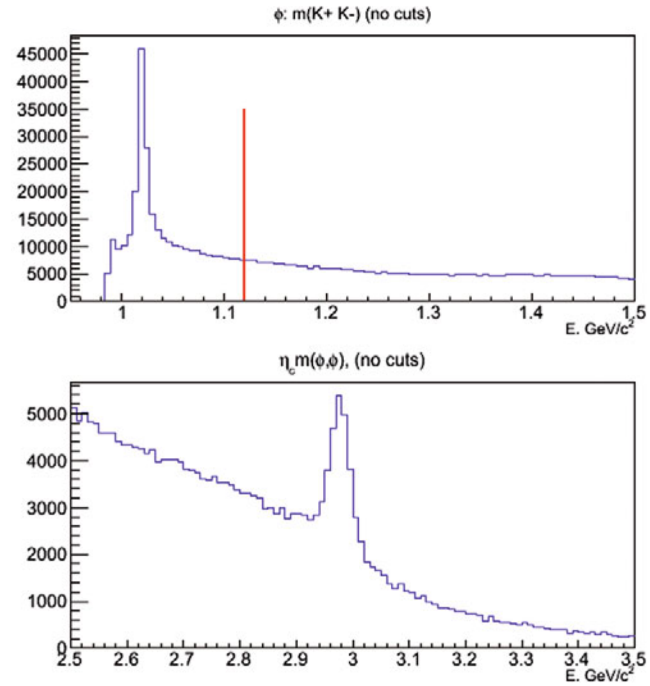

Fig. 172. Reconstructed invariant mass of K^+K^- pairs and $\phi\phi$ pairs with preselection on ϕ invariant mass with background mixing.

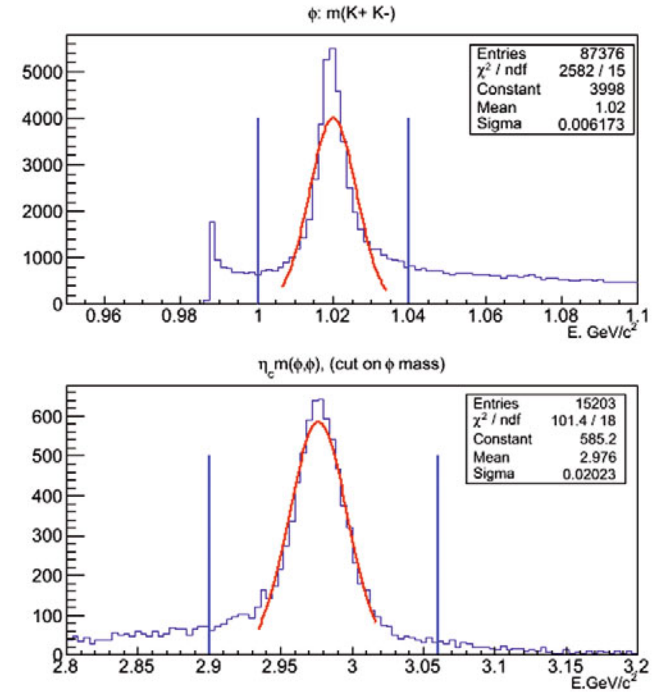

Fig. 174. Reconstructed invariant mass of K^+K^- pairs and $\phi\phi$ pairs after full selection chain with background mixing and without Monte Carlo truth PID.

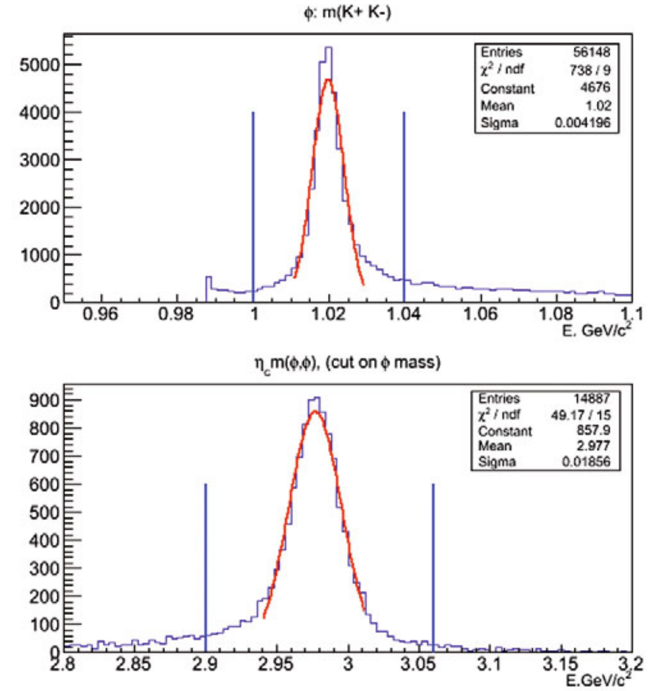

Fig. 173. Reconstructed invariant mass of K^+K^- pairs and $\phi\phi$ pairs after full selection chain with background mixing.

projects of the different group institutions. In particular the construction experience from the Straw Tube Tracker at COSY, consisting of about 3200 straws in total and similar assembly techniques, is a major input for the definition of the construction packages and time scales for the $\overline{\text{P}}$ANDA-STT realization.

The timeline of the STT construction consists of four main periods: the completion of the final design; the main construction phase; the final assurance test of the assembled STT with cosmics; and the pre-assembly of the STT in the $\overline{\text{P}}$ANDA target spectrometer. The detailed timeline shown in fig. 183 lists the different construction items and their projected time slots. After the TDR is approved, the funding applications will start and the workshop time slots for the project will be booked.

The first phase of the STT construction with the definition of the complete final design has already started and will be finished by the middle of 2013. Here, all designs, the mechanical parts with straws and frame structure as well as the electronic readout parts, cables, and systems, have to be designed in detail. The integration of the detector in the $\overline{\text{P}}$ANDA central spectrometer will be made and the main dimensions, environment conditions, and requirements will be defined and assigned. Few aspects are still under discussion concerning the final mechanical layout, including cable and services routing, and the final electronic readout design. The latter decision between the two current electronic readout options will be based on further test measurements with existing prototype setups, consisting of up to 400 straws. Within the next 12 months this decision will be made, latest by the middle of 2013.

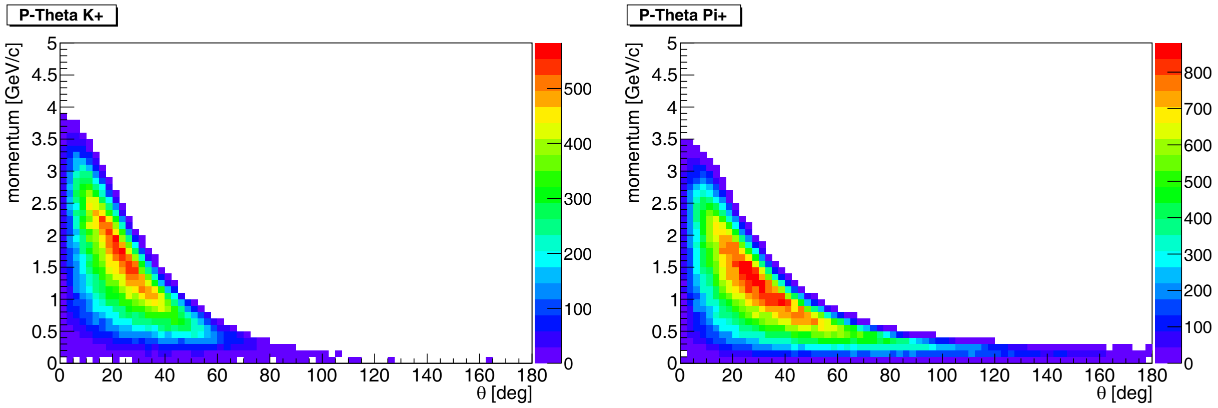

Fig. 175. Momentum and polar angle distribution of the generated kaons (left) and pions (right).

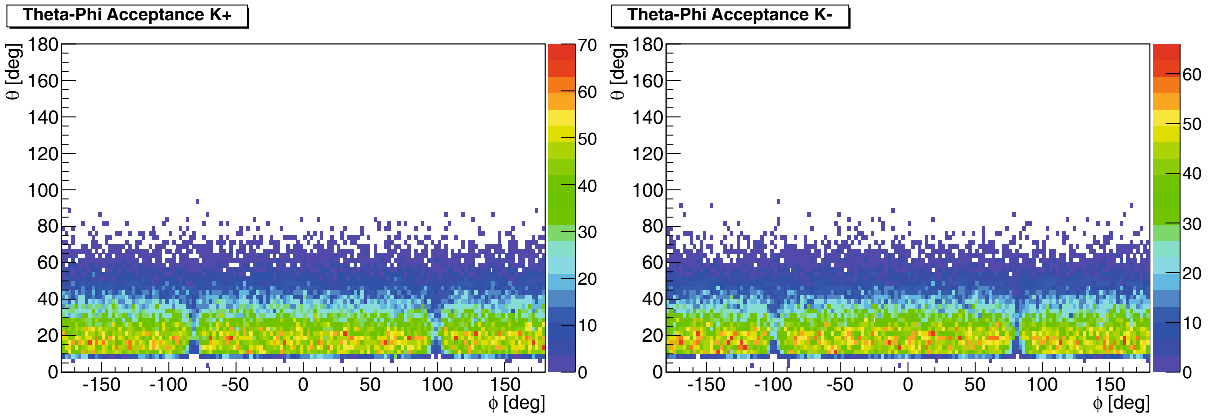

(a) (b)

Fig. 176. Polar and azimuthal angle distribution of the reconstructed kaons. (a) K^+ angular distribution; (b) K^- angular distribution.

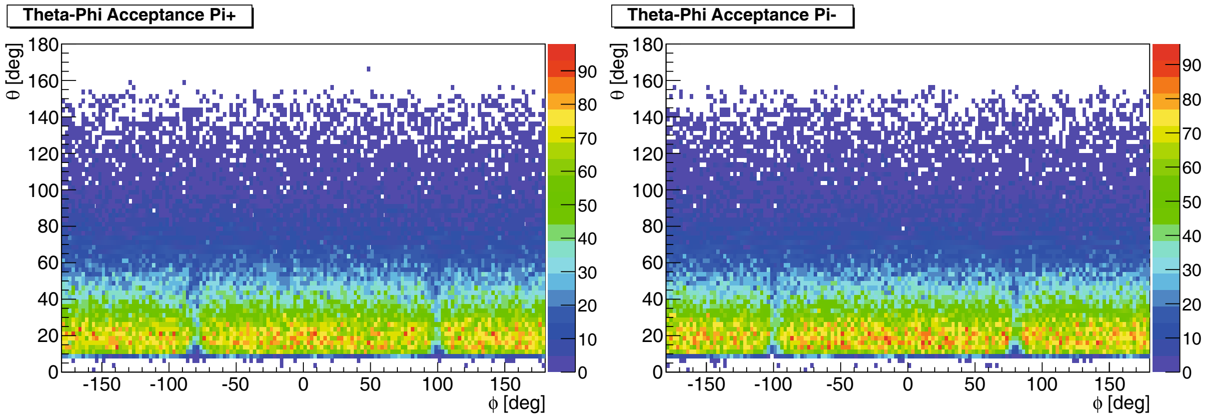

(a) (b)

Fig. 177. Polar and azimuthal angle distribution of the reconstructed pions. (a) π^+ angular distribution; (b) π^- angular distribution.

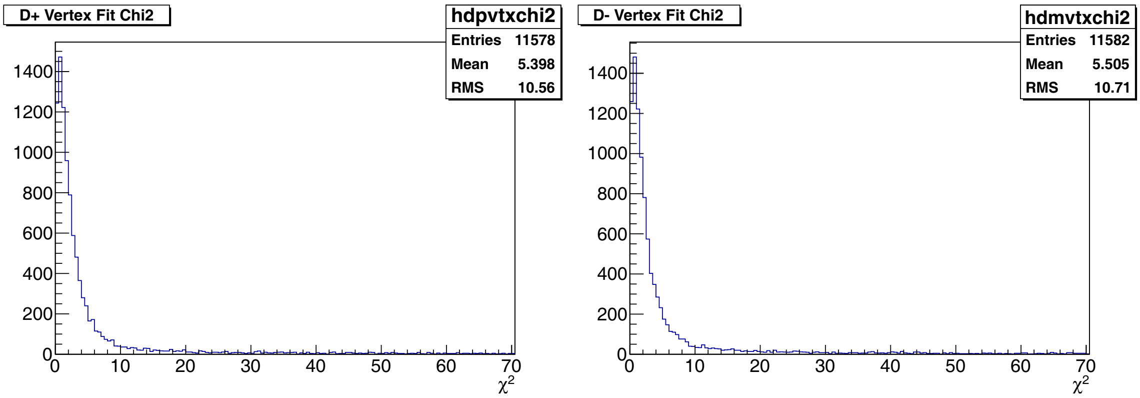

(a) (b)

Fig. 178. χ^2 distribution of the D meson decay vertex fit. (a) D^+; (b) D^-.

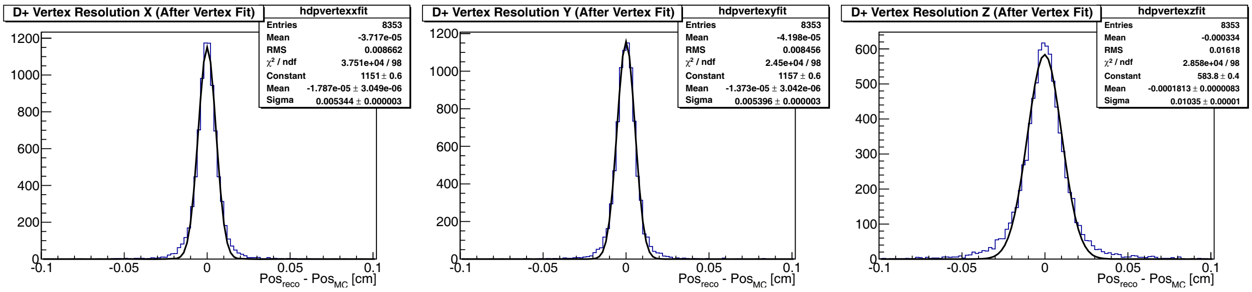

Fig. 179. Spatial resolution of the reconstructed D^+ decay vertex.

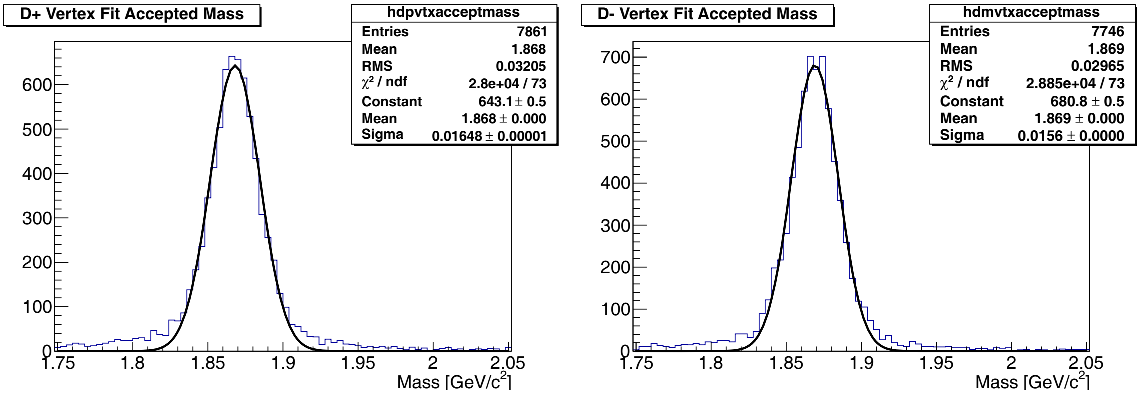

Fig. 180. Mass resolution of the reconstructed D mesons after the vertex fit.

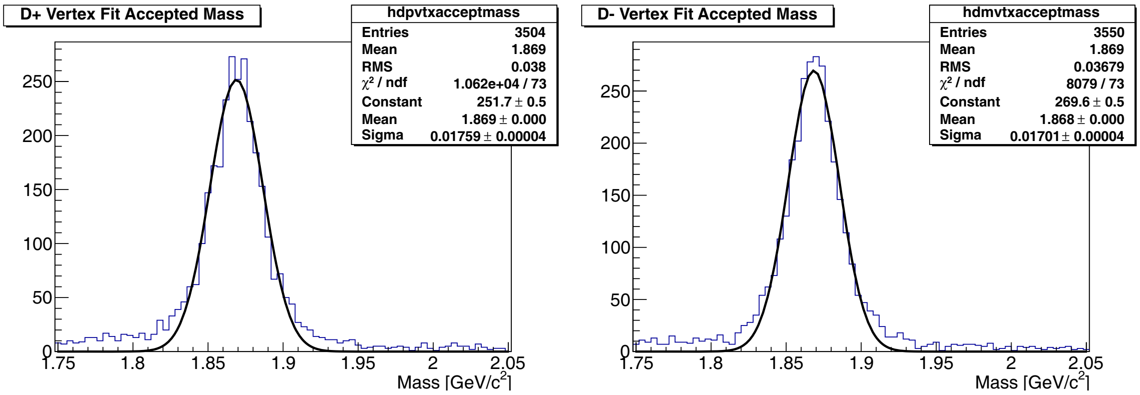

Fig. 181. Mass resolution of the reconstructed D mesons after the vertex fit for mixed events.

Table 23. Summary of event rate and tracking chamber parameters for various experiments comparable to $\overline{\text{P}}$ANDA. For the $\overline{\text{P}}$ANDA-STT the average number of layers is given.

	Event rate	Trigger rate (L1/(L2)/L3)	Avg. track multi.	Layers	Cell size (mm)
e^+e^- Experiments					
CLEO III [107,108]	250 kHz	< 1 kHz/130 Hz	$\sim$ 8 ($B\overline{B}$) 2 (e^+e^-)	47	7
BaBar [109]	2 kHz	970 Hz/120 Hz		40	6–8
Belle [110]	5 kHz	500 Hz/500 Hz		50	8–10
BES–III [111]	$\sim$ 3 kHz	> 4 kHz/3 kHz	$\sim$ 4	43	6–8
ep Experiments					
ZEUS [112,113]	$\sim$1 MHz	600 Hz/100 Hz/20 Hz	$\sim$ 10	72	$\sim$ 25
H1 [114–116]		1 kHz/200 Hz/50 Hz/$\sim$10 Hz		56	23–43
pp + p$\bar{\text{p}}$ Experiments					
CDF [117–119]	7.5 MHz	30 kHz/750 Hz/75 Hz	$\sim$ 35	96	8.8
DØ [120,121]		10 kHz/1.5 kHz/50 Hz		32	0.4
CMS [122]	$\leq$40 MHz	100 kHz/$\sim$ 100 Hz	> 100	$\sim$ 12	—
ATLAS [123,124]		100 kHz/2 kHz/200 Hz		36	2
$\overline{\text{P}}$ANDA	$\sim$ 20 MHz		$\sim$ 4 − 6	24	10

Fig. 182. v-shaped reference plate for multi-layer assembly.

Table 24. Work package list with involved institutions.

Work package	Involved institutes
Straw tube materials	**FZ-J** LNF
Mechanical frame	**LNF** FZ-J
Front End Electronics, DAQ, Low and High voltages	**FZ-J** AGH **JU** IFJ GSI
Crates, cables	LNF FZ-J IFIN-HH
Slow control	**IFIN-HH**
Gas system	**LNF**
Online tracking	**NU**
Monitoring calibration	**PV** Fe

At the end of the design phase all technical specifications are fixed and technical drawings are prepared to start the tendering and order processes at the external production companies. Since most of the involved production companies have been already contacted during the R&D phase of the project or during former similar projects, we estimate not more than about 18 months for sending out tenders, placing orders, and delivery times for the external components.

The main construction phase of the STT assembly will take about 30 months for the mass production of 6000 straw tubes (about 30% spare), gluing of the straw layers, construction of the mechanical frame, and insertion of the straw layers in the frame structure. The assembly will be split between the two main involved laboratories, Forschungszentrum Jülich and INFN Frascati. At both sites clean rooms (class 10000) are available for the construction. The straw mass production already in-

	Task/Year	2012		2013		2014		2015		2016	
		I	II	I	II	I	II	I	II	I	II
1	TDR Central Tracker	🟦									
2	Funding applications		🟦	🟦							
3	Allocation of workshop time slots			🟦							
4	Final design	🟥	🟥								
4.1	Mechanical design	🟦	🟦								
	Straw design and layout	🟦	🟦								
	Straw tube materials	🟦	🟦								
	Straw layer design (axial, stereo)	🟦	🟦								
	Mechanical frame structure	🟦	🟦								
	Support and alignment structures	🟦	🟦								
	Electronics support cage	🟦	🟦								
	Final decision of mechanical design		■								
4.2	Electronics readout	🟦	🟦	🟦	🟦						
	Frontend electronics R&D	🟦	🟦	🟦	🟦						
	Digitizers and readout R&D	🟦	🟦	🟦	🟦						
	Test measurements (beam, cosmics)	🟦	🟦	🟦	🟦						
	Final decision of electronics readout				■						
4.3	Gas system		🟦	🟦							
4.4	Slow control		🟦	🟦							
4.5	Integration in the PANDA central spectrometer				🟦						
4.6	Final design freeze				■						
5	Tenders and orders				🟦	🟦	🟦	🟦			
6	Construction				🟥	🟥	🟥	🟥	🟥	🟥	
6.1	Straw mass production and assurance tests			🟦	🟦	🟦	🟦	🟦			
6.2	Straw layers production and assurance tests				🟦	🟦	🟦	🟦	🟦		
6.3	Mechanical frame construction					🟦	🟦				
6.4	Assembly of straw layers in mechanical frame							🟦	🟦		
6.5	Electronics readout and production					🟦	🟦	🟦	🟦		
6.6	Gas system and supply lines						🟦	🟦	🟦		
6.7	Slow control system							🟦	🟦		
6.7	Mounting STT electronics									🟦	
7	STT commissioning with cosmics (data taking)										🟦■
8	STT preassembly in PANDA										🟥

Fig. 183. Timeline for the STT realization. Milestones are marked in black.

cludes assurance tests of gas leakage and wire tension measurements of each assembled straw. Individual straws showing gas leakage, deviation from the nominal wire tension, or broken wires are rejected. For the previous prototype constructions with about 1000 straws, the fraction of straws showing such failures was about one percent.

The straws are glued to the axial and stereo layer modules with integrated gas manifolds and electronic coupling boards. For the final assurance test of all straws in a layer module, the module is flushed with an Ar/CO_2 gas mixture, straws are set on high voltage, a test board containing a preamplifier circuit is connected to the coupling boards and the signals from cosmic tracks are checked to identify dead or improper straws. Bad identified straws are removed from a layer module and replaced by single new straws. The modular layout of the STT allows to carry out the most time consuming construction steps of the straw mass production and layer module assembly highly in parallel. As soon as the first couple of hundred straws are produced and tested, we can start with the construction of the first layer modules. After the completion of the mechanical frame structure the layer modules are inserted and fixed to the frame.

In parallel to the mechanical STT assembly the electronic parts, cables, and readout boards will be produced and the complete readout system will be set up. After a test of all electronic channels with test pulses, the readout will be mounted in the STT mechanical frame structure and connected to the straws. By the first half of 2016 the construction phase will be finished including the setup of the gas system and slow control system.

In the second half of 2016 the final commissioning of the full STT detector will be done with data takings of cosmic ray tracks to set up the whole electronic readout and to calibrate the STT geometry with reconstructed tracks. After finishing these tests the detector will be ready for installation and pre-assembly in the $\overline{\mathsf{P}}$ANDA central spectrometer.

9.4 Work packages and contributing institutes

The design, construction and installation of the STT will be performed by a number of institutions which have gained specific expertise in past and ongoing large scale experiments at several accelerator facilities. The responsibilities for the various work packages are listed in table 24, in which the coordinating group of the task is denoted by boldface. A summary of the participating groups and of their members is given below:

- IFIN-HH Bukarest-Magurele, Romania (M. Bragadireanu, M. Caprini, D. Pantea, D. Pantelica, D. Pietreanu, L. Serbina, P.D. Tarta) (**IFIN-HH**);
- IFJ PAN, Cracow, Poland (B. Czech, M. Kistryn, S. Kliczewski, A. Kozela, P. Kulessa, P. Lebiedowicz, K. Pysz, W. Schäfer, R. Siudak, A. Szczurek) (**IFJ**);
- Jagiellonian University of Cracow, Poland (S. Jowzaee, M. Kajetanowicz, B. Kamys, S. Kistryn, G. Korcyl, K. Korcyl, W. Krzemien, A. Magiera, P. Moskal, Z. Rudy, P. Salabura, J. Smyrski, A. Wroñska) (**JU**);
- AGH Cracow, Poland (T. Fiutowski, M. Idzik, B. Mindur, D. Przyborowski, K. Swientek) (**AGH**);
- Gesellschaft für Schwerionenforschung GmbH, Darmstadt, Germany (M. Traxler) (**GSI**);
- INFN Frascati, Italy (N. Bianchi, D. Orecchini, P. Gianotti, C. Guaraldo, V. Lucherini, E. Pace) (**LNF**);
- FZ Jülich, Germany (A. Erven, G. Kemmerling, H. Kleines, V. Kozlov, N. Paul, M. Mertens, R. Nellen, H. Ohm, S. Orfanitski, J. Ritman, T. Sefzick, V. Serdyuk, P. Wintz, P. Wüstner) (**FZ-J**);
- INFN and Univ. of Pavia, Italy (G. Boca, A. Braghieri, S. Costanza, P. Genova, L. Lavezzi, P. Montagna, A. Rotondi) (**PV**);
- INFN and Univ. of Ferrara, Italy (D. Bettoni, V. Carassiti, A. Cotta Ramusino, P. Dalpiaz, A. Drago, E. Fioravanti, I. Garzia, M. Savriè, G. Stancari) (**Fe**);
- Northwestern Univ., Evanston U.S.A. (S. Dobbs, K. Seth, A. Tomaradze, T. Xiao) (**NU**).

We acknowledge financial support from the Bundesministerium für Bildung und Forschung (bmbf), the Deutsche Forschungsgemeinschaft (DFG), the Forschungszentrum Jülich GmbH, the University of Groningen, Netherlands, the Gesellschaft für Schwerionenforschung mbH (GSI), Darmstadt, the Helmholtz-Gemeinschaft Deutscher Forschungszentren (HGF), the Schweizerischer Nationalfonds zur Förderung der wissenschaftlichen Forschung (SNF), the Russian funding agency "State Corporation for Atomic Energy Rosatom", the CNRS/IN2P3 and the Université Paris-sud, the British funding agency "Science and Technology Facilities Council" (STFC), the Instituto Nazionale di Fisica Nucleare (INFN), the Swedish Research Council, the Polish Ministry of Science and Higher Education, the European Community FP6 FAIR Design Study: DIRAC secondary-Beams, contract number 515873, the European Community FP7 Integrated Infrastructure Initiative: HadronPhysics2, contract number 227431, the INTAS, and the Deutscher Akademischer Austauschdienst (DAAD).

References

1. $\overline{\mathsf{P}}$ANDA Collaboration, letter of intent for $\overline{\mathsf{P}}$ANDA - *Strong Interaction Studies with Antiprotons*, Technical report FAIR-ESAC (2004).
2. GSI Helmholtzzentrum für Schwerionenforschung, FAIR - An International Accelerator Facility for Beams of Ions and Antiprotons, Baseline technical report (2006) `http://www.gsi.de/fair/reports/btr.html`.
3. Technical report, `http://www.fair-center.de/fileadmin/fair/publications_FAIR/FAIR_GreenPaper_2009.pdf`.
4. P. Spiller, G. Franchetti, Nucl. Instrum. Methods A **561**, 305 (2006).
5. W.F. Henning, Nucl. Instrum. Methods A **805**, 502c (2008).
6. $\overline{\mathsf{P}}$ANDA Collaboration, Physics Performance Report (2009) `arXiv:0903.3905v1`.
7. FAIR Technical Design Report, HESR, Technical report, Gesellschaft für Schwerionenforschung (GSI) Darmstadt (2008) `http://www-win.gsi.de/FAIR-EOI/PDF/TDR_PDF/TDR_HESR-TRV3.1.2.pdf`.
8. A. Lehrach *et al.*, Int. J. Mod. Phys. E **18**, 420 (2009).
9. B. Gålnander *et al.*, Proc. EPAC08, Genoa, Italy **THPP049**, 3473 (2008).
10. H. Stockhorst, D. Prasuhn, R. Maier, B. Lorentz, AIP Conf. Proc. **821**, 190 (2006).
11. B. Lorentz *et al.*, Proc. EPAC08, Genoa, Italy **MOPPC112**, 325 (2008).
12. D. Welsch *et al.*, Proc. EPAC08, Genoa, Italy **THPC076**, 3161 (2008).
13. A. Lehrach *et al.*, Nucl. Instrum. Methods A **561**, 289 (2006).
14. F. Hinterberger, in *Beam-Target Interaction and Intrabeam Scattering in the HESR Ring*, Report of the Forschungszentrum Jülich (2006) Jül-4206, ISSN 0944-2952.
15. O. Boine-Frankenheim, R. Hasse, F. Hinterberger, A. Lehrach, P. Zenkevich, Nucl. Instrum. Methods A **560**, 245 (2006).
16. D. Reistad *et al.*, *Proceedings of the Workshop on Beam Cooling and Related Topics COOL2007, Bad Kreuznach, MOA2C05* (2007) p. 44.

17. H. Stockhorst *et al.*, Proc. EPAC08, Genoa, Italy **THPP055**, 3491 (2008).
18. A. Täschner *et al.*, Nucl. Instrum. Methods A **660**, 22 (2011).
19. C. Bargholtz *et al.*, Nucl. Instrum. Methods A **587**, 178 (2008).
20. M. Büscher *et al.*, AIP Conf. Proc. **814**, 614 (2006).
21. M. Büscher *et al.*, Int J. Mod. Phys. E **18**, 505 (2009).
22. A. Smirnov *et al.*, in *Proceedings of COOL2009, Lanzhou, China, MOM2MCIO02.*
23. $\overline{\text{P}}$ANDA Collaboration, Technical Design Report for the Solenoid and Dipole Spectrometer Magnets, `arXiv:0907.0169v1` (2009).
24. H. Staengle *et al.*, Nucl. Instrum. Methods A **397**, 261 (1997).
25. K. Mengel *et al.*, IEEE Trans. Nucl. Sci. **45**, 681 (1998).
26. R. Novotny *et al.*, IEEE Trans. Nucl. Sci. **47**, 1499 (2000).
27. M. Hoek *et al.*, Nucl. Instrum. Methods A **486**, 136 (2002).
28. $\overline{\text{P}}$ANDA Collaboration, EMC Technical Design Report, Technical report, Darmstadt (2008) `arXiv:0810.1216v1`.
29. N. Akopov *et al.*, Nucl. Instrum. Methods A **479**, 511 (2002).
30. I.-H. Chiang *et al.*, KOPIO Proposal (1999) `http://project-x-kaons.fnal.gov/detector/Kopio%20proposal.pdf`.
31. I. Peric, Nucl. Instrum. Methods A **582**, 876 (2007).
32. P. Fabbricatore *et al.*, IEEE Trans. Appl. Supercond. **9**, 847 (1999).
33. Mylar, polyester film, registered trademark of DuPont, `www.dupont.com`.
34. Thermo-plastic, Acrylonitrile-Butadiene-Styrene.
35. P. Wintz, A large tracking detector in vacuum consisting of self-supporting straw tubes, in *Intersections of Particle and Nuclear Physics: 8th Conference CIPANP2003*, Vol. **698**, issue 1, AIP Conf. Proc. (2004) pp. 789–792.
36. L. Aysto *et al.*, Conceptual Design Report, GSI, Darmstadt (2001).
37. R. Veenhof, *GARFIELD, Simulation of gaseous detectors*, version 7.04 edition, CERN Program library write-up W 5050.
38. C. Avanzini *et al.*, Nucl. Instrum. Methods A **449**, 237 (2000).
39. Pattex plastik is an Henkel product, `www.pattex.de/Pattex_Plastic.1514.0.html`.
40. UHU endfest 300, UHU GmbH & Co. KG - P.O. Box 1552, D-77813 Bühl, `www.uhu.de`.
41. Loctite 408, Henkel Loctite Europe, Gutenbergstr. 3, 85748 Garching, `www.henkel.com`.
42. L. Benussi *et al.*, Nucl. Instrum. Methods A **419**, 648 (1998).
43. E. Basile *et al.*, IEEE Trans. Nucl. Sci. **53**, 1375 (2006).
44. Bronkhorst High-Tech, Nijverheidsstraat 1A, NL-7261 AK Ruurlo (NL), `http://www.bronkhorst.com`.
45. Garfield - simulation of gaseous detectors, `http://garfield.web.cern.ch/garfield/`.
46. I. Peric *et al.*, Nucl. Instrum. Methods A **565**, 178 (2006).
47. T. Kugathasan, G. Mazza, A. Rivetti, L. Toscano, *A* $15\,\mu$*W 12-bit Dynamic Range Charge Measuring Front-End in* $0.13\,\mu$*m CMOS*, IEEE Nuclear Science Symposium Conference Record (2010) pp. 1667–1673.
48. J. Kalisz, IEEE Trans. Instrum. Meas. **46**, 55 (1997).
49. J. Wu, *The 10-ps wave union TDC: Improving FPGA TDC resolution beyond its cell delay*, IEEE Nuclear Science Symposium Conference Record (2008) pp. 1082–3654.
50. E. Bayer, IEEE Trans. Nucl. Sci. **58**, 1547 (2011).
51. J. Wu, *ADC and TDC implemented using FPGA*, IEEE Nuclear Science Symposium Conference Record (2007) pp. 281–286.
52. C. Ugur, GSI annual report (2010).
53. Experimental Physics and Industrial Control System, Technical report, Argonne National Laboratory, `http://www.aps.anl.gov/epics/`.
54. G. Avolio *et al.*, Nucl. Instrum. Methods A **523**, 309 (2004).
55. A. Biscossa *et al.*, Nucl. Instrum. Methods A **419**, 331 (1998).
56. M. Bellomo *et al.*, Nucl. Instrum. Methods A **573**, 340 (2007).
57. S. Costanza, *Design of the Central Tracker of the* $\overline{\text{P}}$ANDA *experiment*, PhD thesis, Università degli Studi di Pavia (2010).
58. B. Aubert *et al.*, Nucl. Instrum. Methods A **479**, 1 (2002).
59. M. Ablikim *et al.*, Nucl. Instrum. Methods A **614**, 345 (2010).
60. G. Agakishiev *et al.*, Eur. Phys. J. A **41**, 243 (2009).
61. W. Blum, W.R.R. Rolandi, *Particle Detection with Drift Chambers* (Springer Verlag, Berlin, 1994).
62. A. Alikhanov *et al.*, Proc. CERN Symp. High Energy Acc. Pion Phys. **2**, 87 (1956).
63. W. Allison, J. Cobb, Annu. Rev. Nucl. Part. Sci. **30**, 253 (1980).
64. B. Dolgoshein, Nucl. Instrum. Methods A **433**, 533 (1999).
65. V. Bashkirov *et al.*, Nucl. Instrum. Methods A **433**, 560 (1999).
66. T. Akesson *et al.*, Nucl. Instrum. Methods A **474**, 172 (2001).
67. E. Badura *et al.*, Part. Nucl. Lett. **1**, 73 (2000).
68. M. Newcomer, IEEE Trans. Nucl. Sci. **40**, 630 (1993).
69. M. Hohlmann, C. Padilla, N. Tesch, M. Titov, Nucl. Instrum. Methods A **494**, 179 (2002).
70. T. Ferguson *et al.*, Nucl. Instrum. Methods A **478**, 254 (2002).
71. M. Titov, *Innovative detectors for supercolliders*, in *Proceedings of the 42nd Workshop of the INFN ELOISATRON Project*, edited by E. Nappi, J. Seguinot (World Scientific Publishing Co. Pte. Ltd., 2004) pp. 199–226, ISBN 9789812702951 arXiv:physics/0403055v2.
72. A. Gillitzer *et al.*, *Strangeness Physics at COSY-TOF*, Technical report, Forschungszentrum Jülich (2007) COSY Proposal no. 178.
73. P. Wintz, *Commissioning of the COSY-TOF Straw Tube Tracker and the silicon-microstrip Quirl*, Technical report, Forschungszentrum Jülich (2007) COSY Proposal no. 179.
74. F. Sauli, *Principles of operation of multiwire proportional and drift chambers*, Technical report, CERN 77-09, Geneva (1977).
75. F. Lapique, F. Piuz, Nucl. Instrum. Methods **175**, 297 (1980).
76. J. Fischle, H. Heintze, B. Schmidt, Nucl. Instrum. Methods A **301**, 202 (1991).

77. J. Allison *et al.*, Nucl. Instrum. Methods **133**, 325 (1976).
78. K. Lassilla-Perini, L. Urban, Nucl. Instrum. Methods A **362**, 416 (1995).
79. Geant3 manual, Technical report (1993) CERN program library W5013.
80. *GEANT4: An object oriented toolkit for simulation in HEP*, Technical report, Geneva (1998) `http://geant4.cern.ch`.
81. S. Biagi, Nucl. Instrum. Methods A **421**, 234 (1999).
82. P. Branchini *et al.*, IEEE Trans. Nucl. Sci. **53**, 317 (2006).
83. W. Riegler *et al.*, Nucl. Instrum. Methods A **443**, 156 (2000).
84. For the PANDA Collaboration (S. Spataro), J. Phys. Conf. Ser. **331**, 032031 (2011).
85. M. Al-Turany, F. Uhlig, PoS **ACAT08**, 048 (2008).
86. `http://www.gsi.de/forschung/fair_experiments/CBM/index_e.html`.
87. `http://www-hades.gsi.de/`.
88. `http://www.gsi.de/forschung/kp/kr/R3B_e.html`.
89. `http://root.cern.ch/drupal/content/vmc`.
90. I. Hřivnàčovà *et al.*, eConf **C0303241**, THJT006 (2003) arXiv:cs/0306005.
91. V. Innocente *et al.*, CERN Program Library, W5013-E (1991).
92. $\overline{\mathsf{P}}$ANDA Computing Group, *A data analysis and simulation framework for the* $\overline{\mathsf{P}}$ANDA *Collaboration*, Technical report (2006) Scientific Report GSI.
93. $\overline{\mathsf{P}}$ANDA Computing Group, *Status of the PandaRoot simulation and analysis framework*, Technical report (2007) Scientific Report GSI.
94. A. Wronska, Simulation of the $\overline{\mathsf{P}}$ANDA experiment with PandaRoot, in *Proceedings of MENU2007*, eConf C070910 (2007) p. 307.
95. R. Fruhwirth *et al.*, Nucl. Instrum. Methods A **490**, 366 (2002).
96. P. Hough, U.S. patent 3069654 (1962).
97. `http://www.slac.stanford.edu/~lange/EvtGen`.
98. R.E. Kalman, J. Basic Eng. **82**, 34 (1961).
99. R. Fruhwirth *et al.*, Nucl. Instrum. Methods A **262**, 444 (1987).
100. A. Fontana, P. Genova, L. Lavezzi, A. Rotondi, *Track following in dense media and inhomogeneous magnetic fields*, Technical report (2007).
101. L. Lavezzi, *The fit of nuclear tracks in high precision spectroscopy experiments*, PhD thesis, Università degli Studi di Pavia (2007).
102. C. Höppner *et al.*, Nucl. Instrum. Methods A **620**, 518 (2010).
103. R. Fruhwirth *et al.*, *Data Analysis Techniques For High Energy Physics* (Cambridge University Press, 1990).
104. V. Innocente, E. Nagy, Nucl. Instrum. Methods A **324**, 297 (1993).
105. G. Schepers *et al.*, *Particle Identification at* $\overline{\mathsf{P}}$ANDA , Technical report (2009) Report of the PID TAG.
106. V. Flaminio *et al.*, Compilation Of Cross-Sections, 3, P And Anti-P Induced Reactions, Technical report (1984) CERN-HERA-84-01.
107. M.A. Selen, R.M. Hans, M.J. Haney, IEEE Trans. Nucl. Sci. **48**, 562 (2001).
108. R.M. Hans, C.L. Plager, M.A. Selen, M.J. Haney, IEEE Trans. Nucl. Sci. **48**, 552 (2001).
109. B. Aubert *et al.*, Nucl. Instrum. Methods A **479**, 1 (2002).
110. A. Abashian *et al.*, Nucl. Instrum. Methods A **479**, 117 (2002).
111. M. Ablikim *et al.*, Nucl. Instrum. Methods A **614**, 345 (2010).
112. G.P. Heath *et al.*, Nucl. Instrum. Methods A **315**, 431 (1992).
113. P.D. Allfrey *et al.*, Nucl. Instrum. Methods A **580**, 1257 (2007).
114. I. Abt *et al.*, Nucl. Instrum. Methods A **386**, 310 (1997).
115. A. Baird *et al.*, IEEE Trans. Nucl. Sci. **48**, 310 (2001).
116. Y.H. Fleming, *The H1 First Level Fast Track Trigger*, PhD thesis, DESY-THESIS-2003-045 (2003).
117. T. Affolder *et al.*, Nucl. Instrum. Methods A **526**, 249 (2004).
118. E.J. Thomsonand *et al.*, IEEE Trans. Nucl. Sci. **49**, 1063 (2002).
119. R. Downing *et al.*, Nucl. Instrum. Methods A **570**, 36 (2007).
120. V. Abazov *et al.*, Nucl. Instrum. Methods A **565**, 463 (2005).
121. J. Olsen *et al.*, IEEE Trans. Nucl. Sci. **51**, 345 (2004).
122. S. Chatrchyan *et al.*, JINST **3**, S08004 (2008).
123. G. Aad *et al.*, JINST **3**, S08003 (2008).
124. A. dos Anjos *et al.*, IEEE Trans. Nucl. Sci. **51**, 909 (2004).